Title
Transport and topology in strongly correlated two-dimensional systems, using techniques from one dimension

Author
Szasz, Aaron Miklos Strimling

Publication Date
2019

Peer reviewed|Thesis/dissertation

Transport and topology in strongly correlated two-dimensional systems, using techniques from one dimension

by

Aaron Miklos Strimling Szasz

A dissertation submitted in partial satisfaction of the

requirements for the degree of

Doctor of Philosophy

in

Physics

in the

Graduate Division

of the

University of California, Berkeley

Committee in charge:

Professor Joel E. Moore, Chair
Professor Ehud Altman
Professor Umesh Vazirani

Summer 2019

Transport and topology in strongly correlated two-dimensional systems, using techniques from one dimension

Abstract

Transport and topology in strongly correlated two-dimensional systems, using techniques from one dimension

by

Aaron Miklos Strimling Szasz

Doctor of Philosophy in Physics

University of California, Berkeley

Professor Joel E. Moore, Chair

Many of the most interesting problems in theoretical condensed matter physics involve the study of two- and three-dimensional materials, but this is in general very difficult. On the other hand, one-dimensional quantum systems are much better understood, with exact solutions possible using techniques like bosonization, and with extremely efficient numerical approaches based on matrix product states. Thus one promising route to studying higher-dimensional systems is the application of techniques developed for one-dimensional systems. In this dissertation I discuss two research projects in which I use this approach.

In the first study, motivated by intriguing experiments that have shown two-dimensional polymer films to be promising materials for thermoelectric devices, I consider a two-dimensional material consisting of an array of one-dimensional systems. Each is treated as a strongly-interacting Luttinger liquid, and I assume weak (incoherent) coupling between them, an approximation which I refer to as the "quasi-atomic limit." I find integral expressions for the (interchain) transport coefficients, including the electrical and thermal conductivities and the thermopower, and I extract their power law dependencies on temperature. Luttinger liquid physics is manifested in a violation of the Wiedemann-Franz law; the Lorenz number is larger than the Fermi liquid value by a factor between γ^2 and γ^4, where $\gamma \geq 1$ is a measure of the electron-electron interaction strength in the system.

In the second project, motivated by experimental studies that have found signatures of a quantum spin liquid phase in organic crystals whose structure is well described by the two-dimensional triangular lattice, I study the Hubbard model on this lattice at half filling using the infinite-system density matrix renormalization group (iDMRG) method. On infinite cylinders with finite circumference, I identify an intermediate phase between observed metallic behavior at low interaction strength and Mott insulating spin-ordered behavior at strong interactions. Chiral ordering from spontaneous breaking of time-reversal symmetry, a fractionally quantized spin Hall response, and characteristic level statistics in the entanglement spectrum in the intermediate phase provide strong evidence for the existence of a chiral spin liquid in the full two-dimensional limit of the model.

To my parents

Contents

Acknowledgments

The Ph.D. is a massive undertaking, even more so than I realized nearly seven years ago when I entered the program, and it would have been impossible without the support of many people. First and foremost, I owe a great thanks to my Ph.D. advisor, Joel Moore; his support has been constant and essential. I appreciate both the guidance he provided in picking projects and progressing on them and also the freedom he allowed me to pursue my own interests as they developed. At times I found myself feeling stuck and frustrated, and as a result making little progress, and I would go into a meeting with Joel expecting him to react with disappointment; instead, I always came away feeling encouraged and refreshed, ready to continue and make progress. This sort of kindness and supportiveness is not valued as highly as it ought to be. I also would like to thank the other members of my thesis committee, Professor Ehud Altman and Professor Umesh Vazirani, for reading this dissertation and for helping me to, at long last, graduate.

I am very grateful also to the support of my coauthors on the papers I worked on during my Ph.D. Early on in my graduate studies, I worked on transport studies with Roni Ilan, who was then a postdoc in the group, and she was very helpful with my adjustment to research in theoretical condensed matter. Johannes Motruk, a postdoc who I have worked with for the past two years, has been immensely helpful. The study of the Hubbard model that I have been working on was his idea, and so of course I am grateful that he led me to a project which arguably is the reason I am now able to continue in academic physics research as a postdoc once I receive my degree. Even more than this, though, as an expert in the numerical methods I was just beginning to learn, he was patient and helpful in his explanations, and never judgmental; I was able to feel totally comfortable asking questions and thus revealing holes in my knowledge, without worry that he would think poorly of me, for which I am extremely grateful. When he becomes a professor, his students will be lucky to have such an advisor. Finally, I worked with Michael Zaletel. We had overlapped briefly as graduate students as I was arriving and he was leaving, though at that time we had no opportunity to work together; it was a great pleasure, then, to do so when he returned to Berkeley as a professor. I have benefited tremendously from Mike's inexhaustible knowledge of tensor networks, spin liquids, entanglement, and basically any other subject in which I am interested.

Many others proved very helpful in completing various research projects. For the coupled Luttinger liquid paper, input from Lena Evans, Snir Gazit, Christoph Karrasch, Takahiro Morimoto, and Benjamin Ponedel was quite helpful. For the triangular lattice Hubbard model study, we had useful conversations and input from many people: Bryan Clark, Ryan Mishmash, Roger Mong, Frank Pollmann, Tomonori Shirakawa, Shigetoshi Sota, Senthil Todadri, Hiroshi Ueda, Ruben Verresen, and Seiji Yunoki were all very helpful. For my entanglement study, I received helpful advice from Eric Dodds, Lena Evans, Yichen Huang, and Quntao Zhuang.

Beyond those I worked with directly on research projects, many others in the physics department have provided invaluable support. I entered Joel's research group alongside

Byungmin Kang and Shudan Zhong, and I enjoyed sharing office space and research discussions with them throughout the many years of the Ph.D., especially with Byungmin, who I shared an office with for longer than anyone else and who became a great friend. More recently, it has been a pleasure to work with and get to know the more recent students to join the group, including Will Berdanier, Dan Parker, Vir Bulchandani, Tianrui Xu, Jonny Cookmeyer, and Yanqi Wang. I also had the good fortune of getting to know the many postdocs who passed through the group over the past seven years, and I am grateful to all of them for sharing their wisdom about physics (and more than a few conversations about politics as well).

I am also grateful for many years of support from the physics department administrative staff, including Donna Sakima, Joelle Miles, Kathy Lee, Claudia Trujillo, Amanda Dillon, and Anthony Vitan. I especially want to thank Anne Takizawa, who was the first person to make me feel at home in the physics department. It sometimes seemed like she single-handedly kept the entire department functioning.

I also owe a special thanks to Irfan Siddiqi, who in many ways served as a second advisor. Although I never worked with him on research, I was a graduate student instructor for his class for three semesters, and it was always a wonderful experience. Each semester he placed successively more trust in me and my ability to contribute to running the class; the experience I had as his GSI will be invaluable when I am eventually teaching classes of my own. He also was happy to offer me advice about things like applying for postdocs, and I cannot overstate how helpful he has been.

Getting through the Ph.D. requires not just the help of those in the physics department, but also the love and support of friends and family. I was lucky enough to become great friends with several of my classmates who entered the graduate program alongside me, especially Eric Dodds, Benjamin Ponedel, Lena Evans, and Ziqi Yan. Daily lunches with Eric, Lenny, and Ziqi kept me grounded through the most difficult years of grad school, and long meandering walks discussing politics with Ben were always enjoyable. Outside of the physics department, I have also become great friends with Rachel Chin and Tristan Lall. I have shared fun and adventure, from boardgames to camping to puzzle competitions, with all of these friends and many others, especially Maribel Sierra, Alex Anderson, Jacob Emmert-Aronson, Nicolas Ferland, Sylvia Lewin, Ryan Janish, Greg Affeldt, Fabio Sanches, and Song Zhang.

I owe special thanks to Philip Mocz and Charles Herrmann. It has been 11 years since we first emailed back and forth in preparation for sharing a room in freshman year of college, and their constant friendship and support ever since has been truly invaluable. As the three of us have all gone through graduate school in parallel, it has felt like we are doing it together even if in different subjects and separated by a continent. Thank you so much for all the years of friendship, and I look forward to many more. More friends from college for whose continued support through grad school I am very grateful include Tiffany Cai, Blake Wilkey, Marta Bryan, and Lucia Mocz.

Finally, I want to thank my family. I have been fortunate these past seven years to live near to almost my entire extended family, and it has been wonderful to have that love and

support through everything that has happened, joyful and sad, over this time. Both of my siblings, Emily and Justin, have been very supportive throughout my time in grad school. It was especially wonderful for four of my seven years to have Emily in Berkeley with me, sharing dinners and providing exercise I didn't know I needed in the form of moving her furniture to a new apartment every year. She also gave me a great reminder to hurry up and finish, since she started her undergraduate studies a year after I began my Ph.D. and finished when I was still far from done!

Most of all, I want to thank my parents. Their love and encouragement has been constant for the past 29-ish years, and I would (and not just literally) not be here without them. They instilled in me a love of learning and fostered my interest in math, while giving me complete freedom to study the subjects I found interesting. I think my dad can also be blamed for my wanting to become an academic, despite his best efforts to tell me not to; watching him teach a giant roomful of students was inspiring, and it was hard not to see him enjoying both the teaching and the opportunity to think about research projects that interested him. Although I can now see that these are the best parts of a career that also includes things like a terrible job market and excessive publication pressure, I do not regret the path that I have chosen. So to my parents: thank you so much, for everything.

Chapter 1

Introduction

The work presented in this dissertation primarily belongs to two research projects, which have previously been discussed in the following papers:

- Aaron Szasz, Roni Ilan, and Joel E. Moore, "Electronic and thermal transport in the quasiatomic limit of coupled Luttinger liquids," Physical Review B **95**, 085122 (2017).[110]
- Aaron Szasz, Johannes Motruk, Michael P. Zaletel, and Joel E. Moore, "Chiral spin liquid phase of the triangular lattice Hubbard model," arXiv 1808.00463.[111]

I include in the dissertation the key results of those studies, as well as the scientific context for each and details of the calculations and the methods used. I hope that readers will find the dissertation to be both of scientific interest and helpful as background future work.

At first glance, the two projects appear to be entirely unrelated—one concerns transport phenomena in two-dimensional materials formed by coupling one-dimensional conductive wires in a plane, while the other is about determining the nature of the ground state in a full two-dimensional model, and furthermore one is largely analytical while the other is primarily numerical. In fact, what the two projects share is a general approach to studying complex and strongly interacting systems in two dimensions using an understanding of the much better-understood physics of one-dimensional systems.

In general, studying two-dimensional systems with strongly interacting electrons is extremely difficult. Exact solutions are possible only for very special models with many conserved quantities. Field theory approaches using renormalization group flows are very powerful, as are variational methods with physically inspired simple ansatze, but for many of the most interesting and difficult systems these methods, too, are unreliable. In such cases, one must use heavily numerical approaches, but these are also limited. Exact diagonalization is limited to exceedingly small system sizes, while density functional theory often fails to correctly capture correlation effects, quantum Monte Carlo is often prevented from being useful due to the sign problem, and two-dimensional tensor network-based methods can only capture a limited amount of entanglement.

One-dimensional systems, on the other hand, are far easier to study. From the perspective of analytical calculations, the Bethe ansatz and bosonization allow for the exact solution of even strongly interacting models. From the numerical perspective, techniques like the density matrix renormalization group (DMRG) that are based on matrix product states are extremely efficient, allowing ground state computations scaling only linearly in the system size for gapped systems and remaining relatively efficient even for gapless ones. Studying finite temperature systems and time evolution is still difficult with such numerical methods, but even for these problems they remain quite useful.

It is therefore not surprising that one of the best ways to study two-dimensional systems is to invoke either knowledge or methods from the study of one-dimensional systems, giving as a result a controlled approximation that provides substantial insight into the original system. I now explain how my collaborators and I used this approach in each of the two projects.

1.1 Transport in weakly coupled Luttinger liquids

The coupled Luttinger liquid study is motivated by the surprising transport behavior of polymer thin films.[139, 59, 18, 32] These are materials where long one-dimensional molecules combine into a two-dimensional layer, which is partially ordered and partially amorphous. Experiments on such materials have revealed remarkable transport behavior, distinct both from transport in individual conductive one-dimensional systems as described by the Luttinger liquid theory[37, 31] and from transport in two-dimensional conductive systems described by the Fermi liquid theory. In particular, the polymer films are very promising as thermoelectric materials, showing remarkably high thermoelectric figure of merit while also being made from abundant and nontoxic materials, unlike traditional thermoelectrics.

These polymer thin films are strongly correlated, and as a result a direct approach to the two-dimensional system will, as discussed above, be very difficult. Instead, my collaborators and I make use of the fact that the physical components of the material are one-dimensional systems (the polymers), and we make the assumption that the strong electron interactions occur only within each 1D system and not between electrons on different ones. We are then able to use well-known properties of conductive wires, as described by the Luttinger liquid theory, to account for the difficult-to-model interactions, resulting in tractable transport calculations. We call this approximation of strong interactions within each one-dimensional chain and weak coupling between them the "quasi-atomic limit."

Using this approach, we are able to compute electrical and thermal conductivites as well as the thermopower, and we extract their power law dependencies on temperature. We find behavior distinct both from one-dimensional Luttinger liquid physics and from two-dimensional Fermi liquid physics. The latter in particular is manifested in a violation of the Wiedemann-Franz law; the Lorenz number, which measures the ratio between electrical and thermal conductivity, is larger than the Fermi liquid value by a factor between γ^2 and γ^4, where $\gamma \geq 1$ is a measure of the electron-electron interaction strength in the system.

The discussion of this project is contained in chapters 2, 3, and 4. Chapter 2 discusses the context for the work, including past experimental and theoretical studies, and presents the main results. In chapter 3 I present some details of the calculations, and in chapter 4 I show nearly every step of the calculations and also explain in some depth the methods I used for linear response and numerical analytic continuation.

For background material on Luttinger liquids and the technique of bosonization, I refer the reader to the book by Thierry Giamarchi, reference [31]. For background on linear response theory, the precise version of the formalism that I use is explained in section 4.1 below, and is largely based off of the third edition of the book by Gerald Mahan, reference [70].

1.2 Chiral spin liquid phase of the triangular lattice Hubbard model

In the second project I have studied a very different kind of physical system, namely crystals composed of large organic molecules. The key example is the crystal κ-$(ET)_2Cu_2(CN)_3$, which has nearly independent layers composed of the ET molecule, also known as BEDT-TTF or bis(ethylenedithio)-tetrathiafulvalene; each ET layer acts approximately like a simple triangular lattice with one electron per site.[105] This crystal, and others like it, show a remarkable lack of magnetic ordering down to extremely low temperatures, suggesting that geometric frustration of antiferromagnetism may lead to a so-called spin liquid ground state.[105, 135, 134, 50, 48, 133, 49, 81, 16, 132] To investigate this possibility, I have modeled this kind of organic crystal with the Hubbard model on the triangular lattice.

The Hubbard model is one of the premier models for studying correlated-electron physics. It is quite conceptually simple: electrons are considered localized on lattice sites, and they have kinetic energy from moving around the lattice (characterized by an energy scale t) and interaction energy from Coulomb repulsion if multiple electrons are on the same lattice site (characterized by an energy scale U). Despite this conceptual simplicity, the model gives rise to complex behavior. Even on bipartite two-dimensional lattices, its behavior is not well understood, much less in the presence of frustration on the triangular lattice.

When U is large in comparison to t, the charges will be gapped when there is one electron per site, and only the spin degrees of freedom will be relevant at low energy. These might magnetically order, or alternatively they could form a (possibly topological) spin liquid, with no magnetic ordering down to zero temperature. An antiferromagnetically ordered state is strongly favored on a bipartite lattice, but the ordering becomes destabilized on a frustrated lattice, making these great candidates to realize spin liquids.

In this project, my collaborators and I investigate the triangular lattice Hubbard model, and we show that for a range of U/t, the ground state is a chiral spin liquid, a topological state that spontaneously breaks the underlying time-reversal symmetry of the Hamiltonian.[53, 125] This is an exciting and surprising result. In particular, it is to my knowledge the first

demonstration of a topological state with spontaneous time-reversal symmetry-breaking in a model of itinerant fermions, and it also can potentially explain some behaviors of the above-mentioned organic crystals that were not previously understood.

I performed the computations for this project using the density matrix renormalization group (DMRG) technique.[128, 127, 86, 99] DMRG works by assuming a particular ansatz for the wave function, namely a matrix product state (MPS), which has many thousands of parameters, then optimizing those parameters to find the state with the lowest energy. The number of parameters provides a controllable way to improve the accuracy of the simulation, and the end result is an unbiased approximation to the true ground state.

There is, however, a catch: an MPS naturally describes one-dimensional systems, not two-dimensional ones; as with the Luttinger liquid study discussed above, here too we are using a one-dimensional computational method to approach a higher-dimensional problem. To do so, we limit the two-dimensional triangular lattice to a finite width strip, which we roll into a cylinder. By increasing the cylinder circumference, it is possible to get successively better approximations to the full two-dimensional model. We also use magnetic flux insertion through the cylinder to get information about the two-dimensional system from the quasi-one-dimensional cylinders.

This project is discussed below in chapters 5, 6, and 7. In chapter 5, I present the context of the work including a history of past experimental and theoretical studies, and I present our key findings. In particular, I show that the model has metallic, nonmagnetic insulating, and magnetically ordered phases, and I show that the second phase is in fact a chiral spin liquid. In chapter 6, I provide some useful details of our approach to the calculation, especially regarding the use of the one-dimensional DMRG approach to study a two-dimensional system. Finally, in chapter 7, I present additional data from the numerical simulations that help to support the claims in chapter 5.

Background material on spin liquids can be found in a number of reviews, including by Balents[8]; Savary and Balents[97]; Zhou, Kanoda, and Ng[145]; and Knolle and Moessner[62]. For background on matrix product states, I refer the reader to the excellent review by Schollwöck, reference [99]. A clear discussion of the infinite-system DMRG method can be found in a paper by Kjäll et al., reference [61], and an introduction to the mixed-space approach to DMRG that my collaborators and I use can be found in a paper by Motruk et al., reference [78].

Part I

Study of transport in weakly coupled Luttinger liquids

Chapter 2

Electrical and thermal transport in the quasi-atomic limit of coupled Luttinger liquids

I first present my work on transport in weakly coupled one-dimensional systems, as published in Physical Review B[110]. This work was performed in collaboration with Roni Ilan and Joel Moore. In this chapter I present the context for the work and the key results, and I discuss their significance. In chapter 3, I present some details of the calculations, and in chapter 4 I discuss the methods used and present many further details.

2.1 Introduction

Recent experiments on thin films of doped polymers such as PEDOT-PSS, PEDOT-Tos, and PBTTT have found both high conductivity and a large thermopower [139, 59, 18, 32]. There are some possible explanations for the source of conductive behavior in polymers [40, 96], but they are not yet definitive; in the work presented here, we will bypass this question and instead analyze a different facet of the problem. Namely, since we take for granted the conductive nature of individual polymers and can can therefore describe each polymer as a Luttinger liquid, and we look for possible signatures of the Luttinger liquid behavior that survive even when the one-dimensional systems are coupled to form a quasi-two-dimensional material.

The Luttinger liquid model [37, 31] represents a one-dimensional electron gas modified by interaction between the electrons and can therefore be viewed as the one-dimensional analogue of the more well-known Fermi liquid model, though the generic behavior of the system is quite different. In the Fermi liquid theory for two- and three-dimensional systems, the interacting system actually behaves very much like the corresponding non-interacting electron gas—the excitations are fermionic quasiparticles which behave qualitatively like electrons even if specific properties like mass are renormalized to new values.

By contrast, in one dimension interactions between electrons have a strong qualitative effect on the behavior of the system. Schematically, one can picture electrons in higher-dimensional systems having space to "go around" each other and thus they still remain roughly independent (noninteracting), while in one dimension this is impossible, and so electrons will move together, forming collective (bosonic) excitations. The Luttinger liquid theory and the technique of bosonization make this intuitive idea concrete.

There are numerous convincing experimental results on one-dimensional systems that confirm various predictions of the Luttinger liquid theory. For instance, Luttinger liquids are expected to exhibit spin-charge separation, where charge and spin degrees of freedom act independently [31]; spin-charge separation has been convincingly observed via photoemission experiments in artificially created one-dimensional structures [101]. Likewise, the density of states around the Fermi level is predicted to show a distinctive power law behavior [17]; this was also observed in an artificially created 1D chain [15]. Other observations of Luttinger liquid-like behavior, however, have been made not on actual one-dimensional chains but rather on two-dimensional collections of one-dimensional systems such as in the polymer films that motivated this work[139] or on highly anisotropic three-dimensional crystals[77, 119, 9]; it is not immediately clear that the results of these experiments should be directly compared to theories of single Luttinger liquids. Rather, the coupling of 1D chains to form a quasi-2D material may modify or destroy altogether the distinctive signatures of Luttinger liquid behavior. A theory of coupled Luttinger liquids would thus be very helpful.

While the theory of weakly coupled Luttinger liquids has been considered in the past by many different authors, there are very few results for thermal transport in a system of infinitely many coupled chains. Some results deal with "ladders" consisting of just two coupled chains [21, 31], while some of the most well-known treat coupling two half-infinite chains at their ends as a way of modeling an impurity in the Luttinger liquid[56, 55, 54]. Both electrical and thermal transport have also been computed for many impurities on a single chain[67]. Papers that do consider an infinite array of weakly coupled Luttinger liquids have mostly focused only on the electrical conductivity [77, 22, 29] and not on any kind of thermal transport. There is one recent paper on the off-diagonal terms of the thermopower tensor for infinitely many coupled chains[98], but I am not aware of any previous results for the thermal conductivity or Lorenz number in the type of model we consider. This is the gap this work is intended to fill.

In this work we consider a model of coupled one-dimensional systems in which each 1D chain is treated as a (spinless) Luttinger liquid, and the individual chains are coupled by a perturbatively weak interchain hopping. We refer to this situation of strong interactions within 1D chains and weak, incoherent coupling between them as the "quasi-atomic limit." The approximations and assumptions inherent in this model, as well as some justifications of their validity, are discussed in section 2.2.

We consider two somewhat different versions of the model, which incorporate Luttinger liquid behavior at different stages of the calculation. In both cases, we calculate transport coefficients using the Kubo formalism. In the first model, discussed in section 2.3, the electronic system is initially assumed to be noninteracting so that the state of the system

can be described by occupation of single-particle orbitals; we introduce Luttinger behavior via the electronic density of states. In the second model (section 2.4), we use the full Luttinger liquid correlation functions. In section 2.5, we summarize our key results and their applicability to experimental systems, and we further discuss the comparison between the two models.

We find that both models predict the same power law dependence on temperature for the transport coefficients, $\sigma \propto T^{2\gamma-3}$ and $\kappa \propto T^{2\gamma-2}$, where γ is a measure of interaction strength as defined in equation (2.11), but that the precise values of the transport coefficients (as measured by the Lorenz number) vary with electron-electron interaction strength more strongly in the second, more complete, calculation. In the generalized noninteracting model (section 2.3) we find that the Lorenz number is larger than the value predicted by the Wiedemann-Franz law by a factor between γ^2 and $\gamma^{2.4}$. In the full Luttinger liquid model (section 2.4), we find an even larger violation, with the Lorenz number augmented by as much as $\gamma^{3.6}$.

2.2 Assumptions and approximations: the quasi-atomic limit

In the Hubbard model, the "atomic limit" is the limit as the hopping between lattice sites vanishes while electron-electron interaction is held constant [11, 80]. We study the problem of weakly coupled chains with a similar approach, in which we do a perturbative calculation to lowest order in the interchain hopping while treating each one-dimensional chain as a single coherent quantum system. This limit of full coherence in one direction (along chains) and weak incoherent hopping in the other direction (between chains) we call the "quasi-atomic limit."[1]

To be more precise, we make the following assumptions:

(1) There is no electron-electron interaction between the 1D chains.

(2) The different chains are perturbatively coupled through a weak hopping of electrons between adjacent chains.

(3) The 1D chains are located at evenly spaced points along a one-dimensional line, meaning that electrons may hop from one polymer to adjacent ones on either side of it and that the hopping strength between any pair of adjacent polymers is the same.

We will briefly justify the applicability of these assumptions to real physical systems, beginning with assumption (2). To measure transport properties for a macroscopic object (like a polymer film) we really want to use not the microscopic model of the system but rather an

[1]Note that the term "quasi-atomic limit" has been used in the past to describe situations between full coherence and the atomic limit[107, 92]; we use it instead to indicate a system that is fully in the atomic limit in one direction and not at all in the other.

effective theory that results from a renormalization group flow. At zero temperature, any coupling between chains is a relevant perturbation in the renormalization group sense, but fortunately this is not the case at finite temperature[23, 21, 12]. This means that, so long as the temperature is much higher than the energy scale of the interchain coupling, the atomic limit will be valid. For any particular material, this sets a lower bound on the temperature regime in which our results are applicable.

In this temperature regime of validity, the thermalization time within each chain (proportional to $1/T$) will be much less than the interchain hopping time (proportional to the inverse hopping strength), so that each individual one-dimensional chain will thermalize between hopping events. We can therefore intuitively think of the interchain hopping as incoherent, though we do not explicitly use that fact anywhere in our calculations.

Assumption (3) is an accurate description for the case of anisotropic crystals. The application to polymer films is less direct, as they are known to have regions where the polymers are relatively aligned in some organized array (as in assumption 3), as well as amorphous regions [83, 18, 109]. In the latter regions, which may account for a significant fraction of the overall film, as long as the polymers form a single two-dimensional layer and do not cross, at a sufficiently small scale the polymers should still form a neat array and our assumption will apply. We can therefore approximately treat the film as consisting of a collection of randomly oriented domains, each of which individually satisfies the assumption. We discuss this further in section 2.5.

2.3 Generalized noninteracting model

The first version of our model is intended to capture the key Luttinger liquid behavior while still being simple enough to provide helpful physical intuition about the system we study. We thus use a noninteracting model for most of the calculation, finally substituting the Luttinger liquid density of states at the end.

To be precise, we add two more simplifying assumptions to those given in section 2.2 above:

(4) Each individual 1D chain can be described by a set of non-interacting single-particle orbitals, given by the Fourier modes of the localized on-site orbitals; the orbitals' energies are distributed according to the tunneling density of states of a Luttinger liquid, and each chain's orbitals are the same.

(5) Electrons hop from a well-defined single-particle eigenstate on one chain to an eigenstate with approximately the same energy and momentum on an adjacent chain. The hopping strength is sharply peaked in $|k - k'|$ where k and k' are the wavenumbers on the two chains, and the value at $k = k'$ is independent of k. (In practice, we assume the hopping is Gaussian in $k - k'$, but this assumption is only needed when we compare the two versions of our model, see section 3.3 of the next chapter.)

The five assumptions above lead to a specific interpretation of the standard tight-binding Hamiltonian

$$H = \sum_{j,k} E_k c^\dagger_{jk} c_{jk} - \sum_{jkk'} \left(t_{kk'} c^\dagger_{j,k} c_{j+1,k'} + \text{h.c.} \right) \tag{2.1}$$

The index j labels 1D chains, while k and k' label extended (Fourier state) orbitals on each chain. $c^\dagger$ and c are the usual fermion creation and annihilation operators, while E_k is the single-particle energy corresponding to the orbital k.

In the noninteracting limit, the E_k are just the energies of a one-dimensional tight-binding model $H_0 = -t_{//} \sum_i c^\dagger_i c_{i+1} + \text{h.c.}$; if the lattice spacing is a, the energy levels are $E_k = -2t_{//} \cos(ka)$, which are then linearized around the Fermi points $k = \pm k_F$. When interactions are introduced, there are no longer well-defined single-particle orbitals, so we cannot give an explicit formula for the energies E_k. Instead, we will derive an expressions for the transport coefficients in which the energy spectrum only appears via the density of states, for which we can use the well-defined single-particle tunneling density of states of a Luttinger liquid.

Calculation of transport coefficients

We calculate the transport coefficients in this model using the Kubo formalism. For consistency with standard references, we use the conventions of reference [70], in which case the electrical conductivity, thermal conductivity, and thermopower are given by

$$\sigma = \frac{e^2}{T} L^{(11)} \tag{2.2a}$$

$$\kappa = \frac{1}{T^2} \left[L^{(22)} - \frac{(L^{(12)})^2}{L^{(11)}} \right] \tag{2.2b}$$

$$S = -\frac{1}{eT} \frac{L^{(12)}}{L^{(11)}} \tag{2.2c}$$

In a two dimensional material, each of these coefficients is actually a 2x2 matrix; the diagonal entries give the response in the direction of an applied field, while the off-diagonal entries give the response in a perpendicular direction (e.g., the Hall conductivity). We will specifically focus on the longitudinal response in the interchain direction.

The $L^{(il)}$ coefficients in the transport coefficient formulas are defined by[70, eqs. 3.487, 3.488]

$$J = -\frac{1}{T} L^{(11)} \nabla(eV) + L^{(12)} \nabla \left(\frac{1}{T} \right) \tag{2.3a}$$

$$J_E = -\frac{1}{T} L^{(21)} \nabla(eV) + L^{(22)} \nabla \left(\frac{1}{T} \right) \tag{2.3b}$$

where J is the particle current, or electrical current divided by the charge per particle, and J_E is the energy current. Note that $L^{(12)} = L^{(21)}$. In practice, we find the $L^{(il)}$ coefficients in terms of current-current correlation functions as[2]

$$L^{(il)} = \lim_{\omega\to 0}\lim_{\delta\to 0}\frac{1}{\omega}\left[\frac{-i}{\Omega\beta}\int_0^\beta d\tau e^{i\omega_n\tau}\langle T_\tau j_l(\tau)j_i(0)\rangle\right]_{i\omega_n\to\omega+i\delta} \tag{2.4}$$

where j_1 is the particle current operator J and j_2 is the energy current operator J_E. Both are the current operators for the interchain direction. Ω is the volume of the system. Because we calculate the transport coefficients at finite temperature, we perform the calculation using the Matsubara formalism. τ is the imaginary time, $\omega_n = 2\pi n/\beta$ for $n = 0, 1, 2, \cdots$ are the discrete (bosonic) Matsubara frequencies, and $i\omega_n \to \omega + i\delta$ indicates analytic continuation from the positive imaginary axis to just above the positive real axis. In practice we will take only the real part of $L^{(il)}$, since we are interested specifically in transport.

The current operators we find using [80]

$$J = \lim_{k\to 0}\frac{1}{k}\sum_j [N_j, H]e^{ika_c j} \tag{2.5a}$$

$$J_E = \lim_{k\to 0}\frac{1}{k}\sum_j [H_j, H]e^{ika_c j} \tag{2.5b}$$

in units where $\hbar = 1$. Here a_c is the distance between 1D chains and N_j is the total number operator on chain j, $N_j = \sum_k c^\dagger_{jk}c_{jk}$. H_j is the part of the Hamiltonian associated with chain j, which includes both the on-chain portion

$$h_j = \sum_k E_k c^\dagger_{jk}c_{jk} \tag{2.6a}$$

and the hopping portion

$$h'_j = -\frac{1}{2}\sum_{kk'} t_{kk'}\left(c^\dagger_{j,k}c_{j+1,k'} + c^\dagger_{j-1,k}c_{j,k'}\right) + \text{h.c.} \tag{2.6b}$$

This leads, after some algebra, to the expressions

$$J = ia_c\sum_{jkk'} t_{kk'}c^\dagger_{j-1,k}c_{j,k'} - t^*_{kk'}c^\dagger_{j,k'}c_{j-1,k} \tag{2.7a}$$

$$J_E = ia_c\sum_{jkk'}\left[\left(\frac{E_k + E_{k'}}{2}\right)\left(t_{kk'}c^\dagger_{j-1,k}c_{jk'} - \text{h.c.}\right)\right] \tag{2.7b}$$

[2]Equation (2.4) is a corrected version of (3.518) from reference [70]; see chapter 4 for details.

From these current operators and equation (2.4), we derive (see section 3.1 of the next chapter) the expression

$$\mathrm{Re}\left[L^{(il)}\right] = \frac{Aa_c t^2 v \beta^{-n_{il}}}{2\pi^4} \int \frac{g^2(y/\beta) y^{n_{il}}}{(1+e^y)(1+e^{-y})}\, dy \tag{2.8}$$

where $n_{il} = i + l - 2$ (e.g., 0 for $L^{(11)}$), v is the (possibly renormalized by interactions) Fermi velocity, A is a dimensionless number, t is the peak value of the interchain hopping $t = t_{kk}$, β as usual is $1/T$ (we use units of $k_B = 1$), and $g(E)$ is the electronic density of states. The integral over the dimensionless variable $y = \beta E$ runs from $-\infty$ to ∞.

The form of the integrand can be intuitively understood from a semiclassical perspective. If a particle is hopping from an orbital at energy E on one chain to an orbital at energy E on another, then the number of ways that can happen is the number of orbitals at that energy on the first chain, $g(E)$, multiplied by the fraction that are occupied, $(1+e^{\beta E})^{-1}$, times the number of orbitals at that energy on the second chain, $g(E)$, multiplied by the fraction that are unoccupied, $(1+e^{-\beta E})^{-1}$. Multiplying all of these factors and integrating over the energy gives

$$\int \frac{g^2(E)}{(1+e^{\beta E})(1+e^{-\beta E})} dE. \tag{2.9}$$

This should be proportional to the hopping rate, and therefore to the electrical conductivity. Indeed, equation (2.9) looks just like the integrand in equation (2.8) for $L^{(11)}$, which is proportional to the electrical conductivity. The fact that a semiclassical picture is helpful in understanding equation (2.8) is not too surprising given that our weak hopping assumption is only valid when the temperature is high enough for the interchain hopping to be incoherent.

This is the point in the calculation where the fact that each 1D chain is a Luttinger liquid becomes important. The density of states for a Luttinger liquid is given by Eq. (61) of reference [17] as

$$g_{LL}(E) = 2\frac{|E/W|^{\gamma-1}}{2\pi v \Gamma(\gamma)}, \tag{2.10}$$

valid for $E \ll W$, where $W = v/a$ is proportional to the Fermi energy ($E_F \propto k_F^2/m = (k_F/m)/k_F^{-1} \propto v/a$) or bandwidth of the underlying 1D model and γ is a measure of interaction strength in the Luttinger liquid defined by

$$\gamma = \frac{K + K^{-1}}{2}. \tag{2.11}$$

K is the usual Luttinger liquid interaction parameter, as defined for the Luttinger liquid Hamiltonian below (equation 2.23). (Note that using K for this parameter is a relatively standard convention, used for instance in the book by Giamarchi[31], though some authors refer to it as g or K^2.[56, 55, 54, 71]) $K = 1$ corresponds to noninteracting electrons, while $K < 1$ corresponds to repulsive interactions and $K > 1$ corresponds to attractive interactions. We have introduced the new parameter γ, which is symmetric in K and K^{-1}

and thus is independent of whether the interactions happen to be attractive or repulsive. It always satisfies $\gamma \geq 1$, and $\gamma = 1$ if and only if the system is noninteracting.

Substituting equation (2.10) into equation (2.8) and using that result in equations (2.2), we find the following results for the transport coefficients:

$$\sigma = \frac{a_c e^2 t^2}{vT} \left(\frac{T}{W}\right)^{2(\gamma-1)} \times \frac{A}{2\pi^6 \Gamma(\gamma)^2} \int_y \frac{|y|^{2(\gamma-1)}}{(1+e^y)(1+e^{-y})} dy \tag{2.12a}$$

$$\kappa = \frac{a_c t^2}{v} \left(\frac{T}{W}\right)^{2(\gamma-1)} \times \frac{A}{2\pi^6 \Gamma(\gamma)^2} \int_y \frac{y^2 |y|^{2(\gamma-1)}}{(1+e^y)(1+e^{-y})} dy \tag{2.12b}$$

$$S = 0 \tag{2.12c}$$

Both the thermopower and the second term of equation (2.2b) for the thermal conductivity vanish because $L^{(12)}$ is 0 when the density of states is particle-hole symmetric. Mathematically this follows because the integrand in equation (2.8) is odd when $g(E)$ is an even function.

Correction for nonzero thermopower

To model a real material and get nonzero thermopower, we can introduce an asymmetry in the band structure. In particular, the Tomonaga-Luttinger model begins by linearizing a typical 1D band structure around the Fermi points, so we adopt the picture that the Luttinger liquid arises from adding interactions to a 1D electron gas with a typical dispersion $E = \frac{\hbar^2 k^2}{2m} \propto k^2$. In that case, the density of states is $dk/dE \propto E^{-1/2}$. In our calculations above we have set the Fermi level to $E = 0$, in which case the noninteracting density of states becomes

$$g_{1\mathrm{D}}(E) \propto (E_F + E)^{-1/2}. \tag{2.13}$$

The Fermi energy is proportional to v/a, so for consistency with equation (2.10) we can write it as $E_F = b\,W$ for a dimensionless constant b. Using this 1D density of states as a correction to the Luttinger liquid one gives

$$g(E) = \frac{g_{\mathrm{LL}}(E)}{\sqrt{1 + E/(b\,W)}} \approx g_{\mathrm{LL}}(E) \left(1 - \frac{1}{2}\frac{E}{b\,W}\right). \tag{2.14}$$

This density of states is a phenomenological way of capturing the real physical behavior of the system which should be accurate enough to find how the thermopower depends on temperature. The most important features are the violation of particle-hole symmetry by the introduction of a bandwidth and the preservation of the density of states to lowest order in E/W when E is small (near the Fermi energy).

If we calculate $L^{(12)}$ with equation (2.14) replacing equation (2.10) as the density of states, we find for the thermopower

$$S = \frac{k_B^2 T}{We} \times \frac{\int \frac{y^2|y|^{2(\gamma-1)}}{(1+e^y)(1+e^{-y})}dy}{b\int \frac{|y|^{2(\gamma-1)}}{(1+e^y)(1+e^{-y})}dy} \tag{2.15}$$

where Boltzmann's constant has been restored to get the correct final units.

Note that in principle we could also use the same correction for the conductivities, equations (2.12), but any additional terms would be higher order in k_BT/W than those given above. k_BT/W must be small, otherwise the Tomonaga-Luttinger model, which is based on a linearized band structure (i.e., $W \to \infty$), would not be applicable at that temperature.

Lorenz number

The expressions for the conductivities, equations (2.12), are clear and understandable, but they do contain material-dependent parameters like a_c, v, and W. To find a robust result that can be tested experimentally, we would like a quantity in which these material-dependent quantities do not appear. One such parameter is the Lorenz number,

$$L = \frac{\kappa}{\sigma T}. \tag{2.16}$$

This is a particularly useful quantity to consider, since the Wiedemann-Franz law states that for a noninteracting system or for a Fermi liquid, the Lorenz number should take a specific value, namely

$$L_0 = \frac{\pi^2}{3}\left(\frac{k_B}{e}\right)^2. \tag{2.17}$$

The Lorenz number for our model can be found by dividing the results from equations (2.12) to get

$$L = \frac{k_B^2}{e^2}\frac{\int \frac{y^2|y|^{2(\gamma-1)}}{(1+e^y)(1+e^{-y})}dy}{\int \frac{|y|^{2(\gamma-1)}}{(1+e^y)(1+e^{-y})}dy}. \tag{2.18}$$

As expected from the Wiedemann-Franz law, in the noninteracting limit of $\gamma = 1$ we get precisely L_0. At $\gamma > 1$, this expression for L can be evaluated via numerical integration. With interactions, $\gamma > 1$, we find that $L > L_0$, violating the Wiedemann-Franz law. The Lorenz number is plotted as a function of the interaction strength γ in the lower curve in figure 2.1.

The Lorenz number should scale approximately as γ^2 in this model, since the extra two powers of y in equation (2.8) that appear for $L^{(22)}$ (and therefore κ) but not for $L^{(11)}$ (and therefore σ) become derivatives with respect to x if the expression is rewritten via Fourier transform; these derivatives act on the Green's function that looks roughly like $f(x)^{-\gamma}$ and

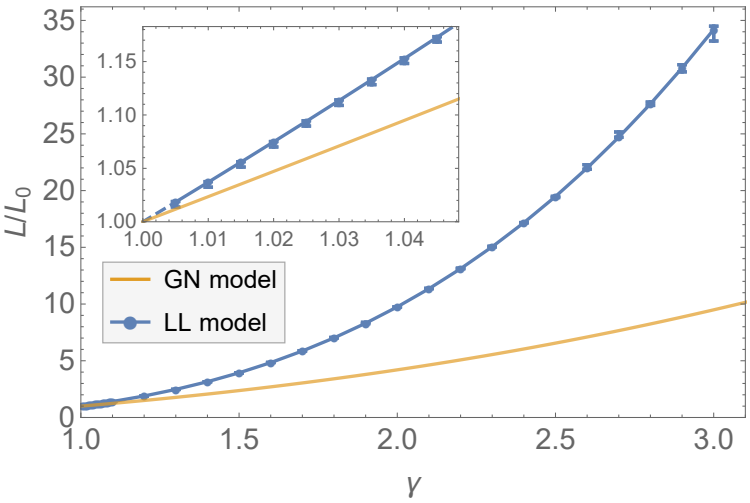

Figure 2.1: (Color online) Lorenz number, L, as calculated in the generalized noninteracting (GN) and Luttinger liquid (LL) models. The Lorenz number is plotted as a function of the interaction strength γ in units of L_0, the value expected from the Wiedemann-Franz law. For both models, we find that $L = L_0$ in the noninteracting case $\gamma = 1$. Electron-electron interactions ($\gamma > 1$) lead to a violation of the Wiedemann-Franz law; the violation is stronger in the LL model than in the GN model. The Lorenz number is evaluated at discrete points in the LL model; error bars indicate the precision of numerical results as described in the text. Lines connecting the data points for the LL model show linear interpolation between adjacent points, and the dashed line below $\gamma = 1.005$ in the inset shows extrapolation to $\gamma = 1$.

thus pull down two factors of γ. To test that it is indeed the case that $L \approx L_0\gamma^2$, we define $a(\gamma)$ by $L = L_0\gamma^{a(\gamma)}$ in which case

$$a(\gamma) = \frac{\log(L/L_0)}{\log(\gamma)}. \tag{2.19}$$

This quantity is plotted in figure 2.2. From the plot we see that the exponent a is between 2.35 and 2 for all interaction strengths γ. For large γ, the scaling of the Lorenz number is close to γ^2; for small γ, expanding around $\gamma = 1$ gives

$$\begin{aligned} a(\gamma \approx 1) &= 1 - 2\log(\pi) + \frac{6}{\pi^2}\left(\gamma_1{}'\left(\frac{1}{2}\right) - \gamma_1{}'(1)\right) \\ &\approx 2.3432 \end{aligned} \tag{2.20}$$

where $\gamma_1(\nu)$ is a generalized Stieltjes constant[13][3].

[3]For purposes of calculation, the generalized Stieltjes constant is implemented in the commercial software Wolfram Mathematica as $\gamma_n(\nu) = \text{StieltjesGamma}[n, \nu]$[121]

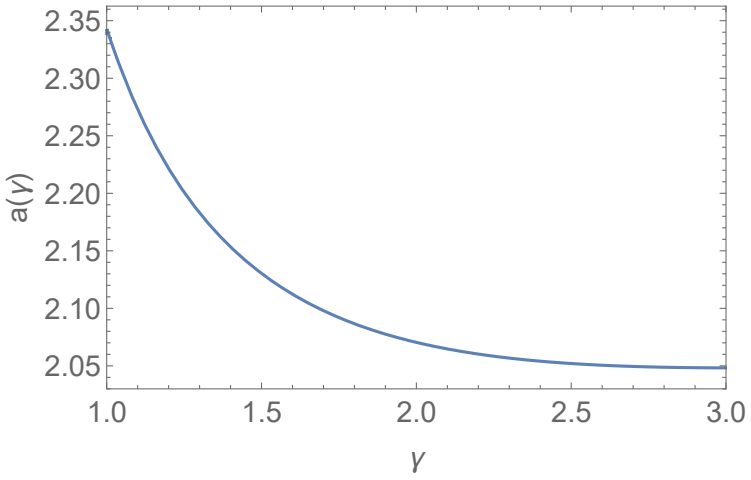

Figure 2.2: The Lorenz number scales as $L/L_0 = \gamma^{a(\gamma)}$. For the generalized noninteracting model we find $2 < a(\gamma) < 2.35$ for all γ, with $L \approx L_0\gamma^2$ for large γ.

Summary of generalized noninteracting model

Our most robust predictions are those that do not depend on any material-dependent parameter but the interaction strength. These are (a) the power law dependencies of σ, κ, and S on temperature and (b) the Lorenz number. We find that

$$\sigma \propto T^{2\gamma-3} \tag{2.21a}$$
$$\kappa \propto T^{2\gamma-2} \tag{2.21b}$$
$$S \propto T \tag{2.21c}$$

and

$$L = \frac{k_B^2}{e^2} \frac{\int \frac{y^2|y|^{2(\gamma-1)}}{(1+e^y)(1+e^{-y})} dy}{\int \frac{|y|^{2(\gamma-1)}}{(1+e^y)(1+e^{-y})} dy}$$
$$\approx L_0\gamma^2 \tag{2.22}$$

In the noninteracting case, $\gamma = 1$, the Lorenz number agrees with the usual Wiedemann-Franz Law. With either attractive or repulsive interactions, the Wiedemann-Franz law is violated as shown in figure 2.1.

2.4 Luttinger liquid model

In the second version of our model, we introduce Luttinger liquid physics much earlier in the analysis. To do so, we replace assumptions (4) and (5) with two new, corresponding assumptions:

(4') Each individual 1D chain is described by the Luttinger liquid Hamiltonian[31],

$$H = \frac{1}{2\pi}\int dx \left[vK(\nabla\theta)^2 + \frac{v}{K}(\nabla\phi)^2\right] \tag{2.23}$$

where again we have set $\hbar = 1$. As above, K is a parameter that measures interaction strength and v is the renormalized Fermi velocity. ϕ and θ are bosonic field operators related to the fermion operators by[31]

$$\psi_\alpha(x) = U_\alpha \lim_{a\to 0} \frac{1}{\sqrt{2\pi a}} e^{i\alpha k_F x} e^{-i(\alpha\phi(x)-\theta(x))} \tag{2.24a}$$

$$\psi_\alpha^\dagger(x) = U_\alpha^\dagger \lim_{a\to 0} \frac{1}{\sqrt{2\pi a}} e^{-i\alpha k_F x} e^{i(\alpha\phi(x)-\theta(x))} \tag{2.24b}$$

where α can be R or L (labeling right-movers versus left-movers) when used as an index and 1 or -1, respectively, when used as a multiplicative factor. The U_r operators are called Klein factors, and are included to make sure that the fermion operators anticommute and that they do not conserve particle number.

(5') Electrons hop between real-space localized orbitals. The hopping strength is sharply peaked in $|x - x'|$, where x and x' are the locations along the two chains, measured from the same "center" point (so that all the "$x = 0$" points lie on a line perpendicular to the chains). In the thermodynamic limit, a delta-function hopping in real space is consistent with the sharply peaked hopping in Fourier space from assumption (5) from the first version of our model (see section 3.3 in the next chapter). We also assume that right-movers on one chain can only hop to right-movers on the adjacent chain and the same for left-movers; this is needed for consistency with the approximate momentum conserving hopping in the generalized noninteracting model.

Including both on-chain and hopping terms, the Hamiltonian for this second version of our model is:

$$\begin{aligned} H &= \sum_j H_j = \sum_j h_j + h_j' \\ h_j &= \frac{1}{2\pi}\int dx \left[vK\left(\nabla\theta_j\right)^2 + \frac{v}{K}\left(\nabla\phi_j\right)^2\right] \\ h_j' &= -\frac{1}{2}\sum_{\alpha\beta}\int dx\, dx' \Big[t_{\alpha\beta}(x-x')\left(\psi_{j\alpha}^\dagger(x)\psi_{j+1,\beta}(x') + \psi_{j-1,\alpha}^\dagger(x)\psi_{j\beta}(x')\right) + \text{ h.c.}\Big] \end{aligned} \tag{2.25}$$

Calculation of transport coefficients

As in the generalized noninteracting model, to find the transport coefficients we first find operators for the electrical and energy currents. This can be done using equations (2.5) just

as before, but with the new definitions for h_j and h'_j. The results (for some details of the calculation, see section 3.2 in the next chapter) are

$$J = -ia_c \sum_j \sum_{\alpha\beta=R,L} \int t_{\alpha\beta}(x-x') \left[\psi^\dagger_{j\alpha}(x)\psi_{j-1,\beta}(x') - \psi^\dagger_{j-1,\alpha}(x)\psi_{j\beta}(x')\right] dx\, dx' \tag{2.26a}$$

$$J_E = -\frac{ia_c v}{2} \sum_{j\alpha\beta} \int t_{\alpha\beta}(x-x') \left[\left([\nabla_j]^\alpha_x + [\nabla_{j-1}]^\beta_{x'}\right)\psi^\dagger_{j\alpha}(x)\psi_{j-1,\beta}(x') - \left([\nabla_{j-1}]^\alpha_x + [\nabla_j]^\beta_{x'}\right)\psi^\dagger_{j-1,\alpha}(x)\psi_{j\beta}(x')\right] dx\, dx' \tag{2.26b}$$

where

$$[\nabla_j]^\alpha_y = \alpha K \nabla\theta_j(y) - K^{-1}\nabla\phi_j(y). \tag{2.27}$$

Unlike in the generalized noninteracting model, we do not find a single simple formula like equation (2.8) that gives all the transport coefficients. Instead, the particularly nice expressions that we find are for the current-current correlators in terms of the Green's function for a single Luttinger liquid:

$$\langle J(\tau)J\rangle = -2N_c L \left(\frac{a_c t}{2\pi}\right)^2 \sum_\alpha \int dx\, G_\alpha(x,\tau)G_\alpha(-x,-\tau) \tag{2.28a}$$

$$\langle J_E(\tau)J_E\rangle = -2N_c L\gamma^2 \left(\frac{a_c v t}{2\pi}\right)^2 \sum_\alpha \int dx \left[(k_F + i\alpha\partial_x)G_\alpha(x,\tau)\right]\times\left[(k_F - i\alpha\partial_x)G_\alpha(-x,-\tau)\right] \tag{2.28b}$$

$$\langle J_E(\tau)J\rangle = 2v\gamma N_c L \left(\frac{a_c t}{2\pi}\right)^2 \sum_\alpha \int dx\, G_\alpha(x,\tau)(k_F - i\alpha\partial_x)G_\alpha(-x,-\tau) \tag{2.28c}$$

For the Green's function we use the expression[71, 17]

$$G_\alpha(x,\tau) = -\frac{e^{i\alpha k_F x}}{2\pi a}\left[\frac{-ia}{\frac{v\beta}{\pi}\sinh\left(\frac{x-iv\tau}{v\beta/\pi}\right)}\right]^{\frac{\gamma-\alpha}{2}}\left[\frac{ia}{\frac{v\beta}{\pi}\sinh\left(\frac{x+iv\tau}{v\beta/\pi}\right)}\right]^{\frac{\gamma+\alpha}{2}} \tag{2.29}$$

and we are then able to perform the integration over x exactly, getting results in terms of the Appell hypergeometric function F_1 as defined in §16.13 of reference [82].[4] As an example, the result for $\langle J(\tau)J\rangle$ is

$$\langle J(\tau')J\rangle = 4N_c L \left(\frac{a_c t}{2\pi}\right)^2 \frac{2a}{(2\pi a)^2}\left(\frac{2\pi a}{v\beta}\right)^{2\gamma-1}\left(2f(\gamma,\tau',1,1) - \cos(2\tau')\big(f(\gamma,\tau',0,1)+f(\gamma,\tau',2,1)\big)\right) \tag{2.30}$$

[4] For purposes of calculation, the function F_1 is implemented in the commercial software Wolfram Mathematica as $F_1(a;b_1,b_2;c;x,y) = \text{AppellF1}[a,b1,b2,c,x,y]$[120]

where τ' is a scaled version of the imaginary time, $\tau' = \tau\pi/\beta$, and

$$f(\gamma, \tau, n, m) = \frac{F_1(\gamma + n; \gamma + m, \gamma + m; \gamma + n + 1; e^{2i\tau}, e^{-2i\tau})}{\gamma + n}. \tag{2.31}$$

The analogous expressions for the other two current-current correlators are longer and more complex, and thus proportionally less enlightening. We present them in section 3.2 of the next chapter for the edification of the interested reader.

The next step is to evaluate each of the $L^{(il)}$ coefficients using equation (2.4). In the previous model it was possible to perform the Fourier transform and analytic continuation analytically, but here we must perform the τ integrals of the current-current correlators numerically for each Matsubara frequency and then numerically perform the analytic continuation and limits. The procedure we follow is discussed further in Chapter 3, and in great detail in chapter 4.

For each transport coefficient, we get a numerical part from the procedure mentioned above and a prefactor that contains all the dimensionful quantities, notably the dependence on temperature. Including for now only the dimensionful quantities, we find

$$\sigma \propto \frac{a_c a\, q^2 t^2}{v^2} \left(\frac{a}{v\beta}\right)^{2\gamma-3} \tag{2.32a}$$

$$\kappa \propto \frac{a_c t^2}{v} \left(\frac{a}{v\beta}\right)^{2\gamma-2} \tag{2.32b}$$

$$S = 0 \tag{2.32c}$$

Recalling that the energy scale W introduced in the Luttinger liquid density of states, equation (2.10), was $W = v/a$, the dependence of the transport coefficients on the material-dependent parameters a_c, a, and v in this model (equations 2.32) precisely matches what we found in the generalized noninteracting model (equations 2.12).

In the generalized noninteracting model, we introduced a correction to the density of states to find a nonzero thermopower. Due to the complexity of the full Luttinger liquid model, we consider the equivalent correction here to be beyond the scope of this paper.

Lorenz number

The numerical analytic continuation has not yet been needed for the results presented above. We would like, however, to evaluate the Lorenz number numerically as a function of the interaction strength, γ, just as in the generalized noninteracting model. For that calculation, the full numerics are needed.

To compute the precise transport coefficients, for each interaction strength γ we must separately evaluate the Fourier transform of the current-current correlation functions at a number of Matsubara frequencies, fit an analytic function to these results, analytically

continue the function, and then take the limits as the frequency ω and the infinitesimal parameter δ go to 0. (For details, see chapter 4.)

Due to the complexity of the correlation functions (for instance equation 2.30), the calculation of each Fourier transform, and thus the calculation of transport coefficients for each interaction strength γ, is very computationally expensive. We therefore evaluate the Lorenz number for a limited number of values of the interaction strength, with a higher density around $\gamma = 1$ to make sure that the results in the noninteracting limit are reliable. The results are shown for γ in the range 1 to 3 by the discrete data points in figure 2.1 (connected by linear interpolation for visual clarity). An inset shows a detail of $\gamma \in [1, 1.05]$; from the inset it is clear that in the noninteracting limit the Lorenz number approaches the expected value from the Wiedemann-Franz law.

The error bars on the Luttinger liquid model data in figure 2.1 indicate the numerical precision of the Lorenz number for each γ. We compute the numerical integral for each Fourier transform with a relative precision of 10^{-10}, and allowing the values of the Fourier transforms to vary within this range and recomputing the Lorenz number gives a sharply peaked distribution of possible values of L. The error bars in the figure show one standard deviation of this distribution for each interaction strength γ.

Comparing the results of the full Luttinger liquid model with the corresponding results for the generalized noninteracting model, as shown in the upper and lower curves respectively in figure 2.1, we see that the full Luttinger liquid model exhibits a stronger violation of the Wiedemann-Franz law with increasing interaction strength. We argued that in the generalized noninteracting model the Lorenz number should scale as γ^2 because the two extra factors of energy for $L^{(22)}$ relative to $L^{(11)}$ in equation (2.8) act, in a real-space representation, as derivatives of the Green's function. For the full Luttinger liquid model, we can make a similar argument that $L/L_0 \approx \gamma^4$. There are indeed two derivatives acting on the Green's function in the expression for $\langle J_E(\tau) J_E \rangle$, equation (2.28b), that are not present in the expression for $\langle J(\tau) J \rangle$, equation (2.28a), giving rise to the same two factors of γ as in the generalized noninteracting model.

There are additionally two factors of γ in the prefactor in the expression for $\langle J_E(\tau) J_E \rangle$, which come from the $[\nabla_j]_x^\alpha$ operators in the expression for the energy current operator, equation (2.26b), and are thus missing from the generalized noninteracting model because there the energy current operator was derived in the noninteracting limit where $\gamma = 1$. With these two additional factors of γ included, we find that the Lorenz number should scale approximately as $L/L_0 \approx \gamma^4$.

This argument neglects the full complexity of the correlation functions, so to find more precisely how the Lorenz number scales with γ we again introduce the function $a(\gamma)$ defined by equation (2.19), $L/L_0 = \gamma^{a(\gamma)}$. This is plotted in figure 2.3. We find that L/L_0 satisfies $\gamma^{3.2} < L/L_0 < \gamma^{3.7}$ for $\gamma \leq 3$. This is a slightly weaker dependence than the predicted γ^4, but it is still a much stronger violation of the Wiedemann-Franz law than $L/L_0 \approx \gamma^2$ from the generalized noninteracting model.

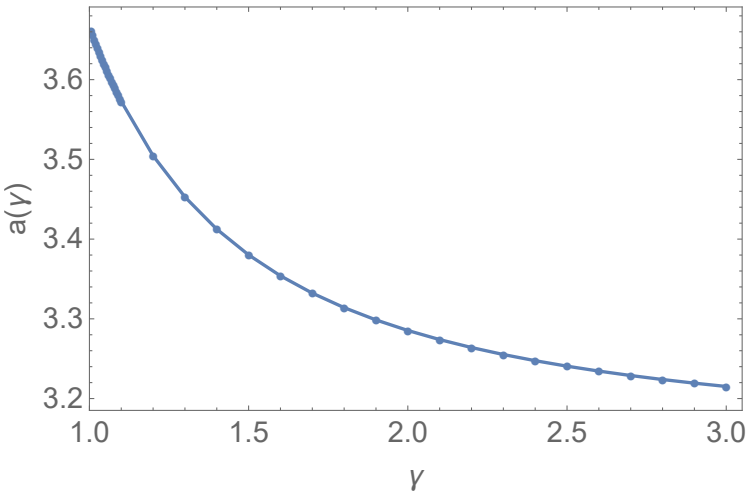

Figure 2.3: Exponent a in $L/L_0 = \gamma^{a(\gamma)}$ for the Luttinger liquid model. The dependence on γ is stronger than in the generalized noninteracting model. Lines are given by linear interpolation between adjacent data points, and error bars are omitted for clarity.

Summary of Luttinger liquid model

As in the generalized noninteracting model, it is useful to summarize those results that do not depend on any material-dependent parameter apart from the interaction strength. For the dependence of the conductivities on temperature, we find the same power laws as in the generalized noninteracting model, namely $\sigma \propto T^{2\gamma-3}$ and $\kappa \propto T^{2\gamma-2}$. For the Lorenz number we find a stronger violation of the Wiedemann-Franz law than in the generalized noninteracting model. We analytically estimate that

$$L \approx L_0 \gamma^4 \tag{2.33}$$

and numerically observe that

$$L_0 \gamma^{3.2} < L < L_0 \gamma^{3.7} \tag{2.34}$$

The precise dependence of the Lorenz number on the interaction strength is shown in figure 2.1. In the noninteracting case, $\gamma = 1$, the Lorenz number is L_0, the expected value from the Wiedemann-Franz Law.

2.5 Discussion and analysis

We have analyzed two different models for weakly coupled Luttinger liquids, finding in both cases the electrical and thermal conductivity. In terms of the interaction parameter γ, the conductivities scale in both models as $\sigma \propto T^{2\gamma-3}$ and $\kappa \propto T^{2\gamma-2}$. In both cases we find a violation of the Wiedemann-Franz law with increasing interaction strength; for the generalized noninteracting model $L \approx L_0 \gamma^2$ as shown in figures 2.1 and 2.2, while for the

Luttinger liquid model $L \approx L_0\gamma^{3.2}$ as shown in figures 2.1 and 2.3. This type of violation of the Wiedemann-Franz law as a power of the interaction strength is similar to the result of Kane and Fisher[54], although the precise dependence is of course different since our models describe a different physical system. In the generalized noninteracting model we also find a nonzero expression for the thermopower if we correct the density of states to account for particle-hole symmetry breaking, in which case $S \propto T$. This linear dependence of thermopower on temperature, which matches the expected behavior in a Fermi liquid, was also found by Kane and Fisher in their coupled chain model[54].

The violation of the Wiedemann-Franz law that we observe in both models is an indication that Luttinger liquid behavior survives when 1D chains are coupled to form a two-dimensional material. Just how large is the violation in practice? Experimental measurements[116] and theoretical calculations[100, 26, 27, 108, 2] have found Luttinger parameters in a typical range of about 0.2 through 1.5, corresponding to values of γ up to about 3. In both our models, $\gamma = 3$ would lead to a large violation of the Wiedemann-Franz law by an order of magnitude or more, an easily measurable effect that could be observed in experiments.

The results summarized here are all independent of any material-dependent parameters apart from the Luttinger liquid interaction parameter, which makes them good candidates for experimental testing and verification on any system with strong anisotropy that might lead to quasi-one-dimensional behavior. One very direct application of our theory would be to highly anisotropic crystals, as they typically have electron hopping strength along one axis which is at least an order of magnitude stronger than the hopping along the other two axes[116]. For temperatures between the two hopping scales, it would be reasonable to treat the system as a collection of weakly coupled 1D chains as we have done here, and by the nature of the crystal they form an ordered array, again matching our model. Such anisotropic crystals are known to show strong violations of the Wiedemann-Franz law, especially in the Hall direction in a magnetic field [119]. By comparing the measured violations of the Wiedemann-Franz law in these systems with our predictions, it should be possible to estimate the effective Luttinger parameter K for the constituent one-dimensional chains. Conversely, if K is independently known then such measurements would serve as a verification of our predictions.

Applying our theory to polymer films, the original motivation of the work, requires some additional effort since the films are partially amorphous. One approach would be to treat the polymer film as a polycrystal, consisting of randomly oriented grains; within each grain, the polymers form an ordered array to which our theory directly applies. The overall transport properties of the polymer film could then be found by averaging using methods like those discussed in reference [47]. The precise level of alignment of polymers can also vary significantly between films[83, 18, 109], and more work is needed to properly take this into account. One experimental result on polymer films which is clearly consistent with our calculations is the fact that some polymers show conductivity increasing with temperature, while others show the opposite behavior[18]. We find that σ increases with temperature if the interaction strength is large enough, $\gamma > 3/2$, but decreases with increasing temperature for $1 \leq \gamma < 3/2$.

Numerical studies of transport and other dynamical properties in quasi-one-dimensional

systems have made great progress since the advent of matrix product state algorithms for time dependence [117, 130, 99]. In the case of a single chain, it is possible to see the characteristic power laws of Luttinger liquid behavior [44], and while coupled chains are considerably more demanding, it has been possible to access at least some excited-state properties [51]. Coupled-chain numerical studies could in principle provide a more precise and tunable "numerical laboratory" to test our predictions than current polymer experiments.

There are a number of ways that our models could be extended for future work. We have dealt only with spinless Luttinger liquids, so a spin sector could be added. Due to the spin-charge separation in Luttinger liquids, this would be a relatively simple change and would just result in extra additive contributions to some $L^{(il)}$ coefficients. The models could also be made more complete via the addition of disorder and by going to higher order in the perturbation theory in the interchain hopping strength. The latter two corrections would be potentially quite difficult, though disorder could be added at a relatively late stage in the calculation by modifying the density of states as used in equation (2.8) or the Green's function in equations (2.28).

To implement these or other extensions of our model, if the goal is only to find how transport properties depend on temperature then it will apparently be sufficient to use a noninteracting model for most of the calculation as in section 2.3; if the precise values of the transport coefficients are needed, such as for calculating the Lorenz number, then a more complete calculation, as in section 2.4, will be required.

Chapter 3

Calculations for the study of weakly coupled Luttinger liquids

In this chapter I present some of the calculations for the results in chapter 2. In particular, I discuss the calculations of the current operators and of the current-current correlation functions and their corresponding response functions. I also address the correspondence between the two models used in the previous chapter, namely the generalized noninteracting model and the model in which each polymer is explicitly treated as a Luttinger liquid. Further details for everything covered here can be found in the following chapter.

3.1 Details of generalized noninteracting model

In the main body of the paper, we focused on the key results of our work and restricted discussion of the calculations to the general formalism that we used. In this chapter, we discuss key steps of the calculations, especially those in which we use one of our assumptions. We also provide some intermediate results such as the current-current correlation functions for the Luttinger liquid model in terms of the hypergeometric function F_1. For a reader interested in seeing more details, the full calculations are available in chapter 4.

Current operators

The computation of the particle and energy current operators, as given in equations (2.7a) and (2.7b), from equations (2.5) involves computing the commutators $[N_j, H]$ and $[H_j, H]$ respectively. In each case, the best way to proceed with the calculation is to break the Hamiltonian into the on-chain and interchain coupling pieces, $H = \sum_i h_i + h_i'$. As the on-chain Hamiltonian conserves the total number of electrons on the chain, it must commute with the number operator on each chain, so that $[N_j, H] = \sum_i [N_j, h_i']$. Similarly, the on-chain

Hamiltonians for different chains all commute so that

$$[H_j, H] = \sum_i [h_j, h_i'] + [h_j', h_i] + [h_j', h_i']. \tag{3.1}$$

We also neglect the last term as it contains two powers of the interchain hopping strength and thus is not lowest order in our perturbative calculation. The remainder of the derivation of the current operators consists of computing the commutators and then observing that half the terms can have their index shifted by 1 in the sum over j from equations (2.5), in which case the limit as $k \to 0$ gives

$$\frac{1 - e^{ika_c}}{k} \to -ia_c. \tag{3.2}$$

For further details, see chapter 4.

Finding $L^{(il)}$

The first step in finding the transport coefficients is to find the time evolution of the current operators. In imaginary time $\tau = it$, the time evolution is given by

$$J(\tau) = e^{H\tau} J e^{-H\tau}. \tag{3.3}$$

In general this would be a very difficult calculation, but it is made much easier by the fact that we do the calculation only to lowest order in the interchain hopping, which allows us to drop the hopping terms entirely from the Hamiltonian used for the time evolution,

$$H \to H_0 = \sum_i h_i. \tag{3.4}$$

This means that the time evolution operator acts separately on each creation and annihilation operator in equations (2.7a) and (2.7b). The resulting time-dependent current operators are

$$J(\tau) = ia_c \sum_{jkk'} e^{\tau(E_k - E_{k'})} t_{kk'} c^\dagger_{j-1,k} c_{j,k'} - e^{\tau(E_{k'} - E_k)} t^*_{kk'} c^\dagger_{j,k'} c_{j-1,k} \tag{3.5a}$$

$$J_E(\tau) = ia_c \sum_{jkk'} \left[\left(\frac{E_k + E_{k'}}{2} \right) \left(e^{\tau(E_k - E_{k'})} t_{kk'} c^\dagger_{j-1,k} c_{j,k'} - e^{\tau(E_{k'} - E_k)} t^*_{kk'} c^\dagger_{jk'} c_{j-1,k} \right) \right] \tag{3.5b}$$

We then calculate the current-current correlators. Here we show only the calculations for $\langle J(\tau) J \rangle$, as the others are quite similar. The brackets $\langle \cdot \rangle$ indicate a thermal expectation value defined as usual by

$$\langle \mathcal{O} \rangle = \mathrm{Tr}[e^{-\beta H} \mathcal{O}] / \mathrm{Tr}[e^{-\beta H}] = \mathrm{Tr}[e^{-\beta H} \mathcal{O}] / Z \tag{3.6}$$

As with the time evolution, the lowest order result in the interchain hopping can be found by simply dropping the interchain hopping terms from H in the thermal density matrix,

$e^{-\beta H} \to e^{-\beta H_0}$, in which case the expression for the current-current correlator can be written in terms of expectation values on single chains,

$$\langle J(\tau)J\rangle = a_c^2 \sum_{jkk'} |t_{kk'}|^2 \left(e^{\tau(E_{k'}-E_k)}(1-\langle n_{j-1,k}\rangle)\langle n_{j,k'}\rangle + e^{\tau(E_k-E_{k'})}\langle(1-\langle n_{j,k'}\rangle)\langle n_{j-1,k}\rangle\right), \tag{3.7}$$

where as usual the number operator is given by $n = c^\dagger c$. The expectation value of each number operator is just given by the Fermi-Dirac distribution and is independent of the chain number j so this becomes

$$\langle J(\tau)J\rangle = N_c a_c^2 \sum_{kk'} |t_{kk'}|^2 \left[\frac{e^{\tau(E_{k'}-E_k)}}{(1+e^{-\beta E_k})\left(1+e^{\beta E_{k'}}\right)} + \frac{e^{\tau(E_k-E_{k'})}}{(1+e^{\beta E_k})\left(1+e^{-\beta E_{k'}}\right)}\right] \tag{3.8a}$$

$$= N_c a_c^2 \left(\frac{L}{2\pi}\right)^2 \int_{kk'} |t(k,k')|^2 \left[\frac{e^{\tau(E(k')-E(k))}}{\left(1+e^{-\beta E(k)}\right)\left(1+e^{\beta E(k')}\right)}\right. \tag{3.8b}$$

$$\left. + \frac{e^{\tau(E(k)-E(k'))}}{\left(1+e^{\beta E(k)}\right)\left(1+e^{-\beta E(k')}\right)}\right] dk\, dk'$$

$$= 2N_c a_c^2 \left(\frac{L}{2\pi}\right)^2 \int_{EE'} |t(E,E')|^2 g(E) g(E') \left[\frac{e^{\tau(E'-E)}}{(1+e^{-\beta E})\left(1+e^{\beta E'}\right)}\right. \tag{3.8c}$$

$$\left. + \frac{e^{\tau(E-E')}}{(1+e^{\beta E})\left(1+e^{-\beta E'}\right)}\right] dE\, dE'$$

$$= 4N_c a_c^2 \left(\frac{L}{2\pi}\right)^2 \int_{EE'} |t(E,E')|^2 g(E) g(E') \left[\frac{e^{\tau(E-E')}}{(1+e^{\beta E})\left(1+e^{-\beta E'}\right)}\right] dE\, dE' \tag{3.8d}$$

where in successive steps we have (1) rewritten the sum over k as an integral over a continuous variable, (2) converted to an integral over energy E, with $t(E,E')$ defined by $t(E(k),E(k')) = t(k,k')$ for all k and k', also getting a factor of 2 for the two branches of the dispersion, and (3) recognized that the two terms are the same if, as we assume, $t(E,E') = t(E',E)$.

In the continuum case, the hopping $t(k,k')$ becomes a Dirac delta function. Thus one factor of $t(E,E')$ collapses the two integrals into one, leaving $t(E,E) \propto \delta(0)$. The appearance of the apparently infinite quantity $\delta(0)$ is not a problem because when we do the conversion from a sum over k to an integral, $t_{kk'}$ (which we initially viewed as a sharply peaked, perhaps Gaussian, function) becomes

$$t_{kk'} = te^{-(k-k')^2L^2/\pi} \to t(k,k') = \frac{t}{L}\delta(k-k') \tag{3.9}$$

with $\delta(0) = L$. (The precise form of $t_{kk'}$ that we use here is discussed in section 3.3 and more thoroughly in chapter 4.) This means that $t(E,E)$ is actually just equal to t, a constant. Using this form for $t(E,E')$ gives

$$\langle J(\tau)J\rangle = \frac{4N_cLv\,(a_ct)^2}{(2\pi)^2}\int \frac{g^2(E)}{(1+e^{\beta E})\,(1+e^{-\beta E})}dE. \tag{3.10}$$

The corresponding expressions for $\langle J_E(\tau)J_E\rangle$ and $\langle J_E(\tau)J\rangle$ are quite similar, but with extra factors of E in the integrand. The most noteworthy aspect of this expression from a calculational perspective is that it does not depend on the imaginary time τ at all. Then when we calculate the Fourier transform in the equation for $L^{(il)}$, equation (2.4), the integral over τ is just

$$\int_0^\beta e^{i\omega_n \tau} d\tau = \beta\, \delta_{n0}, \tag{3.11}$$

proportional to a Kronecker delta in the Matsubara frequency. The analytic continuation of this function is not well-defined, so it is not immediately obvious how to convert the Matsubara correlation function to a retarded one. This problem, however, arises only when the interaction strength is precisely 0, since otherwise the τ dependence would not have vanished. Thus this should be regularized by some small amount of interaction (or by disorder or some other mechanism) in any realistic system. We thus convert to the dimensionless variable $\tau' = \tau\pi/\beta$ and let

$$A = \mathrm{Re}\left(\lim_{n\to 0}\lim_{\delta'\to 0} \frac{-i}{n}\left[\int_0^\pi e^{2in\tau'} d\tau'\right]_{in\to n+i\delta'}\right). \tag{3.12}$$

This constant corresponds to $F_\alpha(0)$ in equation (3) of reference [29]. Rewriting the expression for $L^{(il)}$ from equation (2.4) in terms of τ' and then substituting both the current-current correlator from equation (3.10) (and the corresponding results for $\langle J_E(\tau)J_E\rangle$ and $\langle J_E(\tau)J\rangle$) and the definition of A, we get equation (2.8), our final result for $L^{(il)}$ in the generalized noninteracting model.

3.2 Details of Luttinger liquid model

The calculations for the Luttinger liquid model are substantially more complex. Here we highlight some interesting features particularly of the calculation of the thermal current operator and the correlation function $\langle J_E(\tau)J_E\rangle$. We also present expressions for $\langle J_E(\tau)J_E\rangle$ and $\langle J_E(\tau)J\rangle$ in terms of the hypergeometric function F_1, and we discuss the method we use for numerical analytic continuation to get the transport coefficients from the correlation functions.

Thermal current operator

We calculate the current operators in the full Luttinger liquid model using the same approach as in the generalized noninteracting model. The additional complication in the calculation comes from the more complete Hamiltonian (equation 2.25) and in particular from the on-chain part. As with the calculation of the thermal current operator in the previous model as discussed in section 3.1, the commutator $[H_j, H]$ from equation (2.5b) has only two pieces

that are neither 0 nor negligible in the atomic limit,

$$[H_j, H] \to \sum_i [h_j, h_i'] + [h_j', h_i] = \sum_i [h_j', h_i] - [h_i', h_j]. \tag{3.13}$$

Terms in the commutator $[h_i', h_j]$ look like $[\psi^\dagger_{i+1,\alpha}(x)\psi_{i\beta}(x'), (\nabla\theta_j(\tilde{x}))^2]$. To compute these kinds of terms, we need the canonical commutation relations between the bosonic field operators ϕ and θ, which are given by[31]:

$$[\phi_i(x), \partial_{x'}\theta_j(x')] = i\pi\delta_{ij}\delta(x'-x) \tag{3.14a}$$
$$[\phi_i(x), \theta_j(x')] = i\frac{\pi}{2}\delta_{ij}\text{sign}(x'-x) \tag{3.14b}$$
$$[\phi_i(x), \phi_j(x')] = [\theta_i(x), \theta_j(x')] = 0 \tag{3.14c}$$

We then write out the Fermionic operators ψ and $\psi^\dagger$ in terms of ϕ and θ using equations (2.24) and use the bosonic commutators from equations (3.14) to show

$$[\psi_{i\alpha}(x), \nabla\theta_j(x')] = \alpha\pi\delta_{ij}\delta(x-x')\psi_i(x) \tag{3.15a}$$
$$[\psi^\dagger_{i\alpha}(x), \nabla\theta_j(x')] = -\alpha\pi\delta_{ij}\delta(x-x')\psi^\dagger_i(x) \tag{3.15b}$$
$$[\psi_{i\alpha}(x), \nabla\phi_j(x')] = -\pi\delta_{ij}\delta(x-x')\psi_i(x) \tag{3.15c}$$
$$[\psi^\dagger_{i\alpha}(x), \nabla\phi_j(x')] = \pi\delta_{ij}\delta(x-x')\psi^\dagger_i(x) \tag{3.15d}$$

Combining these commutators with the rule $[AB, C] = A[B, C] + [A, C]B$, we additionally find that

$$[\psi^\dagger_{i\alpha}(\tilde{x})\psi_{i+1,\beta}(x), (\nabla\theta_j(x'))^2] = \begin{bmatrix} 2\pi\nabla\theta_j(x')\left(\beta\delta(x-x')\delta_{i+1,j} - \alpha\delta(x-\tilde{x})\delta_{ij}\right) \\ +\pi^2\left(\beta\delta(x-x')\delta_{i+1,j} - \alpha\delta(x-\tilde{x})\delta_{ij}\right)^2 \end{bmatrix} \psi^\dagger_{i\alpha}(\tilde{x})\psi_{i+1,\beta}(x) \tag{3.16a}$$

$$[\psi^\dagger_{i\alpha}(\tilde{x})\psi_{i+1,\beta}(x), (\nabla\phi_j(x'))^2] = \begin{bmatrix} -2\pi\nabla\phi_j(x')\left(\delta(x-x')\delta_{i+1,j} - \delta(x-\tilde{x})\delta_{ij}\right) \\ +\pi^2\left(\delta(x-x')\delta_{i+1,j} - \delta(x-\tilde{x})\delta_{ij}\right)^2 \end{bmatrix} \psi^\dagger_{i\alpha}(\tilde{x})\psi_{i+1,\beta}(x) \tag{3.16b}$$

and hence

$$[\psi^\dagger_{i\alpha}(\tilde{x})\psi_{i+1,\beta}(x), h_j] = v\begin{bmatrix} \delta_{i+1,j}\left(\beta K\nabla\theta_j(x) - \alpha K^{-1}\nabla\phi_j(x)\right) - \delta_{ij}\left(K\nabla\theta_j(\tilde{x}) - K^{-1}\nabla\phi_j(\tilde{x})\right) \\ +\frac{\pi}{2}\left(K + K^{-1}\right)\delta(0)\left(\delta_{i+1,j} + \delta_{ij}\right) \end{bmatrix} \times \psi^\dagger_{i\alpha}(\tilde{x})\psi_{i+1,\beta}(x) \tag{3.17}$$

There are four terms of this type in $[h_i', h_j]$, and another four in $[h_j', h_i]$. Adding them all and summing over i, then using the trick of shifting the chain index j in half the terms before taking the limit $k \to 0$ as in equation (3.2), gives the thermal current operator, equation (2.26b).

Thermal current-current correlator

The thermal expectation value $\langle J_E(\tau)J_E\rangle$ looks like $P\int dxdx'\sum_j\langle\cdots\rangle$ where P is some (dimensionful) prefactor, four integrals over real-space coordinates have been reduced to two by assuming $t(x-x')\propto\delta(x-x')$ (see section 3.3), and the expectation value is a sum of terms of the form

$$\langle[\nabla_i]_x\psi_j^\dagger(x)\psi_j(x)[\nabla_{i'}]_{x'}\psi_{j'}^\dagger(x')\psi_{j'}(x')\rangle \tag{3.18}$$

where the $[\nabla]$ operators are defined in equation (2.27). The indices satisfy $j'=j\pm1$, with i and i' related to j and j' in one of four possible ways; these four cases are: (1) $i=i'=j$, (2) $i=i'=j'$, (3) $i=j$ and $i'=j'$, and (4) $i=j'$ and $i'=j$. As in the generalized noninteracting model, the fact that we work only to lowest order in the interchain hopping allows us to drop the hopping terms from the Hamiltonian appearing in the density matrix used in the calculation of the expectation values, $e^{-\beta H}\to e^{-\beta H_0}$, and likewise for the time evolution, so that the expectation values for each term of the type in equation (3.18) splits up into a product of expectation values on two individual chains. Cases (1) through (4) lead to eight different types of two-point functions on the individual chains, as follows:

$$(1)\to\langle[\nabla]\psi^\dagger[\nabla]\psi\rangle\langle\psi\psi^\dagger\rangle \tag{3.19a}$$
$$(2)\to\langle\psi^\dagger\psi\rangle\langle[\nabla]\psi[\nabla]\psi^\dagger\rangle \tag{3.19b}$$
$$(3)\to\langle[\nabla]\psi^\dagger\psi\rangle\langle\psi[\nabla]\psi^\dagger\rangle \tag{3.19c}$$
$$(4)\to\langle\psi^\dagger[\nabla]\psi\rangle\langle[\nabla]\psi\psi^\dagger\rangle \tag{3.19d}$$

Both $\langle\psi_\alpha(x,\tau)\psi)_\alpha^\dagger(0,0)\rangle$ and $\langle\psi_\alpha^\dagger(x,\tau)\psi_\alpha(0,0)\rangle$ can be written simply in terms of the single-chain Green's function, being $-G_\alpha(x,\tau)$ and $G_\alpha(-x,-\tau)$ respectively; these are the only two that appear in the calculation of $\langle J(\tau)J\rangle$ and therefore in the calculation of the electrical conductivity.

The other six types of two-point functions we compute by writing them in terms of derivatives of the Green's function. The first step is to separate the $[\nabla]$ operator into two pieces, proportional to $\alpha\phi-\theta$ and $-\alpha\phi-\theta$,

$$[\nabla_j]_y^\alpha=-\alpha\nabla_y\left[\gamma(\alpha\phi_j-\theta_j)+\tilde\gamma(-\alpha\phi_j-\theta_j)\right] \tag{3.20}$$

where $\gamma=(K+K^{-1})/2$ as usual and $\tilde\gamma=(K-K^{-1})/2$. This operator only appears in expectation values with ψ_α and $\psi_\alpha^\dagger$, which according to equations (2.24) contain $\alpha\phi-\theta$ but not $-\alpha\phi-\theta$. Then when $[\nabla]$ is split up inside an expectation value and the expectation values of the two terms are calculated separately, all of the $-\alpha\phi-\theta$ terms vanish. (See further discussion of this point in chapter 4.)

A factor of $\alpha\nabla\phi-\nabla\theta$ is pulled down by every derivative of ψ_α or $\psi_\alpha^\dagger$, so that for instance

$$\begin{aligned}\langle[\nabla]_{x,\tau}^\alpha\psi_\alpha(x,\tau)\psi_\alpha^\dagger(x')\rangle&=\alpha\gamma\langle ie^{i\alpha k_Fx}\nabla_x(e^{-i\alpha k_Fx}\psi_\alpha(x,\tau))\psi_\alpha^\dagger(x')\rangle\\&=-i\alpha\gamma e^{i\alpha k_Fx,\tau}\nabla_x\left(e^{-i\alpha k_Fx}G_\alpha(x-x',\tau)\right).\end{aligned} \tag{3.21}$$

The remaining five two-point functions are calculated in a similar manner. For cases (1) through (4) we find

$$\langle[\nabla]\psi^\dagger[\nabla]\psi\rangle\langle\psi\psi^\dagger\rangle = \gamma^2\left[(\alpha k_F)^2 G_\alpha(x-x',\tau) + 2i\alpha k_F \partial_x G_\alpha(x-x',\tau) - \partial_x^2 G_\alpha(x-x',\tau)\right] \times \tilde{G}_\alpha(x-x',\tau) \tag{3.22a}$$

$$\langle\psi^\dagger\psi\rangle\langle[\nabla]\psi[\nabla]\psi^\dagger\rangle = \gamma^2\left[(\alpha k_F)^2 \tilde{G}_\alpha(x-x',\tau) - 2i\alpha k_F \partial_x \tilde{G}_\alpha(x-x',\tau) - \partial_x^2 \tilde{G}_\alpha(x-x',\tau)\right] \times G_\alpha(x-x',\tau) \tag{3.22b}$$

$$\langle[\nabla]\psi^\dagger\psi\rangle\langle\psi[\nabla]\psi^\dagger\rangle = \gamma^2\left[(k_F - i\alpha\partial_x)\tilde{G}_\alpha(x-x',\tau)\right] \times \left[(k_F + i\alpha\partial_x)G_\alpha(x-x',\tau)\right] \tag{3.22c}$$

$$\langle\psi^\dagger[\nabla]\psi\rangle\langle[\nabla]\psi\psi^\dagger\rangle = \gamma^2\left[(k_F - i\alpha\partial_x)\tilde{G}_\alpha(x-x',\tau)\right] \times \left[(k_F + i\alpha\partial_x)G_\alpha(x-x',\tau)\right] \tag{3.22d}$$

for $\tilde{G}(x,\tau) = -G(-x,-\tau)$. We have omitted indices and coordinates on the left-hand side for clarity. The last two terms are clearly the same, but the first two appear to be different. In fact, all of these expressions are inside an integral over x and x', so we apply integration by parts to move derivatives in the first two terms; the result is that all four terms are equal. These expressions, for instance in equation (3.22c), are now quite reminiscent of equation (2.28b) for $\langle J_E(\tau)J_E\rangle$ in the main paper.

To finish the calculation, we change variables in the integration from x and x' to $x - x'$ and $(x + x')/2$. The integrand does not depend on the center of mass coordinate and thus the integral over $(x + x')/2$ just provides a factor of the length of the 1D chain. The result is equation (2.28b).

Correlator results in terms of F_1

By substituting the Luttinger liquid Green's function, equation (2.29), into the current-current correlators, equations (2.28), and integrating over the position x from $-\infty$ to ∞, we find expressions for the correlators that are functions only of the imaginary time τ. In practice we write the results in terms of the dimensionless parameter $\tau' = \tau\pi/\beta$ because that makes it easy to separate the dimensionful parts of the transport coefficients as given in equations (2.32) from the purely numerical parts that we need only for finding the Lorenz number.

The expression for $\langle J(\tau')J\rangle$ is given in equation (4.162) in the main paper. The corre-

sponding expressions for the remaining two correlators are

$$\langle J_E(\tau')J_E\rangle = N_c L\gamma^2 \left(\frac{a_c v t}{2\pi}\right)^2 \frac{1}{2a^3\pi^2}\left(\frac{2\pi a}{v\beta}\right)^{2\gamma+1} \tag{3.23a}$$
$$\times \begin{pmatrix} -4(2+\gamma^2-2\cos(4\tau'))f(\gamma,\tau',3,3) \\ +\cos(2\tau')(2+\gamma^2-2\cos(4\tau'))(f(\gamma,\tau',2,3)+f(\gamma,\tau',4,3)) \\ +2(1+\gamma^2-\cos(4\tau'))(f(\gamma,\tau',1,3)+f(\gamma,\tau',5,3)) \\ -\gamma^2\cos(2\tau')(f(\gamma,\tau',0,3)+f(\gamma,\tau',6,3)) \end{pmatrix}$$

$$\langle J_E(\tau')J_E\rangle = 2v\gamma N_c L \left(\frac{a_c t}{2\pi}\right)^2 \frac{1}{a^2\pi^2}\left(\frac{2\pi a}{v\beta}\right)^{2\gamma} \sin(2\tau') \tag{3.23b}$$
$$\times \begin{pmatrix} -2(1+\frac{\gamma}{2})f(\gamma,\tau',2,2) \\ +\cos(2\tau')(f(\gamma,\tau',1,2)+f(\gamma,\tau',3,2)) \\ +\frac{\gamma}{2}(f(\gamma,\tau',0,2)+f(\gamma,\tau',4,2)) \end{pmatrix}$$

The function $f(\gamma,\tau,n,m)$ can be written in terms of the Appell hypergeometric function F_1 as in equation (2.31) in the main paper, and it also has a nice integral representation,

$$f(\gamma,\tau,n,m) = \int_0^1 t^{\gamma+n-1}(1-2t\cos(2\tau)+t^2)^{-(\gamma+m)}\,dt, \tag{3.24}$$

which is derived in chapter 4 from a representation of this type for F_1.

Numerical Fourier transform and analytic continuation

Computing the $L^{(il)}$ coefficients involves evaluating the expression

$$\lim_{\omega\to 0}\lim_{\delta\to 0}\frac{1}{\omega}\left[\int_0^\beta e^{i\omega_n\tau}\langle j_l(\tau)j_i\rangle\,d\tau\right]_{i\omega_n\to\omega+i\delta}. \tag{3.25}$$

The first step is to write anything that cannot be computed analytically in terms of dimensionless quantities, which we do by the transformation $\tau\to\tau'$. This results in

$$\lim_{n\to 0}\lim_{\delta'\to 0}\frac{\beta^2}{2\pi^2 n}\left[\int_0^\pi e^{2in\tau'}\langle j_l(\tau')j_i\rangle\,d\tau'\right]_{in\to n+i\delta'}. \tag{3.26}$$

In principle we would now find a unique analytic function $f(n)$ such that $\int e^{2in\tau'}\langle j(\tau')j\rangle d\tau' = f(n)$ for every $n=0,1,2,\cdots$, but there is no general formula for the Fourier transforms and

the integrals must therefore be computed individually for each value of n. This provides a limited set of points $(n, f(n))$ to use in fitting an analytic function.

Two standard approaches to this function-fitting problem are the maximum entropy method[52, 36] and the Padé approximation[118, 85]. The maximum entropy method is more robust to numerical errors, but it does depend quite strongly on an initial assumption of the form of the function. In our case, we do not a priori have any strong assumptions about what the function $f(n)$ should look like, and our data comes from numerical integrals for which we can bound the error by requiring a fixed level of precision, with no statistical errors like those that appear in quantum Monte Carlo calculations. We therefore use the Padé approximation and fit a rational function to the calculated Fourier transforms at Matsubara frequencies.

If we evaluate the Fourier transform at $2N$ points, we can find an exact fit for a rational function with $2N$ parameters, namely

$$f(x) = \frac{\sum_{n=1}^{N} a_n x^n}{\sum_{n=0}^{N+1} b_n x^n}. \tag{3.27}$$

This has only $2N$ parameters because $f(0)$ is just the integral of the current-current correlation function so that $b_0 \neq 0$, and therefore we can assume without loss of generality that $b_0 = 1$. Our method for finding f from the $2N$ points is discussed further in chapter 4 and is very similar to the method described in reference [85].

A major benefit of writing $f(x)$ as a rational function is that the analytic continuation can be accomplished simply by the replacement $n \to \delta' - in$. We make this substitution, divide by n (from equation 3.26), and take the imaginary part to get only the real part of $L^{(il)}$; letting both n and δ' go to 0, we find in the case that the correlation function $\langle j_l(\tau') j_i \rangle$ is even about $\tau' = \pi/2$ the very simple expression

$$\lim_{n\to 0} \lim_{\delta' \to 0} \left(\mathrm{Im} \left[\frac{f(\delta' - in)}{n} \right] \right) = a_0 b_1 - a_1 \tag{3.28}$$

which is just minus the derivative of $f(x)$ evaluated at $x = 0$. (Note that under some assumptions about f, this follows from the Cauchy-Riemann equations.) If the correlation function is odd about $\tau' = \pi/2$, then we get 0.

It turns out that the function $f(\gamma, \tau, n, m)$ is even about $\tau' = \pi/2$, which implies that both $\langle J(\tau) J \rangle$ (equation 4.162) and $\langle J_E(\tau) J_E \rangle$ (equation 3.23a) are even, while $\langle J_E(\tau) J \rangle$ (equation 3.23b) is odd. This is the mathematical explanation for why the thermopower vanishes in our calculation for the Luttinger liquid model, although of course this result was expected due to particle-hole symmetry.

There are two complications that must be addressed. First, the form of the function $f(x)$ and hence the calculated value for the numerical part of $L^{(il)}$ depends on the number of points used to fit the function. With a small number of points, the function is highly underdetermined and thus the derivative at the origin is inaccurate. Conversely, finding the parameters in f involves inverting a matrix that quickly becomes ill-conditioned as N grows,

which for a given precision of the numerical integrals sets an upper bound on how many data points we can use. In practice, we compute the transport coefficients for every value of N from 1 through $N_{\max}$, confirm that the resulting numerical series converges, and use the limit of the sequence for the value of the transport coefficient. We use $N_{\max} = 40$ because that value empirically gives good convergence for all transport coefficients that we calculate.

The second complication is that the functions $f(\gamma, \tau, n, m)$ are divergent at $\tau = 0$ and π. We regulate the divergence by introducing a cutoff ϵ at both bounds of the integral in equation (3.26), integrating from ϵ to $\pi - \epsilon$ instead of 0 to π. We compute the transport coefficients for values of ϵ that vary over an order of magnitude (from 0.1 to 0.01) and confirm that the results for the transport coefficients converge as $\epsilon \to 0$. The numerical error grows as $\epsilon \to 0$, so all the numerical results for the Luttinger liquid model shown in figures 2.1 and 2.3 are for $\epsilon = 10^{-1.5}$, for which the results are converged and the error is guaranteed to be small. See chapter 4 for details.

3.3 Correspondence between the two models

In the main text of the paper we have compared the results of our two models, implicitly assuming that the results they give should match at least in the noninteracting limit. In this section we confirm that the two models match in that limit, first by showing that the hopping terms in the two models are equivalent and second by explicitly rewriting the Fourier-space expression for $\langle J(\tau)J\rangle$ from the generalized noninteracting model in a real-space representation and showing that the result matches the noninteracting limit of equation (2.28a) from the Luttinger liquid model.

Correspondence of hopping terms

The correspondence between the Fourier-space operators c_k that appear in the Hamiltonian in equation (2.1) and the real-space operators $\psi_\alpha(x)$ that appear in the Hamiltonian in equation (2.25) is given by a Fourier transform,

$$c_{k\alpha} = \frac{1}{\sqrt{L}} \int e^{-ikx} e^{-i\alpha k_F x} \psi_\alpha(x) dx \tag{3.29a}$$

$$\psi_\alpha(x) = \frac{e^{i\alpha k_F x}}{\sqrt{L}} \sum_k e^{ikx} c_{k\alpha} \tag{3.29b}$$

where the chiral Fourier-space operator $c^\dagger_{k\alpha}$ creates a fermion that has wave-vector k relative to the Fermi point αk_F. We can then find the correspondence between the hopping strength $t_{kk'}$ from equation (2.1) and $t_{\alpha\beta}(x-x')$ from equation (2.25) by substituting equation (3.29b) into the hopping term of the Luttinger liquid Hamiltonian and matching the result to the corresponding term in the noninteracting Hamiltonian. To simplify the calculation, we rewrite

the hopping part of the Luttinger liquid with only two terms, as

$$\sum_{\alpha\beta}\int dx\,dx'\left[t_{\alpha\beta}(x-x')\psi^\dagger_{j\alpha}(x)\psi_{j+1,\beta}(x')+\text{h.c.}\right]. \tag{3.30}$$

In fact, it is sufficient to match just the first term of this to the first term in the hopping part of the noninteracting Hamiltonian, since their Hermitian conjugates will automatically match as well.

Making the substitution with equation (3.29b), we have:

$$\begin{aligned}
&\sum_{\alpha\beta}\int dx\,dx'\,t_{\alpha\beta}(x-x')\psi^\dagger_{j\alpha}(x)\psi_{j+1,\beta}(x') \\
&\quad=\sum_{\alpha\beta}\int dx\,dx'\left[t_{\alpha\beta}(x-x')\left[\frac{e^{-i\alpha k_F x}}{\sqrt{L}}\sum_k e^{-ikx}c^\dagger_{jk\alpha}\right]\left[\frac{e^{i\beta k_F x'}}{\sqrt{L}}\sum_k e^{ikx'}c_{j+1,k\beta}\right]\right] &\text{(3.31a)}\\
&\quad=\frac{1}{L}\sum_{kk'}\sum_{\alpha\beta}\int dx\,dx'\left[t_{\alpha\beta}(x-x')e^{-ik_F(\alpha x-\beta x')}\left[e^{-ikx}e^{ik'x'}\right]c^\dagger_{jk\alpha}c_{j+1,k'\beta}\right] &\text{(3.31b)}
\end{aligned}$$

We can compare this with the equivalent term for the generalized noninteracting model, which looks like

$$\sum_{kk'}t_{kk'}c^\dagger_{j,k}c_{j+1,k'}=\sum_{kk'}\sum_{\alpha\beta}t_{kk'}\delta_{\alpha\beta}c^\dagger_{jk\alpha}c_{j+1,k'\beta}. \tag{3.32}$$

For the two to be equal, we must have $t_{\alpha\beta}(x-x')=\delta_{\alpha\beta}t(x-x')$ and

$$t_{kk'}=\frac{1}{L}\int dx\,dx'\left[t(x-x')e^{-i\alpha k_F(x-x')}e^{-ikx}e^{ik'x'}\right]. \tag{3.33}$$

The inverse relation is

$$t(x-x')e^{-i\alpha k_F(x-x')}=\frac{L}{(2\pi)^2}\int dk\,dk'\,t_{kk'}e^{ikx}e^{-ik'x'}. \tag{3.34}$$

From these relations, we can verify the consistency of the hopping strengths that we used in our calculations, namely $t(k,k')=(t/L)\delta(k-k')$ from equation (3.9) and $t(x-x')\propto\delta(x-x')$. Starting from $t(k,k')$ and using equation (3.34), we find

$$t(x-x')=\frac{t}{2\pi}\delta(x-x'). \tag{3.35}$$

Note that the factor of L^{-1} in $t(k,k')$ is necessary to cancel the factor of L in equation (3.34), so that the hopping strength $t(x-x')$ between localized sites does not depend on the chain length; such a dependence would be unphysical.

The factor of L^{-1} in front of the delta function in $t(k,k')$ appears because the width of the Gaussian describing $t_{kk'}$ is proportional to L^{-1}. We assume the specific form of the hopping $t_{kk'}$ given in equation (3.9) specifically to achieve the cancellation of factors of the length of the system in $t(x,x')$. This ensures that both $t(x-x')$ and $t_{kk'}$ are physically valid, while also being compatible with each other according to equations (3.33) and (3.34).

Real space representation of current-current correlator in generalized noninteracting model

In the noninteracting limit, $\gamma \to 1$, the results of our two models should precisely agree. We confirm that explicitly by writing $\langle J(\tau)J\rangle$ as calculated in the generalized noninteracting model in a real-space representation. We begin from equation (3.8d), first converting back into an integral over k to get

$$\langle J(\tau)J\rangle = 2N_c a_c^2 \left(\frac{L}{2\pi}\right)^2 \sum_\alpha \int_{kk'} |t(k,k')|^2 \left[\frac{e^{\tau(E_\alpha(k)-E_\alpha(k'))}}{(1+e^{\beta E_\alpha(k)})\,(1+e^{-\beta E_\alpha(k')})}\right] dk\,dk' \tag{3.36}$$

where on each branch ($\alpha = R, L$), k is measured from the Fermi point αk_F. Putting in the linear dispersion $E_\alpha(k) = \alpha v k$ and substituting equation (3.33) for $t(k,k')$, this becomes

$$\langle J(\tau)J\rangle = \frac{2N_c a_c^2}{(2\pi)^2} \sum_\alpha \int \begin{matrix} dx_1\,dx_2 \\ dx_3\,dx_4 \end{matrix} \left[t(x_1-x_2)e^{-i\alpha k_F(x_1-x_2)}\right]\left[t(x_3-x_4)^* e^{i\alpha k_F(x_3-x_4)}\right] \times \left[\int dk\, \frac{e^{\alpha\tau'\beta v k/\pi} e^{-ik(x_1-x_3)}}{1+e^{\alpha\beta v k}}\right]\left[\int dk'\, \frac{e^{-\alpha\tau'\beta v k'/\pi} e^{ik'(x_2-x_4)}}{1+e^{-\alpha\beta v k'}}\right] \tag{3.37}$$

Substituting $t(x-x') = (t/2\pi)\delta(x-x')$ and computing the integrals over k and k' gives

$$\langle J(\tau)J\rangle = \frac{2N_c a_c^2 t^2}{(2\pi)^4} \sum_\alpha \int dx\,dx \left[-\frac{i\pi}{v\beta}\mathrm{csch}\left(\frac{\pi}{v\beta}(x'-x-i\tau)\right)\right]\left[\frac{i\pi}{v\beta}\mathrm{csch}\left(\frac{\pi}{v\beta}(x-x'+i\tau)\right)\right] \tag{3.38}$$

$$= -\frac{4N_c L a_c^2 t^2}{(2\pi)^4}\left(\frac{\pi}{v\beta}\right)^2 \int dx \left[\mathrm{csch}\left(\frac{\pi}{v\beta}(x+i\tau)\right)\right]^2 \tag{3.39}$$

This result can be compared with the noninteracting ($\gamma = 1$) limit of $\langle J(\tau)J\rangle$ in the Luttinger liquid model, as given by equation (2.28a). The noninteracting Green's function is found by substituting $\gamma = 1$ into equation (2.29) to get

$$\lim_{\gamma\to 1} G_\alpha(x,\tau) = -\frac{e^{i\alpha k_F x}}{2\pi}\left[\frac{i\alpha}{\frac{v\beta}{\pi}\sinh\left(\frac{x+i\alpha v\tau}{v\beta/\pi}\right)}\right], \tag{3.40}$$

and substituting this into equation (2.28a) gives

$$\langle J(\tau)J\rangle = -\frac{2N_c L a_c^2 t^2}{(2\pi)^4}\left(\frac{\pi}{v\beta}\right)^2 \sum_\alpha \int dx \left[\mathrm{csch}\left(\frac{\pi}{v\beta}(x+i\alpha\tau)\right)\right]^2 \tag{3.41}$$

The integral does not actually depend on α since all terms containing α are odd in x and integrate to 0. We can therefore let $\alpha \to 1$ in the integrand, in which case the sum over α becomes just a factor of 2 and the result precisely matches the real-space representation of the correlator from the generalized noninteracting model, equation (3.39).

Chapter 4

Calculation details for the study of weakly coupled Luttinger liquids

In this chapter, I present the details of techniques used in the study of coupled Luttinger liquids described in chapter 2, such as linear response theory and numerical analytic continuation, and I present many further details of the calculations for the results presented in that chapter, beyond what was shown in chapter 3.

4.1 Kubo formalism for conductivity and thermopower

I begin by explaining the method that we use to calculate the electrical conductivity, thermal conductivity, and thermopower. This section includes basic information on linear response and the Kubo formulas, but also includes details on how we perform, for instance, numerical analytic continuation.

The linear response coefficients

To find physical response functions, such as the electrical conductivity, we first find the $L^{(ij)}$ coefficients defined by the equations [70, eqs. 3.487, 3.488]

$$J = -\frac{1}{T}L^{(11)}\nabla(\mu + eV) + L^{(12)}\nabla\left(\frac{1}{T}\right) \tag{4.1}$$

$$J_Q = -\frac{1}{T}L^{(21)}\nabla(\mu + eV) + L^{(22)}\nabla\left(\frac{1}{T}\right) \tag{4.2}$$

where J is the particle current, or electrical current divided by the charge per particle, and J_Q is the heat current. In the case that $\mu = 0$, the heat current coincides with the energy current J_E. Note that $L^{(12)} = L^{(21)}$. As indicated above, these equations come from the third

edition of Gerald Mahan's book *Many-Particle Physics*, reference [70]. Similar but slightly different definitions can be found in other texts, such as the second edition of Mahan's book[69] or the text by Ashcroft and Mermin [7]. For consistency, I use the conventions of Mahan's third edition throughout this chapter.

In terms of these $L^{(ij)}$ coefficients, the physical response functions are given by [70, eqs. 3.505, 3.504, 3.507 respectively]

$$\sigma = \frac{e^2}{T} L^{(11)} \tag{2.2a}$$

$$\kappa = \frac{1}{T^2}\left[L^{(22)} - \frac{(L^{(12)})^2}{L^{(11)}}\right] \tag{2.2b}$$

$$S = \frac{1}{eT}\frac{L^{(12)}}{L^{(11)}} \tag{2.2c}$$

Kubo formulas

To actually find the $L^{(ij)}$ coefficients in terms of the current operators, we can use the Kubo formulas. In particular, we have

$$\boxed{L^{(il)} = \lim_{\omega\to 0}\lim_{\delta\to 0}\frac{1}{\omega}\left[\frac{-i}{\Omega\beta}\int_0^\beta d\tau e^{i\omega_n\tau}\langle T_\tau j_l(\tau) j_i(0)\rangle\right]_{i\omega_n\to\omega+i\delta}} \tag{2.4}$$

where j_1 is the particle current operator J and j_2 is the heat current operator J_Q (or with $\mu = 0$, the energy current operator J_E). This equation is a corrected version of (3.518) from reference [70]. (For further details on the correction, see the next subsection, 4.1.) Note that Ω is the total volume of the system, δ is an infinitesimal positive constant, and the imaginary time evolution of the current operator is given by substituting $\tau = it$ into the usual time evolution to get

$$J(\tau) = e^{\tau H} J e^{-\tau H}. \tag{4.4}$$

We will ultimately take only the real part of each $L^{(ij)}$ transport coefficient as we are interested in transport and not in dissipation. So in practice we will use

$$\mathrm{Re}\left[L^{(il)}\right] = \lim_{\omega\to 0}\lim_{\delta\to 0}\frac{1}{\omega}\mathrm{Im}\left[\frac{1}{\Omega\beta}\int_0^\beta d\tau e^{i\omega_n\tau}\langle T_\tau j_l(\tau) j_i(0)\rangle\right]_{i\omega_n\to\omega+i\delta} \tag{4.5}$$

in place of equation (2.4).

Kubo formula corrections

Mahan gives the formula for the $L^{(il)}$ coefficients as [70, eq. 3.518]

$$L^{(il)} = \lim_{\omega\to 0}\left[\frac{1}{\omega\beta}\int_0^\beta d\tau e^{i\omega\tau}\langle T_\tau j_l(\tau) j_i(0)\rangle\right]_{i\omega\to\omega+i\delta} \tag{4.6}$$

where the meaning of the symbols is the same as above. (Note that this is not actually equation 3.518 reproduced verbatim; rather, we have combined that equation with some written instructions pertaining to analytic continuation and limits that are found in the following paragraph.) From this we can extract an expression for the electrical conductivity using equation (2.2a) above, which gives the conductivity in terms of the coefficient $L^{(11)}$. The result is

$$\sigma = e^2 \lim_{\omega \to 0} \left[\frac{1}{\omega} \int_0^\beta d\tau e^{i\omega\tau} \langle T_\tau j_l(\tau) j_i(0) \rangle \right]_{i\omega \to \omega + i\delta} \tag{4.7}$$

For comparison, Mahan also gives a similar formula specifically for the electrical conductivity. This expression is [70, eq. 3.388-3.391]

$$\mathrm{Re}(\sigma) = e^2 \lim_{\omega \to 0} \frac{1}{\omega} \mathrm{Im} \left[\frac{1}{\Omega} \int_0^\beta d\tau e^{i\omega\tau} \langle T_\tau j_l(\tau) j_i(0) \rangle \right]_{i\omega \to \omega + i\delta} \tag{4.8}$$

There are some important discrepancies between these two expressions, as follows:

1. Equation (4.7) has the factor of $\frac{1}{\omega}$ inside the analytic continuation $i\omega \to \omega + i\delta$, whereas (4.8) has the ω^{-1} outside.
2. Equation (4.8) has a factor of Ω^{-1} whereas (4.7) does not
3. Equation (4.8) is only the real part of σ, and the imaginary part is taken on the right-hand side.

Based on the detailed derivation and discussion of equations 3.388-3.391, we should conclude that these results (and therefore equation 4.8) are the correct ones in each instance. We will briefly explain why:

1. The results for σ given in equations 3.388 - 3.391 are first derived in a real-time formalism with no analytic continuation required. Mahan demonstrates ([70, sec. 3.3]) that switching to the imaginary time formalism only modifies the current-current correlation function and its Fourier transform. Hence the analytic continuation should be performed only on this part of the expression.
2. The factor of Ω^{-1} is required for the conductivity to be an intensive as opposed to an extensive property, ie to get conductivity rather than conductance.
3. In the derivation of Mahan's equation 3.388, a factor of i appears, so that we must take the imaginary part of what is multiplied by i to get the real part of the entire expression. Thus this factor of i must be restored to equation (4.6).

With the appropriate resolution of each of these 3 issues, we would have:

$$L^{(il)} = \lim_{\omega \to 0} \frac{1}{\omega} \left[\frac{-i}{\Omega\beta} \int_0^\beta d\tau e^{i\omega_n\tau} \langle T_\tau j_l(\tau) j_i(0) \rangle \right]_{i\omega_n \to \omega + i\delta} \tag{4.9}$$

Finally, we need to add in the limit as $\delta \to 0$. The correct order for the limits in δ and ω is discussed in section 4.1. We can then write down the correct expression for $L^{(il)}$ as given above:

$$L^{(il)} = \lim_{\omega\to 0}\lim_{\delta\to 0}\frac{1}{\omega}\left[\frac{-i}{\Omega\beta}\int_0^\beta d\tau e^{i\omega_n\tau}\langle T_\tau j_l(\tau)j_i(0)\rangle\right]_{i\omega_n\to\omega+i\delta} \tag{2.4}$$

Understanding the Kubo formula

Let's now take a moment to review the precise calculational steps implied by the Kubo formula given above, (2.4). The procedure is actually pretty involved; here are the steps we follow:

1) Compute the current-current correlation function in terms of the imaginary time τ. Our computations for the noninteracting model with the substituted density of states and for the full Luttinger liquid model are detailed in sections 4.2 and 4.3 respectively.

2) Compute the integral

$$\int_0^\beta d\tau e^{i\omega_n\tau}\langle T_\tau j_l(\tau)j_i(0)\rangle \tag{4.10}$$

at each Matsubara frequency $\omega_n = 2\pi n/\beta$ for $n = 0, 1, 2, 3, \cdots$. Note that we use bosonic Matsubara frequencies because the current operators each contain an even number of fermion operators (two, to be precise).

3) Fit an analytic function to these points. This gives an analytic function defined on the positive imaginary line in frequency space.

4) Analytically continue this function to cover the whole of the complex plane. Evaluate the analytically continued function along a line offset from the positive real axis by a small amount $i\delta$. (This analytic continuation is the operation denoted by the shorthand $i\omega_n \to \omega + i\delta$.)

5) Take the real part of ($-i$ times this expression), or in other words just the imaginary part of the expression.

6) Finally, multiply by the prefactor (including $1/\omega$) and let ω and δ go to 0. The order of the two limits is important, both in terms of the calculation and the physical interpretation. For further details, see the next subsection, 4.1.

Procedure for analytic continuation and limits

The actual implementations of the calculational steps discussed above are quite different for the two models we consider. The steps will prove relatively simple in the noninteracting model, although one part of the expression cannot be computed and is left as an unknown unitless number; the calculation in the full Luttinger model is somewhat more involved and

requires some rather careful analysis and computation. This section will primarily discuss general methods which we will apply specifically in the case of our Luttinger model. We will also briefly discuss the physical significance of the two limits and the order in which they ought to be taken, and this discussion applies to both models.

Numerical integration simplifications

We will begin our discussion of general methods starting from step 2. Ideally, we would like to compute the integral analytically, but if that is not possible then we must instead do the computation numerically for each Matsubara frequency. In that case, we will start with three assumptions:

(1) The integral (4.10) converges for all Matsubara frequencies ω.

(2) The correlation function $\langle T_\tau j_l(\tau) j_i(0)\rangle$ is either even or odd about $\tau = \beta/2$.

(3) The correlation function is real-valued at all imaginary times, τ.

The second and third assumptions will be satisfied in both our models. The first assumption is actually violated in our Luttinger model, but we regulate the divergence as discussed in section 4.3. (Briefly: we introduce a small cutoff and complete the numerical calculation for progressively smaller values of that cutoff, and we find that the results converge as the cutoff goes to 0. See section 4.1 for more details.) For now, we will take all three assumptions to be satisfied.

We begin by simplifying the required numerical integral. One problem with the expression

$$\int_0^\beta d\tau e^{i\omega_n \tau} \langle T_\tau j_l(\tau) j_i(0)\rangle \tag{4.10}$$

is that the integration variable and the limits of integration are unitful. To correct this, we change variables from τ to $\tau' = \tau\frac{\pi}{\beta}$, giving

$$\frac{\beta}{\pi}\int_0^\pi d\tau' e^{2in\tau'} \langle T_{\tau'} j_l(\tau') j_i(0)\rangle \tag{4.11}$$

for $n = 0, 1, 2, \cdots$. The integral now depends only on unitless numerical parameters, so it can be computed numerically.

This integral can be simplified further using our second assumption, about the parity of the correlation function. We treat the two cases of even and odd parity separately.

In the first case of interest, the correlation function is even around $\tau = \beta/2$ or equivalently around $\tau' = \pi/2$. But if we write $e^{2in\tau'}$ as $\cos(2n\tau') + i\sin(2n\tau')$, we see that the sine term is odd around $\tau' = \pi/2$ so that the integral of $\sin(2n\tau')$ times the correlation function vanishes. We are thus left with the simpler expression

$$\frac{\beta}{\pi}\int_0^\pi d\tau' \cos(2n\tau') \langle T_{\tau'} j_l(\tau') j_i(0)\rangle \tag{4.12}$$

Furthermore, since τ' is always greater than or equal to 0 in the integral, we can also drop the time ordering operator to get

$$\frac{\beta}{\pi}\int_0^\pi d\tau' \cos(2n\tau')\langle j_l(\tau')j_i(0)\rangle \tag{4.13}$$

In the second case, when the correlation function is odd around $\tau = \beta/2$, we drop the cosine from the expansion of $e^{2in\tau'}$, getting

$$i\frac{\beta}{\pi}\int_0^\pi d\tau' \sin(2n\tau')\langle j_l(\tau')j_i(0)\rangle \tag{4.14}$$

Fitting an analytic function

For the rest of this section, we will ignore the prefactor of β/π in equations (4.13) and (4.14), as we would like to work with purely numerical values. The prefactor will of course be used in our later calculations.

Consider the case that the correlation function is even about $\tau = \beta/2$. Then suppose that the integral

$$\int_0^\pi d\tau' \cos(2n\tau')\langle j_l(\tau')j_i(0)\rangle \tag{4.15}$$

has been evaluated at all Matsubara frequencies, $n = 0, 1, 2, \cdots$. Let $f(n)$ denote the value of (4.15) at n. Thus we have

$$\int_0^\beta d\tau e^{i\omega_n\tau}\langle T_\tau j_l(\tau)j_i(0)\rangle = \frac{\beta}{\pi}f(n) \tag{4.16}$$

Likewise in the case of an odd correlation function, we similarly define

$$f(n) = \int_0^\pi d\tau' \sin(2n\tau')\langle j_l(\tau')j_i(0)\rangle, \tag{4.17}$$

so that

$$\int_0^\beta d\tau e^{i\omega_n\tau}\langle T_\tau j_l(\tau)j_i(0)\rangle = i\frac{\beta}{\pi}f(n) \tag{4.18}$$

The remainder of our discussion in this section will be in terms of the function $f(n)$ and thus applies to both cases.

Our goal is to find an analytic function that passes through all points $(n, f(n))$. Some commonly used methods are the Padé approximation[118, 85] and the maximum entropy method [52, 36]. In this case we can evaluate the values $f(n)$ to arbitrary precision if needed and we have no statistical errors like those that arise in Quantum Monte Carlo calculations, so the simpler Padé approximation will be sufficient.

In the Padé approximation, we fit our data points to a limit of rational functions of the form:

$$f(x) = \frac{\sum_{n=1}^{\infty} a_n x^n}{\sum_{n=0}^{\infty} b_n x^n} \tag{4.19}$$

where we can also assume without loss of generality that $b_0 = 1$ since otherwise we could divide all coefficients by b_0. (It is not 0 since that would imply that $f(0)$ diverges, contradicting our first assumption above that said the integral converges for all n.) The value of a_0 can also be found easily—substituting $x = 0$ into the expression for f, we see that $a_0 = f(0)$. Note that $f(0)$ is just the integral of the correlation function in the even case (equation 4.15) and is 0 in the odd case (equation 4.17).

The existence of a unique analytic continuation is not guaranteed unless the value of the function is known on an uncountable set of points. Here we know the function on only a countable set (nonnegative integers) and thus the function $f(x)$ may not be well-defined even in principle. This means that we have to carefully choose the specific procedure we want to follow to fit the function.

In practice, the ill-defined nature of numerical analytic continuation is only exacerbated by the fact that each integral of the type (4.15) or (4.17) must in general be evaluated individually (for each value of n), so that we can only use finitely many data points for fitting the function.

The saving grace is that we are particularly interested in DC transport, which means that we only need to know the behavior of f near to $x = 0$. (In fact, it turns out that we only need to know a_0, a_1, and b_1, as shown in the section 4.1.) We can thus choose to use only small values of n in fitting f.

There is also the question of precisely how to use our data points $(n, f(n))$ to find an approximation to $f(x)$. We have chosen to follow the simplest possible procedure, namely to use $2N$ data points to precisely fit a truncated version of $f(x)$ which has only $2N$ total nonzero coefficients in the sums appearing in the numerator and denominator. (We write the number of points as $2N$ because it will be convenient for the number to be even.) To choose which specific parameters to keep as nonzero, note that since they appear in a power series, for small x only the coefficients of lower order terms will be significant. Furthermore, we expect in general that the asymptotic behavior of f should be proportional to $1/x$ as $x \to \infty$, since $\int e^{ixt} dt \propto x^{-1}$. We thus choose to truncate the series in the numerator and denominator of f so that the denominator has one higher power of x. We therefore truncate f to be

$$f(x) = \frac{\sum_{n=1}^{N} a_n x^n}{\sum_{n=0}^{N+1} b_n x^n} \tag{4.20}$$

(Recall that $b_0 = 1$, so there are indeed $2N$ unknown parameters.) For our $2N$ data points, we just use $n = 0, 1, 2, \cdots, 2N - 1$, again since we are interested in small x.

We still need a way of actually solving for the parameters we have chosen to keep. For that, we rearrange the definition of f to find

$$a_0 + a_1 x + \cdots + a_N x^N = f(x) \left(1 + b_1 x + \cdots + b_{N+1} x^{N+1}\right) \tag{4.21}$$

or, moving all the terms with b parameters to the left-hand side,

$$a_0 + a_1 x + \cdots + a_N x^N - b_1 x f(x) + \cdots + b_{N+1} x^{N+1} f(x) = f(x) \tag{4.22}$$

Plugging all $2N$ data points into this equation, we get a matrix equation:

$$\begin{pmatrix} 1 & 0 & \cdots & 0 & 0 & \cdots & 0 \\ 1 & 1 & \cdots & 1 & -f(1) & \cdots & -f(1) \\ 1 & 2 & \cdots & 2^N & -2f(2) & \cdots & -2^{N+1}f(2) \\ \vdots & & & & & & \vdots \\ 1 & 2N & \cdots & (2N)^N & -(2N)f(2N) & \cdots & -(2N)^{N+1}f(2N) \end{pmatrix} \begin{pmatrix} a_0 \\ a_1 \\ \vdots \\ a_N \\ b_1 \\ \vdots \\ b_{N+1} \end{pmatrix} = \begin{pmatrix} f(0) \\ f(1) \\ f(2) \\ \vdots \\ f(2N) \end{pmatrix} \tag{4.23}$$

Solving this matrix equation gives the parameters for the function $f(x)$.

This method is potentially problematic since the matrix on the left very quickly becomes poorly conditioned as N increases. In practice we solve the equation using the built-in "LinearSolve" command in the commercial software Wolfram Mathematica, which is substantially more numerically stable than simple matrix inversion, but numerical error is still a problem for very large values of N. We compensate by increasing the precision with which we evaluate the integrals (4.15) and (4.17).

In practice, we choose a fixed relative precision for the integral evaluation (typically 10 significant digits, which is quite computationally intensive given the rather complicated functions involved) and then find approximations to f for each value of $N = 1, 2, 3, \cdots, N_{\max}$, where we have (based on empirical results) chosen $N_{\max} = 40$. For each value of N, we compute the transport coefficients using our fit $f(x)$, and we then check that the value converges as N increases and use the limit of that sequence as our result.

We use $N_{\max} = 40$ because, for the precision with which we compute the integrals, the matrix is still well enough conditioned that the linear system can be solved safely at that size while at the same time the numerical results for the transport coefficients as a function of N are converged. (Typically, we find that $N \approx 20$ is sufficient, but we use $N_{\max} = 40$ to be safe.) In figure 4.1, we show the calculated result for one transport coefficient (or more precisely for the quantity $a_0 b_1 - a_1$ as in equation (4.29) below, which is proportional in this case to the thermal conductivity for one representative set of parameters). The successively zoomed in images show the convergence as a function of N, and the variation at high values of N gives a sense of the (quite high) precision of the converged value.

Our method for applying the Padé approximation is similar to the one discussed in reference [85]. In that paper, the authors provide analysis on the stability of the Padé approximation as calculated using the poorly conditioned matrix from the left-hand side of equation (4.23). We refer interested readers to their analysis for further discussion.

Analytic continuation

The point of expressing the function f in terms of a rational function is that we can now perform the analytic continuation very simply, just by making the substitution $i\omega \to \omega + i\delta$. In equation (4.20) we have written f as a function of the unitless variable x; in the same way

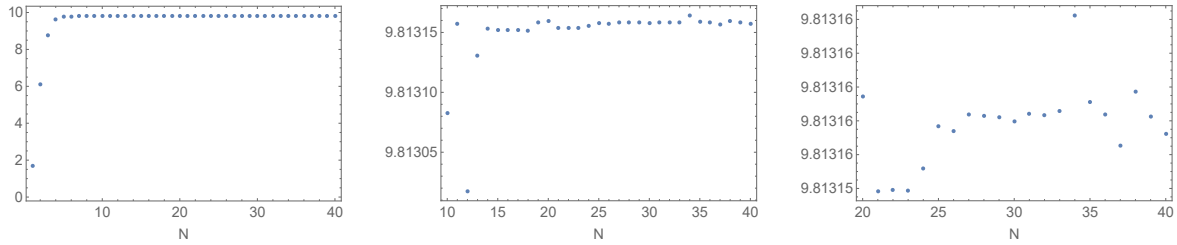

(a) Rapid convergence even for small N.

(b) Some numerical artifacts are visible when zoomed in.

(c) Sequence appears converged with a relative precision of about 10^{-6}.

Figure 4.1: Numerical part of thermal conductivity for a particular (arbitrary) set of physical parameters, evaluated using a Padé approximation with different numbers of data points, N. (a), (b), and (c) show successively zoomed in views on particular ranges of N to show the convergence. Our final result for the conductivity is the limit of this sequence as a function of N.

that τ' is a dimensionless rescaling of the imaginary time, τ, x is a rescaling of the frequency, $x = \omega\frac{\beta}{\pi}$. Thus the analytic continuation is given by the substitution $ix \to x + i\delta'$ where δ' is a rescaled version of δ, $\delta' = \delta\frac{\beta}{\pi}$. The analytic continuation is given by

$$h(ix) = f(x) \to h(x + i\delta') = \frac{\sum_{n=1}^{\infty} a_n(-ix + \delta')^n}{\sum_{n=0}^{\infty} b_n(-ix + \delta')^n} \tag{4.24}$$

where we have introduced the notation $h(ix)$ to emphasize that our original function is defined on the imaginary line in frequency space.

Imaginary part and limits

To complete our analysis, we need to take the real part of $\frac{-i}{\omega} \times h(x + i\delta')$ if the correlation function is even in τ or the real part of $\frac{1}{\omega} \times h(x + i\delta')$ if the correlation function is odd; equivalently we take the imaginary part of $\frac{h(x+i\delta')}{\omega} = \frac{\beta}{\pi} \times \frac{h(x+i\delta')}{x}$ if the correlation function is even and the real part if it is odd. We then take the two limits $x \to 0$ and $\delta' \to 0$. While it is not in general correct to swap the order of these operations and to thus take the limits first and the imaginary part second, it is nevertheless the case that we may first assume that both x and δ' are small to simplify the expression for h before we separate the real and imaginary parts.

In particular, we may keep terms to only first order in both the numerator and denominator of h, which gives the simplified result

$$\frac{h(x + i\delta')}{x} \approx \frac{1}{x} \times \frac{a_0 + a_1(-ix + \delta')}{1 + b_1(-ix + \delta')} \tag{4.25}$$

for small x and δ'. The numerator and the denominator can be combined in the second factor, giving (to first order)

$$\frac{h(x+i\delta')}{x} \approx \frac{1}{x} \times (a_0 + a_1(-ix+\delta'))(1 - b_1(-ix+\delta')) \approx \frac{a_0 + (a_1 - a_0 b_1)(-ix+\delta')}{x} \quad (4.26)$$

With this simplified expression, valid in the case that both x and δ' are small, we can easily find the real and imaginary parts. This is where we use our third assumption from section 4.1, that the current-current correlation function is real-valued at all (imaginary) times τ. This implies that integrals (4.15) and (4.17) are real for each n, so all coefficients in the rational expression (4.24) are real as well. In particular, this means that in equation (4.26) we can assume that a_0, a_1, b_1, x, and δ' are all real.

In that case, the separation into real and imaginary parts becomes quite clear:

$$\mathrm{Re}\left[\frac{h(x+i\delta')}{x}\right] \approx \frac{a_0 + (a_1 - a_0 b_1)\delta'}{x} \quad (4.27)$$

$$\mathrm{Im}\left[\frac{h(x+i\delta')}{x}\right] \approx -(a_1 - a_0 b_1) \quad (4.28)$$

In the case that the correlation function is even in τ, we only care about the imaginary part. In that case we see that both x and δ' have already dropped out of the expression, so the limits as x and δ' go to 0 require no extra analysis. Interestingly, our result is actually just minus the derivative of the function $f(x)$ evaluated at $x = 0$. This is a consequence of the Cauchy-Riemann equations for the type of function $f(x)$ that we consider.

The case where the correlation function is odd is a little less obvious, so we can examine the real part further. In equation (4.27), there are two terms. The first is actually 0. Recalling that a_0 is the value of the integral (4.17) with $n = 0$ and that the correlation function in that integral is odd in τ, we see that $a_0 = 0$. The second term is also simplified by the fact that $a_0 = 0$, and so we end up with just $a_1 \frac{\delta'}{x}$ or equivalently $a_1 \frac{\delta}{\omega}$. Both parameters ω and δ are going to 0, but here we need to know the proper order of the limits.

δ is an infinitesimally small parameter which does not appear in the physical description of the system for which we are computing the transport coefficients. This means that we would ideally like it to drop out of all final expressions. Meanwhile, ω is the frequency at which we want to evaluate the response functions. Since we are interested in DC transport, for which ω is precisely 0 and therefore seemingly less than the the (infinitesimal but) positive parameter δ, it appears that $a_1 \frac{\delta}{\omega}$ is actually infinite. However, as discussed in Wen's book [126, §2.2.6], the Kubo formulas do not behave well at the precise DC limit. Rather, we should get the DC result by finding the AC transport coefficients and then letting $\omega \to 0$, so that actually $\delta \ll \omega$. Thus when the current-current correlator is odd, we conclude that in fact the corresponding $L^{(ij)}$ coefficient is 0.

Summary of analytic continuation results

To summarize our results, we consider separately the two cases of the parity of the current-current correlation function.

1. **Even case:**

   If $\langle j_l(\tau')j_i(0)\rangle$ is even about $\tau' = \pi/2$, then

   $$\lim_{\omega\to 0}\lim_{\delta\to 0}\frac{1}{\omega}\mathrm{Re}\left[-i\int_0^\beta e^{i\omega_n\tau}\langle j_l(\tau')j_i(0)\rangle\right]_{i\omega_n\to\omega+i\delta} = \left(\frac{\beta}{\pi}\right)^2(a_0b_1 - a_1) \tag{4.29}$$

   where a_0, a_1, and b_1 are defined by

   $$\int_0^\pi d\tau' \cos(2n\tau')\langle j_l(\tau')j_i(0)\rangle = f(n) = \frac{\sum_{m=1}^\infty a_m n^m}{\sum_{m=0}^\infty b_m n^m} \tag{4.30}$$

   for $n = 0, 1, 2, \cdots$.

2. **Odd case:**

   If $\langle j_l(\tau')j_i(0)\rangle$ is odd about $\tau' = \pi/2$, then

   $$\lim_{\omega\to 0}\lim_{\delta\to 0}\frac{1}{\omega}\mathrm{Re}\left[-i\int_0^\beta e^{i\omega_n\tau}\langle j_l(\tau')j_i(0)\rangle\right]_{i\omega_n\to\omega+i\delta} = \lim_{\omega\to 0}\lim_{\delta\to 0}\left(\frac{\beta}{\pi}\right)^2 \times a_1\frac{\delta}{\omega} = 0 \tag{4.31}$$

   (where a_1 is defined by

   $$\int_0^\pi d\tau' \sin(2n\tau')\langle j_l(\tau')j_i(0)\rangle = f(n) = \frac{\sum_{m=1}^\infty a_m n^m}{\sum_{m=0}^\infty b_m n^m} \tag{4.32}$$

   for $n = 0, 1, 2, \cdots$.)

From these results we can directly find the $L^{(il)}$ coefficients using equation (2.4), which gives the transport coefficients σ, κ, and S.

Introduction of a cutoff

As noted above, the imaginary-time integrals of the current-current correlation functions used in equations (4.30) and (4.32) actually diverge in our full Luttinger liquid model. The current-current correlators diverge as τ' approaches both 0 and π, so we regulate the divergence by introducing a cutoff ϵ and integrating from ϵ to $\pi - \epsilon$ instead of 0 to π. This allows us to get a finite result for each integral evaluation $f(n)$ and thus for each of the a and b coefficients as well.

This cutoff procedure gives well-defined results for the transport coefficients in the limit $\epsilon \to 0$. While each individual coefficient a_i and b_i depends strongly on the value of ϵ, the dependence cancels out in the difference $a_0b_1 - a_1$. For every numerical evaluation of a transport coefficient, we compute the result for $\epsilon = 10^{-1}$, $10^{-1.5}$, and 10^{-2}. In general we find that the results are nearly converged even for $\epsilon = 0.1$, while the results for the two smaller values of ϵ are typically indistinguishable.

Estimation of numerical error

Numerical errors in computing the Fourier transform integrals, as in equations (4.30) and (4.32), limit the precision of our final results for the transport coefficients. This original source of error may be amplified in two ways:

(1) In solving the linear system of equations (4.23), a poorly conditioned matrix on the left-hand side may lead to a larger relative error in the coefficients a_i and b_i than there was in the original numerical integrals.

(2) Our final results for the transport coefficients are found by subtracting a_1 from $a_0 b_1$. The two terms are of comparable magnitude, so a small relative error in each can lead to a very large relative error in the difference.

Given the relative small number of data points we use ($N_{\max} = 80$) and the numerically stable methods employed by Wolfram Mathematica for solving linear equations, we expect that the error remains small after step 1. The subtraction in (2), however, can introduce significant numerical error.

The amount of error introduced in the subtraction can be roughly approximated as a function of the cutoff ϵ discussed in the previous section, 4.1. For example, the correlator of two electrical current operators, $\langle j_e(\tau') j_e \rangle$, scales as $(\tau')^{1-2\gamma}$ for small τ' (see the end of section 4.3) where $\gamma \geq 1$ is a measure of electron-electron interaction strength as defined in equation (2.11). Thus the integral of the correlation function, which is the coefficient a_0, scales as a power of the cutoff, $a_0 \sim \epsilon^{2-2\gamma}$. If a_1 and $a_0 b_1$ are of a comparable size to a_0, which we empirically find to be the case, then the two terms subtracted to get $a_1 - a_0 b_1$, which is proportional to the electrical conductivity as seen from equations (4.29), (2.4), and (2.2a), are each also of size $\sim \epsilon^{2-2\gamma}$.

We compute all numerical integrals with a guaranteed relative precision of 10^{-10}, so the absolute error in a_0 and hence in $a_1 - a_0 b_1$ is of the order $10^{-10}\epsilon^{2-2\gamma}$. The calculated value of $a_1 - a_0 b_1$ for different interaction strengths γ is shown in figure 4.4 below, and we can compare these values with those of the absolute error to find the expected numerical precision of our final results for the transport coefficient. The worst case is when ϵ is small and γ is large, since the value of $a_1 - a_0 b_1$ decreases with increasing γ and the absolute error (proportional to $\epsilon^{2-2\gamma}$) is large for small ϵ and large γ. The largest value of γ we consider is $\gamma = 3$, giving for our smallest value of ϵ, 10^{-2}, an absolute error of roughly $10^{-10} \times (10^{-2})^{-4} \sim 10^{-2}$. Comparing this with the calculated $a_1 - a_0 b_1 \approx 0.065$, we see that the relative error is still not too large even in this worst case.

The situation is substantially worse for the thermal conductivity. The integral of $\langle J_E(\tau') J_E \rangle$ gives $a_0 \propto \epsilon^{-2\gamma}$ rather than $\epsilon^{2-2\gamma}$ (see the end of section 4.3) so that the absolute error in the worst case of $\gamma = 3$, $\epsilon = 10^{-2}$ is larger by a factor of $\epsilon^{-2} = 10^4$ compared with the corresponding error in the electrical conductivity; the absolute error is on the order of 10^2 in total. By comparison, the calculated value of $a_1 - a_0 b_1$ in this case is about 0.083 so that the relative error is apparently larger than the actual result! This suggests that to

get a reasonable guarantee of numerical precision, we need to either compute the numerical integrals to higher precision or to use a large value of ϵ. Fortunately, as discussed in the previous section, a cutoff of $\epsilon = 10^{-1.5}$ is sufficient to get converged numerical results. This reduces the error by a factor of $(10^{1/2})^6 = 10^3$, so that the error is now apparently of comparable size with the final result.

The above discussion is very imprecise, meant just to give an order of magnitude approximation to the relative precision of our numerical results. In fact the prefactors that we have not included in our estimates of the error improve the relative precision by an order of magnitude or more compared with these estimates, so we conclude that using a cutoff of $\epsilon = 10^{-1.5}$ gives numerically reliable results. We have therefore used this cutoff value for the final results presented in chapter 2.

We have also developed a numerical method to more quantitatively measure the total numerical error including the effects both of solving the linear system and of the subtraction between two large quantities. We randomly vary the values of our numerical integrals by an amount equal to the maximum possible error of those calculations and we estimate the error using the width of the distribution of the corresponding results for the transport coefficients. To be precise, for each value of the cutoff ϵ and each value of the interaction strength γ, we perform the following steps:

1. Directly compute the conductivity. These results are shown as the central data points in all figures.

2. Given that the numerical integrals (4.30) have a guaranteed relative precision of 10^{-10}, we multiply each computed value of $f(n)$ by either $1 + 10^{-10}$ or $1 - 10^{-10}$. This set of modified numerical integrals is one "sample."

3. For each sample, compute the conductivity (or more precisely, the numerical part given by $a_1 - a_0 b_1$).

4. Repeat for some number of samples. We used 10,000 samples for each set of parameters.

5. In the distribution of conductivities corresponding to the many samples, find the smallest interval containing 68% (one sigma) of the samples. This defines the error bars shown in the figures. Note that the distribution for each set of parameters has a single-peak structure so that this is a measure of the width of the distribution.

One of the main results of our work is the numerical evaluation of the Lorenz number, the ratio of thermal conductivity to electrical conductivity, for various values of the electron-electron interaction strength. In that case we modify the procedure slightly, with one sample actually being a pair: one thermal conductivity sample and one electrical conductivity sample. For each sample, we calculate the Lorenz number, and then in the final step we consider the distribution of Lorenz numbers and again take the smallest one sigma interval to find the error bar. In Figure 2.1, we show the Lorenz number as a function of γ calculated for

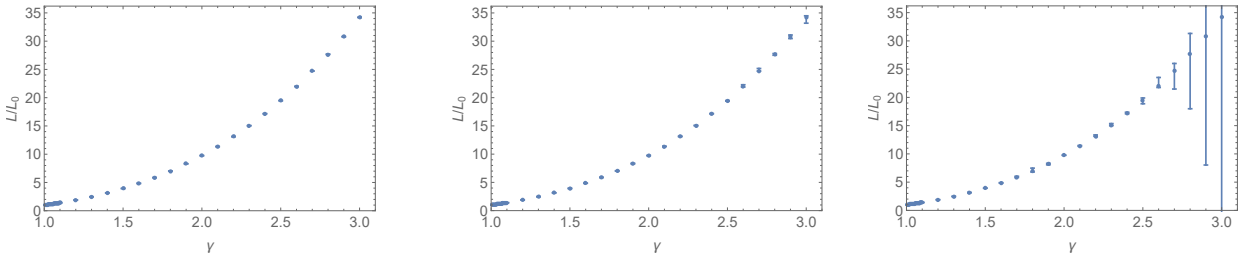

(a) $\epsilon = 10^{-1}$ (b) $\epsilon = 10^{-1.5}$ (c) $\epsilon = 10^{-2}$

Figure 4.2: Calculated Lorenz number and error bars for different values of the cutoff ϵ defined in section 4.1: (a) $\epsilon = 10^{-1}$, (b) $\epsilon = 10^{-1.5}$, and (c) $\epsilon = 10^{-2}$. The error grows rapidly with both γ and $1/\epsilon$. The significance of the Lorenz number in general and of these results in particular is discussed in chapter 2 and in section 4.2.

$\epsilon = 10^{-1.5}$, with error bars computed according to this procedure. In figure 4.2 in these supplementary materials, we show our results for all three values of ϵ for purposes of comparing the error for different values of the cutoff.

As expected based on our rough argument above, the relative error for $\epsilon = 10^{-2}$ is estimated to be more than 100% at the largest interaction strengths, $\gamma \approx 3$. Despite this supposedly large error, the directly computed values are not distinguishable from those with $\epsilon = 10^{1.5}$. The most likely explanation is that the original numerical integrals are more precise than expected; the assumed relative precision of 10^{-10} is guaranteed, but the integrals could be much more precise in practice. Additionally, we have assumed a random distribution of errors in the numerical integration; if instead the numerical errors tended to be all overestimation or all underestimation, the overall error in our final result would be substantially reduced. (We find the slope of a function that passes through points given by the integrals, so if they were all off by some constant amount the final answer would be unaffected.)

Despite the fact that numerical results for the smallest cutoff of $\epsilon = 10^{-2}$ are apparently correct and more precise than expected, we use $\epsilon = 10^{-1.5}$ for the results reported in chapter 2 because we can guarantee that the numerical error is small.

4.2 Noninteracting model with Luttinger density of states

In the discussion above, we have thus far left unresolved the question of what the current-current correlators actually look like. We consider two different models, which give different expressions for the current operators and their correlation functions, and thus for the transport coefficients as well.

The first model is essentially a 2D lattice tight-binding model with some modifications and assumptions to get an effective quasi-1D model with only incoherent transport between the constituent one-dimensional chains.

To be precise, we begin with a noninteracting tight-binding model in 2D:

$$H = -\sum_{jl} t_{//}\left(c_{jl}^{\dagger}c_{j,l+1} + \text{h.c.}\right) + t_{\perp}\left(c_{jl}^{\dagger}c_{j+1,l} + \text{h.c.}\right) \tag{4.33}$$

where j and l index the sites in a two-dimensional square lattice. The hopping strengths are labeled as $t_{//}$ for one direction, which we think of as "along the 1D chains" and as $t_{\perp}$ for the orthogonal direction, which we think of as "between the 1D chains" or "interchain." Thus j indexes 1D chains, while l indexes position along each chain.

The first modification we want to make to this model is to allow for interactions between electrons on each chain (though not between electrons on one chain and electrons on another chain, since we want the different chains to be connected only in an incoherent manner). However, we do not want to specify any particular form of the interaction, so we will take several steps:

1. Switch the description of each chain to be in terms of energy eigenstates by Fourier transforming
2. Replace the resulting tight-binding energies by an unspecified energy for each eigenstate
3. Relax the assumption that the eigenstates on each 1D chain are precisely the same, so that the hopping between chains does not necessarily conserve wave number.

Translating these steps into actual mathematics, we have:

$$\begin{aligned}
H &= -\sum_{jl} t_{//}\left(c_{jl}^{\dagger}c_{j,l+1} + \text{h.c.}\right) + t_{\perp}\left(c_{jl}^{\dagger}c_{j+1,l} + \text{h.c.}\right) \\
&= \sum_{jk}\left(-2\,t_{//}\cos(ka)\right)c_{jk}^{\dagger}c_{jk} - \sum_{jkk'}\left(t_{\perp}\delta_{kk'}\right)\left(c_{jk}^{\dagger}c_{j+1,k'} + \text{h.c.}\right) \\
&\to \sum_{jk} E_k c_{jk}^{\dagger}c_{jk} - \sum_{jkk'}\left(t_{\perp}\delta_{kk'}\right)\left(c_{jk}^{\dagger}c_{j+1,k'} + \text{h.c.}\right) \\
&\to \sum_{jk} E_k c_{jk}^{\dagger}c_{jk} - \sum_{jkk'} t_{kk'}\left(c_{jk}^{\dagger}c_{j+1,k'} + \text{h.c.}\right)
\end{aligned}$$

(Note that a is the lattice spacing along each chain.) This is the Hamiltonian we will be using for our first set of calculations:

$$\boxed{H = \sum_{j,k} E_k c_{jk}^{\dagger}c_{jk} - \sum_{jkk'}\left(t_{kk'}c_{j,k}^{\dagger}c_{j+1,k'} + \text{h.c.}\right)} \tag{2.1}$$

For the purposes of our calculations, we can additionally relax the assumption that the single-particle orbitals labeled by k and k' are extended states given precisely by Fourier transforms of localized orbitals. Instead, we only need to assume that k and k' label single-particle eigenstates and that their creation and annihilation operators satisfy the usual fermion (anti)commutation relations:

$$\{c_{jk}, c_{j'k'}\} = 0 \tag{4.34a}$$
$$\{c^\dagger_{jk}, c^\dagger_{j'k'}\} = 0 \tag{4.34b}$$
$$\{c^\dagger_{jk}, c_{j'k'}\} = \delta_{jj'}\delta_{kk'} \tag{4.34c}$$

In a true interacting system such as the Luttinger liquids we are modeling, such single-particle eigenstates do not actually exist. However, we can meaningfully discuss effective single-particle energies by using the spectral function, so in this model we will take interactions into account *only* by assuming the single-particle energies E_k are distributed according to that spectral function. This assumption will come in via the density of states at the end of our calculation. (This is an uncontrolled approximation, but one purpose of completing our calculation using multiple distinct models is to find the simplest model that correctly captures the behavior of interest, and so we will verify whether this approximation is in fact usable in the future.)

Finally, we must discuss our assumptions regarding the hopping integrals $t_{kk'}$. We will assume that (1) it is a function of only $|k - k'|$ and (2) it is sharply peaked around $k = k'$. The maximum value at $k = k'$ we will denote by t.

Later on in the calculation we will need a more precise expression, especially when we convert from a sum over discrete Fourier states to an integral over a continuous spectrum. We will ultimately use

$$t_{kk'} = te^{-(k-k')^2L^2/\pi} \tag{4.35}$$

(where L is the total length of each 1D chain) in the discrete case and

$$t(k, k') = \frac{t}{L}\delta(k - k') \text{ with } \delta(0) = L \tag{4.36}$$

in the continuum. See section 4.6 for discussion and derivation of these expressions.

Electrical current operator

The electrical current operator in a one-dimensional lattice model is given by [80]

$$J_e = \lim_{k\to 0} \frac{q}{\hbar k} \sum_j [N_j, H]e^{ikaj} \tag{4.37}$$

where j indexes lattice sites, N_j is the total fermion number operator associated with site j, and a is the lattice constant. We can extend this one-dimensional expression to the case of

weakly coupled chains described by a 2D model like the Hamiltonian specified above, which has much weaker coupling in one direction (interchain) than the other (along the chains). In that case, the current operator in each direction is given by

$$J_{e\alpha} = \lim_{k\to 0} \frac{q}{\hbar k} \sum_{\mathbf{j}} [N_{\mathbf{j}}, H] e^{ika_\alpha j_\alpha} \tag{4.38}$$

where α denotes the direction, either along the chains or perpendicular to them. j_α is the site index along that direction, and a_α is the lattice constant in that direction. The composite index $\mathbf{j}$ indicates both the chain and the position along the chain. This could be written as $\mathbf{j} = (j_\alpha, j_{\alpha_\perp})$, where $\alpha_\perp$ is the direction perpendicular to α.

We are interested in computing the current operator for transport between (perpendicular to) the chains (ie α denotes the interchain direction). For simplicity of notation we will denote chain index, j_α, as simply j, and the site index on each chain, $j_{\alpha_\perp}$, as i. Then equation (4.38) becomes

$$J_e = \lim_{k\to 0} \frac{q}{\hbar k} \sum_{ij} [N_{ji}, H] e^{ika_c j} \tag{4.39}$$

where a_c is the interchain spacing (as opposed to a, which is the lattice spacing on each chain). We can slightly rewrite this equation by noting that the index i only appears in N_{ij} and thus we get

$$J_e = \lim_{k\to 0} \frac{q}{\hbar k} \sum_{j} [N_j, H] e^{ika_c j} \tag{4.40}$$

where N_j is the full number operator for chain j, $N_j = \sum_i N_{ij}$. Equivalently, and more usefully for our purposes, we can also write the total number operator as $N_j = \sum_k N_{jk}$ where k indexes single-particle eigenstates on chain j. In the latter formulation, N_{jk} can be written in terms of the fermion creation and annihilation operators as $N_{jk} = c^\dagger_{jk} c_{jk}$.

Now we can calculate the current operator using equation (4.40), above. The first step is to find the commutator $[N_j, H]$ for each j. Here we can separately consider the two terms of H (equation 2.1), and fortunately it turns out that the commutator of N_j with the first term is 0.

To see this, note that N_j is, as above, $\sum_k N_{jk}$, while the first term of H is $\sum_{j'k'} E_{k'} N_{j'k'}$. Then we want to show that each commutator $[N_{jk}, N_{j'k'}]$ is 0. From the perspective of physical intuition, this must be true because the only effect of a number operator is to count the number of excitations without changing the system, so that the order in which you count cannot matter.

Mathematically, we consider two cases. First, if $j' = j$ and $k' = k$ the commutator is 0 because the operators are the same and every operator commutes with itself. Otherwise, we have a commutator of two bosonic operators (since a product of two fermionic operators, such as a number operator, is bosonic) with different indices, a situation which always leads to a vanishing commutator. More generally, the product of any two fermionic operators will commute with any fermionic operator that has disjoint indices:

$$[O_a O_b, O_c] = O_a \{O_b, O_c\} - \{O_a, O_c\} O_b \tag{4.41}$$

which is 0 if O_a, O_b, and O_c are any three fermionic operators with $\delta_{ac} = \delta_{bc} = 0$. Thus any number operator must commute with any fermionic operator with different indices from its own, and hence with a pair of such fermionic operators such as another number operator. This proves that any two number operators with different indices must commute. Combined with the first case, that the commutator vanishes when the indices are the same, we get the desired result.

We must still find the commutator with the hopping terms,

$$[N_j, H] = \left[\sum_q c^\dagger_{jq} c_{jq}, -\sum_{ikk'} t_{kk'} c^\dagger_{i,k} c_{i+1,k'} + \text{h.c.}\right] \tag{4.42}$$

We only have to compute one of the terms, since

$$[A, B^\dagger] = [B, A^\dagger]^\dagger = [B, A]^\dagger = -[A, B]^\dagger \tag{4.43}$$

if $A = A^\dagger$, which is true for the number operator. Then computing the commutator gives

$$[N_j, H] = \sum_{kk'} t_{kk'} [c^\dagger_{j+1,k} c_{j,k'} - c^\dagger_{j,k} c_{j-1,k'}] - \text{h.c.} \tag{4.44}$$

Now we can use the useful fact that for any operator depending on site j, O_j,

$$\lim_{k\to 0} \frac{1}{k} \sum_j (O_{j+1} - O_j) e^{ikaj} = -ia \sum_j O_j \tag{4.45}$$

assuming that the boundary conditions are either periodic or infinite. Then for the current operator we get

$$\boxed{J_e = \frac{ia_c q}{\hbar} \sum_{jkk'} t_{kk'} c^\dagger_{j-1,k} c_{j,k'} - t^*_{kk'} c^\dagger_{j,k'} c_{j-1,k}} \tag{4.46}$$

Thermal current operator

The expression for the energy current in a one-dimensional lattice model is given by [80]

$$J_E = \lim_{k\to 0} \frac{1}{\hbar k} \sum_j [H_j, H] e^{ikaj} \tag{4.47}$$

where j indexes lattice sites and H_j is the portion of the Hamiltonian associated with site j (so $\sum_j H_j = H$). This is quite similar to the expression for the electrical current operator, equation 4.38, but without the overall factor of the electric charge q and with $N_j \to H_j$.

As with the electrical current operator we extend this to the case of coupled chains:

$$J_E = \lim_{k\to 0} \frac{1}{\hbar k} \sum_j [H_j, H] e^{ika_c j} \tag{4.48}$$

where now j indexes 1D chains, a_c is the distance between the chains, and H_j is the portion of the Hamiltonian associated with chain j, including both the Hamiltonian of the isolated chain and hopping terms between chain j and its neighbors (indices $j \pm 1$). There is some ambiguity here, since it is unclear for instance whether hopping terms from chain j to chain $j+1$ or vice-versa should be included in H_j or in H_{j+1}. We have chosen to split the two hopping terms evenly between the two sites, so that

$$H_j = h_j + h'_j \tag{4.49a}$$

$$h_j = \sum_k E_k c^\dagger_{j,k} c_{j,k} \tag{4.49b}$$

$$h'_j = -\frac{1}{2} \sum_{kk'} \left[t_{kk'} (c^\dagger_{j,k} c_{j+1,k'} + c^\dagger_{j,k} c_{j-1,k'}) + \text{h.c.} \right] \tag{4.49c}$$

To find the energy current operator, we must first find the commutator of H_j and H. This actually simplifies quite nicely using the division into local and hopping terms given above:

$$[H_j, H] = \sum_i [H_j, H_i] = \sum_i [h_j, h_i] + [h_j, h'_i] + [h'_j, h_i] + [h'_j, h'_i]$$

The first piece, $[h_i, h_j]$, is 0 because each local Hamiltonian h_i has an even number of fermionic operators in each term. As shown above, any pair of fermionic operators of will commute with a single fermionic operator with disjoint indices, such as a fermionic operator on a different chain, and thus with two of them as in the above commutator. Alternatively, the vanishing of this commutator follows directly from the discussion of commutators of number operators above, since each h_i can be written in terms of those.

Furthermore, the $[h'_j, h'_i]$ term is second order in the interchain hopping strength, $t_{kk'} \sim t_\perp$, and is thus negligible in the limit of weak interchain coupling. This gives the simplified result

$$[H_j, H] \approx \sum_i [h'_j, h_i] - [h'_i, h_j]$$

This we actually have to compute. We can use the nice fact that $[c^\dagger_a c_b, c^\dagger_d c_d] = c^\dagger_a c_b \delta_{bd} - c^\dagger_a c_b \delta_{ad}$

for any (possibly composite) indices a, b, and d. Then we get

$$
\begin{aligned}
[h'_j, h_i] &= -\frac{1}{2}\sum_{kk'q} E_q \left[t_{kk'} c^\dagger_{j,k} c_{j+1,k'} + t^*_{kk} c^\dagger_{j+1,k'} c_{j,k} + t_{kk'} c^\dagger_{j,k} c_{j-1,k'} + t^*_{kk'} c^\dagger_{j-1,k'} c_{j,k}, c^\dagger_{iq} c_{iq} \right] \\
&= -\frac{1}{2}\sum_{kk'q} E_q \begin{bmatrix} t_{kk'} c^\dagger_{j,k} c_{j+1,k'} (\delta_{j+1,i}\delta_{k'q} - \delta_{j,i}\delta_{kq}) \\ +t^*_{kk'} c^\dagger_{j+1,k'} c_{j,k} (\delta_{j,i}\delta_{kq} - \delta_{j+1,i}\delta_{k'q}) \\ +t_{kk'} c^\dagger_{j,k} c_{j-1,k'} (\delta_{j-1,i}\delta_{k'q} - \delta_{j,i}\delta_{kq}) \\ +t^*_{kk'} c^\dagger_{j-1,k'} c_{j,k} (\delta_{j,i}\delta_{kq} - \delta_{j-1,i}\delta_{k'q}) \end{bmatrix} \\
&= -\frac{1}{2}\sum_{kk'q} E_q \begin{bmatrix} \left(t_{kk'} c^\dagger_{j,k} c_{j+1,k'} - t^*_{kk'} c^\dagger_{j+1,k'} c_{j,k} \right) (\delta_{j+1,i}\delta_{k'q} - \delta_{j,i}\delta_{kq}) \\ + \left(t_{kk'} c^\dagger_{j,k} c_{j-1,k'} - t^*_{kk'} c^\dagger_{j-1,k'} c_{j,k} \right) (\delta_{j-1,i}\delta_{k'q} - \delta_{j,i}\delta_{kq}) \end{bmatrix} \\
&= -\frac{1}{2}\sum_{q} E_q \begin{bmatrix} \sum_k \left\{ \left(t_{kq} c^\dagger_{j,k} c_{j+1,q} - t^*_{kq} c^\dagger_{j+1,q} c_{j,k} \right) \delta_{j+1,i} \right. \\ \left. + \left(t_{kq} c^\dagger_{j,k} c_{j-1,q} - t^*_{kq} c^\dagger_{j-1,q} c_{j,k} \right) \delta_{j-1,i} \right\} \\ -\delta_{ji} \sum_{k'} \left\{ \left(t_{qk'} c^\dagger_{j,q} c_{j+1,k'} - t^*_{qk'} c^\dagger_{j+1,k'} c_{j,q} \right) \right. \\ \left. + \left(t_{qk'} c^\dagger_{j,q} c_{j-1,k'} - t^*_{qk'} c^\dagger_{j-1,k'} c_{j,q} \right) \right\} \end{bmatrix}
\end{aligned}
$$

When we subtract $[h'_i, h_j]$, the second line (with δ_{ji}) will cancel. The result is

$$
\begin{aligned}
[H_j, H] &\approx \sum_i [h'_j, h_i] - [h'_i, h_j] \\
&= -\frac{1}{2}\sum_{ikq} E_q \left[\begin{array}{c} t_{kq}\left(c^\dagger_{j,k}c_{j+1,q} - t^*_{kq}c^\dagger_{j+1,q}c_{j,k}\right)\delta_{j+1,i} \\ + \left(t_{kq}c^\dagger_{j,k}c_{j-1,q} - t^*_{kq}c^\dagger_{j-1,q}c_{j,k}\right)\delta_{j-1,i} \\ - \left\{\left(t_{kq}c^\dagger_{i,k}c_{i+1,q} - t^*_{kq}c^\dagger_{i+1,q}c_{i,k}\right)\delta_{i+1,j} \right. \\ \left. + t_{kq}\left(c^\dagger_{i,k}c_{i-1,q} - t^*_{kq}c^\dagger_{i-1,q}c_{i,k}\right)\delta_{i-1,j}\right\} \end{array} \right] \\
&= -\frac{1}{2}\sum_{kq} E_q \left[\begin{array}{c} \left(t_{kq}c^\dagger_{j,k}c_{j+1,q} - t^*_{kq}c^\dagger_{j+1,q}c_{j,k}\right) + \left(t_{kq}c^\dagger_{j,k}c_{j-1,q} - t^*_{kq}c^\dagger_{j-1,q}c_{j,k}\right) \\ - \left\{\left(t_{kq}c^\dagger_{j-1,k}c_{j,q} - t^*_{kq}c^\dagger_{j,q}c_{j-1,k}\right) + \left(t_{kq}c^\dagger_{j+1,k}c_{j,q} - t^*_{kq}c^\dagger_{j,q}c_{j+1,k}\right)\right\} \end{array} \right]
\end{aligned}
$$

Using this result along with equation (4.45), we get

$$
\begin{aligned}
\lim_{k\to 0}\frac{1}{k}\sum_j [H_j, H]e^{ika_cj} &= \frac{ia_c}{2}\sum_{jkq} E_q \left[\begin{array}{c} \left(t_{kq}c^\dagger_{j-1,k}c_{j,q} - t^*_{kq}c^\dagger_{j,q}c_{j-1,k}\right) \\ - \left(t_{kq}c^\dagger_{j,k}c_{j-1,q} - t^*_{kq}c^\dagger_{j-1,q}c_{j,k}\right) \end{array} \right] \\
&= \frac{ia_c}{2}\sum_{jkq} \left[\begin{array}{c} E_q\left(t_{kq}c^\dagger_{j-1,k}c_{j,q} - t^*_{kq}c^\dagger_{j,q}c_{j-1,k}\right) \\ -E_k\left(t_{kq}c^\dagger_{j,q}c_{j-1,k} - t^*_{kq}c^\dagger_{j-1,k}c_{j,q}\right) \end{array} \right] \\
&= \frac{ia_c}{2}\sum_{jkq} \left[(E_q + E_k)\left(t_{kq}c^\dagger_{j-1,k}c_{j,q} - t^*_{kq}c^\dagger_{j,q}c_{j-1,k}\right)\right]
\end{aligned}
$$

So finally we get the energy current operator to first order in $t_{kk'}$:

$$
\boxed{J_E = \frac{ia_c}{\hbar}\sum_{jkk'}\left[\left(\frac{E_k + E_{k'}}{2}\right)\left(t_{kk'}c^\dagger_{j-1,k}c_{jk'} - t^*_{kk'}c^\dagger_{jk'}c_{j-1,k}\right)\right]} \tag{2.7b}
$$

Current-current correlators

According to our procedure for finding transport coefficients as outlined in section 4.1 above, our next step is to find the current-current correlators. We calculate three such expressions here: $\langle J_e J_e\rangle$ that appears in the calculation of electrical conductivity and of thermopower,

$\langle J_E J_E \rangle$ that appears in the calculation of thermal conductivity, and $\langle J_E J_e \rangle$ that appears in the calculation of thermopower. (Note that all three actually appear in the calculation of thermal conductivity, but it will turn out that we need only the second. See section 4.2 for more details.)

$\langle J_e(\tau) J_e(0) \rangle$

The first step in this calculation is to find the time evolution of the current operator. Time evolution of an operator is typically given by

$$J_e(t) = e^{itH} J_e e^{-itH} \tag{4.50}$$

and the imaginary time evolution that we want here is found by making the simple substitution $it \to \tau$, giving (a specific case of equation 4.4)

$$J_e(\tau) = e^{\tau H} J_e e^{-\tau H}. \tag{4.51}$$

Actually finding the time evolution is in general quite difficult, but since we are only interested in the case of very weak interchain coupling, we can find the result only to lowest order in $t_{kk'}$. This simplification makes explicit calculation feasible.

In the time-evolved current operator, equation (4.51), the term lowest-order in $t_{kk'}$ is given by replacing the full Hamiltonian $H = \sum_j h_j + h'_j$ by $H_0 = \sum_j h_j$; that is, we drop the hopping terms entirely from the calculation of the time evolution.

With this approximation, each term h_j in H_0 now commutes with any fermion operator not on chain j, so that

$$e^{\tau H} c^\dagger_{jk} c_{j'k'} e^{-\tau H} \approx e^{\tau \sum_i h_i} c^\dagger_{jk} c_{j'k'} e^{-\tau \sum_i h_i} = e^{\tau(h_j + h_{j'})} c^\dagger_{jk} c_{j'k'} e^{-\tau(h_j + h_{j'})} \tag{4.52}$$

and if $j \neq j'$ (for instance if $j' = j \pm 1$) then

$$e^{\tau(h_j + h_{j'})} c^\dagger_{jk} c_{j'k'} e^{-\tau(h_j + h_{j'})} = e^{\tau h_j} c^\dagger_{jk} e^{-\tau h_j} e^{\tau h_{j'}} c_{j'k'} e^{-\tau h_{j'}} \tag{4.53}$$

Now we can calculate each of the two factors separately. We will show the first calculation explicitly and just cite the result for the second since it is nearly the same. First, some useful

lemmas:

Lemma 1:

$$\begin{aligned}[n_a, c_b^\dagger] &= c_a^\dagger c_a c_b^\dagger - c_b^\dagger c_a^\dagger c_a \\ &= \delta_{ab} c_a^\dagger - c_a^\dagger c_b^\dagger c_a - c_b^\dagger c a^\dagger c_a \\ &= \delta_{ab} c_a^\dagger + c_b^\dagger c_a^\dagger c_a - c_b^\dagger c a^\dagger c_a \\ &= \delta_{ab} c_a^\dagger \end{aligned} \tag{4.54}$$

Lemma 2:

$$\begin{aligned} n_{jk}^m c_{jk}^\dagger &= n_{jk}^{m-1}([n_{jk}, c_{jk}^\dagger] + c_{jk}^\dagger n_{jk}) \\ &= n_{jk}^{m-1}(c_{jk}^\dagger + c_{jk}^\dagger n_{jk}) \\ &= n_{jk}^{m-1} c_{jk}^\dagger (1 + n_{jk}) \\ &\vdots \\ &= c_{jk}^\dagger (1 + n_{jk})^m \end{aligned} \tag{4.55}$$

Using the second lemma, equation (4.55), we have

$$\begin{aligned} e^{\tau h_j} c_{jk}^\dagger e^{-\tau h_j} &= e^{\tau E_k n_{jk}} c_{jk}^\dagger e^{-\tau E_k n_{jk}} \\ &= \left[\sum_{m=0}^{\infty} \frac{(\tau E_k)^m}{m!} n_{jk}^m \right] c_{jk}^\dagger e^{-\tau E_k n_{jk}} \\ &= \left[\sum_{m=0}^{\infty} \frac{(\tau E_k)^m}{m!} \left(n_{jk}^m c_{jk}^\dagger \right) \right] e^{-\tau E_k n_{jk}} \\ &= c_{jk}^\dagger \left[\sum_{m=0}^{\infty} \frac{(\tau E_k)^m}{m!} (1 + n_{jk})^m \right] e^{-\tau E_k n_{jk}} \\ &= c_{jk}^\dagger e^{\tau E_k (1 + n_{jk})} e^{-\tau E_k n_{jk}} \\ &= e^{\tau E_k} c_{jk}^\dagger \end{aligned}$$

The result for the annihilation operator is similar, but the exponent is negative because

$$[n_a, c_b] = [c_b^\dagger, n_a^\dagger]^\dagger = -[n_a, c_b^\dagger]^\dagger = -(c_b^\dagger)^\dagger = -c_b \tag{4.56}$$

To summarize:

$$c_{jk}^\dagger(\tau) = e^{\tau h_j} c_{jk}^\dagger e^{-\tau h_j} = e^{\tau E_k} c_{jk}^\dagger \tag{4.57}$$

$$c_{jk}(\tau) = e^{\tau h_j} c_{jk} e^{-\tau h_j} = e^{-\tau E_k} c_{jk}^\dagger \tag{4.58}$$

Returning now to the calculation from equation (4.52), we have

$$e^{\tau H} c_{jk}^\dagger c_{j'k'} e^{-\tau H} \approx e^{\tau (E_k - E_{k'})} c_{jk}^\dagger c_{j'k'} \tag{4.59}$$

With this result and the current operator already calculated above (equation 4.46), the calculation of the time-evolved current operator becomes quite easy:

$$J_e(\tau) = \frac{ia_c q}{\hbar} \sum_{jkk'} e^{\tau(E_k - E_{k'})} t_{kk'} c^\dagger_{j-1,k} c_{j,k'} - e^{\tau(E_{k'} - E_k)} t^*_{kk'} c^\dagger_{j,k'} c_{j-1,k} \tag{4.60}$$

Note this is not Hermitian (assuming $\tau \in \boldsymbol{R}$), since it is evolved in imaginary time.

Now that we have the time-evolved current operator, we can find the correlation function relatively easily. Before doing the actual calculation, we will briefly review what the $\langle\ ,\ \rangle$ symbols mean in this context. The average denoted by $\langle O \rangle$ for some operator O is a thermal average, meaning it is defined by

$$\langle O \rangle = \mathrm{Tr}[e^{-\beta H} O]/\mathrm{Tr}[e^{-\beta H}] = \mathrm{Tr}[e^{-\beta H} O]/Z \tag{4.61}$$

As with the time evolution, the fact that we are interested only in the result to lowest order in the interchain hopping strength means that in the density matrix $e^{-\beta H}$, we can replace H by $H_0 = \sum_j h_j$. That part of the calculation will be shown explicitly below.

Now let's actually do the calculation:

$$\langle J_e(\tau)J_e(0)\rangle = -\left(\frac{a_c q}{\hbar}\right)^2 \sum_{jkk'}\sum_{iqq'} \left\langle \begin{array}{c} \left(e^{\tau(E_k-E_{k'})}t_{kk'}c^\dagger_{j-1,k}c_{j,k'} - e^{\tau(E_{k'}-E_k)}t^*_{kk'}c^\dagger_{j,k'}c_{j-1,k}\right) \\ \times \left(t_{qq'}c^\dagger_{i-1,q}c_{i,q'} - t^*_{qq'}c^\dagger_{i,q'}c_{i-1,q}\right) \end{array} \right\rangle$$

$$= -\left(\frac{a_c q}{\hbar}\right)^2 \sum_{jkk'}\sum_{iqq'} \left\langle \begin{array}{c} e^{\tau(E_k-E_{k'})}t_{kk'}t_{qq'}c^\dagger_{j-1,k}c_{j,k'}c^\dagger_{i-1,q}c_{i,q'} \\ -e^{\tau(E_k-E_{k'})}t_{kk'}t^*_{qq'}c^\dagger_{j-1,k}c_{j,k'}c^\dagger_{i,q'}c_{i-1,q} \\ -e^{\tau(E_{k'}-E_k)}t^*_{kk'}t_{qq'}c^\dagger_{j,k'}c_{j-1,k}c^\dagger_{i-1,q}c_{i,q'} \\ +e^{\tau(E_{k'}-E_k)}t^*_{kk'}t^*_{qq'}c^\dagger_{j,k'}c_{j-1,k}c^\dagger_{i,q'}c_{i-1,q} \end{array} \right\rangle$$

$$= \left(\frac{a_c q}{\hbar}\right)^2 \sum_{jkk'}\sum_{iqq'} \left\langle \begin{array}{c} e^{\tau(E_{k'}-E_k)}t^*_{kk'}t_{qq'}c^\dagger_{j,k'}c_{j-1,k}c^\dagger_{i-1,q}c_{i,q'} \\ +e^{\tau(E_k-E_{k'})}t_{kk'}t^*_{qq'}c^\dagger_{j-1,k}c_{j,k'}c^\dagger_{i,q'}c_{i-1,q} \end{array} \right\rangle$$

$$= \left(\frac{a_c q}{\hbar}\right)^2 \sum_{jkk'} \left\langle \begin{array}{c} e^{\tau(E_{k'}-E_k)}|t_{kk'}|^2 c^\dagger_{j,k'}c_{j-1,k}c^\dagger_{j-1,k}c_{j,k'} \\ +e^{\tau(E_k-E_{k'})}|t_{kk'}|^2 c^\dagger_{j-1,k}c_{j,k'}c^\dagger_{j,k'}c_{j-1,k} \end{array} \right\rangle$$

$$= \left(\frac{a_c q}{\hbar}\right)^2 \sum_{jkk'} |t_{kk'}|^2 \left\langle e^{\tau(E_{k'}-E_k)}c_{j-1,k}c^\dagger_{j-1,k}c^\dagger_{j,k'}c_{j,k'} + e^{\tau(E_k-E_{k'})}c_{j,k'}c^\dagger_{j,k'}c^\dagger_{j-1,k}c_{j-1,k}\right\rangle$$

$$= \left(\frac{a_c q}{\hbar}\right)^2 \sum_{jkk'} |t_{kk'}|^2 \left(e^{\tau(E_{k'}-E_k)}\langle(1-n_{j-1,k})n_{j,k'}\rangle + e^{\tau(E_k-E_{k'})}\langle(1-n_{j,k'})n_{j-1,k}\rangle\right)$$

The third line follows from the fact that the expectation value is calculated using a trace, coupled with the fact that the two dropped terms can never be diagonal. We can now calculate each expectation value in a relatively straightforward manner. For example, let's find $\langle(1-n_{j-1,k})n_{j,k'}\rangle$.

The first important point is that since in the Hamiltonian appearing in the density matrix we have eliminated all terms that include operators acting on multiple different chains, the

expectation value actually splits up into separate ones on each chain:

$$\begin{aligned}
\langle (1-n_{j-1,k})n_{j,k'}\rangle &= \mathrm{Tr}[e^{-\beta H_0}(1-n_{j-1,k})n_{j,k'}]/\mathrm{Tr}[e^{-\beta H_0}] \\
&= \frac{\left(\prod_{i\neq j,j-1}\mathrm{Tr}[e^{-\beta h_i}]\right)\mathrm{Tr}[e^{-\beta h_{j-1}}(1-n_{j-1,k})]\mathrm{Tr}[e^{-\beta h_j}n_{jk'}]}{\prod_i \mathrm{Tr}[e^{-\beta h_i}]} \\
&= \frac{\mathrm{Tr}[e^{-\beta h_{j-1}}(1-n_{j-1,k})]}{\mathrm{Tr}[e^{-\beta h_{j-1}}]} \times \frac{\mathrm{Tr}[e^{-\beta h_j}n_{jk'}]}{\mathrm{Tr}[e^{-\beta h_j}]} \\
&= \frac{\left(\prod_{i\neq j-1}\mathrm{Tr}[e^{-\beta h_i}]\right)\mathrm{Tr}[e^{-\beta h_{j-1}}(1-n_{j-1,k})]}{\prod_i \mathrm{Tr}[e^{-\beta h_i}]} \\
&\qquad \times \frac{\left(\prod_{i\neq j}\mathrm{Tr}[e^{-\beta h_i}]\right)\mathrm{Tr}[e^{-\beta h_j}n_{jk'}]}{\prod_i \mathrm{Tr}[e^{-\beta h_i}]} \\
&= \langle 1-n_{j-1,k}\rangle\langle n_{jk'}\rangle \\
&= (1-\langle n_{j-1,k}\rangle)\langle n_{jk'}\rangle
\end{aligned}$$

So in reality we just need to calculate the expectation value of a single number operator, $\langle n_{jk}\rangle$. That calculation looks like:

$$\begin{aligned}
\langle n_{jk}\rangle &= \frac{\mathrm{Tr}[e^{-\beta h_j}n_{jk}]}{\mathrm{Tr}[e^{-\beta h_j}]} \\
&= \frac{\mathrm{Tr}[e^{-\beta E_k n_{jk}}n_{jk}]}{\mathrm{Tr}[e^{-\beta E_k n_{jk}}]} \\
&= \frac{\sum_{n_{jk}=0,1}[e^{-\beta E_k n_{jk}}n_{jk}]}{\sum_{n_{jk}=0,1}[e^{-\beta E_k n_{jk}}]} \\
&= \frac{e^{-\beta E_k}}{1+e^{-\beta E_k}} \\
&= \frac{1}{1+e^{\beta E_k}}
\end{aligned}$$

which is just the usual Fermi-Dirac distribution. Plugging this result into $(1-\langle n_{j-1,k}\rangle)\langle n_{jk'}\rangle$, we get:

$$\begin{aligned}
\langle (1-n_{j-1,k})n_{j,k'}\rangle &= \left(1-\frac{1}{1+e^{\beta E_k}}\right)\frac{1}{1+e^{\beta E_{k'}}} \\
&= \frac{e^{\beta E_k}}{(1+e^{\beta E_k})(1+e^{\beta E_{k'}})} \\
&= \frac{1}{(1+e^{-\beta E_k})(1+e^{\beta E_{k'}})}
\end{aligned} \tag{4.62}$$

This result is independent of j, so the sum over j in the current-current correlator just gives a factor of the total number of chains, N. Then we finally get

$$\begin{aligned}
\langle J_e(\tau)J_e(0)\rangle &= N\left(\frac{a_c q}{\hbar}\right)^2 \sum_{kk'} |t_{kk'}|^2 \left[\frac{e^{\tau(E_{k'}-E_k)}}{(1+e^{-\beta E_k})(1+e^{\beta E_{k'}})} + \frac{e^{\tau(E_k-E_{k'})}}{(1+e^{\beta E_k})(1+e^{-\beta E_{k'}})}\right] \\
&= N\left(\frac{a_c q}{\hbar}\right)^2 \left(\frac{L}{2\pi}\right)^2 \int_{kk'} |t(k,k')|^2 \left[\frac{e^{\tau(E(k')-E(k)}}{\left(1+e^{-\beta E(k)}\right)\left(1+e^{\beta E(k')}\right)}\right. \\
&\qquad \left. + \frac{e^{\tau(E(k)-E(k'))}}{\left(1+e^{\beta E(k)}\right)\left(1+e^{-\beta E(k')}\right)}\right] dk\, dk' \\
&= 2N\left(\frac{a_c q}{\hbar}\right)^2 \left(\frac{L}{2\pi}\right)^2 \int_{EE'} |t(E,E')|^2 g(E) g(E') \left[\frac{e^{\tau(E'-E)}}{(1+e^{-\beta E})(1+e^{\beta E'})}\right. \\
&\qquad \left. + \frac{e^{\tau(E-E')}}{(1+e^{\beta E})(1+e^{-\beta E'})}\right] dE\, dE' \\
&= 4N\left(\frac{a_c q}{\hbar}\right)^2 \left(\frac{L}{2\pi}\right)^2 \int_{EE'} |t(E,E')|^2 g(E) g(E') \left[\frac{e^{\tau(E-E')}}{(1+e^{\beta E})(1+e^{-\beta E'})}\right] dE\, dE'
\end{aligned}$$

where in the third line we have changed variables from k and k' to $E = E(k)$ and $E' = E(k')$. This produces two factors of the density of states (or equivalently the spectral function); we also must change $t(k,k')$ to $t(E,E')$, which is defined such that $t(E(k),E(k')) = t(k,k')$ for all k, k'. We have also introduced a factor of 2 for the right- and left-moving excitations, since each energy corresponds to two values of k, $k \approx k_F$ and $k \approx -k_F$. The last line follows from the fact that E and E' are dummy variables and therefore the two terms are actually identical so long as $|t(E,E')| = |t(E',E)|$, which we assumed to be the case when we said that $t_{kk'}$ depends only on the combination $|k-k'|$.

We are left with a rather nice expression for the current-current correlator:

$$\boxed{\langle J_e(\tau)J_e(0)\rangle = 4N\left(\frac{a_c q}{\hbar}\right)^2 \left(\frac{L}{2\pi}\right)^2 \int_{EE'} |t(E,E')|^2 g(E) g(E') \left[\frac{e^{\tau(E-E')}}{(1+e^{\beta E})(1+e^{-\beta E'})}\right] dE\, dE'} \tag{4.63}$$

$\langle J_E(\tau)J_E(0)\rangle$

Just as our first step in finding $\langle J_e(\tau)J_e(0)\rangle$ was to find the time evolution of the electrical current operator J_e, our first step now is to find the time evolution of J_E. Most of the work, however, has already been done! As J_E (equation 2.7b) looks just like J_e (equation 4.46) but with a factor of average energy replacing the factor of charge, the time evolution calculation is identical. The result is

$$J_E(\tau) = \frac{ia_c}{\hbar} \sum_{jkk'} \left[\left(\frac{E_k + E_{k'}}{2}\right)\left(e^{\tau(E_k-E_{k'})} t_{kk'} c^\dagger_{j-1,k} c_{j,k'} - e^{\tau(E_{k'}-E_k)} t^*_{kk'} c^\dagger_{jk'} c_{j-1,k}\right)\right] \tag{4.64}$$

Then we can find $\langle J_E(\tau)J_E(0)\rangle$ just like we found the $\langle J_e(\tau)J_e(0)\rangle$ above:

$$\langle J_E(\tau)J_E(0)\rangle = -\left(\frac{a_c}{\hbar}\right)^2 \sum_{jkk'}\sum_{iqq'} \left\langle \begin{array}{c} \left(\frac{E_k+E_{k'}}{2}\right)\left(e^{\tau(E_k-E_{k'})}t_{kk'}c^\dagger_{j-1,k}c_{jk'} - e^{\tau(E_{k'}-E_k)}t^*_{kk'}c^\dagger_{jk'}c_{j-1,k}\right) \\ \times \left(\frac{E_q+E_{q'}}{2}\right)\left(t_{qq'}c^\dagger_{i-1,q}c_{iq'} - t^*_{qq'}c^\dagger_{iq'}c_{i-1,q}\right) \end{array} \right\rangle$$

This looks just like the calculation with J_e except that two factors of q have been replaced with two factors of average energy in the sum. The trace forces $q = k$ and $q' = k'$, making the two energy factors the same, so by analogy with the result for $\langle J_e(\tau)J_e(0)\rangle$ (replacing q^2 by average energy squared), we get

$$\begin{aligned}
&\langle J_E(\tau)J_E(0)\rangle \\
&= \left(\frac{a_c}{\hbar}\right)^2 \sum_{jkk'} \left(\frac{E_k+E_{k'}}{2}\right)^2 |t_{kk'}|^2 \left(e^{\tau(E_{k'}-E_k)}\langle(1-n_{j-1,k})n_{j,k'}\rangle + e^{\tau(E_k-E_{k'})}\langle(1-n_{j,k'})n_{j-1,k}\rangle\right) \\
&= 4N\left(\frac{a_c}{\hbar}\right)^2\left(\frac{L}{2\pi}\right)^2 \int_{EE'} |t(E,E')|^2 g(E)g(E')\left(\frac{E+E'}{2}\right)^2 \left[\frac{e^{\tau(E-E')}}{(1+e^{\beta E})\,(1+e^{-\beta E'})}\right] dE\, dE'
\end{aligned}$$

Again, we have a relatively nice expression for the current-current correlator,

$$\boxed{\begin{aligned}
&\langle J_E(\tau)J_E(0)\rangle \\
&= 4N\left(\frac{a_c}{\hbar}\right)^2\left(\frac{L}{2\pi}\right)^2 \int_{EE'} |t(E,E')|^2 g(E)g(E')\left(\frac{E+E'}{2}\right)^2 \left[\frac{e^{\tau(E-E')}}{(1+e^{\beta E})\,(1+e^{-\beta E'})}\right] dE\, dE'
\end{aligned}} \tag{4.65}$$

$\langle J_E(\tau)J_e(0)\rangle$

To calculate $\langle J_E(\tau)J_e(0)\rangle$, we can again get the answer quickly by analogy with our results for $\langle J_e(\tau)J_e(0)\rangle$.

$$\begin{aligned}\langle J_E(\tau)J_e(0)\rangle &= -q\left(\frac{a_c}{\hbar}\right)^2\sum_{jkk'}\sum_{iqq'}\\ &\left\langle \left(\tfrac{E_k+E_{k'}}{2}\right)\left(e^{\tau(E_k-E_{k'})}t_{kk'}c^\dagger_{j-1,k}c_{jk'}-e^{\tau(E_{k'}-E_k)}t^*_{kk'}c^\dagger_{jk'}c_{j-1,k}\right)\right.\\ &\left.\qquad\times\left(t_{qq'}c^\dagger_{i-1,q}c_{iq'}-t^*_{qq'}c^\dagger_{iq'}c_{i-1,q}\right)\right\rangle\\ &= q\left(\frac{a_c}{\hbar}\right)^2\sum_{jkk'}\left(\frac{E_k+E_{k'}}{2}\right)|t_{kk'}|^2\left(e^{\tau(E_{k'}-E_k)}\langle(1-n_{j-1,k})n_{j,k'}\rangle+e^{\tau(E_k-E_{k'})}\langle(1-n_{j,k'})n_{j-1,k}\rangle\right)\\ &= 4Nq\left(\frac{a_c}{\hbar}\right)^2\left(\frac{L}{2\pi}\right)^2\int_{EE'}|t(E,E')|^2g(E)g(E')\left(\frac{E+E'}{2}\right)\left[\frac{e^{\tau(E-E')}}{(1+e^{\beta E})(1+e^{-\beta E'})}\right]dE\,dE'\end{aligned}$$

This is a again a nice expression for the correlator,

$$\boxed{\begin{aligned}&\langle J_E(\tau)J_e(0)\rangle\\ &= 4Nq\left(\frac{a_c}{\hbar}\right)^2\left(\frac{L}{2\pi}\right)^2\int_{EE'}|t(E,E')|^2g(E)g(E')\left(\frac{E+E'}{2}\right)\left[\frac{e^{\tau(E-E')}}{(1+e^{\beta E})(1+e^{-\beta E'})}\right]dE\,dE'\end{aligned}} \tag{4.66}$$

Response functions

We have now calculated all the current-current correlation functions that we need in order to calculate the desired transport coefficients. For the purposes of the remaining calculations, it will be helpful to write all the correlators (equations 4.63, 4.65, and 4.66) in a single expression. In particular, we have

$$\begin{aligned}&\langle j_l(\tau)j_i(0)\rangle \qquad (4.67)\\ &= 4N\left(\frac{a_c}{\hbar}\right)^2\left(\frac{L}{2\pi}\right)^2\int_{EE'}|t(E,E')|^2g(E)g(E')\left(\frac{E+E'}{2}\right)^{n_{il}}\left[\frac{e^{\tau(E-E')}}{(1+e^{\beta E})(1+e^{-\beta E'})}\right]dE\,dE'\end{aligned}$$

where $j_1 = J_e/q$, $j_2 = J_E$, and n_{il} is $(i+l-2)$.

Using this result, we want to calculate the $L^{(il)}$ coefficients, which can then be used to find the physical transport coefficients via equation (2.2). Recall that the $L^{(il)}$ are given by equation (2.4), reproduced here for convenience:

$$L^{(il)} = \lim_{\omega\to 0}\lim_{\delta\to 0}\frac{1}{\omega}\left[\frac{-iT}{\Omega}\int_0^\beta d\tau e^{i\omega\tau}\langle T_\tau j_l(\tau)j_i(0)\rangle\right]_{i\omega\to\omega+i\delta} \tag{2.4}$$

Fortunately we can use our expression that encapsulates all the relevant current-current correlators, equation (4.67), to find all the $L^{(il)}$ at once.

Our first step is to non-dimensionalize our expressions so that the dependence on all unitful parameters becomes explicit. We first follow the procedure from section 4.1 above and change variables from τ to $\tau' = \tau\frac{\pi}{\beta}$, ω to $n = \omega\frac{\beta}{2\pi}$, and δ to $\delta' = \delta\frac{\beta}{2\pi}$. This gives

$$L^{(il)} = \lim_{n\to 0}\lim_{\delta'\to 0}\frac{\beta}{2\pi n}\left[\frac{-iT}{\Omega}\left(\frac{\beta}{\pi}\right)\int_0^\pi d\tau' e^{2in\tau'}\langle T_{\tau'} j_l(\tau')j_i(0)\rangle\right]_{i\omega\to n+i\delta'} \tag{4.68}$$

Furthermore, in the expression for $\langle j(\tau')j\rangle$, we can switch the integration variables from E to βE, giving:

$$\begin{aligned}
&\langle j_l(\tau')j_i(0)\rangle \\
&= 4N\left(\frac{a_c}{\hbar}\right)^2\left(\frac{L}{2\pi}\right)^2\int_{EE'}|t(E,E')|^2 g(E)g(E')\left(\frac{E+E'}{2}\right)^{n_{il}}\left[\frac{e^{\tau'\beta(E-E')/\pi}}{(1+e^{\beta E})\,(1+e^{-\beta E'})}\right]dE\,dE' \qquad (4.69)\\
&= 4N\left(\frac{a_c}{\hbar}\right)^2\left(\frac{L}{2\pi}\right)^2\beta^{-(n_{il}+2)}\int_{yy'}|t(y/\beta,y'/\beta)|^2 g(y/\beta)g(y'/\beta) \\
&\qquad\qquad \times\left(\frac{y+y'}{2}\right)^{n_{il}}\left[\frac{e^{\tau'(y-y')/\pi}}{(1+e^{y})\,(1+e^{-y'})}\right]dy\,dy' \qquad (4.70)
\end{aligned}$$

We next have to choose whether to integrate first over the rescaled energy coordinates (y and y') or instead over the rescaled imaginary time τ'. Since it is formally correct to view the correlation function as a function only of τ and then to integrate that, we will integrate over y and y' first. This convention matches the procedure described above in section 4.1 and therefore also the procedure we follow numerically in analyzing our second model (section 4.3).

For this purpose, we need an expression for $t(E,E')$. As discussed in section 4.6 we assume that $t(E,E')$ is sharply peaked (width proportional to L^{-1}) about $E = E'$. In particular, we use

$$t(E,E') = \frac{tv}{L}\delta(E-E') \quad\text{with}\quad \delta(0) = \frac{L}{v} \tag{4.71}$$

so that

$$t(y/\beta,y'/\beta) = \frac{tv}{L}\delta\left(\frac{y-y'}{\beta}\right) = \frac{tv\beta}{L}\delta(y-y') \text{ with } \delta_y(0) = \frac{L}{v\beta} \tag{4.72}$$

where the subscript on the last delta functions indicates that $\delta(0)$ comes from $\delta(y)$ with $y = 0$.

In our expression, we have two powers of the delta function. The first is used as a delta function to collapse the integral over y', setting $y' = y$. The second just contributes a factor of $\frac{tv\beta}{L}\delta_y(0) = t$. We thus find

$$\begin{aligned}
&\langle j_l(\tau')j_i(0)\rangle \\
&= 4N\left(\frac{a_c}{\hbar}\right)^2\left(\frac{L}{2\pi}\right)^2\beta^{-(n_{il}+2)}\int_{yy'}|t(y/\beta,y'/\beta)|^2 g(y/\beta)g(y'/\beta) \\
&\qquad\qquad \times\left(\frac{y+y'}{2}\right)^{n_{il}}\left[\frac{e^{\tau'(y-y')/\pi}}{(1+e^{y})\,(1+e^{-y'})}\right]dy\,dy' \qquad (4.73)\\
&= 4N\left(\frac{a_c}{\hbar}\right)^2\left(\frac{L}{2\pi}\right)^2\beta^{-(n_{il}+2)}\left(\frac{t^2v\beta}{L}\right)\int_{yy'}g^2(y/\beta)\,(y)^{n_{il}}\left[\frac{1}{(1+e^{y})\,(1+e^{-y})}\right]dy \qquad (4.74)\\
&= 4NL\left(\frac{a_c t}{\hbar}\right)^2\left(\frac{v\beta^{-(n_{il}+1)}}{(2\pi)^2}\right)\int_{yy'}\frac{g^2(y/\beta)y^{n_{il}}}{(1+e^{y})\,(1+e^{-y})}\,dy \qquad (4.75)
\end{aligned}$$

Note that τ' has actually dropped out of the expression entirely! This seems worrisome, since to find $L^{(il)}$ from $\langle j_l(\tau')j_i(0)\rangle$ we are now supposed to Fourier transform a constant function over a finite domain, which will give a Kronecker delta:

$$\int_0^{\pi} e^{2in\tau'}d\tau' = \pi\delta_{n0} \qquad (4.76)$$

It is not at all obvious how this ought to be analytically continued in the fashion $in \to n+i\delta'$. Instead of trying to justify some particular choice in this case, we will simply assert that there must exist on physical grounds some regularization which makes the (unitless) quantity

$$\mathrm{Re}\left(\lim_{n\to 0}\lim_{\delta'\to 0}\frac{-i}{n}\left[\int_0^{\pi}e^{2in\tau'}d\tau'\right]_{in\to n+i\delta'}\right) \qquad (4.77)$$

into some finite number. We call this constant A. There is precedent for this approach in the literature. In particular, in reference [29], there is an unspecified scaling function $F_\alpha(\omega/T)$ which, in the $\omega \to 0$ limit, corresponds to our constant A.

Using this approach, we find

$$L^{(il)} = \lim_{n\to 0}\lim_{\delta'\to 0}\frac{\beta}{2\pi n}\left[\frac{-iT}{\Omega}\left(\frac{\beta}{\pi}\right)\int_0^\pi d\tau' e^{2in\tau'}\langle T'_\tau j_l(\tau')j_i(0)\rangle\right]_{i\omega\to n+i\delta'} \tag{4.78}$$

$$= \frac{\beta}{2\pi}\left[\frac{T}{\Omega}\left(\frac{\beta}{\pi}\right)4NL\left(\frac{a_c t}{\hbar}\right)^2\left(\frac{v\beta^{-(n_{il}+1)}}{(2\pi)^2}\right)\int_{yy'}\frac{g^2(y/\beta)y^{n_{il}}}{(1+e^y)(1+e^{-y})}\,dy\right]$$

$$\times \lim_{n\to 0}\lim_{\delta'\to 0}\frac{-i}{n}\left[\int_0^\pi e^{2in\tau'}d\tau'\right]_{in\to n+i\delta'} \tag{4.79}$$

$$\mathrm{Re}\left[L^{(il)}\right] = A\frac{\beta}{2\pi}\left[\frac{T}{\Omega}\left(\frac{\beta}{\pi}\right)4NL\left(\frac{a_c t}{\hbar}\right)^2\left(\frac{v\beta^{-(n_{il}+1)}}{(2\pi)^2}\right)\int_{yy'}\frac{g^2(y/\beta)y^{n_{il}}}{(1+e^y)(1+e^{-y})}\,dy\right] \tag{4.80}$$

$$= \frac{4ANL}{\pi\Omega}\left(\frac{a_c t}{\hbar}\right)^2\frac{v\beta^{-n_{il}}}{(2\pi)^3}\int_{yy'}\frac{g^2(y/\beta)y^{n_{il}}}{(1+e^y)(1+e^{-y})}\,dy \tag{4.81}$$

$$= \frac{Aa_c t^2 v\beta^{-n_{il}}}{2\pi^4\hbar^2}\int_{yy'}\frac{g^2(y/\beta)y^{n_{il}}}{(1+e^y)(1+e^{-y})}\,dy \tag{4.82}$$

Note that in the last line we have used that fact that the volume of the system is $\Omega = Na_cL$. We can also set $\hbar = 1$ to get a nice final answer for $\mathrm{Re}\left[L^{(il)}\right]$:

$$\boxed{\mathrm{Re}\left[L^{(il)}\right] = \frac{Aa_c t^2 v\beta^{-n_{il}}}{2\pi^4}\int_{yy'}\frac{g^2(y/\beta)y^{n_{il}}}{(1+e^y)(1+e^{-y})}\,dy} \tag{4.83}$$

We can now use equations (2.2) to get expressions for the conductivities and the thermopower from $L^{(il)}$. The results are

$$\sigma = \frac{e^2}{T}L^{(11)} = \frac{Aa_c e^2 t^2 v\beta}{2\pi^4}\int_{yy'}\frac{g^2(y/\beta)}{(1+e^y)(1+e^{-y})}\,dy \tag{4.84a}$$

$$\kappa = \frac{1}{T^2}\left[L^{(22)} - \frac{(L^{(12)})^2}{L^{(11)}}\right] = \frac{Aa_c t^2 v}{2\pi^4}\left[\int_{yy'}\frac{y^2 g^2(y/\beta)}{(1+e^y)(1+e^{-y})}\,dy - \frac{\left(\int_{yy'}\frac{y\,g^2(y/\beta)}{(1+e^y)(1+e^{-y})}\,dy\right)^2}{\int_{yy'}\frac{g^2(y/\beta)}{(1+e^y)(1+e^{-y})}\,dy}\right] \tag{4.84b}$$

$$S = -\frac{1}{eT}\frac{L^{(12)}}{L^{(11)}} = -\frac{1}{e}\frac{\int_{yy'}\frac{y\,g^2(y/\beta)}{(1+e^y)(1+e^{-y})}\,dy}{\int_{yy'}\frac{g^2(y/\beta)}{(1+e^y)(1+e^{-y})}\,dy} \tag{4.84c}$$

Before inserting any precise expression for the density of states, we will simplify these expressions in the case that the density of states is particle-hole symmetric, $g(E) = g(-E)$. This is the case in the Tomonaga-Luttinger model, although it is of course not precisely true

in a typical real system. In that case, the integrand for $L^{(12)}$ is odd so that $L^{(12)} = 0$, giving the nicer expressions

$$\sigma = \frac{Aa_c e^2 t^2 v\beta}{2\pi^4} \int_{yy'} \frac{g^2(y/\beta)}{(1+e^y)(1+e^{-y})}\, dy \tag{4.85a}$$

$$\kappa = \frac{Aa_c t^2 v}{2\pi^4} \int_{yy'} \frac{y^2 g^2(y/\beta)}{(1+e^y)(1+e^{-y})}\, dy \tag{4.85b}$$

$$S = 0 \tag{4.85c}$$

In a system with a density of states that is not particle-hole symmetric, $L^{(12)}$ will have a correction that is higher order in the inverse of the bandwidth W (or more precisely, higher order in kT/W). In the case of the thermal conductivity, since there is a lower order term we can safely ignore this higher order correction. In the case of thermopower, the lower order term vanishes so that we need to consider the next order to arrive at the experimentally observable result. See section 4.2 for the calculation of the thermopower correction.

After we find the corrected thermopower equation, we will proceed (in section 4.2) to substitute the single-particle density of states for a Luttinger liquid into each expression and derive how each transport coefficient scales as a power of the temperature.

Alternate approach to analytic continuation

Above, we performed the integral over the energies first and then the Fourier transform (integral over τ'). We believe that approach is the correct one, but it is worth exploring what would happen if we instead integrated first over τ'. We will thus return to equations (4.68) and (4.70) and rederive the transport coefficients, comparing our results at the end.

This time around, we start with the integral over τ':

$$\int_0^\pi e^{2in\tau'} e^{\tau'(y-y')/\pi} d\tau' = \frac{e^{2in\pi+(y-y')} - 1}{2in + (y-y')/\pi} = \frac{e^{(y-y')} - 1}{2in + (y-y')/\pi} \tag{4.86}$$

where the second equality follows because n is an integer so that $e^{2in\pi} = 1$.

Next we perform the analytic continuation, $in \to n + i\delta'$. This gives

$$\frac{e^{(y-y')} - 1}{2in + (y-y')/\pi} \to \frac{1}{2} \times \frac{e^{(y-y')} - 1}{n + (y-y')/(2\pi) + i\delta'} \tag{4.87}$$

We now want to isolate the imaginary part. This is some quick algebra.

$$\frac{1}{2} \times \frac{e^{(y-y')} - 1}{n + (y-y')/(2\pi) + i\delta'} = \left(\frac{e^{(y-y')} - 1}{2}\right) \times \frac{n + (y-y')/(2\pi) - i\delta'}{(n + (y-y')/(2\pi))^2 + \delta'^2} \tag{4.88}$$

so the imaginary part is just

$$\frac{-\delta'}{(n+(y-y')/(2\pi))^2+\delta'^2}\times\left(\frac{e^{(y-y')}-1}{2}\right). \tag{4.89}$$

The first factor is a Lorentzian, which becomes a delta function in the limit of small δ'. This limit gives

$$-\,\delta(n+(y-y')/(2\pi))\left(\frac{e^{(y-y')}-1}{2}\right), \tag{4.90}$$

with $\delta(0)=1/\delta'$. (This will be used later on in the calculation. "Remembering" the functional form that led, in approximation, to the delta function, and therefore also $\delta(0)$ as a function of the small parameter that goes to 0, will allow us to calculate as if we knew the full functional form even while simplifying the calculation by use of a delta function.)

Using this result with equations (4.68) and (4.70), we get

$$\begin{aligned}
L^{(il)} &= \lim_{n\to0}\lim_{\delta'\to0}\frac{\beta}{2\pi n}\left[\frac{-iT}{\Omega}\left(\frac{\beta}{\pi}\right)\int_0^\pi d\tau' e^{2in\tau'}\langle T'_\tau j_l(\tau')j_i(0)\rangle\right]_{i\omega\to n+i\delta'}\\
&= \lim_{n\to0}\lim_{\delta'\to0}\frac{-i\beta^{-(n_{il}+1)}}{2\pi^2\Omega n}\times 4N\left(\frac{a_c}{\hbar}\right)^2\left(\frac{L}{2\pi}\right)^2\\
&\times\left[\int_{yy'}|t(y/\beta,y'/\beta)|^2 g(y/\beta)g(y'/\beta)\left(\frac{y+y'}{2}\right)^{n_{il}}\left[\frac{\int_0^\pi e^{2in\tau'}e^{\tau'(y-y')/\pi}d\tau'}{(1+e^{y})\,(1+e^{-y'})}\right]dy\,dy'\right]_{in\to n+i\delta'}\\
\mathrm{Re}[L^{(il)}] &= -\frac{\beta^{-(n_{il}+1)}}{4\pi^2\Omega}\times 4N\left(\frac{a_c}{\hbar}\right)^2\left(\frac{L}{2\pi}\right)^2\\
&\times\lim_{n\to0}\frac{1}{n}\left[\int_{yy'}|t(y/\beta,y'/\beta)|^2 g(y/\beta)g(y'/\beta)\left(\frac{y+y'}{2}\right)^{n_{il}}\left[\frac{\delta(n+\frac{y-y'}{2\pi})(e^{y-y'}-1)}{(1+e^{y})\,(1+e^{-y'})}\right]dy\,dy'\right]\\
&= -\frac{\beta^{-(n_{il}+1)}}{(2\pi)^2\Omega}\times 4N\left(\frac{a_c}{\hbar}\right)^2\left(\frac{L}{2\pi}\right)^2\\
&\times\lim_{n\to0}\frac{1}{n}\left[\int_{yy'}|t(y/\beta,y'/\beta)|^2 g(y/\beta)g(y'/\beta)\left(\frac{y+y'}{2}\right)^{n_{il}}\left[\frac{\delta(n+\frac{y-y'}{2\pi})(e^{-2\pi n}-1)}{(1+e^{y})\,(1+e^{-y'})}\right]dy\,dy'\right]\\
&= \frac{\beta^{-(n_{il}+1)}}{\Omega}\times 4N\left(\frac{a_c}{\hbar}\right)^2\left(\frac{L}{2\pi}\right)^2\\
&\qquad\times\left[\int_{yy'}|t(y/\beta,y'/\beta)|^2 g(y/\beta)g(y'/\beta)\left(\frac{y+y'}{2}\right)^{n_{il}}\left[\frac{\delta(y-y')}{(1+e^{y})\,(1+e^{-y'})}\right]dy\,dy'\right]
\end{aligned}$$

where the fourth line follows because the delta function allows us to replace $(y-y')$ by $-2\pi n$ and the last line follows from the fact that

$$\lim_{n\to0}\frac{-(e^{-2\pi n}-1)}{n}=2\pi \tag{4.91}$$

and from $\delta(x/a) = a\,\delta(x)$ which provides an additional factor of 2π. Also note that in going from $\delta(\frac{y-y'}{2\pi})$ to $\delta(y-y')$, $\delta(0)$ changes from $1/\delta'$ to $1/(2\pi\delta')$ as can be confirmed by writing out the delta function as a Lorentzian (equation (4.89)).

At this point it would be tempting to simply use the delta function appearing in our expression for $\mathrm{Re}[L^{(il)}]$ to collapse the two integrals into one and replace $t(y/\beta, y'/\beta)$ by $t(y/\beta, y/\beta)$. Depending on the order of various limits, however, this may not be correct. In fact, when we treat $t(y/\beta, y'/\beta)$ carefully, we find (as discussed above and in section 4.6) that it is also proportional to a delta function and in fact that this delta function is the one we want to use to collapse the two energy integrals. As derived in section 4.6, the precise expression we want to use for $t(E, E')$ is

$$t(E, E') = \frac{tv}{L}\delta(E - E') \quad \text{with} \quad \delta(0) = \frac{L}{v} \tag{4.71}$$

and hence

$$t(y/\beta, y'/\beta) = \frac{tv}{L}\delta_E\left(\frac{y-y'}{\beta}\right) = \frac{tv\beta}{L}\delta_y(y-y') \text{ with } \delta_y(0) = \frac{L}{v\beta} \tag{4.72}$$

If we try to evaluate our expression for $\mathrm{Re}[L^{(il)}]$ with both possible choices for which delta function to use to collapse the two integrals into one (the from $t(E, E')$ or the one from analytic continuation), it will become immediately clear based on physical interpretation of the results which choice is correct.

The first possibility is to use the delta function from analytic continuation of the integral over τ. If we do so, we get

$$\mathrm{Re}[L^{(il)}] = \frac{4N\beta^{-(n_{il}+1)}}{\Omega}\left(\frac{a_c}{\hbar}\right)^2\left(\frac{L}{2\pi}\right)^2\int_y |t(y/\beta, y/\beta)|^2 g^2(y/\beta)\left[\frac{y^{n_{il}}}{(1+e^y)(1+e^{-y})}\right]dy \tag{4.92a}$$

$$= \frac{4N\beta^{-(n_{il}+1)}}{\Omega}\left(\frac{a_c}{\hbar}\right)^2\left(\frac{L}{2\pi}\right)^2\int_y \left(\frac{tv\beta}{L}\delta(0)\right)^2 g^2(y/\beta)\left[\frac{y^{n_{il}}}{(1+e^y)(1+e^{-y})}\right]dy \tag{4.92b}$$

$$= \frac{4N\beta^{-(n_{il}+1)}}{\Omega}\left(\frac{a_c t}{\hbar}\right)^2\left(\frac{L}{2\pi}\right)^2\int_y \frac{y^{n_{il}} g^2(y/\beta)}{(1+e^y)(1+e^{-y})}dy \tag{4.92c}$$

We can simplify this result using the fact that the total area, Ω, is equal to the length of the chains times the number of chains times the interchain spacing, or in other words $\Omega = Na_cL$. This gives (also setting $\hbar = 1$)

$$\mathrm{Re}[L^{(il)}] = \frac{t^2 a_c L\beta^{-(n_{il}+1)}}{\pi^2}\int_y \frac{y^{n_{il}} g^2(y/\beta)}{(1+e^y)(1+e^{-y})}dy \tag{4.93}$$

The other possibility is to instead use one of the delta functions from $t(E, E')$. Then we have instead

$$\mathrm{Re}[L^{(il)}] = \frac{4N\beta^{-(n_{il}+1)}}{\Omega}\left(\frac{a_c}{\hbar}\right)^2\left(\frac{L}{2\pi}\right)^2\int_y\left(\frac{tv\beta}{L}\right)t(y/\beta, y/\beta)\left[\frac{\delta(0)y^{n_{il}}g^2(y/\beta)}{(1+e^y)(1+e^{-y})}\right]dy \tag{4.94a}$$

$$= \frac{4N\beta^{-(n_{il}+1)}}{\Omega}\left(\frac{a_c}{\hbar}\right)^2\left(\frac{L}{2\pi}\right)^2\int_y\left(\frac{tv\beta}{L}\right)^2\delta(0)\left[\frac{\delta(0)y^{n_{il}}g^2(y/\beta)}{(1+e^y)(1+e^{-y})}\right]dy \tag{4.94b}$$

$$= \frac{4N\beta^{-(n_{il}+1)}}{\Omega}\left(\frac{a_c}{\hbar}\right)^2\left(\frac{L}{2\pi}\right)^2\int_y\left(\frac{t^2v\beta}{2\pi L\delta'}\right)\left[\frac{y^{n_{il}}g^2(y/\beta)}{(1+e^y)(1+e^{-y})}\right]dy \tag{4.94c}$$

$$= \frac{4N\beta^{-(n_{il}+1)}}{\Omega}\left(\frac{a_c}{\hbar}\right)^2\left(\frac{L}{2\pi}\right)^2\int_y\left(\frac{t^2v}{L\delta}\right)\left[\frac{y^{n_{il}}g^2(y/\beta)}{(1+e^y)(1+e^{-y})}\right]dy \tag{4.94d}$$

$$= \frac{N\beta^{-(n_{il}+1)}}{\pi^2\Omega}\left(\frac{a_ct}{\hbar}\right)^2\left(\frac{Lv}{\delta}\right)\int_y\frac{y^{n_{il}}g^2(y/\beta)}{(1+e^y)(1+e^{-y})}dy \tag{4.94e}$$

$$= \frac{t^2a_cv\beta^{-(n_{il}+1)}}{\pi^2\delta}\int_y\frac{y^{n_{il}}g^2(y/\beta)}{(1+e^y)(1+e^{-y})}dy \tag{4.94f}$$

These two expressions for $\mathrm{Re}[L^{(il)}]$ differ by a factor of $L\delta/v$. (As a quick check, note that this is indeed unitless, since δ has units of inverse time.)

Which version is more correct? On the one hand, δ is an additional parameter that appeared only in the context of analytic continuation and otherwise was not part of the physical setup of the problem, and thus its appearance in our result is potentially problematic. On the other hand, conductivity should be an intrinsic property, independent of the system size, so a dependence on L in $L^{(il)}$ is certainly a problem. We find the argument that the conductivity should be intrinsic to be more convincing, since it is possible to assign a physical significance to δ while an extrinsic conductivity does not make sense. (Namely, δ can be introduced into the linear response formalism as an adiabatically slow rate of switching on the perturbation that produces the linear response.[3])

Mathematically, we still need to justify using the delta function from analytic continuation to replace $e^{y-y'}$ by $e^{-2\pi n}$ before sending $\omega \to 0$. Thinking of this "delta function" as a peak of width δ', we really have $-2\pi n - \delta' \lesssim y - y' \lesssim -2\pi n + \delta'$. Then $-(e^{-2\pi n} - 1)/n$ becomes not just 2π as $n \to 0$ but rather $2\pi(1 + a\delta'/n) = 2\pi(1 + a\delta/\omega)$ where a is a number of order 1 which could be positive or negative. This becomes just 2π as assumed above if $\delta \ll \omega$, the same order that we argued for in section 4.1 above.

We therefore use

$$\mathrm{Re}[L^{(il)}] = \frac{t^2a_cv\beta^{-(n_{il}+1)}}{\pi^2\delta}\int_y\frac{y^{n_{il}}g^2(y/\beta)}{(1+e^y)(1+e^{-y})}dy \tag{4.95}$$

As in our first approach to evaluating the analytic continuation in $L^{(il)}$, we can now use equations (2.2) to get expressions for the conductivities and the thermopower. The results

are

$$\sigma = \frac{e^2}{T} L^{(11)} = \frac{a_c e^2 t^2 v}{\pi^2 \delta} \int_{yy'} \frac{g^2(y/\beta)}{(1+e^y)(1+e^{-y})}\, dy \tag{4.96a}$$

$$\kappa = \frac{1}{T^2}\left[L^{(22)} - \frac{(L^{(12)})^2}{L^{(11)}}\right] = \frac{a_c t^2 v T}{\pi^2 \delta}\left[\int_{yy'} \frac{y^2 g^2(y/\beta)}{(1+e^y)(1+e^{-y})}\, dy - \frac{\left(\int_{yy'} \frac{y\, g^2(y/\beta)}{(1+e^y)(1+e^{-y})}\, dy\right)^2}{\int_{yy'} \frac{g^2(y/\beta)}{(1+e^y)(1+e^{-y})}\, dy}\right] \tag{4.96b}$$

$$S = -\frac{1}{eT}\frac{L^{(12)}}{L^{(11)}} = -\frac{1}{e}\frac{\int_{yy'} \frac{y\, g^2(y/\beta)}{(1+e^y)(1+e^{-y})}\, dy}{\int_{yy'} \frac{g^2(y/\beta)}{(1+e^y)(1+e^{-y})}\, dy} \tag{4.96c}$$

Assuming a particle-hole symmetric density of states, so that $g(E) = g(-E)$, we get the simplified expressions

$$\sigma = \frac{a_c e^2 t^2 v}{\pi^2 \delta} \int_{yy'} \frac{g^2(y/\beta)}{(1+e^y)(1+e^{-y})}\, dy \tag{4.97a}$$

$$\kappa = \frac{a_c t^2 v T}{\pi^2 \delta} \int_{yy'} \frac{y^2 g^2(y/\beta)}{(1+e^y)(1+e^{-y})}\, dy \tag{4.97b}$$

$$S = 0 \tag{4.97c}$$

We can compare these results with those of equations (4.85), and we see that the integrals that appear are precisely the same, but that the prefactors are different by a factor proportional to T/δ. The different approach to analytic continuation thus results in a different power law of the transport coefficients as a function of temperature! This result is somewhat unfortunate, as it makes the results of the two approaches differ in an experimentally measurable way.

This result, however, contains the nonphysical parameter δ, suggesting that indeed our previous approach to analytic continuation was the correct one. (Note that although we discussed one possible physical interpretation for δ, it is formally supposed to disappear from all expressions. That it *is* better to have δ in our answer than L does not contradict the fact that, on physical grounds, neither should appear.)

Since the two approaches affect σ and κ the same way, the Lorenz number at least will be unaffected by our choice of how to perform analytic continuation.

Moving forward with the calculation, we will return to the more correct results of equations (4.85) and neglect those derived in this section.

Correction to get nonzero thermopower

We now want to derive a nonzero expression for the thermopower by correcting the density of states. We will denote the usual Luttinger liquid density of states by $g_{LL}(E)$, and we want

to find some physically motivated correction, $g_{LL}(E) \to g(E)$.

To find such a correction, we will adopt the picture that the Luttinger liquid in question arises from adding interactions to a 1D electron gas with a typically parabolic dispersion $E = \frac{\hbar^2 k^2}{2m} \propto k^2$. In that case, the density of states is $dk/dE \propto E^{-1/2}$. For our purposes we would like to shift the energies so that the Fermi level is labeled as $E = 0$, in which case the density of states becomes

$$g_{\rm 1D}(E) \propto (E_F + E)^{-1/2}. \tag{4.98}$$

The Fermi energy acts as a kind of bandwidth in that it cuts off the otherwise infinite linear dispersion, so we label it as W, and we use this 1D density of states as a correction to the Luttinger liquid one:

$$g(E) = \frac{g_{\rm LL}(E)}{\sqrt{1 + E/W}} \tag{4.99}$$

This density of states is a phenomenologically reasonable model that captures the real physical behavior well enough to find a power law dependence on temperature. The most important features are the violation of particle-hole symmetry by the introduction of a bandwidth and the preservation of the density of states to lowest order in E/W when E is small (near the Fermi energy).

The importance of the small E limit comes from the nature of the integrals appearing in our transport coefficents. In particular, any function of the form

$$\frac{y^\alpha}{(1 + e^y)(1 + e^{-y})} \tag{4.100}$$

is sharply peaked around $y = 0$ for any power α, and since these types of functions appear in the integrand in our expression for $L^{(il)}$, in our case only $E \approx 0$ will be important.

With this in mind, we can now expand our new density of states, equation 4.99, in the small E/W limit. To first order, we get

$$g(E) = g_{\rm LL}(E)\left(1 - \frac{1}{2}\frac{E}{W}\right) \tag{4.101}$$

or equivalently

$$g(y/\beta) = g_{\rm LL}(y/\beta)\left(1 - \frac{1}{2}\frac{y}{W\beta}\right) \tag{4.102}$$

Plugging this into the integral for $L^{(12)}$ that vanished, we have

$$\begin{aligned}\int_y \frac{y\, g^2(y/\beta)}{(1 + e^y)(1 + e^{-y})} dy &\approx \int_y \frac{y\, g_{\rm LL}^2(y/\beta)(1 - \frac{y}{W\beta})}{(1 + e^y)(1 + e^{-y})} dy \\ &= \int_y \frac{y g_{\rm LL}^2(y/\beta)}{(1 + e^y)(1 + e^{-y})} dy - \frac{1}{W\beta}\int_y \frac{y^2 g_{\rm LL}^2(y/\beta)}{(1 + e^y)(1 + e^{-y})} dy\end{aligned}$$

The first term vanishes as before, since the integrand is odd in y, but the second term is nonzero. That integral is, in fact, now the same one that appears in the calculation of $L^{(22)}$.

With this correction to $L^{(12)}$, we can now give a new expression for thermopower which will give the lowest nonzero contribution, replacing equation (4.84c) above:

$$S = \frac{T}{We} \frac{\int_y \frac{y^2 g_{\mathrm{LL}}^2(y/\beta)}{(1+e^y)(1+e^{-y})} dy}{\int_y \frac{g_{\mathrm{LL}}^2(y/\beta)}{(1+e^y)(1+e^{-y})} dy} \tag{4.103}$$

Should we include this same correction in the calculations of the electrical and thermal conductivities, σ and κ? In the case of σ, the first order correction to the integrand will be an odd term and vanish, so the first nonzero correction will have an extra factor of $(y/W\beta)^2$ in the integral and the correction term will therefore be smaller by a factor of $(kT/W)^2$. If this number were not much less than 1, then the entire Luttinger liquid picture would be inapplicable, so we can safely ignore this correction.

A similar argument shows that both the lowest order correction to the $L^{(22)}$ term in κ and the lowest order contribution to the $(L^{(12)})^2/L^{(11)}$ term are also smaller by a factor of $(kT/W)^2$ compared with the lowest order part of $L^{(22)}$ (equation 4.85b), so again the correction can be ignored.

Transport coefficients with unspecified Luttinger density of states

For completeness and clarity, we list here our final expressions for the three transport coefficients in terms of a corrected density of states, replacing equation (4.85).

$$\sigma = \frac{A a_c e^2 t^2 v \beta}{2\pi^4} \int_{yy'} \frac{g_{\mathrm{LL}}^2(y/\beta)}{(1+e^y)(1+e^{-y})} \, dy \tag{4.104a}$$

$$\kappa = \frac{A a_c t^2 v}{2\pi^4} \int_{yy'} \frac{y^2 g_{\mathrm{LL}}^2(y/\beta)}{(1+e^y)(1+e^{-y})} \, dy \tag{4.104b}$$

$$S = \frac{T}{We} \frac{\int_y \frac{y^2 g_{\mathrm{LL}}^2(y/\beta)}{(1+e^y)(1+e^{-y})} dy}{\int_y \frac{g_{\mathrm{LL}}^2(y/\beta)}{(1+e^y)(1+e^{-y})} dy} \tag{4.104c}$$

Lorenz number

One important quantity that can be derived from the transport coefficients is the Lorenz number,

$$L = \frac{\kappa}{\sigma T}. \tag{4.105}$$

Looking at the Lorenz number has two very important advantages. First, the Wiedemann-Franz law provides a benchmark value for the Lorenz number that is observed in Fermi liquids; comparisons of the calculated Lorenz number with the Wiedemann-Franz law are therefore very good tests of non-Fermi liquid behavior. Second, material-dependent constants

such as the interchain spacing disappear in the ratio between the two conductivities, allowing us to make specific numerical predictions that could be tested in an experiment.

If we calculate the Lorenz number using our results for σ and κ from equations (4.104), we get

$$L = \frac{k_B^2}{e^2} \frac{\int_y \frac{y^2 g_{\mathrm{LL}}^2(y/\beta)}{(1+e^y)(1+e^{-y})} dy}{\int_y \frac{g_{\mathrm{LL}}^2(y/\beta)}{(1+e^y)(1+e^{-y})} dy} \tag{4.106}$$

Here we have put Boltzmann's constant k_B back into the expression to get the correct units.

Note that using our density of states correction from the previous section, our expression for the thermopower is proportional to the Lorenz number:

$$S = \frac{eT}{W} \times L \tag{4.107}$$

Power laws and numerics using the Luttinger liquid spectral function

Finally, we can substitute an expression for the Luttinger liquid density of states into our equations for the transport coefficients that are given above in equations (4.104) and (4.106).

As described in the next section, 4.3, a Luttinger liquid is characterized by an interaction strength parameter that we call K. (This is the same notation as used in the book by Giamarchi[31]; the same parameter is also labeled as g or as K^2 in some works.[56, 55, 54, 71]) In the case of a non-interacting system, $K = 1$, while for repulsive interactions it is in the range $0 < K < 1$ and for attractive interactions $K > 1$.

The density of states is given by a power-law of the energy with an exponent dependent on K [17, eq 61]:

$$g(E) = 2\frac{|E/W|^{\gamma-1}}{2\pi v \Gamma(\gamma)} \tag{4.108}$$

where W is the bandwidth, v is a renormalized Fermi velocity, and γ is defined by

$$\boxed{\gamma = \frac{K + K^{-1}}{2}.} \tag{2.11}$$

Note that γ is a measure of interaction strength which is independent of whether the interactions happen to be attractive or repulsive. It always satisfies $\gamma \geq 1$, and $\gamma = 1$ if and only if the system is noninteracting. (In that case, the density of states is constant since the Tomonaga-Luttinger model assumes a linear dispersion before the introduction of interactions.)

Substituting this density of states into our expressions for the transport coefficients (equations 4.104) and the Lorenz number (equation 4.106), we get expressions in terms of dimensionless integrals dependent on γ that must be evaluated numerically. We will show the derivation of this expression for σ and then give the remaining results.

$$\begin{aligned}\sigma &= \frac{Aa_c e^2 t^2 v\beta}{2\pi^4}\int_y \frac{(\pi v\Gamma(\gamma))^{-2}|y/W\beta|^{2(\gamma-1)}}{(1+e^y)(1+e^{-y})}dy \\ &= \frac{Aa_c e^2 t^2 v\beta}{2\pi^4}\times\frac{(\pi v\Gamma(\gamma))^{-2}}{(\beta W)^{2(\gamma-1)}}\int_y \frac{|y|^{2(\gamma-1)}}{(1+e^y)(1+e^{-y})}dy \\ &= \frac{a_c e^2 t^2}{vT}\left(\frac{T}{W}\right)^{2(\gamma-1)}\times\frac{A}{2\pi^6\Gamma(\gamma)^2}\int_y \frac{|y|^{2(\gamma-1)}}{(1+e^y)(1+e^{-y})}dy\end{aligned}$$

As promised, we have written σ in terms of a dimensionless integral that we can evaluate numerically, with all of the dimensionful constants including the power law dependence on temperature being apparent in the prefactor. When we follow a similar procedure for each of the transport coefficients, we ultimately get the following results:

$$\sigma = \frac{a_c e^2 t^2}{vT}\left(\frac{T}{W}\right)^{2(\gamma-1)}\times\frac{A}{2\pi^6\Gamma(\gamma)^2}\int_y \frac{|y|^{2(\gamma-1)}}{(1+e^y)(1+e^{-y})}dy \tag{2.12a}$$

$$\kappa = \frac{a_c t^2}{v}\left(\frac{T}{W}\right)^{2(\gamma-1)}\times\frac{A}{2\pi^6\Gamma(\gamma)^2}\int_y \frac{y^2|y|^{2(\gamma-1)}}{(1+e^y)(1+e^{-y})}dy \tag{2.12b}$$

$$L = \frac{k_B^2}{e^2}\frac{\int \frac{y^2|y|^{2(\gamma-1)}}{(1+e^y)(1+e^{-y})}dy}{\int \frac{|y|^{2(\gamma-1)}}{(1+e^y)(1+e^{-y})}dy} \tag{4.109a}$$

$$S = \frac{eT}{W}\times L \tag{4.109b}$$

The most interesting results to extract here are those that do not involve specific material-dependent parameters such as the Fermi velocity v, the interchain spacing a_c, or the bandwidth W. In particular, those do not appear in the temperature power laws, nor do they appear in the Lorenz number at all! Thus we have two main results: (1) the temperature dependence of the electrical and thermal conductivities and the thermopower, and (2) the numerical evaluation of the Lorenz number as a function of the interaction strength γ.

(1) Here are the power laws, summarized:

$$\sigma \propto T^{2\gamma-3} \tag{4.110a}$$

$$\kappa \propto T^{2\gamma-2} \tag{4.110b}$$

$$S \propto T \tag{4.110c}$$

A couple features are worth noting.

1. In the noninteracting limit we find $\sigma \propto T^{-1}$ and $\kappa \propto T^0$.

2. At low interaction strength, the electrical conductivity decreases with temperature, consistent with a picture of coherent transport in which increasing temperature leads

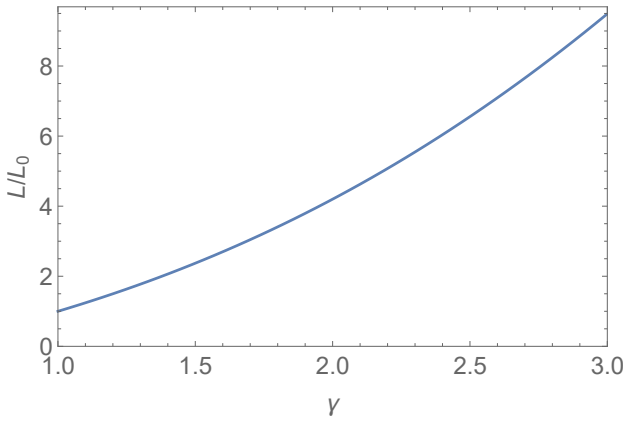

Figure 4.3: Lorenz number in the generalized noninteracting model. The Wiedemann-Franz Law is satisfied ($L = L_0$) in the noninteracting case $\gamma = 1$ and is strongly violated for large interaction strength.

to increased scattering. Conversely, at larger interaction strength the conductivity increases with temperature, corresponding to incoherent transport with thermally activated hopping. Taken together, this shows a crossover at $\gamma = 3/2$ between a coherent and an incoherent regime as interaction strength increases.

3. The thermopower is always proportional to the temperature, which matches the typical behavior in a Fermi liquid.

(2) Our second main result is the numerical evaluation of the Lorenz number. This is shown in figure 4.3, where it is plotted in units of the expected value from the Wiedemann-Franz Law, or

$$L_0 = \frac{\pi^2}{3}\left(\frac{k_B}{e}\right)^2. \tag{4.111}$$

Our result agrees perfectly with the Wiedemann-Franz Law in the noninteracting limit of $\gamma = 1$, but it shows a violation of the law with increasing interaction strength. The violation turns out to be quite similar to a γ^2 dependence, a fact which is not immediately apparent from the graph but which can be explained intuitively. We discuss the physical reason for the γ^2 dependence in section 4.3.

Here we will show numerically that the Lorenz number indeed scales as approximately γ^2. If $\frac{L}{L_0}$ had a precise power law dependence on γ, we could write $\frac{L}{L_0} = \gamma^a$ for some constant a. Here $\frac{L}{L_0}$ follows only an approximate power law, so when we write $\frac{L}{L_0} = \gamma^a$, a is now a function $a(\gamma)$ which is approximately but not precisely constant.

To actually find this function $a(\gamma)$, we can take the log of both sides of the equation, in which case we find that

$$a(\gamma) = \frac{\log(L/L_0)}{\log(\gamma)} \tag{4.112}$$

This is plotted in figure 2.2. As claimed, the exponent a is near to 2, though the value is not precise and has some dependence on γ.

We can derive the precise value of the exponent at small γ by expanding around the noninteracting limit of $\gamma = 1$.

To do this expansion, we write $\gamma = 1 + \epsilon$, so that equation 4.112 becomes

$$a(\gamma) \approx \frac{1}{\epsilon} \log\left(\frac{L}{L_0}\right) \tag{4.113}$$

We next want to expand $\frac{L}{L_0}$ to lowest order in ϵ, giving

$$\begin{aligned}
\frac{L}{L_0} &= \frac{L}{\frac{\pi^2}{3}\left(\frac{k_B}{e}\right)^2} \\
&= \frac{3}{\pi^2} \frac{\int \frac{x^2 |x|^{2(\gamma-1)}}{(1+e^x)(1+e^{-x})} dx}{\int \frac{|x|^{2(\gamma-1)}}{(1+e^x)(1+e^{-x})} dx} \\
&= \frac{3}{\pi^2} \frac{\int_0^\infty \frac{x^{2+2\epsilon}}{(1+e^x)(1+e^{-x})} dx}{\int_0^\infty \frac{x^{2\epsilon}}{(1+e^x)(1+e^{-x})} dx} \\
&\approx \frac{3}{\pi^2} \frac{\int_0^\infty \frac{x^2(1+2\epsilon\log(x))}{(1+e^x)(1+e^{-x})} dx}{\int_0^\infty \frac{(1+2\epsilon\log(x))}{(1+e^x)(1+e^{-x})} dx} \\
&= \frac{\frac{3}{\pi^2}\int_0^\infty \frac{x^2}{(1+e^x)(1+e^{-x})} dx + 2\epsilon\frac{3}{\pi^2}\int_0^\infty \frac{x^2\log(x)}{(1+e^x)(1+e^{-x})} dx}{\int_0^\infty \frac{1}{(1+e^x)(1+e^{-x})} dx + 2\epsilon\int_0^\infty \frac{\log(x)}{(1+e^x)(1+e^{-x})} dx} \\
&= \frac{\frac{3}{\pi^2}\int_0^\infty \frac{x^2}{(1+e^x)(1+e^{-x})} dx + 2\epsilon\frac{3}{\pi^2}\int_0^\infty \frac{x^2\log(x)}{(1+e^x)(1+e^{-x})} dx}{\int_0^\infty \frac{1}{(1+e^x)(1+e^{-x})} dx \left(1 + 2\epsilon\frac{\int_0^\infty \frac{\log(x)}{(1+e^x)(1+e^{-x})} dx}{\int_0^\infty \frac{1}{(1+e^x)(1+e^{-x})} dx}\right)} \\
&\approx \frac{\frac{3}{\pi^2}\int_0^\infty \frac{x^2}{(1+e^x)(1+e^{-x})} dx + 2\epsilon\frac{3}{\pi^2}\int_0^\infty \frac{x^2\log(x)}{(1+e^x)(1+e^{-x})} dx}{\int_0^\infty \frac{1}{(1+e^x)(1+e^{-x})} dx} \left(1 - 2\epsilon\frac{\int_0^\infty \frac{\log(x)}{(1+e^x)(1+e^{-x})} dx}{\int_0^\infty \frac{1}{(1+e^x)(1+e^{-x})} dx}\right) \\
&\approx 1 + 2\epsilon\frac{3}{\pi^2}\left(\frac{\int_0^\infty \frac{x^2\log(x)}{(1+e^x)(1+e^{-x})} dx}{\int_0^\infty \frac{1}{(1+e^x)(1+e^{-x})} dx} - \frac{\left(\int_0^\infty \frac{x^2}{(1+e^x)(1+e^{-x})} dx\right)\left(\int_0^\infty \frac{\log(x)}{(1+e^x)(1+e^{-x})} dx\right)}{\left(\int_0^\infty \frac{1}{(1+e^x)(1+e^{-x})} dx\right)^2}\right) \\
&= 1 + 2\epsilon\left(\frac{3}{\pi^2}\frac{\int_0^\infty \frac{x^2\log(x)}{(1+e^x)(1+e^{-x})} dx}{\int_0^\infty \frac{1}{(1+e^x)(1+e^{-x})} dx} - \frac{\int_0^\infty \frac{\log(x)}{(1+e^x)(1+e^{-x})} dx}{\int_0^\infty \frac{1}{(1+e^x)(1+e^{-x})} dx}\right) \\
&= 1 + 4\epsilon\left(\frac{3}{\pi^2}\int_0^\infty \frac{x^2\log(x)}{(1+e^x)(1+e^{-x})} dx - \int_0^\infty \frac{\log(x)}{(1+e^x)(1+e^{-x})} dx\right)
\end{aligned}$$

This is of the form $1+\epsilon A$ for small ϵ so that $\log(L/L_0) \approx \epsilon A$ and therefore dividing by ϵ (as in equation 4.113) to get the exponent we find

$$\begin{aligned} a(\gamma \approx 1) &= 1 - 2\log(\pi) + \frac{6}{\pi^2}\left(\gamma_1{}'\left(\frac{1}{2}\right) - \gamma_1{}'(1)\right) \\ &\approx 2.3432 \end{aligned} \tag{4.114}$$

where $\gamma_1(\nu)$ is a generalized Stieltjes constant[13][1].

We thus conclude that in our noninteracting model,

$$L \approx \gamma^2 L_0 \tag{4.115}$$

for large γ, while

$$L \approx \gamma^{2.3} L_0 \tag{4.116}$$

for $\gamma \approx 1$.

4.3 Luttinger liquid model

The model we discussed above involves substantial simplifications, most notably the assumption that the behavior of a Luttinger liquid compared with a noninteracting 1D system can be largely captured in the density of states/spectral function alone.

We now want to perform an analogous computation on a more complete model to get more rigorously correct results for the conductivities, thermopower, and Lorenz number in the physical systems of interest. We would hope, of course, that the results turn out to look similar so that future computations could take the relatively simpler approach detailed above. In fact, what we find (as we will show in the remainder of these Supplementary Materials) is that the first model *does* get some of the most important features right, notably the power law dependence on temperature, but it fails to accurately predict the precise dependence of transport on the interaction strength; for instance, in the more complete model we find that the scaling of the Lorenz number with interaction strength, g, is closer to γ^4 than to the γ^2 dependence from the noninteracting model.

Luttinger liquid basics

Before we perform the actual calculation, it will be helpful to briefly review the properties of Luttinger liquids. In the same way that any typical interacting system in three dimensions shows the same generic behavior and is thus classified as a Fermi liquid, a typical conductive 1D system with interactions behaves as a Luttinger liquid[37, 31]. Fermi liquids look very much like a noninteracting electron gas: the basic excitations are noninteracting fermionic

[1]For purposes of calculation, the generalized Stieltjes constant is implemented in the commercial software Wolfram Mathematica as $\gamma_n(\nu) = \text{StieltjesGamma}[n, \nu]$[121]

quasiparticles, there is still a well-defined Fermi surface, and so forth. Luttinger liquids, on the other hand, look remarkably different from a noninteracting 1D electron gas. In this case, the interactions result in low-lying excitations that are collective and thus bosonic in nature.

From a computational perspective, Luttinger liquids are a very attractive system to work with because the interacting fermions in 1D become a system of noninteracting bosons, resulting in an exactly solvable theory. Following the conventions of Giamarchi [31], the new bosonic degrees of freedom are described using two field operators, θ and ϕ, that satisfy the canonical commutation relations

$$[\phi_i(x), \partial_{x'}\theta_j(x')] = i\pi\delta_{ij}\delta(x' - x) \tag{4.117a}$$

$$[\phi_i(x), \theta_j(x')] = i\frac{\pi}{2}\delta_{ij}\text{sign}(x' - x) \tag{4.117b}$$

$$[\phi_i(x), \phi_j(x')] = [\theta_i(x), \theta_j(x')] = 0 \tag{4.117c}$$

where x and x' denote position along the Luttinger liquid and i and j denote species (eg which Luttinger liquid the operator acts on). Additionally, ϕ and θ have the nice property that $\phi^\dagger = \phi$ and $\theta^\dagger = \theta$.

The bosonic fields are related to the real electrons in the system by the Fermion operators

$$\psi_r(x) = U_r \lim_{a\to 0} \frac{1}{\sqrt{2\pi a}} e^{ir(k_F - \pi/L)x} e^{-i(r\phi(x) - \theta(x))} \tag{4.118a}$$

$$\psi_r^\dagger(x) = U_r^\dagger \lim_{a\to 0} \frac{1}{\sqrt{2\pi a}} e^{-ir(k_F - \pi/L)x} e^{i(r\phi(x) - \theta(x))} \tag{4.118b}$$

where r is 1 for right-moving fermions and -1 for left-moving fermions.

We can calculate the fermion commutation relations from the boson ones by writing out the exponentials and doing some algebra. The results, also using the fact that the Klein factors U_r anticommute for different species (left/right and/or different Luttinger liquids), are just the usual Fermion anticommutation rules:

$$\{\psi_\alpha(x), \psi_\beta(x')\} = \{\psi_\alpha^\dagger(x), \psi_\beta^\dagger(x')\} = 0$$
$$\{\psi_\alpha^\dagger(x), \psi_\beta(x')\} = B\delta(x - x')\delta_{\alpha\beta}$$

where B is a numerical constant that depends on our precise normalization convention. In practice, instead of computing these from the bosonic commutators of equations (3.14), we calculate these anticommutation relations by writing the fermion field operators as Fourier transforms of the momentum-space operators c_k. This will allow us both to easily find the value of the constant B and to relate the hopping term in the Luttinger Hamiltonian (see section 4.3) to the one in the noninteracting model (section 4.2).

Fourier transform definition of field operators

Our next step, then, is to formalize the relation between the ψ and c operators. The general form must be

$$\psi(r) = A \sum_k e^{ikx} c_k \tag{4.119}$$

and therefore also

$$\psi^\dagger(r) = A^* \sum_k e^{-ikx} c_k^\dagger \tag{4.120}$$

We can find the value of A by careful normalization. For the sake of concreteness, consider a 1D chain with N sites, total length L, and periodic boundary conditions. Then k takes the values $\frac{2\pi}{L}n$ for $n = 0, 1, \cdots, N-1$. Note that the spacing in k values is $dk = 2\pi/L$. Also suppose that the total number of electrons is N_e.

Then we have

$$\begin{aligned}
N_e &= \int \left\langle \psi^\dagger(x)\psi(x) \right\rangle dx \\
&= |A|^2 \int \left\langle \sum_k e^{-ikx} c_k^\dagger \sum_q e^{iqx} c_q \right\rangle dx \\
&= |A|^2 \sum_{kq} \left\langle c_k^\dagger c_q \right\rangle \int dx e^{i(q-k)x} \\
&= |A|^2 \sum_{kq} \left\langle c_k^\dagger c_q \right\rangle \times 2\pi\delta(q-k) \\
&= |A|^2 \sum_k n_k \times 2\pi \sum_q \delta(q-k) \\
&= |A|^2 \sum_k n_k \times L \int_q \delta(q-k) dq \\
&= L|A|^2 \sum_k n_k \\
&= L|A|^2 \sum_k n_k \\
&= L|A|^2 N_e
\end{aligned}$$

Thus $|A| = 1/\sqrt{L}$, and we can choose $A = 1/\sqrt{L}$.

With this value of A determined, we now have the relation between the real-space and

Fourier-space creation and annihilation operators:

$$\psi(r) = \frac{1}{\sqrt{L}} \sum_k e^{ikx} c_k \tag{4.121a}$$

$$\psi^\dagger(r) = \frac{1}{\sqrt{L}} \sum_k e^{-ikx} c_k^\dagger \tag{4.121b}$$

The inverse Fourier transform relations are

$$c_k = \frac{1}{\sqrt{L}} \int e^{-ikx} \psi(x)\, dx \tag{4.122a}$$

$$c_k^\dagger = \frac{1}{\sqrt{L}} \int e^{ikx} \psi^\dagger(x)\, dx \tag{4.122b}$$

We also want to find expressions for the creation and annihilation operators corresponding to right- and left-moving real-space fermions, ψ_R and ψ_L. These represent fermions with momentum "near to" the right and left Fermi points, $\pm k_F$. This is in quotation marks because in fact we will still write ψ_R and ψ_L in the style of equations (4.121), as a sum over all k values in the range $-\infty$ to ∞; however, it will be "centered" at $\pm k_F$ in the sense that the Fermi wave vector will be the new $k = 0$ point. Working this out in the example case of ψ_R, we begin with:

$$\psi_R(x) = \frac{1}{\sqrt{L}} \sum_{k \approx k_F} e^{ikx} c_k$$

Let $k = k_F + k'$:

$$= \frac{1}{\sqrt{L}} \sum_{k'} e^{i(k_F + k')x} c_{k_F + k'}$$

Let $c_{k',R} = c_{k_F + k'}$:

$$= \frac{e^{ik_F x}}{\sqrt{L}} \sum_{k'} e^{ik'x} c_{k',R}$$

$$= \frac{e^{ik_F x}}{\sqrt{L}} \sum_{k} e^{ikx} c_{k,R}$$

For left-movers, the definition is basically the same except that $c_{k',L} = c_{-k_F + k'}$, so we use the substitution $k = -k_F + k'$, giving

$$\psi_L(x) = \frac{e^{-ik_F x}}{\sqrt{L}} \sum_{k} e^{ikx} c_{k,L}$$

In total, then, we have the four definitions

$$\psi_R(x) = \frac{e^{ik_F x}}{\sqrt{L}} \sum_k e^{ikx} c_{k,R} \tag{4.123a}$$

$$\psi_R^\dagger(x) = \frac{e^{-ik_F x}}{\sqrt{L}} \sum_k e^{-ikx} c_{k,R}^\dagger \tag{4.123b}$$

$$\psi_L(x) = \frac{e^{-ik_F x}}{\sqrt{L}} \sum_k e^{ikx} c_{k,L} \tag{4.123c}$$

$$\psi_L^\dagger(x) = \frac{e^{ik_F x}}{\sqrt{L}} \sum_k e^{-ikx} c_{k,L}^\dagger \tag{4.123d}$$

To get the inverse relationships, we can multiply by $e^{\pm ik_F x}$ on both sides and then compare with the relationships between the centered (original) $\psi(x)$ and c_k operators. For example,

$$e^{-ik_F x}\psi_R(x) = \frac{1}{\sqrt{L}} \sum_k e^{ikx} c_{k,R}$$

Compare this with equation 4.121a and notice that it looks the same but with the substitutions $\psi(x) \to e^{-ik_F x}\psi_R(x)$ and $c_k \to c_{k,R}$. Then if we make the same substitutions in equation 4.122a, we will find the analogous statement for the right-moving operators, which is

$$c_{k,R} = \frac{1}{\sqrt{L}} \int e^{-ikx} e^{-ik_F x} \psi_R(x) dx$$

The four statements of this type are

$$c_{k,R} = \frac{1}{\sqrt{L}} \int e^{-ikx} e^{-ik_F x} \psi_R(x) dx \tag{4.124a}$$

$$c_{k,R}^\dagger = \frac{1}{\sqrt{L}} \int e^{ikx} e^{ik_F x} \psi_R^\dagger(x) dx \tag{4.124b}$$

$$c_{k,L} = \frac{1}{\sqrt{L}} \int e^{-ikx} e^{ik_F x} \psi_L(x) dx \tag{4.124c}$$

$$c_{k,L}^\dagger = \frac{1}{\sqrt{L}} \int e^{ikx} e^{-ik_F x} \psi_L^\dagger(x) dx \tag{4.124d}$$

For our later calculations, it will be helpful to rewrite the expressions above in terms of $\alpha = \pm 1$, 1 for right-movers and -1 for left-movers. We have:

$$c_{k\alpha} = \frac{1}{\sqrt{L}} \int e^{-ikx} e^{-i\alpha k_F x} \psi_\alpha(x) dx \tag{3.29a}$$

$$\psi_\alpha(x) = \frac{e^{i\alpha k_F x}}{\sqrt{L}} \sum_k e^{ikx} c_{k\alpha} \tag{3.29b}$$

The fact that the ψ operators can be written as linear combinations of the c makes it immediately clear that $\{\psi_\alpha(x), \psi_\beta(x')\} = \{\psi_\alpha^\dagger(x), \psi_\beta^\dagger(x')\} = 0$ as claimed above. We can also now easily and explicitly compute $\{\psi_\alpha^\dagger(x), \psi_\beta(x')\}$.

We begin by calculating for the full ψ operator, not just for ψ_R and ψ_L, in which case the α and β indices can be written as j and l, labeling specific Luttinger liquids on which the ψ operators act. Then we have:

$$\begin{aligned}
\{\psi_j^\dagger(x'), \psi_l(x)\} &= \frac{1}{L}\sum_{kq} e^{i(kx-qx')}\{c_{j,q}^\dagger, c_{l,k}\} \\
&= \frac{1}{L}\sum_{kq} e^{i(kx-qx')}\delta_{qk}\delta_{jl} \\
&= \frac{\delta_{jl}}{L}\sum_{k} e^{ik(x-x')} \\
&= \frac{\delta_{jl}}{2\pi}\int_k e^{ik(x-x')}dk \\
&= \delta_{jl}\delta(x-x')
\end{aligned}$$

We also want to do the same calculation for ψ operators for right- and left-moving excitations. We must be a little bit careful, as there are two naive approaches, both of which are not correct. First, we might look at just the technical definitions of ψ_R and ψ_L above (equations 4.123), which makes it clear that they are in fact both identical to each other and to ψ since all we did is relabel indices. This would suggest that

$$\{\psi_R^\dagger(x), \psi_R(x')\} = \{\psi_L^\dagger(x), \psi_L(x')\} = \{\psi_R^\dagger(x), \psi_L(x')\} = \{\psi_L^\dagger(x), \psi_R(x')\} = \delta(x-x')$$

Alternatively, we might forget about equations (4.123) entirely, and instead make the natural-seeming assumption that $\psi(x) = \psi_R(x) + \psi_L(x)$ and that right- and left-movers are completely uncorrelated from each other so that $\{\psi_R^\dagger(x), \psi_L(x')\} = 0$. In that case we would find:

$$\begin{aligned}
\{\psi^\dagger(x'), \psi(x)\} &= \{\psi_R^\dagger(x') + \psi_L^\dagger(x'), \psi_R(x) + \psi_L(x)\} \\
&= \{\psi_R^\dagger(x'), \psi_R(x)\} + \{\psi_R^\dagger(x'), \psi_L(x)\} + \{\psi_L^\dagger(x'), \psi_R(x)\} + \{\psi_L^\dagger(x'), \psi_L(x)\} \\
&= \{\psi_R^\dagger(x'), \psi_R(x)\} + 0 + 0 + \{\psi_L^\dagger(x'), \psi_L(x)\} \\
&= 2\{\psi_R^\dagger(x'), \psi_R(x)\} = 2\{\psi_L^\dagger(x'), \psi_L(x)\} \\
\{\psi_R^\dagger(x'), \psi_R(x)\} &= \{\psi_L^\dagger(x'), \psi_L(x)\} = \frac{1}{2}\delta(x-x')
\end{aligned}$$

In practice, we will do something different from either of these options, but which captures the spirit of both. In particular, the usual construction of the Tomonaga-Luttinger model begins by linearizing a band structure around the Fermi points and then separating the band into two independent linear bands with no correlation to each other. In this case,

the equations (4.123) still apply, but $c_{k,R}$ and $c_{k,L}$ are now considered to be completely independent. In other words, we choose to forget that $c_{k,R} = c_{k+2k_F,L}$, which we think of as neglecting $2k_F$ scattering between the Fermi points. In practice, this means that we assume $\{c^\dagger_{kR}, c_{k'L}\} = 0$ for any k and k', and therefore also $\{\psi^\dagger_R(x), \psi_L(x')\} = 0$ for any x and x'.

On the other hand, the k states in the sums in the definitions of both ψ_R and ψ_L are viewed as a complete set (a whole band, not just half of one) and so $\{\psi^\dagger_R(x), \psi_R(x')\} = \delta(x - x')$, not $\frac{1}{2}\delta(x - x')$. This can also be confirmed by direct calculation from equations (4.123). (Actually doing this calculation, there appears to be an extra factor of $e^{-ik_F(x-x')}$, but it can be dropped because it is multiplied by a delta function that forces $x = x'$.) Note that this implies that it is not correct to say that $\psi(x) = \psi_R(x) + \psi_L(x)$. Instead of each excitation in real space having a right-moving part and a left-moving part, our picture is that the excitation is either entirely right-moving or entirely left-moving.

Fourier transform results summary

We have found the following relations between the operators in the momentum space and real space pictures:

$$\psi(r) = \frac{1}{\sqrt{L}} \sum_k e^{ikx} c_k \tag{4.121a}$$

$$c_k = \frac{1}{\sqrt{L}} \int e^{-ikx} \psi(x)\, dx \tag{4.122a}$$

$$\psi_\alpha(x) = \frac{e^{i\alpha k_F x}}{\sqrt{L}} \sum_k e^{ikx} c_{k\alpha} \tag{3.29b}$$

$$c_{k\alpha} = \frac{1}{\sqrt{L}} \int e^{-ikx} e^{-i\alpha k_F x} \psi_\alpha(x) dx \tag{3.29a}$$

where in the last two equations α is R or L when used as a label and is 1 or -1 respectively when used in an expression.

From these relations, we also determined that

$$\{\psi_\alpha(x), \psi_\beta(x')\} = 0 \tag{4.127}$$

$$\{\psi^\dagger_\alpha(x), \psi^\dagger_\beta(x')\} = 0 \tag{4.128}$$

$$\{\psi^\dagger_\alpha(x), \psi_\beta(x')\} = \delta_{\alpha\beta}\delta(x - x') \tag{4.129}$$

These results for the anticommutators are correct regardless of whether the indices α and β denote the Luttinger liquid on which the operators act, the direction of the excitations (R or L), or some composite of these and other labels.

Luttinger liquid Hamiltonian

The last thing that we need for computations on Luttinger liquids is the Hamiltonian itself. When written in terms of the bosonic fields, the Hamiltonian is given by [31]

$$H = \frac{\hbar}{2\pi}\int dx \left[\frac{vK}{\hbar^2}(\nabla\theta)^2 + \frac{v}{K}(\nabla\phi)^2\right] \tag{4.130}$$

This Hamiltonian is quadratic, meaning that things like correlation functions can be calculated exactly. It is also worth making a quick note about the parameters that appear. K is a measure of the strength of electron-electron interactions in the original fermion model. In rewriting the theory in terms of the bosons, the interactions are now reflected simply in numerical prefactors to existing (noninteracting) terms! $K = 1$ in the noninteracting limit, and $K < 1$ and $K > 1$ correspond to repulsive and attractive interactions respectively. The parameter v is a renormalized Fermi velocity. (v depends on K [31, eq 2.43], but that will not be important for our purposes.)

Our model

For our computations, we are of course are studying a system described not just by a single Luttinger liquid but rather by many coupled Luttinger liquids. The total Hamiltonian that we use is given by

$$H = \sum_j H_j = \sum_j h_j + h'_j \tag{4.131a}$$

$$h_j = \frac{\hbar}{2\pi}\int dx \left[\frac{vK}{\hbar^2}\left(\nabla\theta_j\right)^2 + \frac{v}{K}\left(\nabla\phi_j\right)^2\right] \tag{4.131b}$$

$$h'_j = \frac{1}{2}\sum_{\alpha\beta}\int dx\, dx' \left[t_{\alpha\beta}(x-x')\psi^\dagger_{j\alpha}(x)\psi_{j+1,\beta}(x') + t_{\alpha\beta}(x-x')\psi^\dagger_{j-1,\alpha}(x)\psi_{j\beta}(x') + \text{h.c.}\right] \tag{4.131c}$$

where h_j is the Luttinger liquid Hamiltonian for chain j and h'_j has half of each hopping term to and from chain j. (Note that we could have chosen to write the h'_j term differently by, for instance, only including the hopping to [but not from] chain j and removing the factor of $1/2$, or only including hopping between chain j and chain $j-1$ but not between j and $j+1$ and again removing the $1/2$. We have instead chosen to write the Hamiltonian this way in anticipation of the calculation of the energy current operator.)

Electrical current operator

We derive an expression for the electrical current operator for this model in precisely the same way as in the previous model:

$$J_e = \lim_{k\to 0}\frac{q}{\hbar k}\sum_j [N_j, H]e^{ika_c j} \tag{4.40}$$

where j indexes 1D chains, a_c is the interchain spacing, and N_j is the total fermion number operator associated with chain j. For the Hamiltonian, H, we use the coupled Luttinger liquid model from equation (4.131).

As in the calculations for the previous model, we begin by calculating the commutator $[N_j, H]$. There are two parts that we need to calculate, $[N_j, h_i]$ and $[N_j, h_i']$. The first is 0 for the same reason as in the previous model: each h_i only contains terms with an even number of fermion operators and thus commutes with the number operator on a different chain. (That $[N_j, h_i] = 0$ is less obvious in the case of $i = j$. However, N_j as given in equation (4.132) below looks like the hopping term h_j' but with $j-1$ and $j+1$ both replaced by j and with $x' \to x$ and $\beta \to \alpha$. Making these changes in our result for $[N_j, H]$ below, it is clear that the commutator will vanish.) Physically, the vanishing of this commutator is because each h_i is the Hamiltonian of an isolated Luttinger liquid, on which the total fermion number cannot change (independent of what the theory looks like, the underlying physical system it represents must in fact have a conserved number of electrons). If h_i does not connect states with different fermion number, it must commute with the number operator.

It remains to find the commutator of the N_j with the hopping terms of H, or $[N_j, h_i']$. The number operator is given by

$$N_j = \int_x dx \, [\psi_{j,R}^\dagger(x)\psi_{j,R}(x) + \psi_{j,L}^\dagger(x)\psi_{j,L}(x)] \tag{4.132}$$

Note that this expression does not contain terms like $\psi_R^\dagger \psi_L$. These would be expected if $\psi(x) = \psi_R(x) + \psi_L(x)$, since we would then integrate over $\psi^\dagger\psi$; however, as discussed above it is not correct to decompose ψ in this way because we have split the model into separate bands. In that case, a term like $\psi_R^\dagger \psi_L$ would represent a scattering process rather than particle enumeration.

The hopping terms from the Hamiltonian are the ones from equation (4.131), although in this case we can simplify a bit by instead using the form

$$h_i' = \sum_{\alpha,\beta=R,L} \int dx \, dx' \, t_{\alpha\beta}(x-x')[\psi_{i,\alpha}^\dagger(x)\psi_{i+1,\beta}(x') + \psi_{i+1,\alpha}^\dagger(x)\psi_{i,\beta}(x')] \tag{4.133}$$

since this has fewer terms. In the calculation of electrical current, the Hamiltonian only appears in the form of $H = \sum_i H_i$, so that which H_i we put the hopping terms in clearly cannot matter and therefore we might as well take this form that somewhat simplifies our calculations.

Even with this simpler expression, h_i' still has 8 terms in total so that each commutator $[N_j, h_i']$ has 16 terms. Fortunately, the various terms are all quite similar so we only really need the following two rules:

$$[AB, CD] = ABCD - CDAB = A\{B, C\}D - C\{D, A\}B \tag{4.134}$$

$$\{\psi_a^\dagger(x), \psi_b(x')\} = \delta_{ab}\delta(x-x') \tag{4.129}$$

We then perform the actual computation of the commutator:

$$
\begin{aligned}
[N_j, H] &= \sum_i [N_j, h_i'] \\
&= \sum_i \sum_{\alpha\beta\gamma=R,L} \int dx\, dx'\, dx''\, t_{\beta\gamma}(x'-x'') \\
&\qquad \times [\psi^\dagger_{j,\alpha}(x)\psi_{j,\alpha}(x), (\psi^\dagger_{i,\beta}(x')\psi_{i+1,\gamma}(x'') + \psi^\dagger_{i+1,\beta}(x')\psi_{i,\gamma}(x''))] \\
&= \sum_i \sum_{\alpha\beta\gamma=R,L} \int dx\, dx'\, dx''\, t_{\beta\gamma}(x'-x'') \begin{bmatrix} \psi^\dagger_{j,\alpha}(x)\{\psi_{j,\alpha}(x), \psi^\dagger_{i,\beta}(x')\}\psi_{i+1,\gamma}(x'') \\ -\psi^\dagger_{i,\beta}(x')\{\psi_{i+1,\gamma}(x''), \psi^\dagger_{j,\alpha}(x)\}\psi_{j,\alpha}(x) \\ +\psi^\dagger_{j,\alpha}(x)\{\psi_{j,\alpha}(x), \psi^\dagger_{i+1,\beta}(x')\}\psi_{i,\gamma}(x'') \\ -\psi^\dagger_{i+1,\beta}(x')\{\psi_{i,\gamma}(x''), \psi^\dagger_{j,\alpha}(x)\}\psi_{j,\alpha}(x) \end{bmatrix} \\
&= \sum_i \sum_{\alpha\beta\gamma=R,L} \int dx\, dx'\, dx''\, t_{\beta\gamma}(x'-x'') \begin{bmatrix} \psi^\dagger_{j,\alpha}(x)\psi_{i+1,\gamma}(x'')\delta_{\alpha\beta}\delta_{ji}\delta(x-x') \\ -\psi^\dagger_{i,\beta}(x')\psi_{j,\alpha}(x)\delta_{\alpha\gamma}\delta_{ji+1}\delta(x-x'') \\ +\psi^\dagger_{j,\alpha}(x)\psi_{i,\gamma}(x'')\delta_{\alpha\beta}\delta_{ji+1}\delta(x-x') \\ -\psi^\dagger_{i+1,\beta}(x')\psi_{j,\alpha}(x)\delta_{\alpha\gamma}\delta_{ji}\delta(x-x'') \end{bmatrix} \\
&= \sum_{\alpha\beta\gamma=R,L} \int dx\, dx' \begin{bmatrix} t_{\beta\gamma}(x-x')\psi^\dagger_{j,\alpha}(x)\psi_{j+1,\gamma}(x')\delta_{\alpha\beta} - t_{\beta\gamma}(x'-x)\psi^\dagger_{j-1,\beta}(x')\psi_{j,\alpha}(x)\delta_{\alpha\gamma} \\ +t_{\beta\gamma}(x-x')\psi^\dagger_{j,\alpha}(x)\psi_{j-1,\gamma}(x')\delta_{\alpha\beta} - t_{\beta\gamma}(x'-x)\psi^\dagger_{j+1,\beta}(x')\psi_{j,\alpha}(x)\delta_{\alpha\gamma} \end{bmatrix} \\
&= \sum_{\alpha\beta=R,L} \int dx\, dx'\, t_{\alpha\beta}(x-x') \begin{bmatrix} \psi^\dagger_{j,\alpha}(x)\psi_{j+1,\beta}(x') - \psi^\dagger_{j-1,\alpha}(x)\psi_{j,\beta}(x') \\ +\psi^\dagger_{j,\alpha}(x)\psi_{j-1,\beta}(x') - \psi^\dagger_{j+1,\alpha}(x)\psi_{j,\beta}(x') \end{bmatrix}
\end{aligned}
$$

Now we can again use the useful fact that for any operator depending on site j, O_j,

$$\lim_{k\to 0} \frac{1}{k} \sum_j (O_{j+1} - O_j) e^{ikaj} = -ia \sum_j O_j \tag{4.45}$$

With this, we get our final result for the current operator:

$$\boxed{J_e = \frac{ia_c q}{\hbar} \sum_j \sum_{\alpha\beta=R,L} \int \begin{bmatrix} t_{\alpha\beta}(x-x')\psi^\dagger_{j,\alpha}(x)\psi_{j-1,\beta}(x') \\ -\, t_{\beta\alpha}(x'-x)\psi^\dagger_{j-1,\beta}(x')\psi_{j,\alpha}(x) \end{bmatrix} dx\, dx'} \tag{4.135}$$

Thermal current operator

As in the noninteracting model, the expression for the energy current is

$$J_E = \lim_{k\to 0} \frac{1}{\hbar k} \sum_j [H_j, H] e^{ika_c j} \tag{4.48}$$

where j indexes chains and H_j is the portion of the Hamiltonian associated with chain j (so $\sum_j H_j = H$). There is some ambiguity here, since it is unclear for instance whether hopping

terms from chain j to chain $j+1$ or vice-versa should be included in H_j or in H_{j+1}. We have chosen to split the two hopping terms evenly between the two sites, so that H_j is given by the expressions in equation (4.131) above.

The first step in the calculation is to find the commutator of H_j and H. This actually simplifies quite nicely using the division into local and hopping terms, $H_j = h_j + h'_j$:

$$[H_j, H] = \sum_i [H_j, H_i] = \sum_i [h_j, h_i] + [h_j, h'_i] + [h'_j, h_i] + [h'_j, h'_i] \tag{4.136}$$

The first term is 0 because each local Hamiltonian h_α preserves particle number and hence has an even number of fermion operators in each term; as discussed in section 4.2 above, this leads to a vanishing commutator because fermion operators of two different species (say, on two different chains) anticommute so that any pair of fermion operators of one species will collectively commute with any fermion operator(s) of a different species.

Furthermore, the fourth term is second order in the interchain hopping strength, t, and is thus negligible in the weak-coupling quasi-atomic limit. This gives the simplified result

$$[H_j, H] \approx \sum_i [h'_j, h_i] - [h'_i, h_j]$$

Unfortunately, these commutators still require a substantial amount of computation. In particular, we must compute terms like $[\psi^\dagger_{i+1,\alpha}(x)\psi_{i\beta}(x'), (\nabla\theta_j(\tilde{x}))^2]$. After some algebra we find the useful results:

$$[\psi_{i\alpha}(x), \nabla\theta_j(x')] = \alpha\pi\delta_{ij}\delta(x-x')\psi_i(x) \tag{3.15a}$$
$$[\psi^\dagger_{i\alpha}(x), \nabla\theta_j(x')] = -\alpha\pi\delta_{ij}\delta(x-x')\psi^\dagger_i(x) \tag{3.15b}$$
$$[\psi_{i\alpha}(x), \nabla\phi_j(x')] = -\pi\delta_{ij}\delta(x-x')\psi_i(x) \tag{3.15c}$$
$$[\psi^\dagger_{i\alpha}(x), \nabla\phi_j(x')] = \pi\delta_{ij}\delta(x-x')\psi^\dagger_i(x) \tag{3.15d}$$

where α may take the values R and L when used as an index and the values 1 and -1 respectively when used as a multiplicative factor. For the sake of completeness, we give a

full derivation of the first of these results, equation (3.15a).

$$\begin{aligned}
[\psi_{i\alpha}(x), \nabla\theta_j(x')] &= U_\alpha \lim_{a\to 0} \frac{1}{\sqrt{2\pi a}} e^{i\alpha(k_F - \pi/L)} \left[e^{-i(\alpha\phi_i(x) - \theta_i(x))}, \nabla\theta_j(x')\right] \\
&= U_\alpha \lim_{a\to 0} \frac{1}{\sqrt{2\pi a}} e^{i\alpha(k_F - \pi/L)} \sum_{n=0}^{\infty} \frac{(-i)^n}{n!} \left[(\alpha\phi_i(x) - \theta_i(x))^n, \nabla\theta_j(x')\right] \\
(\alpha\phi_i(x) - \theta_i(x))^n \nabla\theta_j(x') &= (\alpha\phi_i(x) - \theta_i(x))^{n-1} \nabla\theta_j(x') (\alpha\phi_i(x) - \theta_i(x)) \\
&\quad + (\alpha\phi_i(x) - \theta_i(x))^{n-1} [\alpha\phi_i(x) - \theta_i(x), \nabla\theta_j(x')] \\
&= (\alpha\phi_i(x) - \theta_i(x))^{n-1} \nabla\theta_j(x') (\alpha\phi_i(x) - \theta_i(x)) \\
&\quad + \alpha i\pi\delta(x - x')\delta_{ij} (\alpha\phi_i(x) - \theta_i(x))^{n-1} \\
&\vdots \\
&= \nabla\theta_j(x') (\alpha\phi_i(x) - \theta_i(x))^n + \alpha i n\pi\delta(x - x')\delta_{ij} (\alpha\phi_i(x) - \theta_i(x))^{n-1} \\
\left[(\alpha\phi_i(x) - \theta_i(x))^n, \nabla\theta_j(x')\right] &= \alpha i n\pi\delta(x - x')\delta_{ij} (\alpha\phi_i(x) - \theta_i(x))^{n-1} \\
[\psi_{i\alpha}(x), \nabla\theta_j(x')] &= U_\alpha \lim_{a\to 0} \frac{1}{\sqrt{2\pi a}} e^{i\alpha(k_F - \pi/L)} \\
&\quad \times \sum_{n=0}^{\infty} \frac{(-i)^n}{n!} \left[\alpha i n\pi\delta(x - x')\delta_{ij} (\alpha\phi_i(x) - \theta_i(x))^{n-1}\right] \\
&= U_\alpha \lim_{a\to 0} \frac{1}{\sqrt{2\pi a}} e^{i\alpha(k_F - \pi/L)} \\
&\quad \times \sum_{n=1}^{\infty} \frac{(-i)^{(n-1)}(-i)}{(n-1)!} \left[\alpha i\pi\delta(x - x')\delta_{ij} (\alpha\phi_i(x) - \theta_i(x))^{n-1}\right] \\
&= U_\alpha \lim_{a\to 0} \frac{1}{\sqrt{2\pi a}} e^{i\alpha(k_F - \pi/L)} e^{-i(\alpha\phi_i(x) - \theta_i(x))} \alpha\pi\delta(x - x')\delta_{ij} \\
&= \alpha\pi\delta(x - x')\delta_{ij}\psi_{i\alpha}(x)
\end{aligned}$$

For equation (3.15b), the only difference in the derivation is that $(-i)^n$ becomes i^n, so when the extra factor leftover from shifting the summation index is multiplied by the i from the commutator of ϕ and $\nabla\theta$, we get -1 instead of 1. For the ϕ commutators, (3.15c) and (3.15d), the only difference is that $[\alpha\phi - \theta, \nabla\theta]$ is replaced by $[\alpha\phi - \theta, \nabla\phi]$; in the first case we have $\alpha[\phi_i(x), \nabla\theta_j(x')] = i\alpha\pi\delta_{ij}\delta(x - x')$ whereas in the second we have $-[\theta_i(x), \nabla\phi_j(x')]$. To find this commutator, we can start from the commutator of ϕ and θ:

$$\begin{aligned}
[\phi(x), \theta(x')] = i\frac{\pi}{2}\text{sign}(x' - x) &\Rightarrow [\theta(x'), \phi(x)] = -i\frac{\pi}{2}\text{sign}(x' - x) \\
&\Rightarrow [\theta(x'), \nabla\phi(x)] = i\pi\delta(x' - x) \\
&\Rightarrow -[\theta_i(x), \nabla\phi_j(x')] = -i\pi\delta(x' - x)\delta_{ij}
\end{aligned}$$

This is the same result as for $[\phi, \nabla\theta]$ but with $\alpha \to -1$. Thus the results (3.15c) and (3.15d) are found by making the subsitution $\alpha \to -1$ in (3.15a) and (3.15b). This completes the confirmation of all four results given in equations (3.15).

With some further algebra, the commutators in equations (3.15) lead to

$$[\psi^\dagger_{i\alpha}(\tilde{x})\psi_{i+1,\beta}(x), (\nabla\theta_j(x'))^2] = \left[\begin{array}{c} 2\pi\nabla\theta_j(x')\left(\beta\delta(x-x')\delta_{i+1,j} - \alpha\delta(x-\tilde{x})\delta_{ij}\right) \\ +\pi^2\left(\beta\delta(x-x')\delta_{i+1,j} - \alpha\delta(x-\tilde{x})\delta_{ij}\right)^2 \end{array} \right] \psi^\dagger_{i\alpha}(\tilde{x})\psi_{i+1,\beta}(x) \tag{4.138a}$$

$$[\psi^\dagger_{i\alpha}(\tilde{x})\psi_{i+1,\beta}(x), (\nabla\phi_j(x'))^2] = \left[\begin{array}{c} -2\pi\nabla\phi_j(x')\left(\delta(x-x')\delta_{i+1,j} - \delta(x-\tilde{x})\delta_{ij}\right) \\ +\pi^2\left(\delta(x-x')\delta_{i+1,j} - \delta(x-\tilde{x})\delta_{ij}\right)^2 \end{array} \right] \psi^\dagger_{i\alpha}(\tilde{x})\psi_{i+1,\beta}(x) \tag{4.138b}$$

and using these results, we can conclude that

$$[\psi^\dagger_{i\alpha}(\tilde{x})\psi_{i+1,\beta}(x), h_j] = v \left[\begin{array}{c} \delta_{i+1,j}\left(\beta\frac{K}{\hbar}\nabla\theta_j(x) - \alpha\frac{\hbar}{K}\nabla\phi_j(x)\right) \\ -\delta_{ij}\left(\frac{K}{\hbar}\nabla\theta_j(\tilde{x}) - \frac{\hbar}{K}\nabla\phi_j(\tilde{x})\right) \\ +\frac{\pi}{2}\left(\frac{K}{\hbar} + \frac{\hbar}{K}\right)\delta(0)\left(\delta_{i+1,j} + \delta_{ij}\right) \end{array} \right] \psi^\dagger_{i\alpha}(\tilde{x})\psi_{i+1,\beta}(x) \tag{4.139}$$

In total, $[h'_j, h_i] - [h'_i, h_j]$ has eight such terms, which we must add up. We then also perform a sum over the index i to find $[H_j, H]$. In the case that the index i (which labels the various 1D chains) is either infinite or periodic, we can perform various tricks with relabeling indices to cancel terms. When we do this, the eight terms with $\delta(0)$ end up canceling, so that in the end we have:

$$[H_j, H] = \frac{v}{2}\int t_{\alpha\beta}(x'-x) \left[\begin{array}{c} [\nabla_{j+1}]^\beta_x \psi^\dagger_{j\alpha}(x')\psi_{j+1,\beta}(x) - [\nabla_j]^\beta_x \psi^\dagger_{j-1,\alpha}(x')\psi_{j\beta}(x) \\ +[\nabla_{j-1}]^\beta_x \psi^\dagger_{j\alpha}(x')\psi_{j-1,\beta}(x) - [\nabla_j]^\beta_x \psi^\dagger_{j-1,\alpha}(x')\psi_{j\beta}(x) \\ -\left(\begin{array}{c} [\nabla_{j+1}]^\alpha_{x'} \psi^\dagger_{j+1,\alpha}(x')\psi_{j\beta}(x) - [\nabla_j]^\alpha_{x'} \psi^\dagger_{j\alpha}(x')\psi_{j-1,\beta}(x) \\ +[\nabla_{j-1}]^\alpha_{x'} \psi^\dagger_{j-1,\alpha}(x')\psi_{j\beta}(x) - [\nabla_j]^\alpha_{x'} \psi^\dagger_{j\alpha}(x')\psi_{j+1,\beta}(x) \end{array} \right) \end{array} \right] dx\, dx' \tag{4.140}$$

where

$$[\nabla_j]^\alpha_y = \alpha\frac{K}{\hbar}\nabla\theta_j(y) - \frac{\hbar}{K}\nabla\phi_j(y) \tag{4.141}$$

Finally, we can combine equations (4.40), (4.140), and (4.45) to calculate the current operator. The result is

$$\boxed{J_E = \frac{ia_c v}{2\hbar}\sum_{j\alpha\beta}\int t_{\alpha\beta}(x'-x) \left[\begin{array}{c} \left([\nabla_j]^\alpha_{x'} + [\nabla_{j-1}]^\beta_x\right)\psi^\dagger_{j\alpha}(x')\psi_{j-1,\beta}(x) \\ \\ -\left([\nabla_{j-1}]^\alpha_{x'} + [\nabla_j]^\beta_x\right)\psi^\dagger_{j-1,\alpha}(x')\psi_{j\beta}(x) \end{array} \right] dx\, dx'} \tag{2.26b}$$

Using the commutators given above, one can check that $[\psi^\dagger_{j\alpha}(x), [\nabla_j]^\alpha_x] = -\pi\delta(0)\left(\frac{K}{\hbar} + \frac{\hbar}{K}\right)$, $[\psi_{j\alpha}(x), [\nabla_j]^\alpha_x] = \pi\delta(0)\left(\frac{K}{\hbar} + \frac{\hbar}{K}\right)$, and hence $[\psi^\dagger_{j\alpha}(x')\psi_{j-1,\beta}(x), [\nabla_{j-1}]^\beta_{x'} + [\nabla_j]^\alpha_x] = 0$, so the current operator is indeed Hermitian.

Current-current correlators

As in the noninteracting model, to find the transport coefficients using the Kubo formulas we must first find several current-current correlation functions, namely $\langle J_e(\tau)J_e(0)\rangle$, $\langle J_E(\tau)J_E(0)\rangle$, and $\langle J_E(\tau)J_e(0)\rangle$. Those calculations are somewhat more involved in this model, but we nevertheless present full details of our work here.

$\langle J_e(\tau)J_e(0)\rangle$

The first step in our calculation is to find the time-dependence of the current operator. We first make the same approximation as in the previous model, namely that to lowest order in the interchain hopping we can drop the hopping terms entirely from the Hamiltonian appearing in the time-evolution operator,

$$e^{-\tau H} = e^{-\tau \sum_j H_j} \to e^{-\tau \sum_j h_j} = e^{-\tau H_0} \tag{4.142}$$

We will not calculate the time evolution explicitly, but rather we will just denote the time evolution of each $\psi(x)$ operator by $\psi(x,\tau)$. Since we use only H_0 in calculating the time-dependence, $\psi(x,\tau)$ is just the time-evolved fermion operator for a single uncoupled Luttinger liquid.

With this approach, we can begin the calculation. First recall that we found above

$$J_e = \frac{ia_c q}{\hbar} \sum_j \sum_{\alpha\beta=R,L} \int \left[\begin{array}{l} t_{\alpha\beta}(x-x')\psi^\dagger_{j,\alpha}(x)\psi_{j-1,\beta}(x') \\ -\, t_{\beta\alpha}(x'-x)\psi^\dagger_{j-1,\beta}(x')\psi_{j,\alpha}(x) \end{array} \right] dx\, dx' \tag{4.135}$$

We thus have the corresponding time-evolved expression:

$$J_e(\tau) = \frac{ia_c q}{\hbar} \sum_j \sum_{\alpha\beta=R,L} \int \left[\begin{array}{l} t_{\alpha\beta}(x-x')\psi^\dagger_{j,\alpha}(x,\tau)\psi_{j-1,\beta}(x',\tau) \\ -\, t_{\beta\alpha}(x'-x)\psi^\dagger_{j-1,\beta}(x',\tau)\psi_{j,\alpha}(x,\tau) \end{array} \right] dx\, dx' \tag{4.143}$$

Note that the ability to distribute the time-evolution to the individual fermion operators does not depend on any approximation, but rather is just a result of inserting a factor of $e^{-\tau H}e^{\tau H}$ between the two operators in each term.

Next, in calculating $\langle J_e(\tau)J_e\rangle$, the brackets indicate a thermal average just as in the previous model, and again we drop the interchain hopping from the Hamiltonian appearing in the density matrix,

$$e^{-\beta H} \to e^{-\beta H_0} = e^{-\beta \sum_j h_j} = \prod_j e^{-\beta h_j}, \tag{4.144}$$

an approximation that, along with the equivalent approximation to the time-evolution operators, allows us to split the expectation value into a product of expectation values on separate chains.

With the preliminaries out of the way, we can proceed to the actual calculation:

$$\begin{aligned}
\langle J_e(\tau)J_e\rangle &= \sum_{ij}\sum_{\alpha\beta\gamma\delta}\int dx_1\,dx_2\,dx_3\,dx_4\,\left(\frac{a_c q}{\hbar}\right)^2 t_{\alpha\beta}(x_1-x_2)t_{\gamma\delta}(x_3-x_4)\,\langle\cdots\rangle \\
\langle\cdots\rangle &= \left\langle \begin{array}{c} e^{\tau H}[\psi^\dagger_{j-1,\alpha}(x_1)\psi_{j,\beta}(x_2)-\psi^\dagger_{j,\alpha}(x_1)\psi_{j-1,\beta}(x_2)] \\ \\ \times e^{-\tau H}[\psi^\dagger_{i,\gamma}(x_3)\psi_{i-1,\delta}(x_4)-\psi^\dagger_{i-1,\gamma}(x_3)\psi_{i,\delta}(x_4)] \end{array}\right\rangle \\
&= \delta_{ij}\left\langle \begin{array}{c} e^{\tau H}\psi^\dagger_{j-1,\alpha}(x_1)\psi_{j,\beta}(x_2)e^{-\tau H}\psi^\dagger_{j,\gamma}(x_3)\psi_{j-1,\delta}(x_4) \\ + e^{\tau H}\psi^\dagger_{j,\alpha}(x_1)\psi_{j-1,\beta}(x_2)e^{-\tau H}\psi^\dagger_{j-1,\gamma}(x_3)\psi_{j,\delta}(x_4) \end{array}\right\rangle \\
&= \delta_{ij}\left\langle \begin{array}{c} e^{\tau h_{j-1}}\psi^\dagger_{j-1,\alpha}(x_1)e^{-\tau h_{j-1}}e^{\tau h_j}\psi_{j,\beta}(x_2)e^{-\tau h_j}\psi^\dagger_{j,\gamma}(x_3)\psi_{j-1,\delta}(x_4) \\ + e^{\tau h_j}\psi^\dagger_{j,\alpha}(x_1)e^{-\tau h_j}e^{\tau h_{j-1}}\psi_{j-1,\beta}(x_2)e^{-\tau h_{j-1}}\psi^\dagger_{j-1,\gamma}(x_3)\psi_{j,\delta}(x_4) \end{array}\right\rangle \\
&= \delta_{ij}\left\langle \begin{array}{c} \psi^\dagger_{j-1,\alpha}(x_1,\tau)\psi_{j,\beta}(x_2,\tau)\psi^\dagger_{j,\gamma}(x_3)\psi_{j-1,\delta}(x_4) \\ + \psi^\dagger_{j,\alpha}(x_1,\tau)\psi_{j-1,\beta}(x_2,\tau)\psi^\dagger_{j-1,\gamma}(x_3)\psi_{j,\delta}(x_4) \end{array}\right\rangle \\
&= \delta_{ij}\langle\psi^\dagger_{j-1,\alpha}(x_1,\tau)\psi_{j-1,\delta}(x_4)\rangle\langle\psi_{j,\beta}(x_2,\tau)\psi^\dagger_{j,\gamma}(x_3)\rangle \\
&\quad + \delta_{ij}\langle\psi^\dagger_{j,\alpha}(x_1,\tau)\psi_{j,\delta}(x_4)\rangle\langle\psi_{j-1,\beta}(x_2,\tau)\psi^\dagger_{j-1,\gamma}(x_3)\rangle \\
&= \delta_{ij}\langle\psi^\dagger_{j-1,\alpha}(x_1-x_4,\tau)\psi_{j-1,\delta}(0)\rangle\langle\psi_{j,\beta}(x_2-x_3,\tau)\psi^\dagger_{j,\gamma}(0)\rangle \\
&\quad + \delta_{ij}\langle\psi^\dagger_{j,\alpha}(x_1-x_4,\tau)\psi_{j,\delta}(0)\rangle\langle\psi_{j-1,\beta}(x_2-x_3,\tau)\psi^\dagger_{j-1,\gamma}(0)\rangle \\
&= 2\delta_{ij}\langle\psi^\dagger_{j-1,\alpha}(x_1-x_4,\tau)\psi_{j-1,\delta}(0)\rangle\langle\psi_{j,\beta}(x_2-x_3,\tau)\psi^\dagger_{j,\gamma}(0)\rangle \\
&= 2\delta_{ij}\delta_{\alpha\delta}\delta_{\beta\gamma}\langle\psi^\dagger_{j-1,\alpha}(x_1-x_4,\tau)\psi_{j-1,\alpha}(0)\rangle\langle\psi_{j,\beta}(x_2-x_3,\tau)\psi^\dagger_{j,\beta}(0)\rangle
\end{aligned}$$

In the third line, we eliminated two of four terms because they either move electrons to lower j twice and never to higher j or vice versa. Either way, these terms are not diagonal and vanish in the trace when calculating the expectation value. In the fourth line, we used the fact that the Hamiltonian for each individual Luttinger liquid commutes with the Fermion operators on other chains and the fact that we can ignore the hopping terms in the Hamiltonian for purposes of time evolution if we want the conductivity to lowest order in t. Likewise, in the sixth line I used the fact that the expectation values are taken with respect to the $t = 0$ density matrix if the conductivity is to be found to the lowest order in t, so that the expectation value of a product of operators on two different chains is the product of the expectation values of the operators on each chain taken independently. The second-to-last line follows from the fact that the correlation functions don't depend on which polymer is under consideration, and the two terms differ only in the substitution $j \leftrightarrow j-1$. The last line follows from the fact that left-and right-moving excitations are uncorrelated.

We then have a complete expression for the current-current correlator:

$$\langle J_e(\tau)J_e\rangle = 2\sum_j\sum_{\alpha\beta}\int dx_1\,dx_2\,dx_3\,dx_4\left[\begin{array}{c} \left(\frac{a_c q}{\hbar}\right)^2 t_{\alpha\beta}(x_1-x_2)t_{\beta\alpha}(x_3-x_4) \\ \times\langle\psi^\dagger_{j-1,\alpha}(x_1-x_4,\tau)\psi_{j-1,\alpha}(0)\rangle \\ \times\langle\psi_{j,\beta}(x_2-x_3,\tau)\psi^\dagger_{j,\beta}(0)\rangle \end{array}\right] \tag{4.145}$$

Before we put in an exact functional form for the single-particle correlation functions, we can make two more simplifying approximations. First, we will assume that a right-mover on one chain can only hop to a right-mover on an adjacent chain and likewise for left-movers, or in other words $t_{\alpha\beta}(x-x')$ is 0 for $\alpha \neq \beta$. This assumption is well-justified if we view our system as initially coming from a 2D lattice tight-binding model. In that case, if we go to Fourier components along one direction (along chains), the momentum in that direction will be conserved when the excitation hops in the orthogonal (inter-chain) direction, which in particular means that right- and left-movers will not be interchanged. This assumption simplifies $t_{\alpha\beta}(x-x')$ to $t_{RR}(x-x')\delta_{\alpha R}\delta_{\beta R} + t_{LL}(x-x')\delta_{\alpha L}\delta_{\beta L}$. By symmetry, it must be the case that $t_{RR} = t_{LL}$, so $t_{\alpha\beta}(x-x') = t(x-x')\delta_{\alpha\beta}$ where $t(x-x') = t_{RR}(x-x') = t_{LL}(x-x')$.

Additionally, hopping should be more or less local. This implies that $t(x-x')$ should be sharply peaked around $x = x'$. For simplicity, we will assume a precisely peaked hopping: $t(x-x') \propto t\delta(x-x')$, where on the right-hand side t is a constant that does not depend on position. As discussed in section 4.6, the precise expression we want to use is $\frac{t}{2\pi}\delta(x-x')$.

Putting these two assumptions together, we get the nice simplification that

$$t_{\alpha\beta}(x-x') = \frac{t}{2\pi}\delta_{\alpha\beta}\delta(x-x') \tag{4.146}$$

where t is a constant. With this simplification, our expression for the correlator becomes

$$\langle J_e(\tau)J_e\rangle \approx 2\left(\frac{a_c q t}{2\pi\hbar}\right)^2 \sum_{j\alpha}\int dx\, dx' \left[\langle\psi^\dagger_{j-1,\alpha}(x-x',\tau)\psi_{j-1,\alpha}(0)\rangle\langle\psi_{j,\alpha}(x-x',\tau)\psi^\dagger_{j,\alpha}(0)\rangle\right] \tag{4.147}$$

We can do even slightly better. Since the only dependence is on $x-x'$, we can switch to a coordinate system with variables $x-x'$ and $(x+x')/2$.

Before actually making this variable transformation, let us note a sleight of hand which we have glossed over. In modeling a given 1D chain, we can choose either to have periodic or open boundary conditions, although either way we ought to get the same result when we consider the limit of chain length going to infinity. Here we have mixed the two approaches: in assuming that $t_{\alpha\beta} = t\delta_{\alpha\beta}$, we argued using conservation of momentum along each chain, but that argument if made rigorous requires periodic boundary conditions. On the other hand, $t(x-x') = t\delta(x-x')$ requires open boundary conditions, since otherwise we would have $t(x-x') = t\sum_i \delta(x-x'-iL)$ where L is the length of the (periodic) chain. Since the two models coincide as $L\to\infty$, I will continue to use them interchangeably in this manner. The following coordinate transformation uses open boundary conditions, though the same result is of course obtained with periodic ones if $L\to\infty$, a limit which we will take in the calculations that follow.

With this caveat in mind, we can continue. Note that the Jacobian of the transformation $(x,x') \to (\frac{x+x'}{2}, x-x')$ has determinant -1, so there is no scaling factor needed for the new integration measure that appears here. If we assume the polymer has total length L, so that the integrals over x and x' run from $-L/2$ to $L/2$, then we should find the limits of integration in the new coordinates. Unfortunately, the integration region does not have

horizontal and vertical sides in the new coordinates, so we must order the two integrals carefully; the limits of the inner integral will depend on the value of the coordinate in the outer integral.

In the new coordinate system the region of integration is diamond-shaped. The ends of the diagonals are at $\pm L/2$ along $\frac{x+x'}{2}$ and at $\pm L$ along $x - x'$. To be explicit, we choose the outer integral to be over $x - x'$ and the inner to be over $\frac{x+x'}{2}$, in which case the integral over $x - x'$ runs from $-L$ to L, and the integral over the average coordinate runs from $(|x - x'| - L)/2$ to $(L - |x - x'|)/2$. Thus the integral over $\frac{x+x'}{2}$ gives a factor of $L - |x - x'|$ inside the $x - x'$ integral (because there is no explicit dependence on $x + x'$). Then for any function $f(x - x')$, we have the result that

$$\int_{-L/2}^{L/2}\int_{-L/2}^{L/2} dx\, dx'\ f(x - x') = \int_{-L}^{L}(L - |x|)f(x) \tag{4.148}$$

which in our particular case becomes

$$\begin{aligned}\langle J_e(\tau)J_e\rangle \approx\ & 2L\left(\frac{a_c q t}{2\pi\hbar}\right)^2 \sum_{j\alpha}\int dx\left[\langle\psi^\dagger_{j-1,\alpha}(x,\tau)\psi_{j-1,\alpha}(0)\rangle\langle\psi_{j,\alpha}(x,\tau)\psi^\dagger_{j,\alpha}(0)\rangle\right] \\ & - 2\left(\frac{a_c q t}{2\pi\hbar}\right)^2 \sum_{j\alpha}\int dx\left[|x|\times\langle\psi^\dagger_{j-1,\alpha}(x,\tau)\psi_{j-1,\alpha}(0)\rangle\langle\psi_{j,\alpha}(x,\tau)\psi^\dagger_{j,\alpha}(0)\rangle\right]\end{aligned} \tag{4.149}$$

Fortunately, the second term can be neglected. As we will see shortly, the correlation functions in the integrand are sharply peaked, going roughly as $(\cosh(\pi x/v\beta))^{-\gamma}$ where γ is at least 1. Thus at any location x where the integrand is not negligible, $|x|$ is on the order of $v\beta/\pi$. This means that as long as $v\beta/\pi \ll L$, we can neglect the second term completely. Since we consider the thermodynamic limit, that will be the case for all $T \neq 0$. Furthermore, to make the problem computationally tractable we will let the limits of the x integral go to $\pm\infty$; this approximation is valid if and only if the integral is exponentially small when $|x| > L$, which again is when $L \gg v\beta/\pi$. Thus the second term in equation (4.149) can always be dropped in any case in which our calculation is valid. To ensure that we can always drop the second term and also that we can extend the limits of the x integral to $\pm\infty$, we will henceforth assume that $v\beta/\pi \ll L$. We will therefore work with the expression

$$\langle J_e(\tau)J_e\rangle \approx 2L\left(\frac{a_c q t}{2\pi\hbar}\right)^2 \sum_{j\alpha}\int dx\left[\langle\psi^\dagger_{j-1,\alpha}(x,\tau)\psi_{j-1,\alpha}(0)\rangle\langle\psi_{j,\alpha}(x,\tau)\psi^\dagger_{j,\alpha}(0)\rangle\right] \tag{4.150}$$

Finally we should turn to known results from the literature for the correlation functions. $-\langle\psi_{j,\alpha}(x,\tau)\psi^\dagger_{j,\alpha}(0)\rangle$ is the single-particle Green's function, which is given by (see section 4.4):

$$G_\alpha(x,\tau) = -\frac{e^{i\alpha k_F x}}{2\pi a}\left[\frac{-ia}{\frac{v\beta}{\pi}\sinh\left(\frac{x-iv\tau}{v\beta/\pi}\right)}\right]^{\frac{\gamma-\alpha}{2}}\left[\frac{ia}{\frac{v\beta}{\pi}\sinh\left(\frac{x+iv\tau}{v\beta/\pi}\right)}\right]^{\frac{\gamma+\alpha}{2}} \tag{2.29}$$

where α on the RHS is either +1 for right-movers or -1 for left-movers and γ is a measure of interaction strength as defined in equation (2.11),

$$\gamma = \frac{K + K^{-1}}{2} \tag{2.11}$$

Recall that $\gamma = 1$ in the noninteracting limit and $\gamma > 1$ if there are either attractive or repulsive interactions.

It is critical to realize that the expression in equation (2.29) is the Green's function for an *isolated* Luttinger liquid; we are able to use this expression because we dropped the interchain hopping terms from the Hamiltonian appearing in the time evolution operator and the thermal density matrix.

We also need an expression for $\langle \psi^\dagger_{j,\alpha}(x,\tau)\psi_{j,\alpha}(0)\rangle$. This will look similar to the Green's function, equation (2.29), but not identical. The correct expression is

$$G_\alpha(-x,-\tau) = \frac{e^{-i\alpha k_F x}}{2\pi a}\left[\frac{ia}{\frac{v\beta}{\pi}\sinh\left(\frac{x-iv\tau}{v\beta/\pi}\right)}\right]^{\frac{\gamma-\alpha}{2}}\left[\frac{-ia}{\frac{v\beta}{\pi}\sinh\left(\frac{x+iv\tau}{v\beta/\pi}\right)}\right]^{\frac{\gamma+\alpha}{2}} \tag{4.151}$$

For a derivation, see section 4.4. We will call this function $\tilde{G}_\alpha(x,\tau)$. To summarize, we have:

$$-\langle \psi_{j\alpha}(x,\tau)\psi^\dagger_{j\alpha}(0)\rangle = G_\alpha(x,\tau) \tag{4.152a}$$

$$-\langle \psi^\dagger_{j\alpha}(x,\tau)\psi_{j\alpha}(0)\rangle = \tilde{G}_\alpha(x,\tau) = -G_\alpha(-x,-\tau) \tag{4.152b}$$

Substituting these into our expression for the current-current correlator, equation (4.150) becomes

$$\boxed{\langle J_e(\tau)J_e\rangle = -2N_cL\left(\frac{a_c q t}{2\pi\hbar}\right)^2 \sum_\alpha \int G_\alpha(x,\tau)G_\alpha(-x,-\tau)\,dx}\,, \tag{4.153}$$

where we have also summed over the chain index j to get a factor of N_c, the total number of chains. We could also replace the sum over α with a factor of 2, as done in the last line above. Physically, this is because for calculating the interchain conductivity, symmetry dictates that left- and right-movers along each chain must contribute equally. Mathematically, however, the fact that the integral does not depend on α is not immediately obvious, so we will leave the sum over α in place for now so that later in the calculation we can show precisely how α disappears.

The last step in calculating the current-current correlator is to substitute the actual expression for the Green's function as given in equation (2.29). (Note that this is also a possible branching point for future work; (4.153) can serve as a starting point for adding more features, such as disorder, to the model just by modifying the expression for the Green's function.)

$$\begin{aligned}\langle J_e(\tau)J_e\rangle &= -2N_cL\left(\frac{a_cqt}{2\pi\hbar}\right)^2\sum_\alpha\int G_\alpha(x,\tau)G_\alpha(-x,-\tau)dx\\ &= -2N_cL\left(\frac{a_cqt}{2\pi\hbar}\right)^2\frac{a^{2\gamma}}{(2\pi a)^2}\left(\frac{\pi}{v\beta}\right)^{2\gamma}\\ &\quad\times\sum_\alpha\int dx\left[\sinh\left(\frac{x+iv\tau}{v\beta/\pi}\right)\sinh\left(\frac{x-iv\tau}{v\beta/\pi}\right)\right]^{-\gamma}\left(\frac{\sinh\left(\frac{x-iv\tau}{v\beta/\pi}\right)}{\sinh\left(\frac{x+iv\tau}{v\beta/\pi}\right)}\right)^\alpha\end{aligned}$$

Now we'll make a substitution, $(x',\tau')=(\pi x/v\beta,\pi\tau/\beta)$, to get

$$\begin{aligned}\langle J_e(\tau')J_e\rangle &= -2N_cL\left(\frac{a_cqt}{2\pi\hbar}\right)^2\frac{a^{2\gamma}}{(2\pi a)^2}\left(\frac{\pi}{v\beta}\right)^{2\gamma-1}\\ &\quad\times\sum_\alpha\int dx'\left[\sinh\left(x'+i\tau'\right)\sinh\left(x'-i\tau'\right)\right]^{-\gamma}\left(\frac{\sinh\left(x'-i\tau'\right)}{\sinh\left(x'+i\tau'\right)}\right)^\alpha\end{aligned}$$

Using some trig identities, we can helpfully rewrite the integrand:

$$\begin{aligned}&= -2N_cL\left(\frac{a_cqt}{2\pi\hbar}\right)^2\frac{a^{2\gamma}}{(2\pi a)^2}\left(\frac{\pi}{v\beta}\right)^{2\gamma-1}\\ &\quad\times\sum_\alpha\int dx'\frac{\cos^2(\tau')\sinh^2(x')-\cosh^2(x')\sin^2(\tau')-i\frac{\alpha}{2}\sin(2\tau')\sinh(2x')}{\left[\frac{\cosh(2x')-\cos(2\tau')}{2}\right]^{\gamma+1}}\end{aligned}$$

The only term with α now vanishes because it is odd in x'. So we see that, as predicted based on physical grounds above, α vanishes from the expression.

$$= -4N_cL\left(\frac{a_cqt}{2\pi\hbar}\right)^2\frac{a^{2\gamma}2^{\gamma+1}}{(2\pi a)^2}\left(\frac{\pi}{v\beta}\right)^{2\gamma-1}\int dx'\frac{\cos^2(\tau')\sinh^2(x')-\cosh^2(x')\sin^2(\tau')}{[\cosh(2x')-\cos(2\tau')]^{\gamma+1}}$$

We can make the integral over x look a bit nicer by writing the numerator in terms of $2\tau'$ to match the denominator, which gives

$$\langle J_e(\tau')J_e\rangle = 4N_cL\left(\frac{a_cqt}{2\pi\hbar}\right)^2\frac{a^{2\gamma}2^{\gamma}}{(2\pi a)^2}\left(\frac{\pi}{v\beta}\right)^{2\gamma-1}\int dx'\frac{1-\cos(2\tau')\cosh(2x')}{[\cosh(2x')-\cos(2\tau')]^{\gamma+1}} \tag{4.154}$$

or, rearranging the prefactor a little bit to clean up the expression,

$$\boxed{\langle J_e(\tau')J_e\rangle = 4N_cL\left(\frac{a_cqt}{2\pi\hbar}\right)^2\frac{2^{\gamma}a}{(2\pi a)^2}\left(\frac{\pi a}{v\beta}\right)^{2\gamma-1}\int dx'\frac{1-\cos(2\tau')\cosh(2x')}{[\cosh(2x')-\cos(2\tau')]^{\gamma+1}}} \tag{4.155}$$

Note that α vanished from our expressions just as we expected it would.

The integral over x' can be done exactly (we have used the commercial software Wolfram Mathematica) if the limits of integration are $-\infty$ and ∞. It is easiest to break the integrand into two pieces with different x dependence. Both are of the form

$$\int_{-\infty}^{\infty} \frac{\cosh(nx)}{(\cosh(2x)-\cos(2\tau))^{\gamma+1}} dx \tag{4.156}$$

with $n = 0$ or 2. For use both here and in the calculations for thermal conductivity and thermopower, we will use a slightly more general result, as follows:

$$\int_{-\infty}^{\infty} \frac{\cosh(nx)}{(\cosh(2x)-\cos(2\tau))^{\gamma+m}} dx = 2^{\gamma+m-1}\left(f(\gamma,\tau,m-\frac{n}{2},m)+f(\gamma,\tau,m+\frac{n}{2},m)\right) \tag{4.157}$$

as long as $n > 2(\gamma+m)$, where

$$f(\gamma,\tau,n,m) = \frac{F_1(\gamma+n;\gamma+m,\gamma+m;\gamma+n+1;e^{2i\tau},e^{-2i\tau})}{\gamma+n} \tag{4.158}$$

and $F_1(a;b_1,b_2;c;x,y)$ is the first Appell hypergeometric function[82, §16.13]. Note that the function f also has a relatively simple and convenient integral representation, namely

$$f(\gamma,\tau,n,m) = \int_0^1 t^{\gamma+n-1}(1-2t\cos(2\tau)+t^2)^{-(\gamma+m)}\, dt \tag{4.159}$$

This integral representation is derived from a similar one for F_1 in section 4.7.

Using equation (4.157), when we compute our two separate integrals over x, we get:

$$\int_{-\infty}^{\infty} \frac{1}{(\cosh(2x)-\cos(2\tau))^{\gamma+1}} dx = 2^{\gamma+1} f(\gamma,\tau,1,1) \tag{4.160a}$$

$$\int_{-\infty}^{\infty} \frac{\cosh(2x)}{(\cosh(2x)-\cos(2\tau))^{\gamma+1}} dx = 2^{\gamma}\left(f(\gamma,\tau,0,1)+f(\gamma,\tau,2,1)\right) \tag{4.160b}$$

Substituting these results into equation (4.155), we get:

$$\begin{aligned}\langle J_e(\tau')J_e\rangle =& 4N_cL\left(\frac{a_cqt}{2\pi\hbar}\right)^2 \frac{2^{2\gamma}a}{(2\pi a)^2}\left(\frac{\pi a}{v\beta}\right)^{2\gamma-1} \\ &\times\left(2f(\gamma,\tau',1,1)-\cos(2\tau')\left(f(\gamma,\tau',0,1)+f(\gamma,\tau',2,1)\right)\right)\end{aligned} \tag{4.161}$$

Again rearranging to clean up the prefactor, we have an explicit expression for the correlator in terms of the scaled imaginary time, τ':

$$\boxed{\begin{aligned}\langle J_e(\tau')J_e\rangle =& 4N_cL\left(\frac{a_cqt}{2\pi\hbar}\right)^2\frac{2a}{(2\pi a)^2}\left(\frac{2\pi a}{v\beta}\right)^{2\gamma-1}\\ &\times\left(2f(\gamma,\tau',1,1)-\cos(2\tau')\big(f(\gamma,\tau',0,1)+f(\gamma,\tau',2,1)\big)\right)\end{aligned}} \tag{4.162}$$

The units provide a quick check on the validity of this expression. The combination $a/v\beta$ is unitless if $\hbar = 1$. Likewise N_cLa/a^2 is unitless, as is F_1. All that remains is $\left(\frac{a_cqt}{\hbar}\right)^2$, which has units of (Coulomb meters/second)^2, and Coulomb meters/second is precisely the correct unit for electrical current.

Asymptotic behavior for small τ':

In section 4.1 above, we discuss the origin of numerical error in our results for the transport coefficients. That error comes from the numerical integration of the current-current correlation functions, so we need to know the rough order of magnitude of the size of those integrals. The function $\langle J_e(\tau')J_e\rangle$ diverges at $\tau' = 0$ and π, and these poles give the dominant contribution to the integral from ϵ to $\pi - \epsilon$ when the cutoff ϵ is much less than 1. To find the exact scaling with ϵ, we therefore need the asymptotic behavior of $\langle J_e(\tau')J_e\rangle$ for τ' near 0 and π. Since the function is symmetric about $\tau' = \pi/2$, we can in fact look at just $\tau' \approx 0$. We now examine $\langle J_e(\tau')J_e\rangle$ in that limit.

The divergence of $\langle J_e(\tau')J_e\rangle$ as $\tau' \to 0$ comes from the divergence of the integrand in equation (4.155) when $x \approx 0$. We can thus approximate the contribution of the pole to the current-current correlator by taking a lowest order approximation of the integrand in both x' and τ', which gives

$$\int dx' \frac{1-\cos(2\tau')\cosh(2x')}{[\cosh(2x')-\cos(2\tau')]^{\gamma+1}} \approx 2^{-\gamma}\int dx' \frac{(\tau')^2-(x')^2}{[(x')^2+(\tau')^2]^{\gamma+1}} \propto (\tau')^{1-2\gamma}. \tag{4.163}$$

Thus we conclude that for small τ', $\langle J_e(\tau')J_e\rangle \propto (\tau')^{1-2\gamma}$. Then integrating over τ' from ϵ to $\pi - \epsilon$, the contribution from the pole at $\tau' = 0$ is proportional to $\epsilon^{2-2\gamma}$. This is the fact used in our error approximation in section 4.1.

$\langle J_E(\tau)J_E(0)\rangle$

This calculation is similar to the one for $\langle J_e(\tau)J_e\rangle$, though the more complicated expression for J_E compared with J_e results in rather messier algebra. As a reminder before beginning

the calculation, the expression we derived for the energy current is

$$J_E = \frac{ia_c v}{2\hbar} \sum_{j\alpha\beta} \int t_{\alpha\beta}(x'-x) \begin{bmatrix} \left([\nabla_j]^\alpha_{x'} + [\nabla_{j-1}]^\beta_x\right) \psi^\dagger_{j\alpha}(x')\psi_{j-1,\beta}(x) \\ \\ -\left([\nabla_{j-1}]^\alpha_{x'} + [\nabla_j]^\beta_x\right) \psi^\dagger_{j-1,\alpha}(x')\psi_{j\beta}(x) \end{bmatrix} dx\, dx' \quad (2.26b)$$

Again we will not give the time dependence explicitly, so we can immediately begin the calculation:

$$\langle J_E(\tau) J_E\rangle = \sum_{ij} \sum_{\alpha\beta\gamma\delta} \int dx_1\, dx_2\, dx_3\, dx_4 \left(\frac{a_c v}{2\hbar}\right)^2 t_{\alpha\beta}(x_1-x_2) t_{\gamma\delta}(x_3-x_4) \langle \cdots \rangle \quad (4.164)$$

$$\langle \cdots \rangle = \left\langle \begin{array}{c} e^{\tau H} \begin{bmatrix} \left([\nabla_i]^\alpha_{x_1} + [\nabla_{i-1}]^\beta_{x_2}\right) \psi^\dagger_{i\alpha}(x_1)\psi_{i-1,\beta}(x_2) \\ -\left([\nabla_{i-1}]^\alpha_{x_1} + [\nabla_i]^\beta_{x_2}\right) \psi^\dagger_{i-1,\alpha}(x_1)\psi_{i\beta}(x_2) \end{bmatrix} e^{-\tau H} \\ \times \begin{bmatrix} \left([\nabla_{j-1}]^\gamma_{x_3} + [\nabla_j]^\delta_{x_4}\right) \psi^\dagger_{j-1,\gamma}(x_3)\psi_{j,\delta}(x_4) \\ -\left([\nabla_j]^\gamma_{x_3} + [\nabla_{j-1}]^\delta_{x_4}\right) \psi^\dagger_{j,\gamma}(x_3)\psi_{j-1,\delta}(x_4) \end{bmatrix} \end{array} \right\rangle$$

$$= \left\langle \begin{array}{c} e^{\tau H} \left([\nabla_i]^\alpha_{x_1} + [\nabla_{i-1}]^\beta_{x_2}\right) \psi^\dagger_{i\alpha}(x_1)\psi_{i-1,\beta}(x_2) e^{-\tau H} \\ \times \left([\nabla_{j-1}]^\gamma_{x_3} + [\nabla_j]^\delta_{x_4}\right) \psi^\dagger_{j-1,\gamma}(x_3)\psi_{j\delta}(x_4) \\ \\ + e^{\tau H} \left([\nabla_{i-1}]^\alpha_{x_1} + [\nabla_i]^\beta_{x_2}\right) \psi^\dagger_{i-1,\alpha}(x_1)\psi_{i,\beta}(x_2) e^{-\tau H} \\ \times \left([\nabla_j]^\gamma_{x_3} + [\nabla_{j-1}]^\delta_{x_4}\right) \psi^\dagger_{j\gamma}(x_3)\psi_{j-1,\delta}(x_4) \end{array} \right\rangle$$

Note that $\alpha = \delta$ and $\beta = \gamma$ in order to conserve the number of left- and right-movers (mathematically this follows from the presence of the Klein factors, U)

$$= \delta_{ij}\delta_{\alpha\delta}\delta_{\beta\gamma} \left\langle \begin{array}{c} e^{\tau H} \left([\nabla_j]^\alpha_{x_1} + [\nabla_{j-1}]^\beta_{x_2}\right) \psi^\dagger_{j\alpha}(x_1)\psi_{j-1,\beta}(x_2) e^{-\tau H} \\ \times \left([\nabla_{j-1}]^\beta_{x_3} + [\nabla_j]^\alpha_{x_4}\right) \psi^\dagger_{j-1,\beta}(x_3)\psi_{j\alpha}(x_4) \\ \\ + e^{\tau H} \left([\nabla_{j-1}]^\alpha_{x_1} + [\nabla_j]^\beta_{x_2}\right) \psi^\dagger_{j-1,\alpha}(x_1)\psi_{j,\beta}(x_2) e^{-\tau H} \\ \times \left([\nabla_j]^\beta_{x_3} + [\nabla_{j-1}]^\alpha_{x_4}\right) \psi^\dagger_{j\beta}(x_3)\psi_{j-1,\alpha}(x_4) \end{array} \right\rangle$$

$$= 2\delta_{ij}\delta_{\alpha\delta}\delta_{\beta\gamma} \left\langle \begin{array}{c} e^{\tau H} \left([\nabla_j]^\alpha_{x_1} + [\nabla_{j-1}]^\beta_{x_2}\right) \psi^\dagger_{j\alpha}(x_1)\psi_{j-1,\beta}(x_2) e^{-\tau H} \\ \times \left([\nabla_{j-1}]^\beta_{x_3} + [\nabla_j]^\alpha_{x_4}\right) \psi^\dagger_{j-1,\beta}(x_3)\psi_{j\alpha}(x_4) \end{array} \right\rangle$$

because the only difference between the two terms was $j \leftrightarrow j-1$

$$
\begin{aligned}
&= 2\delta_{ij}\delta_{\alpha\delta}\delta_{\beta\gamma} \left\langle \begin{array}{l} e^{\tau H}[\nabla_j]^\alpha_{x_1}\psi^\dagger_{j,\alpha}(x_1)\psi_{j-1,\beta}(x_2)e^{-\tau H}[\nabla_{j-1}]^\beta_{x_3}\psi^\dagger_{j-1,\beta}(x_3)\psi_{j\alpha}(x_4) \\ + e^{\tau H}[\nabla_{j-1}]^\beta_{x_2}\psi^\dagger_{j\alpha}(x_1)\psi_{j-1,\beta}(x_2)e^{-\tau H}[\nabla_{j-1}]^\beta_{x_3}\psi^\dagger_{j-1,\beta}(x_3)\psi_{j\alpha}(x_4) \\ + e^{\tau H}[\nabla_j]^\alpha_{x_1}\psi^\dagger_{j\alpha}(x_1)\psi_{j-1,\beta}(x_2)e^{-\tau H}[\nabla_j]^\alpha_{x_4}\psi^\dagger_{j-1,\beta}(x_3)\psi_{j\alpha}(x_4) \\ + e^{\tau H}[\nabla_{j-1}]^\beta_{x_2}\psi^\dagger_{j\alpha}(x_1)\psi_{j-1,\beta}(x_2)e^{-\tau H}[\nabla_j]^\alpha_{x_4}\psi^\dagger_{j-1,\beta}(x_3)\psi_{j\alpha}(x_4) \end{array} \right\rangle \\
&= 2\delta_{ij}\delta_{\alpha\delta}\delta_{\beta\gamma} \left[\begin{array}{l} \langle e^{\tau H}[\nabla_j]^\alpha_{x_1}\psi^\dagger_{j,\alpha}(x_1)\psi_{j-1,\beta}(x_2)e^{-\tau H}[\nabla_{j-1}]^\beta_{x_3}\psi^\dagger_{j-1,\beta}(x_3)\psi_{j\alpha}(x_4)\rangle \\ + \langle e^{\tau H}[\nabla_{j-1}]^\beta_{x_2}\psi^\dagger_{j\alpha}(x_1)\psi_{j-1,\beta}(x_2)e^{-\tau H}[\nabla_{j-1}]^\beta_{x_3}\psi^\dagger_{j-1,\beta}(x_3)\psi_{j\alpha}(x_4)\rangle \\ + \langle e^{\tau H}[\nabla_j]^\alpha_{x_1}\psi^\dagger_{j\alpha}(x_1)\psi_{j-1,\beta}(x_2)e^{-\tau H}[\nabla_j]^\alpha_{x_4}\psi^\dagger_{j-1,\beta}(x_3)\psi_{j\alpha}(x_4)\rangle \\ + \langle e^{\tau H}[\nabla_{j-1}]^\beta_{x_2}\psi^\dagger_{j\alpha}(x_1)\psi_{j-1,\beta}(x_2)e^{-\tau H}[\nabla_j]^\alpha_{x_4}\psi^\dagger_{j-1,\beta}(x_3)\psi_{j\alpha}(x_4)\rangle \end{array} \right] \\
&= 2\delta_{ij}\delta_{\alpha\delta}\delta_{\beta\gamma} \left[\begin{array}{l} \langle [\nabla_j]^\alpha_{x_1,\tau}\psi^\dagger_{j\alpha}(x_1,\tau)\psi_{j\alpha}(x_4)\rangle\langle \psi_{j-1,\beta}(x_2,\tau)[\nabla_{j-1}]^\beta_{x_3}\psi^\dagger_{j-1,\beta}(x_3)\rangle \\ + \langle [\nabla_{j-1}]^\beta_{x_2,\tau}\psi_{j-1,\beta}(x_2,\tau)[\nabla_{j-1}]^\beta_{x_3}\psi^\dagger_{j-1,\beta}(x_3)\rangle\langle \psi^\dagger_{j\alpha}(x_1,\tau)\psi_{j\alpha}(x_4)\rangle \\ + \langle [\nabla_j]^\alpha_{x_1,\tau}\psi^\dagger_{j\alpha}(x_1,\tau)[\nabla_j]^\alpha_{x_4}\psi_{j\alpha}(x_4)\rangle\langle \psi_{j-1,\beta}(x_2,\tau)\psi^\dagger_{j-1,\beta}(x_3)\rangle \\ + \langle [\nabla_{j-1}]^\beta_{x_2,\tau}\psi_{j-1,\beta}(x_2,\tau)\psi^\dagger_{j-1,\beta}(x_3)\rangle\langle \psi^\dagger_{j\alpha}(x_1,\tau)[\nabla_j]^\alpha_{x_4}\psi_{j\alpha}(x_4)\rangle \end{array} \right]
\end{aligned}
\tag{4.165}
$$

There are eight distinct types of two-point functions that appear in the expression: $\langle\psi^\dagger\psi\rangle$, $\langle[\nabla]\psi^\dagger\psi\rangle$, $\langle\psi^\dagger[\nabla]\psi\rangle$, $\langle[\nabla]\psi^\dagger[\nabla]\psi\rangle$, $\langle\psi\psi^\dagger\rangle$, $\langle[\nabla]\psi\psi^\dagger\rangle$, $\langle\psi[\nabla]\psi^\dagger\rangle$, and $\langle[\nabla]\psi[\nabla]\psi^\dagger\rangle$. Two of these we already know in terms of the single-chain Green's function from our calculation of $\langle J_e(\tau)J_e\rangle$ above,

$$-\langle\psi_{j\alpha}(x,\tau)\psi^\dagger_{j\alpha}(0)\rangle = G_\alpha(x,\tau) \tag{4.152a}$$

$$-\langle\psi^\dagger_{j\alpha}(x,\tau)\psi_{j\alpha}(0)\rangle = \tilde{G}_\alpha(x,\tau) = -G_\alpha(-x,-\tau) \tag{4.152b}$$

The remaining two-point functions can be calculated as derivatives of the Green's function. To demonstrate this, we first recall the definition of $[\nabla_j]^\alpha_x$:

$$[\nabla_j]^\alpha_y = \alpha\frac{K}{\hbar}\nabla\theta_j(y) - \frac{\hbar}{K}\nabla\phi_j(y) = \nabla_y\left[\alpha\frac{K}{\hbar}\theta_j(y) - \frac{\hbar}{K}\phi_j(y)\right] \tag{4.141}$$

We can split this into right- and left-moving parts, those being proportional to $\alpha\phi-\theta$ and $-\alpha\phi-\theta$ (which one is which depends on whether α is ±1). Doing so gives

$$[\nabla_j]^\alpha_y = -\frac{\alpha}{2}\nabla_y\left[\left(\frac{K}{\hbar}+\frac{\hbar}{K}\right)(\alpha\phi_j-\theta_j) + \left(\frac{K}{\hbar}-\frac{\hbar}{K}\right)(-\alpha\phi_j-\theta_j)\right] \tag{4.166}$$

To check this, recall that $\alpha=\pm1$, so $\alpha^2=1$. At this point, we can drop the chain index j because each two-point function we are evaluating contains operators for only a single chain

and is independent of which chain that happens to be. Continuing with the calculation, we will want two useful lemmas,

$$\nabla_x(\alpha\phi(x) - \theta(x))\psi_\alpha^\dagger(x) = -ie^{-i\alpha k_F x}\nabla_x(e^{i\alpha k_F x}\psi_\alpha^\dagger(x)) \tag{4.167a}$$

$$\nabla_x(\alpha\phi(x) - \theta(x))\psi_\alpha(x) = ie^{i\alpha k_F x}\nabla_x(e^{-i\alpha k_F x}\psi_\alpha(x)) \tag{4.167b}$$

These can be confirmed by writing out the expression for the fermion operators in terms of the boson operators θ and ϕ.

We are now finally ready to compute the six remaining two-point function. We first complete the computation for $\tau = 0$ and then make an argument that the time-evolution only has the effect of changing $G_\alpha(x, 0)$ to $G_\alpha(x, \tau)$.

As a representative example, we will start by calculating $\langle[\nabla]_x^\alpha\psi_\alpha^\dagger(x)\psi_\alpha(x')\rangle$. Using equation (4.166), this splits into two terms,

$$\begin{aligned}\langle[\nabla]_x^\alpha\psi_\alpha^\dagger(x)\psi_\alpha(x')\rangle = \frac{\alpha}{2}\left(\frac{K}{\hbar} + \frac{\hbar}{K}\right)\langle\nabla_x(\alpha\phi - \theta)\psi_\alpha^\dagger(x)\psi_\alpha(x')\rangle \\ - \frac{\alpha}{2}\left(\frac{K}{\hbar} - \frac{\hbar}{K}\right)\langle\nabla_x(-\alpha\phi - \theta)\psi_\alpha^\dagger(x)\psi_\alpha(x')\rangle\end{aligned} \tag{4.168}$$

The first term features a factor $\langle\nabla_x(\alpha\phi - \theta)\psi_\alpha^\dagger(x)\psi_\alpha(x')\rangle$, with $\alpha\phi - \theta$, while the second contains $\langle\nabla_x(-\alpha\phi - \theta)\psi_\alpha^\dagger(x)\psi_\alpha(x')\rangle$, with $-\alpha\phi - \theta$. We will later argue that averages of the second type, containing $(-\alpha\phi - \theta)$, will be either 0 or higher order in $v\beta/L$ and hence negligible. For now, we will explicitly calculate expectation values of the first type, containing the combination $(\alpha\phi - \theta)$. The calculations rely heavily on the lemmas (4.167).

We begin with the expectation value $\langle\nabla_x(\alpha\phi - \theta)\psi_\alpha^\dagger(x)\psi_\alpha(x')\rangle$ and three others that are

very similar to it:

$$\begin{aligned}
\langle \nabla_x(\alpha\phi-\theta)\psi_\alpha^\dagger(x)\psi_\alpha(x')\rangle &= \langle \nabla_x(\alpha\phi-\theta)\psi_\alpha^\dagger(x)\psi_\alpha(x')\rangle \\
&= \langle -ie^{-i\alpha k_F x}\nabla_x(e^{i\alpha k_F x}\psi_\alpha^\dagger(x))\psi_\alpha(x')\rangle \\
&= -ie^{-i\alpha k_F x}\nabla_x\left(e^{i\alpha k_F x}\langle\psi_\alpha^\dagger(x)\psi_\alpha(x')\rangle\right) \\
&= ie^{-i\alpha k_F x}\nabla_x\left(e^{i\alpha k_F x}\tilde{G}_\alpha(x-x')\right) \\
&= -\alpha k_F\tilde{G}_\alpha(x-x') + i\partial_x\tilde{G}_\alpha(x-x') \\
\langle \psi_\alpha^\dagger(x)\nabla_{x'}(\alpha\phi-\theta)\psi_\alpha(x')\rangle &= \left\langle \psi_\alpha^\dagger(x)\left(ie^{i\alpha k_F x'}\nabla_{x'}(e^{-i\alpha k_F x'}\psi_\alpha(x'))\right)\right\rangle \\
&= ie^{i\alpha k_F x'}\nabla_{x'}\left(e^{-i\alpha k_F x'}\langle\psi_\alpha^\dagger(x)\psi_\alpha(x')\rangle\right) \\
&= -ie^{i\alpha k_F x'}\nabla_{x'}\left(e^{-i\alpha k_F x'}\tilde{G}_\alpha(x-x')\right) \\
&= -\alpha k_F\tilde{G}_\alpha(x-x') - i\partial_{x'}\tilde{G}_\alpha(x-x') \\
&= -\alpha k_F\tilde{G}_\alpha(x-x') + i\partial_x\tilde{G}_\alpha(x-x') \\
\langle \psi_\alpha(x)\nabla_{x'}(\alpha\phi-\theta)\psi_\alpha^\dagger(x')\rangle &= \left\langle \psi_\alpha(x)\left(-ie^{-i\alpha k_F x'}\nabla_{x'}(e^{i\alpha k_F x'}\psi_\alpha^\dagger(x'))\right)\right\rangle \\
&= -ie^{-i\alpha k_F x'}\nabla_{x'}\left(e^{i\alpha k_F x'}\langle\psi_\alpha(x)\psi_\alpha^\dagger(x')\rangle\right) \\
&= +ie^{-i\alpha k_F x'}\nabla_{x'}\left(e^{i\alpha k_F x'}G_\alpha(x-x')\right) \\
&= -\alpha k_F G_\alpha(x-x') + i\partial_{x'}G_\alpha(x-x') \\
&= -\alpha k_F G_\alpha(x-x') - i\partial_x G_\alpha(x-x') \\
\langle \nabla_x(\alpha\phi-\theta)\psi_\alpha(x)\psi_\alpha^\dagger(x')\rangle &= \left\langle \left(ie^{i\alpha k_F x}\nabla_x(e^{-i\alpha k_F x}\psi_\alpha(x))\right)\psi_\alpha^\dagger(x')\right\rangle \\
&= ie^{i\alpha k_F x}\nabla_x\left(e^{-i\alpha k_F x}\langle\psi_\alpha(x)\psi_\alpha^\dagger(x')\rangle\right) \\
&= -ie^{i\alpha k_F x}\nabla_x\left(e^{-i\alpha k_F x}G_\alpha(x-x')\right) \\
&= -\alpha k_F G_\alpha(x-x') - i\partial_x G_\alpha(x-x')
\end{aligned}$$

The calculations for the expectation values from the $\langle[\nabla]\psi^\dagger[\nabla]\psi\rangle$ and $\langle[\nabla]\psi[\nabla]\psi^\dagger\rangle$ expres-

sions are similar though a little more involved:

$$\begin{aligned}
&\langle \nabla_x(\alpha\phi-\theta)\psi_\alpha(x)\nabla_{x'}(\alpha\phi-\theta)\psi_\alpha^\dagger(x')\rangle \\
&\quad= \left\langle \left(ie^{i\alpha k_F x}\nabla_x(e^{-i\alpha k_F x}\psi_\alpha(x))\right)\left(-ie^{-i\alpha k_F x'}\nabla_{x'}(e^{i\alpha k_F x'}\psi_\alpha^\dagger(x'))\right)\right\rangle \\
&\quad= e^{i\alpha k_F(x-x')}\nabla_x\nabla_{x'}\left(e^{i\alpha k_F(x'-x)}\langle\psi_\alpha(x)\psi_\alpha^\dagger(x')\rangle\right) \\
&\quad= -e^{i\alpha k_F(x-x')}\nabla_x\nabla_{x'}\left(e^{i\alpha k_F(x'-x)}G_\alpha(x-x')\right) \\
&\quad= -e^{i\alpha k_F(x-x')}\nabla_x\left[i\alpha k_F e^{i\alpha k_F(x'-x)}G_\alpha(x-x')+e^{i\alpha k_F(x'-x)}\partial_{x'}G_\alpha(x-x')\right] \\
&\quad= -e^{i\alpha k_F(x-x')}\left[\begin{array}{l}(\alpha k_F)^2 e^{i\alpha k_F(x'-x)}G_\alpha(x-x')+i\alpha k_F e^{i\alpha k_F(x'-x)}\partial_x G_\alpha(x-x') \\ -iak_F e^{i\alpha k_F(x'-x)}\partial_{x'}G_\alpha(x-x')+e^{i\alpha k_F(x'-x)}\partial_x\partial_{x'}G_\alpha(x-x')\end{array}\right] \\
&\quad= -(\alpha k_F)^2 G_\alpha(x-x')-2i\alpha k_F\partial_x G_\alpha(x-x')+\partial_x^2 G_\alpha(x-x') \\
&\langle \nabla_x(\alpha\phi-\theta)\psi_\alpha^\dagger(x)\nabla_{x'}(\alpha\phi-\theta)\psi_\alpha(x')\rangle \\
&\quad= \left\langle \left(-ie^{-i\alpha k_F x}\nabla_x(e^{i\alpha k_F x}\psi_\alpha^\dagger(x))\right)\left(ie^{i\alpha k_F x'}\nabla_{x'}(e^{-i\alpha k_F x'}\psi_\alpha(x'))\right)\right\rangle \\
&\quad= e^{i\alpha k_F(x'-x)}\nabla_x\nabla_{x'}\left(e^{i\alpha k_F(x-x')}\langle\psi_\alpha^\dagger(x)\psi_\alpha(x')\rangle\right) \\
&\quad= -e^{i\alpha k_F(x'-x)}\nabla_x\nabla_{x'}\left(e^{i\alpha k_F(x-x')}\tilde{G}_\alpha(x-x')\right) \\
&\quad= -e^{i\alpha k_F(x'-x)}\nabla_x\left[-i\alpha k_F e^{i\alpha k_F(x-x')}\tilde{G}_\alpha(x-x')+e^{i\alpha k_F(x-x')}\partial_{x'}\tilde{G}_\alpha(x-x')\right] \\
&\quad= -e^{i\alpha k_F(x'-x)}\left[\begin{array}{l}(\alpha k_F)^2 e^{i\alpha k_F(x-x')}\tilde{G}_\alpha(x-x')-i\alpha k_F e^{i\alpha k_F(x-x')}\partial_x\tilde{G}_\alpha(x-x') \\ +iak_F e^{i\alpha k_F(x-x')}\partial_{x'}\tilde{G}_\alpha(x-x')+e^{i\alpha k_F(x-x')}\partial_x\partial_{x'}\tilde{G}_\alpha(x-x')\end{array}\right] \\
&\quad= -(\alpha k_F)^2\tilde{G}_\alpha(x-x')+2i\alpha k_F\partial_x\tilde{G}_\alpha(x-x')+\partial_x^2\tilde{G}_\alpha(x-x')
\end{aligned}$$

Here we summarize our results so far:

$$-\left\langle\psi_\alpha(x)\psi_\alpha^\dagger(x')\right\rangle = G_\alpha(x-x') \tag{4.169a}$$

$$-\left\langle\psi_\alpha^\dagger(x)\psi_\alpha(x')\right\rangle = \tilde{G}_\alpha(x-x') \tag{4.169b}$$

$$-\left\langle(\alpha\nabla\phi-\nabla\theta)_x\psi_\alpha(x)\psi_\alpha^\dagger(x')\right\rangle = \alpha k_F G_\alpha(x-x')+i\partial_x G_\alpha(x-x') \tag{4.169c}$$

$$-\left\langle(\alpha\nabla\phi-\nabla\theta)_x\psi_\alpha^\dagger(x)\psi_\alpha(x')\right\rangle = \alpha k_F\tilde{G}_\alpha(x-x')-i\partial_x\tilde{G}_\alpha(x-x') \tag{4.169d}$$

$$-\left\langle\psi_\alpha(x)(\alpha\nabla\phi-\nabla\theta)_{x'}\psi_\alpha^\dagger(x')\right\rangle = \alpha k_F G_\alpha(x-x')+i\partial_x G_\alpha(x-x') \tag{4.169e}$$

$$-\left\langle\psi_\alpha^\dagger(x)(\alpha\nabla\phi-\nabla\theta)_{x'}\psi_\alpha(x')\right\rangle = \alpha k_F\tilde{G}_\alpha(x-x')-i\partial_x\tilde{G}_\alpha(x-x') \tag{4.169f}$$

$$\begin{aligned}-\left\langle(\alpha\nabla\phi-\nabla\theta)_x\psi_\alpha(x)(\alpha\nabla\phi-\nabla\theta)_{x'}\psi_\alpha^\dagger(x')\right\rangle &= (\alpha k_F)^2 G_\alpha(x-x')+2i\alpha k_F\partial_x G_\alpha(x-x') \\ &\quad-\partial_x^2 G_\alpha(x-x')\end{aligned} \tag{4.169g}$$

$$\begin{aligned}-\left\langle(\alpha\nabla\phi-\nabla\theta)_x\psi_\alpha^\dagger(x)(\alpha\nabla\phi-\nabla\theta)_{x'}\psi_\alpha(x')\right\rangle &= (\alpha k_F)^2\tilde{G}_\alpha(x-x')-2i\alpha k_F\partial_x\tilde{G}_\alpha(x-x') \\ &\quad-\partial_x^2\tilde{G}_\alpha(x-x')\end{aligned} \tag{4.169h}$$

Notice the useful fact that for the two-point functions with one factor of $(\alpha\nabla\phi-\nabla\theta)$, it does not matter whether that acts on the first or second fermion operator.

This completes our calculation of the expectation values containing $(\alpha\phi - \theta)$, but what about those containing $(-\alpha\phi - \theta)$? For the most part these terms will be 0. Look, for instance, at

$$\langle(-\alpha\nabla_x\phi(x,t) - \nabla_x\theta(x,t))\psi_\alpha(x,t)\psi_\alpha(x')\rangle \tag{4.170}$$

This can be evaluated in a path integral formalism, integrating over the two functions ϕ and θ. The action breaks into two pieces, one for right-movers and one for left-movers, $S = S_R + S_L$, or equivalently $S = S_\alpha + S_{-\alpha}$. S_α depends on ϕ and θ only in the combination $\alpha\phi - \theta$, while $S_{-\alpha}$ contains only $-\alpha\phi - \theta$. Then the expectation value also breaks into two separate pieces:

$$\left\langle(-\alpha\nabla_x\phi(x,t) - \nabla_x\theta(x,t))\psi_\alpha(x,t)\psi_\alpha(x')\right\rangle = \langle(-\alpha\nabla_x\phi(x,t) - \nabla_x\theta(x,t))\rangle_{-\alpha}\left\langle\psi_\alpha(x,t)\psi_\alpha(x')\right\rangle_\alpha \tag{4.171}$$

where $\langle\cdot\rangle_\alpha$ is evaluated with respect to the action S_α and likewise $\langle\cdot\rangle_{-\alpha}$ is evaluated with respect to the action $S_{-\alpha}$. But $S_{-\alpha}$ is invariant under the transformation $-\alpha\phi(x) - \theta(x) \to -(-\alpha\phi(x) - \theta(x))$, so the integrand in $\langle(-\alpha\nabla_x\phi(x,t) - \nabla_x\theta(x,t))\rangle_{-\alpha}$ is overall odd in $-\alpha\phi - \theta$ and hence vanishes. This means that indeed

$$\langle(-\alpha\nabla_x\phi(x,t) - \nabla_x\theta(x,t))\psi_\alpha(x,t)\psi_\alpha(x')\rangle = 0 \tag{4.172}$$

The same argument also applies to the expectation values from $\langle[\nabla]\psi^\dagger[\nabla]\psi\rangle$ and $\langle[\nabla]\psi[\nabla]\psi^\dagger\rangle$ that have $(\alpha\nabla\phi - \nabla\theta)$ acting on one fermion operator and $(-\alpha\nabla\phi - \nabla\theta)$ acting on the other.

The only possible exception to this argument is when there are two factors of $(-\alpha\nabla\phi - \nabla\theta)$. In general if the two factors are at different values of x, then it is still possible to perform a transformation in the correlation function path integral where the signs are flipped at x but not x', and the integrand is odd under such a transformation and thus again gives 0. However, if $x = x'$, this logic may not apply, so terms $\langle[\nabla]\psi^\dagger[\nabla]\psi\rangle$ with two factors of $-\alpha\nabla\phi - \nabla\theta$ may give a contribution proportional to $\delta(x - x')$. However, these terms may still be ignored because the expectation value $\langle(-\alpha\nabla\phi(x) - \nabla\theta(x))^2\rangle$ is finite, so that the "delta function" has finite weight at $x = x'$ and thus doesn't contribute when we integrate over x and x'. (It it a finite contribution on a set of measure 0 in the integration domain.)

We have thus far glossed over one potentially important part of our expression, namely the (imaginary-) time dependence. What we really want to calculate is not just, for instance, $\langle[\nabla]^\alpha_x\psi^\dagger_\alpha(x)\psi_\alpha(x')\rangle$, but rather $\langle[\nabla]^\alpha_{x,\tau}\psi^\dagger_\alpha(x,\tau)\psi_\alpha(x')\rangle$. First, note that $[\nabla]^\alpha_{x,\tau}$ is just the time evolution of $[\nabla]^\alpha_x$, or

$$[\nabla_j]^\alpha_{y,\tau} = \alpha\frac{K}{\hbar}\nabla\theta_j(y,\tau) - \frac{\hbar}{K}\nabla\phi_j(y,\tau) = \nabla_y\left[\alpha\frac{K}{\hbar}\theta_j(y,\tau) - \frac{\hbar}{K}\phi_j(y,\tau)\right] \tag{4.173}$$

This change alters neither our calculational procedure nor the form of the results. For example, looking at $\langle[\nabla]^\alpha_{x,\tau}\psi^\dagger_\alpha(x,\tau)\psi_\alpha(x')\rangle$ instead of $\langle[\nabla]^\alpha_x\psi^\dagger_\alpha(x)\psi_\alpha(x')\rangle$, the difference is that the left-hand side of equation (4.169c) will be replaced with

$$\langle(\alpha\nabla_x\phi(x,\tau) - \nabla_x\theta(x,\tau))\psi_\alpha(x,\tau)\psi_\alpha(x')\rangle \tag{4.174}$$

but all that must be changed in $\psi(x) \propto e^{i(\alpha\phi-\theta)}$ to get $\psi(x,\tau)$ is to replace $\phi(x)$ with $\phi(x,\tau)$ and $\theta(x)$ with $\theta(x,\tau)$. Then just as at $\tau = 0$ an x derivative pulls down a factor of $(\alpha\nabla_x\phi(x) - \nabla_x\theta(x))$, at nonzero τ you get a factor $(\alpha\nabla_x\phi(x,\tau) - \nabla_x\theta(x,\tau))$. In short, in the same way that the $\tau = 0$ results above were obtained by taking x derivatives of the $\tau = 0$ Green's function, the τ-dependent results can be obtained via derivatives of the τ-dependent Green's function. The expressions look the same because the time evolution operator commutes with taking a derivative with respect to x.

Thus to get the time-dependent versions of our above expressions from equation (4.169), on the right-hand side we should just replace $G(x-x')$ by $G(x-x',\tau)$.

At this point we can look at the full 4 terms from the current-current correlator, equation (4.165). For instance, the first is

$$\begin{aligned}\langle[\nabla_j]^\alpha_{x_1,\tau}\psi^\dagger_{j\alpha}(x_1,\tau)\psi_{j\alpha}(x_4)\rangle\langle\psi_{j-1,\beta}(x_2,\tau)[\nabla_{j-1}]^\beta_{x_3}\psi^\dagger_{j-1,\beta}(x_3)\rangle \\ = -\frac{\alpha}{2}\left(\frac{K}{\hbar}+\frac{\hbar}{K}\right)\left(\alpha k_F\tilde{G}_\alpha(x_1-x_4,\tau) - i\partial_{x_1}\tilde{G}_\alpha(x_1-x_4,\tau)\right) \\ \times -\frac{\beta}{2}\left(\frac{K}{\hbar}+\frac{\hbar}{K}\right)\left(\beta k_F G_\beta(x_2-x_3,\tau) + i\partial_{x_2}G_\beta(x_2-x_3,\tau)\right)\end{aligned}$$

This is a rather complicated expression, but it can be simplified substantially by making the same assumptions on $t_{\alpha\beta}(x-x')$ as made for $\langle J_e(\tau)J_e\rangle$ above, namely that $t_{\alpha\beta}(x-x') = \frac{t}{2\pi}\delta_{\alpha\beta}\delta(x-x')$. Thus we only need to consider the case where $\alpha = \beta$, $x_1 = x_2 = x$, and

$x_3 = x_4 = x'$. In that case, the four terms from equation (4.165) look like

$$\begin{aligned}
&\langle [\nabla_j]^\alpha_{x,\tau} \psi^\dagger_{j\alpha}(x,\tau)\psi_{j\alpha}(x')\rangle \langle \psi_{j-1,\alpha}(x,\tau)[\nabla_{j-1}]^\alpha_{x'}\psi^\dagger_{j-1,\alpha}(x')\rangle \\
&\quad = -\frac{\alpha}{2}\left(\frac{K}{\hbar}+\frac{\hbar}{K}\right)\left(\alpha k_F \tilde{G}_\alpha(x-x',\tau) - i\partial_x \tilde{G}_\alpha(x-x',\tau)\right) \\
&\qquad \times -\frac{\alpha}{2}\left(\frac{K}{\hbar}+\frac{\hbar}{K}\right)\left(\alpha k_F G_\alpha(x-x',\tau) + i\partial_x G_\alpha(x-x',\tau)\right) \\
&\quad = \frac{1}{4}\left(\frac{K}{\hbar}+\frac{\hbar}{K}\right)^2 \left[(k_F - i\alpha\partial_x)\tilde{G}_\alpha(x-x',\tau)\right] \times \left[(k_F + i\alpha\partial_x)G_\alpha(x-x',\tau)\right] \\
&\langle [\nabla_{j-1}]^\alpha_{x,\tau} \psi_{j-1,\alpha}(x,\tau)\psi^\dagger_{j-1,\alpha}(x')\rangle \langle \psi^\dagger_{j\alpha}(x,\tau)[\nabla_j]^\alpha_{x'}\psi_{j\alpha}(x')\rangle \\
&\quad = -\frac{\alpha}{2}\left(\frac{K}{\hbar}+\frac{\hbar}{K}\right)\left(\alpha k_F G_\alpha(x-x',\tau) + i\partial_x G_\alpha(x-x',\tau)\right) \\
&\qquad \times -\frac{\alpha}{2}\left(\frac{K}{\hbar}+\frac{\hbar}{K}\right)\left(\alpha k_F \tilde{G}_\alpha(x-x',\tau) - i\partial_x \tilde{G}_\alpha(x-x',\tau)\right) \\
&\quad = \frac{1}{4}\left(\frac{K}{\hbar}+\frac{\hbar}{K}\right)^2 \left[(k_F + i\alpha\partial_x)G_\alpha(x-x',\tau)\right] \times \left[(k_F - i\alpha\partial_x)\tilde{G}_\alpha(x-x',\tau)\right] \\
&\langle [\nabla_{j-1}]^\alpha_{x,\tau} \psi_{j-1,\alpha}(x,\tau)[\nabla_{j-1}]^\alpha_{x'}\psi^\dagger_{j-1,\alpha}(x')\rangle \langle \psi^\dagger_{j\alpha}(x,\tau)\psi_{j\alpha}(x')\rangle \\
&\quad = \frac{1}{4}\left(\frac{K}{\hbar}+\frac{\hbar}{K}\right)^2 \left[(\alpha k_F)^2 G_\alpha(x-x',\tau) + 2i\alpha k_F \partial_x G_\alpha(x-x',\tau) - \partial_x^2 G_\alpha(x-x',\tau)\right] \\
&\qquad \times \tilde{G}_\alpha(x-x',\tau) \\
&\langle [\nabla_j]^\alpha_{x,\tau} \psi^\dagger_{j\alpha}(x,\tau)[\nabla_j]^\alpha_{x'}\psi_{j\alpha}(x')\rangle \langle \psi_{j-1,\alpha}(x,\tau)\psi^\dagger_{j-1,\alpha}(x')\rangle \\
&\quad = \frac{1}{4}\left(\frac{K}{\hbar}+\frac{\hbar}{K}\right)^2 \left[(\alpha k_F)^2 \tilde{G}_\alpha(x-x',\tau) - 2i\alpha k_F \partial_x \tilde{G}_\alpha(x-x',\tau) - \partial_x^2 \tilde{G}_\alpha(x-x',\tau)\right] \\
&\qquad \times G_\alpha(x-x',\tau)
\end{aligned}$$

Combining the last two of these four contributions, we get (suppressing the factor of $(K/\hbar + \hbar/K)^2/4$ for now):

$$\begin{aligned}
&\langle [\nabla_{j-1}]^\alpha_{x,\tau} \psi_{j-1,\alpha}(x,\tau)[\nabla_{j-1}]^\alpha_{x'}\psi^\dagger_{j-1,\alpha}(x')\rangle \langle \psi^\dagger_{j\alpha}(x,\tau)\psi_{j\alpha}(x')\rangle \\
&\qquad + \langle [\nabla_j]^\alpha_{x,\tau} \psi^\dagger_{j\alpha}(x,\tau)[\nabla_j]^\alpha_{x'}\psi_{j\alpha}(x')\rangle \langle \psi_{j-1,\alpha}(x,\tau)\psi^\dagger_{j-1,\alpha}(x')\rangle \\
&\sim 2k_F^2 G_\alpha(x-x',\tau)\tilde{G}_\alpha(x-x',\tau) \\
&\quad + 2i\alpha k_F(\partial_x G_\alpha(x-x',\tau))\tilde{G}_\alpha(x-x',\tau) - 2i\alpha k_F(\partial_x \tilde{G}_\alpha(x-x',\tau))G_\alpha(x-x',\tau) \\
&\quad - (\partial_x^2 \tilde{G}_\alpha(x-x',\tau))G_\alpha(x-x',\tau) - (\partial_x^2 G_\alpha(x-x',\tau))\tilde{G}_\alpha(x-x',\tau)
\end{aligned}$$

We need to remember that we are integrating this over x from $-\infty$ to ∞, in which case we can use integration by parts to move partial derivatives around, in particular to make the last two terms identical:

$$\begin{aligned}
&= 2\Big[k_F^2 G_\alpha(x-x',\tau)\tilde{G}_\alpha(x-x',\tau) \\
&+ i\alpha k_F\Big((\partial_x G_\alpha(x-x',\tau))\tilde{G}_\alpha(x-x',\tau) - (\partial_x \tilde{G}_\alpha(x-x',\tau))G_\alpha(x-x',\tau)\Big) \\
&+(\partial_x \tilde{G}_\alpha(x-x',\tau))(\partial_x G_\alpha(x-x',\tau))\Big] \\
&= 2\left[(k_F + i\alpha\partial_x)G_\alpha(x-x',\tau)\right] \times \Big[(k_F - i\alpha\partial_x)\tilde{G}_\alpha(x-x',\tau)\Big]
\end{aligned}$$

Now we can sum all four contributions (with the last two modified using integration by parts as above), to get simply

$$\left(\frac{K}{\hbar} + \frac{\hbar}{K}\right)^2 \left[(k_F + i\alpha\partial_x)G_\alpha(x-x',\tau)\right] \times \Big[(k_F - i\alpha\partial_x)\tilde{G}_\alpha(x-x',\tau)\Big] \tag{4.175}$$

Now we can recognize that, setting $\hbar = 1$, the factor $(K + K^{-1})$ is actually just 2γ (see equation (2.11)), so we have

$$(2\gamma)^2 \left[(k_F + i\alpha\partial_x)G_\alpha(x-x',\tau)\right] \times \Big[(k_F - i\alpha\partial_x)\tilde{G}_\alpha(x-x',\tau)\Big] \tag{4.176}$$

We can substitute this rather nice result into the expression for the current-current cor-

relator found in equation (4.164), getting

$$\begin{aligned}
\langle J_E(\tau)J_E\rangle &= \sum_{ij}\sum_{\alpha\beta\gamma\delta}\int dx_1\,dx_2\,dx_3\,dx_4\,\left(\frac{a_c v}{2\hbar}\right)^2 t_{\alpha\beta}(x_1-x_2)t_{\gamma\delta}(x_3-x_4)\,\langle\cdots\rangle \\
&= \sum_{ij}\sum_{\alpha\beta\gamma\delta}\int dx_1\,dx_2\,dx_3\,dx_4\,\left(\frac{a_c v t}{4\pi\hbar}\right)^2 \delta_{\alpha\beta}\delta_{\gamma\delta}\delta(x_1-x_2)\delta(x_3-x_4)\,\langle\cdots\rangle \\
\langle\cdots\rangle &= 2\delta_{ij}\delta_{\alpha\delta}\delta_{\beta\gamma}\left[\begin{array}{l}
\langle[\nabla_j]^\alpha_{x_1,\tau}\psi^\dagger_{j\alpha}(x_1,\tau)\psi_{j\alpha}(x_4)\rangle\langle\psi_{j-1,\beta}(x_2,\tau)[\nabla_{j-1}]^\beta_{x_3}\psi^\dagger_{j-1,\beta}(x_3)\rangle \\
+\langle[\nabla_{j-1}]^\beta_{x_2,\tau}\psi_{j-1,\beta}(x_2,\tau)[\nabla_{j-1}]^\beta_{x_3}\psi^\dagger_{j-1,\beta}(x_3)\rangle\langle\psi^\dagger_{j\alpha}(x_1,\tau)\psi_{j\alpha}(x_4)\rangle \\
+\langle[\nabla_j]^\alpha_{x_1,\tau}\psi^\dagger_{j\alpha}(x_1,\tau)[\nabla_j]^\alpha_{x_4}\psi_{j\alpha}(x_4)\rangle\langle\psi_{j-1,\beta}(x_2,\tau)\psi^\dagger_{j-1,\beta}(x_3)\rangle \\
+\langle[\nabla_{j-1}]^\beta_{x_2,\tau}\psi_{j-1,\beta}(x_2,\tau)\psi^\dagger_{j-1,\beta}(x_3)\rangle\langle\psi^\dagger_{j\alpha}(x_1,\tau)[\nabla_j]^\alpha_{x_4}\psi_{j\alpha}(x_4)\rangle
\end{array}\right] \\
\langle J_E(\tau)J_E\rangle &= \sum_j\sum_\alpha\int dx\,dx'\,\left(\frac{a_c v t}{4\pi\hbar}\right)^2\langle\cdots\rangle \\
\langle\cdots\rangle &= 2\left[\begin{array}{l}
\langle[\nabla_j]^\alpha_{x,\tau}\psi^\dagger_{j\alpha}(x,\tau)\psi_{j\alpha}(x')\rangle\langle\psi_{j-1,\alpha}(x,\tau)[\nabla_{j-1}]^\alpha_{x'}\psi^\dagger_{j-1,\alpha}(x')\rangle \\
+\langle[\nabla_{j-1}]^\alpha_{x,\tau}\psi_{j-1,\alpha}(x,\tau)[\nabla_{j-1}]^\beta_{x'}\psi^\dagger_{j-1,\alpha}(x')\rangle\langle\psi^\dagger_{j\alpha}(x,\tau)\psi_{j\alpha}(x')\rangle \\
+\langle[\nabla_j]^\alpha_{x,\tau}\psi^\dagger_{j\alpha}(x,\tau)[\nabla_j]^\alpha_{x'}\psi_{j\alpha}(x')\rangle\langle\psi_{j-1,\alpha}(x,\tau)\psi^\dagger_{j-1,\alpha}(x')\rangle \\
+\langle[\nabla_{j-1}]^\alpha_{x,\tau}\psi_{j-1,\alpha}(x,\tau)\psi^\dagger_{j-1,\alpha}(x')\rangle\langle\psi^\dagger_{j\alpha}(x,\tau)[\nabla_j]^\alpha_{x'}\psi_{j\alpha}(x')\rangle
\end{array}\right] \\
&= 8\gamma^2\left[(k_F+i\alpha\partial_x)G_\alpha(x-x',\tau)\right]\times\left[(k_F-i\alpha\partial_x)\tilde{G}_\alpha(x-x',\tau)\right] \\
\langle J_E(\tau)J_E\rangle &= 2\gamma^2\left(\frac{a_c v t}{2\pi\hbar}\right)^2 \\
&\qquad\times\sum_{j\alpha}\int dx\,dx'\,\left[(k_F+i\alpha\partial_x)G_\alpha(x-x',\tau)\right]\times\left[(k_F-i\alpha\partial_x)\tilde{G}_\alpha(x-x',\tau)\right]
\end{aligned}$$

The integrand is explicitly independent of j, so that sum just gives a factor of N_c. As in the case of $\langle J_e J_e\rangle$, it will also prove to be independent of α, but as in that case we will leave the sum over α for the time being since the independence is not obvious. This gives

$$\langle J_E(\tau)J_E\rangle = 2N_c\gamma^2\left(\frac{a_c v t}{2\pi\hbar}\right)^2 \tag{4.177}$$

$$\times\sum_\alpha\int dx\,dx'\,\left[(k_F+i\alpha\partial_x)G_\alpha(x-x',\tau)\right]\times\left[(k_F-i\alpha\partial_x)\tilde{G}_\alpha(x-x',\tau)\right] \tag{4.178}$$

Finally, we change coordinates from x and x' to $x-x'$ and $(x+x')/2$, in which case the integral over the average coordinate gives $L-|x-x'|$ as discussed in the calculation of $\langle J_e(\tau)J_e\rangle$. Again as before, we approximate this as just a factor of L since the second term is negligible, in which case our final expression for the current-current correlator in terms of

an as-yet unspecified Green's function is

$$\langle J_E(\tau)J_E\rangle = 2N_cL\gamma^2\left(\frac{a_cvt}{2\pi\hbar}\right)^2\sum_\alpha\int dx\left[(k_F+i\alpha\partial_x)G_\alpha(x,\tau)\right]\times\left[(k_F-i\alpha\partial_x)\tilde{G}_\alpha(x,\tau)\right] \tag{4.179}$$

or, substituting for $\tilde{G}$ using equation (4.152b),

$$\boxed{\langle J_E(\tau)J_E\rangle = -2N_cL\gamma^2\left(\frac{a_cvt}{2\pi\hbar}\right)^2\sum_\alpha\int dx\left[(k_F+i\alpha\partial_x)G_\alpha(x,\tau)\right]\times\left[(k_F-i\alpha\partial_x)G_\alpha(-x,-\tau)\right]} \tag{2.28b}$$

To complete the calculation, we plug in the precise expression for the Luttinger liquid Green's function as given in equation (2.29) and integrate over x. We can achieve a significant simplification first by writing $G_\alpha(x,\tau) = e^{i\alpha k_Fx}f_\alpha(x,\tau)$, in which case

$$\begin{aligned}(k_F+i\alpha\partial_x)G_\alpha(x,\tau) &= i\alpha e^{i\alpha k_Fx}\partial_x f_\alpha(x,\tau)\\ &\equiv i\alpha e^{i\alpha k_Fx}f_{\alpha,x}(x,\tau)\end{aligned}$$

and likewise

$$\begin{aligned}(k_F-i\alpha\partial_x)\tilde{G}_\alpha(x,\tau) &= -(k_F-i\alpha\partial_x)G_\alpha(-x,-\tau)\\ &= -(-i\alpha e^{-i\alpha k_Fx})\partial_x f_\alpha(-x,-\tau)\\ &= -i\alpha e^{-i\alpha k_Fx}f_{\alpha,x}(-x,-\tau)\end{aligned}$$

where in the last line we got an extra minus sign from the chain rule. Then the integrand simplifies to

$$i\alpha e^{i\alpha k_Fx}f_{\alpha,x}(x,\tau)\times -i\alpha e^{-i\alpha k_Fx}f_{\alpha,x}(-x,-\tau) = f_{\alpha,x}(x,\tau)f_{\alpha,x}(-x,-\tau) \tag{4.180}$$

where

$$f(x,\tau) = -\frac{1}{2\pi a}\left[\frac{-ia}{\frac{v\beta}{\pi}\sinh\left(\frac{x-iv\tau}{v\beta/\pi}\right)}\right]^{\frac{\gamma-\alpha}{2}}\left[\frac{ia}{\frac{v\beta}{\pi}\sinh\left(\frac{x+iv\tau}{v\beta/\pi}\right)}\right]^{\frac{\gamma+\alpha}{2}} \tag{4.181}$$

and thus

$$\begin{aligned}f_{\alpha,x}(x,\tau)f_{\alpha,x}(-x,-\tau) &= -\frac{\pi^{2\gamma}}{(4av\beta)^2}\left(\coth\left(\frac{x+iv\tau}{v\beta/\pi}\right)(\gamma+\alpha)+\coth\left(\frac{x-iv\tau}{v\beta/\pi}\right)(\gamma-\alpha)\right)^2\\ &\quad\times\left(\frac{a}{v\beta}\right)^{2\gamma}\left[\sinh\left(\frac{x+iv\tau}{v\beta/\pi}\right)\sinh\left(\frac{x-iv\tau}{v\beta/\pi}\right)\right]^{-\gamma}\left(\frac{\sinh\left(\frac{x-iv\tau}{v\beta/\pi}\right)}{\sinh\left(\frac{x+iv\tau}{v\beta/\pi}\right)}\right)^{\alpha}\\ &= \frac{1}{16a^4\pi^2}\left(\frac{a\pi}{v\beta}\right)^{2\gamma+2}\frac{\left(\alpha\sin\left(\frac{2\tau}{\beta/\pi}\right)+i\gamma\sinh\left(\frac{2x}{v\beta/\pi}\right)\right)^2}{\left[\sinh\left(\frac{x+iv\tau}{v\beta/\pi}\right)\sinh\left(\frac{x-iv\tau}{v\beta/\pi}\right)\right]^{\gamma+2}}\left(\frac{\sinh\left(\frac{x-iv\tau}{v\beta/\pi}\right)}{\sinh\left(\frac{x+iv\tau}{v\beta/\pi}\right)}\right)^{\alpha}\end{aligned}$$

Now we can convert to our scaled (x', τ') coordinates as we did in the case of $\langle J_e J_e \rangle$, to get:

$$\begin{aligned}
&\frac{1}{16a^4\pi^2}\left(\frac{a\pi}{v\beta}\right)^{2\gamma+2}\frac{\left(\alpha\sin\left(2\tau'\right)+i\gamma\sinh\left(2x'\right)\right)^2}{\left[\sinh\left(x'+i\tau'\right)\sinh\left(x'-i\tau'\right)\right]^{\gamma+2}}\left(\frac{\sinh\left(x'-i\tau'\right)}{\sinh\left(x'+i\tau'\right)}\right)^{\alpha}\\
&=\frac{2^{\gamma+2}}{16a^4\pi^2}\left(\frac{a\pi}{v\beta}\right)^{2\gamma+2}\left(\frac{\sin^2\left(2\tau'\right)-\gamma^2\sinh^2\left(2x'\right)+2i\alpha\sin(2\tau')\sinh(2x')}{\left[\cosh(2x')-\cos(2\tau')\right]^{\gamma+2}}\right)\left(\frac{\sinh\left(x'-i\tau'\right)}{\sinh\left(x'+i\tau'\right)}\right)^{\alpha}\\
&=\frac{2^{\gamma+3}}{16a^4\pi^2}\left(\frac{a\pi}{v\beta}\right)^{2\gamma+2}\left(\frac{\sin^2\left(2\tau'\right)-\gamma^2\sinh^2\left(2x'\right)+2i\alpha\sin(2\tau')\sinh(2x')}{\left[\cosh(2x')-\cos(2\tau')\right]^{\gamma+2}}\right)\\
&\quad\times\left(\frac{\cos^2(\tau')\sinh^2(x')-\cosh^2(x')\sin^2(\tau')-i\frac{\alpha}{2}\sin(2\tau')\sinh(2x')}{\cosh(2x')-\cos(2\tau')}\right)
\end{aligned}$$

In multiplying the two numerators, the imaginary part will be odd in x' and thus vanish in the integral, so we keep only the even part:

$$\begin{aligned}
&\to\frac{2^{\gamma+3}}{16a^4\pi^2}\left(\frac{a\pi}{v\beta}\right)^{2\gamma+2}\\
&\quad\times\left(\frac{\left(\sin^2\left(2\tau'\right)-\gamma^2\sinh^2\left(2x'\right)\right)\left(\cos^2(\tau')\sinh^2(x')-\cosh^2(x')\sin^2(\tau')\right)+\sin^2(2\tau')\sinh^2(2x')}{\left[\cosh(2x')-\cos(2\tau')\right]^{\gamma+3}}\right)
\end{aligned}$$

Note that the dependence on α has again disappeared as expected.

Thus for the full current-current correlator we find the integral expression

$$\begin{aligned}
&\langle J_E(\tau)J_E\rangle=4N_cL\gamma^2\left(\frac{a_cvt}{2\pi\hbar}\right)^2\frac{2^{\gamma+3}}{16a^4\pi^2}\left(\frac{a\pi}{v\beta}\right)^{2\gamma+2}\left(\frac{v\beta}{\pi}\right) &(4.182)\\
&\times\int dx'\left(\frac{\left(\sin^2(2\tau')-\gamma^2\sinh^2(2x')\right)\left(\cos^2(\tau')\sinh^2(x')-\cosh^2(x')\sin^2(\tau')\right)+\sin^2(2\tau')\sinh^2(2x')}{\left[\cosh(2x')-\cos(2\tau')\right]^{\gamma+3}}\right)\\
&=N_cL\gamma^2\left(\frac{a_cvt}{2\pi\hbar}\right)^2\frac{2^{\gamma+1}}{a^3\pi^2}\left(\frac{\pi a}{v\beta}\right)^{2\gamma+1} &(4.183)\\
&\times\int dx'\left(\frac{\left(\sin^2(2\tau')-\gamma^2\sinh^2(2x')\right)\left(\cos^2(\tau')\sinh^2(x')-\cosh^2(x')\sin^2(\tau')\right)+\sin^2(2\tau')\sinh^2(2x')}{\left[\cosh(2x')-\cos(2\tau')\right]^{\gamma+3}}\right)
\end{aligned}$$

Assuming that each chain is infinitely long, so that we can let the limits of integration in x go to $\pm\infty$, the integral over x can be done exactly. To do so, we split up the terms of the numerator in the integrand by their x-dependence to get

$$\boxed{\langle J_E(\tau)J_E\rangle=N_cL\gamma^2\left(\frac{a_cvt}{2\pi\hbar}\right)^2\frac{2^{\gamma+1}}{a^3\pi^2}\left(\frac{\pi a}{v\beta}\right)^{2\gamma+1}\int dx'\left(\frac{a+b\cosh(2x')+c\cosh(4x')+d\cosh(6x')}{\left[\cosh(2x')-\cos(2\tau')\right]^{\gamma+3}}\right)} \tag{4.184}$$

where

$$a = \frac{1}{4}(2\cos(4\tau') - 2 - \gamma^2) \tag{4.185a}$$

$$b = \frac{1}{4}\cos(2\tau')(1 + \frac{1}{2}\gamma^2 - \cos(4\tau')) \tag{4.185b}$$

$$c = \frac{1}{4}(1 + \gamma^2 - \cos(4\tau')) \tag{4.185c}$$

$$d = -\frac{1}{8}\gamma^2\cos(2\tau') \tag{4.185d}$$

We thus have four integrals over x to perform. Using equation (4.157), we find the result:

$$\int_{-\infty}^{\infty} \frac{\cosh(nx)}{(\cosh(2x) - \cos(2\tau))^{\gamma+3}} dx = 2^{\gamma+2}\left(f(\gamma, \tau, 3 - \frac{n}{2}, 3) + f(\gamma, \tau, 3 + \frac{n}{2}, 3)\right) \tag{4.186}$$

so long as $n < 6 + 2\gamma$ (thus guaranteed for $n < 8$), where as above

$$f(\gamma, \tau, n, m) = \frac{F_1(\gamma + n; \gamma + m, \gamma + m; \gamma + n + 1; e^{2i\tau}, e^{-2i\tau})}{\gamma + n} \tag{4.158}$$

and $F_1(a; b_1, b_2; c; x, y)$ is the first Appell hypergeometric function.

Specializing to the actual integrals over x that appear in equation (4.184), we have:

$$\int_{-\infty}^{\infty} \frac{1}{(\cosh(2x) - \cos(2\tau))^{\gamma+3}} dx = 2^{\gamma+3} f(\gamma, \tau, 3, 3) \tag{4.187a}$$

$$\int_{-\infty}^{\infty} \frac{\cosh(2x)}{(\cosh(2x) - \cos(2\tau))^{\gamma+3}} dx = 2^{\gamma+2}\left(f(\gamma, \tau, 2, 3) + f(\gamma, \tau, 4, 3)\right) \tag{4.187b}$$

$$\int_{-\infty}^{\infty} \frac{\cosh(4x)}{(\cosh(2x) - \cos(2\tau))^{\gamma+3}} dx = 2^{\gamma+2}\left(f(\gamma, \tau, 1, 3) + f(\gamma, \tau, 5, 3)\right) \tag{4.187c}$$

$$\int_{-\infty}^{\infty} \frac{\cosh(6x)}{(\cosh(2x) - \cos(2\tau))^{\gamma+3}} dx = 2^{\gamma+2}\left(f(\gamma, \tau, 0, 3) + f(\gamma, \tau, 6, 3)\right) \tag{4.187d}$$

When all of these contributions are included, the result is a rather long expression, with 7 distinct f functions. This expression is not particularly enlightening, but we include it here for completeness.

$$\langle J_E(\tau')J_E\rangle = N_c L\gamma^2 \left(\frac{a_c v t}{2\pi\hbar}\right)^2 \frac{1}{2a^3\pi^2}\left(\frac{2\pi a}{v\beta}\right)^{2\gamma+1} \tag{3.23a}$$
$$\times \begin{pmatrix} -4(2+\gamma^2-2\cos(4\tau'))f(\gamma,\tau',3,3) \\ +\cos(2\tau')(2+\gamma^2-2\cos(4\tau'))(f(\gamma,\tau',2,3)+f(\gamma,\tau',4,3)) \\ +2(1+\gamma^2-\cos(4\tau'))(f(\gamma,\tau',1,3)+f(\gamma,\tau',5,3)) \\ -\gamma^2\cos(2\tau')(f(\gamma,\tau',0,3)+f(\gamma,\tau',6,3)) \end{pmatrix}$$

Asymptotic behavior for small τ':

As we did for $\langle J_e(\tau')J_e\rangle$ above, we want to find asymptotic behavior for small τ' for purposes of estimating the numerical error in our evaluation of the transport coefficients (section 4.1 above). We examine $\langle J_E(\tau')J_E\rangle$ in the limit of small τ' by focusing on the $x,\tau'\approx 0$ pole of the integrand in equation (4.184). We find

$$\int dx' \left(\frac{a+b\cosh(2x')+c\cosh(4x')+d\cosh(6x')}{[\cosh(2x')-\cos(2\tau')]^{\gamma+3}}\right) \approx \frac{(5+\gamma^2)}{2^{\gamma+1}}\int dx' \frac{(x')^2(\tau')^2}{[(x')^2+(\tau')^2]^{\gamma+3}}$$
$$\propto (\tau')^{-1-2\gamma} \tag{4.188}$$

Thus we conclude that for small τ', $\langle J_E(\tau')J_E\rangle \propto (\tau')^{-1-2\gamma}$. Then integrating over τ' from ϵ to $\pi-\epsilon$, the contribution from the pole at $\tau'=0$ is proportional to $\epsilon^{-2\gamma}$. This is the fact used in our error approximation in section 4.1.

$\langle J_E(\tau)J_e(0)\rangle$

The calculation of this correlator is quite similar to the calculation for the previous two, with a level of complexity that is between those two computations. The calculation itself follows a similar procedure:

$$\langle J_E(\tau)J\rangle = \sum_{ij}\sum_{\alpha\beta\gamma\delta}\int dx_1\,dx_2\,dx_3\,dx_4\,\frac{v}{2}\left(\frac{a_c}{2\pi\hbar}\right)^2 t_{\alpha\beta}(x_1-x_2)t_{\gamma\delta}(x_3-x_4)\,\langle\cdots\rangle$$

$$\langle\cdots\rangle = \left\langle \begin{array}{c} e^{\tau H}\left[\begin{array}{c}\left([\nabla_i]^\alpha_{x_1}+[\nabla_{i-1}]^\beta_{x_2}\right)\psi^\dagger_{i\alpha}(x_1)\psi_{i-1,\beta}(x_2)\\ -\left([\nabla_{i-1}]^\alpha_{x_1}+[\nabla_i]^\beta_{x_2}\right)\psi^\dagger_{i-1,\alpha}(x_1)\psi_{i\beta}(x_2)\end{array}\right]e^{-\tau H}\\ \\ \times\left[\psi^\dagger_{j-1,\gamma}(x_3)\psi_{j,\delta}(x_4)-\psi^\dagger_{j,\gamma}(x_3)\psi_{j-1,\delta}(x_4)\right]\end{array}\right\rangle$$

$$= \left\langle \begin{array}{c} e^{\tau H}\left([\nabla_i]^\alpha_{x_1}+[\nabla_{i-1}]^\beta_{x_2}\right)\psi^\dagger_{i\alpha}(x_1)\psi_{i-1,\beta}(x_2)e^{-\tau H}\psi^\dagger_{j-1,\gamma}(x_3)\psi_{j\delta}(x_4)\\ +\,e^{\tau H}\left([\nabla_{i-1}]^\alpha_{x_1}+[\nabla_i]^\beta_{x_2}\right)\psi^\dagger_{i-1,\alpha}(x_1)\psi_{i,\beta}(x_2)e^{-\tau H}\psi^\dagger_{j\gamma}(x_3)\psi_{j-1,\delta}(x_4)\end{array}\right\rangle$$

$$= \delta_{ij}\delta_{\alpha\delta}\delta_{\beta\gamma}\left\langle \begin{array}{c} e^{\tau H}\left([\nabla_j]^\alpha_{x_1}+[\nabla_{j-1}]^\beta_{x_2}\right)\psi^\dagger_{j\alpha}(x_1)\psi_{j-1,\beta}(x_2)e^{-\tau H}\psi^\dagger_{j-1,\beta}(x_3)\psi_{j\alpha}(x_4)\\ +\,e^{\tau H}\left([\nabla_{j-1}]^\alpha_{x_1}+[\nabla_j]^\beta_{x_2}\right)\psi^\dagger_{j-1,\alpha}(x_1)\psi_{j,\beta}(x_2)e^{-\tau H}\psi^\dagger_{j\beta}(x_3)\psi_{j-1,\alpha}(x_4)\end{array}\right\rangle$$

Note that $\alpha=\delta$ and $\beta=\gamma$ because of the U operators (Klein factors)

$$= 2\delta_{ij}\delta_{\alpha\delta}\delta_{\beta\gamma}\left\langle e^{\tau H}\left([\nabla_j]^\alpha_{x_1}+[\nabla_{j-1}]^\beta_{x_2}\right)\psi^\dagger_{j\alpha}(x_1)\psi_{j-1,\beta}(x_2)e^{-\tau H}\psi^\dagger_{j-1,\beta}(x_3)\psi_{j\alpha}(x_4)\right\rangle$$

because the only difference between the two terms was $j\leftrightarrow j-1$

$$= 2\delta_{ij}\delta_{\alpha\delta}\delta_{\beta\gamma}\left\langle \begin{array}{l} e^{\tau H}[\nabla_j]^\alpha_{x_1}\psi^\dagger_{j,\alpha}(x_1)\psi_{j-1,\beta}(x_2)e^{-\tau H}\psi^\dagger_{j-1,\beta}(x_3)\psi_{j\alpha}(x_4)\\ +e^{\tau H}[\nabla_{j-1}]^\beta_{x_2}\psi^\dagger_{j\alpha}(x_1)\psi_{j-1,\beta}(x_2)e^{-\tau H}\psi^\dagger_{j-1,\beta}(x_3)\psi_{j\alpha}(x_4)\end{array}\right\rangle$$

$$= 2\delta_{ij}\delta_{\alpha\delta}\delta_{\beta\gamma}\left[\begin{array}{l}\langle e^{\tau H}[\nabla_j]^\alpha_{x_1}\psi^\dagger_{j,\alpha}(x_1)\psi_{j-1,\beta}(x_2)e^{-\tau H}\psi^\dagger_{j-1,\beta}(x_3)\psi_{j\alpha}(x_4)\rangle\\ +\langle e^{\tau H}[\nabla_{j-1}]^\beta_{x_2}\psi^\dagger_{j\alpha}(x_1)\psi_{j-1,\beta}(x_2)e^{-\tau H}\psi^\dagger_{j-1,\beta}(x_3)\psi_{j\alpha}(x_4)\rangle\end{array}\right]$$

$$= 2\delta_{ij}\delta_{\alpha\delta}\delta_{\beta\gamma}\left[\begin{array}{l}\langle[\nabla_j]^\alpha_{x_1,\tau}\psi^\dagger_{j\alpha}(x_1,\tau)\psi_{j\alpha}(x_4)\rangle\langle\psi_{j-1,\beta}(x_2,\tau)\psi^\dagger_{j-1,\beta}(x_3)\rangle\\ +\langle[\nabla_{j-1}]^\beta_{x_2,\tau}\psi_{j-1,\beta}(x_2,\tau)\psi^\dagger_{j-1,\beta}(x_3)\rangle\langle\psi^\dagger_{j\alpha}(x_1,\tau)\psi_{j\alpha}(x_4)\rangle\end{array}\right]$$

As before, we will assume that $t_{\alpha\beta}(x-x') = \frac{t}{2\pi}\delta_{\alpha\beta}\delta(x-x')$. Then we can calculate both of these terms, letting $x_1=x_2=x$ and $x_3=x_4=x'$:

$$\begin{aligned}
&\langle [\nabla_j]^\alpha_{x,\tau}\psi^\dagger_{j\alpha}(x,\tau)\psi_{j\alpha}(x')\rangle\langle\psi_{j-1,\alpha}(x,\tau)\psi^\dagger_{j-1,\alpha}(x')\rangle \\
&\qquad = -\frac{\alpha}{2}\left(\frac{K}{\hbar}+\frac{\hbar}{K}\right)\Big(\alpha k_F\tilde{G}_\alpha(x-x',\tau) - i\partial_x\tilde{G}_\alpha(x-x',\tau)\Big)\times G_\alpha(x-x',\tau) \\
&\qquad = -\frac{1}{2}\left(\frac{K}{\hbar}+\frac{\hbar}{K}\right)\Big[(k_F - i\alpha\partial_x)\tilde{G}_\alpha(x-x',\tau)\Big]\times G_\alpha(x-x',\tau) \\
&\langle [\nabla_{j-1}]^\alpha_{x,\tau}\psi_{j-1,\alpha}(x,\tau)\psi^\dagger_{j-1,\alpha}(x')\rangle\langle\psi^\dagger_{j\alpha}(x,\tau)[\nabla_j]^\alpha_{x'}\psi_{j\alpha}(x')\rangle \\
&\qquad = -\frac{\alpha}{2}\left(\frac{K}{\hbar}+\frac{\hbar}{K}\right)\big(\alpha k_F G_\alpha(x-x',\tau) + i\partial_x G_\alpha(x-x',\tau)\big)\times G^*_\alpha(x-x',\tau) \\
&\qquad = -\frac{1}{2}\left(\frac{K}{\hbar}+\frac{\hbar}{K}\right)\big[(k_F + i\alpha\partial_x)G_\alpha(x-x',\tau)\big]\times \tilde{G}_\alpha(x-x',\tau)
\end{aligned}$$

The two contributions appear to be different, but recall that they are inside an integral over x and hence we can modify them using integration by parts. This precisely converts the two expressions into one another, so the two contributions to the correlation function are actually the same. The sum thus gives

$$\begin{aligned}
&\langle [\nabla_j]^\alpha_{x,\tau}\psi^\dagger_{j\alpha}(x,\tau)\psi_{j\alpha}(x')\rangle\langle\psi_{j-1,\alpha}(x,\tau)\psi^\dagger_{j-1,\alpha}(x')\rangle \\
&\qquad\qquad + \langle [\nabla_{j-1}]^\alpha_{x,\tau}\psi_{j-1,\alpha}(x,\tau)\psi^\dagger_{j-1,\alpha}(x')\rangle\langle\psi^\dagger_{j\alpha}(x,\tau)[\nabla_j]^\alpha_{x'}\psi_{j\alpha}(x')\rangle \\
&\quad = -\left(\frac{K}{\hbar}+\frac{\hbar}{K}\right)G_\alpha(x-x',\tau)(k_F - i\alpha\partial_x)\tilde{G}_\alpha(x-x',\tau) \\
&\quad = -2\gamma\Big(G_\alpha(x-x',\tau)(k_F - i\alpha\partial_x)\tilde{G}_\alpha(x-x',\tau)\Big)
\end{aligned}$$

This expression can be substituted into our calculation of $\langle J_E(\tau)J\rangle$ above:

$$\begin{aligned}
\langle J_E(\tau)J\rangle &= \sum_{ij}\sum_{\alpha\beta\gamma\delta}\int dx_1\,dx_2\,dx_3\,dx_4\,\frac{v}{2}\left(\frac{a_c}{2\pi\hbar}\right)^2 t_{\alpha\beta}(x_1-x_2)t_{\gamma\delta}(x_3-x_4)\,\langle\cdots\rangle \\
&= -2v\gamma\left(\frac{a_c t}{2\pi\hbar}\right)^2\sum_{j\alpha}\int dx\,dx'\,G_\alpha(x-x',\tau)(k_F - i\alpha\partial_x)\tilde{G}_\alpha(x-x',\tau)
\end{aligned}$$

Now switch to relative and CM coordinates, again dropping the smaller second term, and perform the sum over j to get:

$$= -2v\gamma N_c L\left(\frac{a_c t}{2\pi\hbar}\right)^2\sum_{\alpha}\int dx\,G_\alpha(x,\tau)(k_F - i\alpha\partial_x)\tilde{G}_\alpha(x,\tau)$$

This is our final result in terms of the as-yet unspecified Green's function,

$$\boxed{\langle J_E(\tau)J\rangle = -2v\gamma N_c L\left(\frac{a_c t}{2\pi\hbar}\right)^2\sum_{\alpha}\int dx\,G_\alpha(x,\tau)(k_F - i\alpha\partial_x)\tilde{G}_\alpha(x,\tau)} \tag{4.189}$$

or equivalently

$$\langle J_E(\tau)J\rangle = 2v\gamma N_c L\left(\frac{a_c t}{2\pi\hbar}\right)^2 \sum_\alpha \int dx\, G_\alpha(x,\tau)(k_F - i\alpha\partial_x)G_\alpha(-x,-\tau) \tag{2.28c}$$

The expression looks a little unbalanced at first glance, since the $(k_F - i\alpha\partial_x)$ operator is applied to $\tilde{G}$ but not to G. This is artificial, however, since the operator is Hermitian and could just as easily be applied to G instead.

Next, as with the other two correlators we will substitute in our expression for the Green's function, equation (2.29). As we did in our calculation of $\langle J_E(\tau)J_E\rangle$, we simplify the required work by writing $G_\alpha(x,\tau) = e^{i\alpha k_F x} f_\alpha(x,\tau)$, in which case

$$\begin{aligned}(k_F - i\alpha\partial_x)G_\alpha(-x,-\tau) &= (-i\alpha e^{-i\alpha k_F x})\partial_x f_\alpha(-x,-\tau)\\ &= i\alpha e^{-i\alpha k_F x} f_{\alpha,x}(-x,-\tau)\end{aligned}$$

so

$$\begin{aligned}G_\alpha(x,\tau)(k_F - i\alpha\partial_x)G_\alpha(-x,-\tau) &= i\alpha f_\alpha(x,\tau) f_{\alpha,x}(-x,-\tau)\\ &= \frac{\pi^{2\gamma-1}\alpha}{8a^2 v\beta}\left(\frac{a}{v\beta}\right)^{2\gamma} \frac{\alpha\sin\left(\frac{2\tau}{v\beta/\pi}\right) + i\gamma\sinh\left(\frac{2x}{v\beta/\pi}\right)}{\left(\sinh\left(\frac{x-i\tau}{v\beta/\pi}\right)\sinh\left(\frac{x+i\tau}{v\beta/\pi}\right)\right)^{\gamma+1}} \left(\frac{\sinh\left(\frac{x-i\tau}{v\beta/\pi}\right)}{\sinh\left(\frac{x+i\tau}{v\beta/\pi}\right)}\right)^{\alpha}\end{aligned}$$

If we now substitute this into our expression for $\langle J_E(\tau)J_E\rangle$, we can then convert to the unitless coordinates x' and τ' and simplify the expression:

$$\begin{aligned}\langle J_E(\tau)J\rangle &= 2v\gamma N_c L\left(\frac{a_c t}{2\pi\hbar}\right)^2 \sum_\alpha \int dx\, G_\alpha(x,\tau)(k_F - i\alpha\partial_x)G_\alpha(-x,-\tau)\\ &= 2v\gamma N_c L\left(\frac{a_c t}{2\pi\hbar}\right)^2 \frac{\pi^{2\gamma-1}}{8a^2 v\beta}\left(\frac{a}{v\beta}\right)^{2\gamma}\\ &\quad\times \sum_\alpha \alpha \int dx\, \frac{\alpha\sin\left(\frac{2\tau}{v\beta/\pi}\right) + i\gamma\sinh\left(\frac{2x}{v\beta/\pi}\right)}{\left(\sinh\left(\frac{x-i\tau}{v\beta/\pi}\right)\sinh\left(\frac{x+i\tau}{v\beta/\pi}\right)\right)^{\gamma+1}} \left(\frac{\sinh\left(\frac{x-i\tau}{v\beta/\pi}\right)}{\sinh\left(\frac{x+i\tau}{v\beta/\pi}\right)}\right)^{\alpha}\end{aligned}$$

$$\begin{aligned}
\langle J_E(\tau')J\rangle &= 2v\gamma N_c L\left(\frac{a_c t}{2\pi\hbar}\right)^2 \frac{\pi^{2\gamma-2}}{8a^2}\left(\frac{a}{v\beta}\right)^{2\gamma} \\
&\quad\times\sum_\alpha \alpha\int dx' \frac{\alpha\sin(2\tau')+i\gamma\sinh(2x')}{(\sinh(x'-i\tau')\sinh(x'+i\tau'))^{\gamma+1}}\left(\frac{\sinh(x'-i\alpha\tau')}{\sinh(x'+i\alpha\tau')}\right) \\
&= 2v\gamma N_c L\left(\frac{a_c t}{2\pi\hbar}\right)^2 \frac{1}{8a^2\pi^2}\left(\frac{\pi a}{v\beta}\right)^{2\gamma} \\
&\quad\times\sum_\alpha \alpha\int dx' \frac{(\alpha\sin(2\tau')+i\gamma\sinh(2x'))\sinh^2(x'-i\alpha\tau')}{(\sinh(x'-i\tau')\sinh(x'+i\tau'))^{\gamma+2}} \\
&= 2v\gamma N_c L\left(\frac{a_c t}{2\pi\hbar}\right)^2 \frac{2^{\gamma+2}}{8a^2\pi^2}\left(\frac{\pi a}{v\beta}\right)^{2\gamma} \\
&\quad\times\sum_\alpha \alpha\int dx' \frac{(\alpha\sin(2\tau')+i\gamma\sinh(2x'))\sinh^2(x'-i\alpha\tau')}{(\cosh(2x')-\cos(2\tau'))^{\gamma+2}}
\end{aligned}$$

The imaginary part of the numerator is

$$\left[\gamma(\cos^2(\tau')\sinh^2(x')-\cosh^2(x')\sin^2(\tau'))-\frac{\sin^2(2\tau')}{2}\right]\sinh(2x) \tag{4.190}$$

which vanishes in the integral over x (since this is an odd function and the denominator is even). The remaining expression is

$$\begin{aligned}
\langle J_E(\tau')J\rangle &= 2v\gamma N_c L\left(\frac{a_c t}{2\pi\hbar}\right)^2 \frac{2^{\gamma+2}}{8a^2\pi^2}\left(\frac{\pi a}{v\beta}\right)^{2\gamma} \\
&\quad\times\sum_\alpha \alpha\int dx' \frac{(\alpha\sin(2\tau')+i\gamma\sinh(2x'))\sinh^2(x'-i\alpha\tau')}{(\cosh(2x')-\cos(2\tau'))^{\gamma+2}} \\
&= 2v\gamma N_c L\left(\frac{a_c t}{2\pi\hbar}\right)^2 \frac{2^{\gamma+2}}{8a^2\pi^2}\left(\frac{\pi a}{v\beta}\right)^{2\gamma} \\
&\quad\times\sum_\alpha \alpha\int dx' \frac{\alpha\sin(2\tau')\left[\cos^2(\tau')\sinh^2(x')-\cosh^2(x')\sin^2(\tau')+\frac{\gamma\sinh^2(2x')}{2}\right]}{(\cosh(2x')-\cos(2\tau'))^{\gamma+2}} \\
&= 4v\gamma N_c L\left(\frac{a_c t}{2\pi\hbar}\right)^2 \frac{2^{\gamma+2}}{8a^2\pi^2}\left(\frac{\pi a}{v\beta}\right)^{2\gamma} \\
&\quad\times\int dx' \frac{\sin(2\tau')\left[\cos^2(\tau')\sinh^2(x')-\cosh^2(x')\sin^2(\tau')+\frac{\gamma\sinh^2(2x')}{2}\right]}{(\cosh(2x')-\cos(2\tau'))^{\gamma+2}}
\end{aligned}$$

We can pull the factor of $\sin(2\tau')$ out of the integral to get our final expression in terms of an as-yet unevaluated integral over x. This gives

$$\langle J_E(\tau')J\rangle = 4v\gamma N_c L\left(\frac{a_c t}{2\pi\hbar}\right)^2 \frac{2^{\gamma+2}}{8a^2\pi^2}\left(\frac{\pi a}{v\beta}\right)^{2\gamma}\sin(2\tau') \times \int dx' \frac{\cos^2(\tau')\sinh^2(x') - \cosh^2(x')\sin^2(\tau') + \frac{\gamma}{2}\sinh^2(2x')}{(\cosh(2x') - \cos(2\tau'))^{\gamma+2}} \tag{4.191}$$

Writing this in terms of $2\tau'$ gives

$$\boxed{\langle J_E(\tau')J\rangle = 2v\gamma N_c L\left(\frac{a_c t}{2\pi\hbar}\right)^2 \frac{2^{\gamma+2}}{8a^2\pi^2}\left(\frac{\pi a}{v\beta}\right)^{2\gamma}\sin(2\tau') \times \int dx' \frac{\frac{\gamma}{2}\cosh(4x') + \cos(2\tau')\cosh(2x') - \left(1+\frac{\gamma}{2}\right)}{(\cosh(2x') - \cos(2\tau'))^{\gamma+2}}} \tag{4.192}$$

Now we perform the integral over x. We can follow a similar procedure to the one used for $\langle J_e(\tau)J_e\rangle$ and $\langle J_E(\tau)J_E\rangle$, where we split up the terms in the numerator by their x-dependence and compute each one separately. These x-integrals are found in equation (4.157), though of course we must specialize to the case of $m = 2$. We get:

$$\int_{-\infty}^{\infty} \frac{1}{(\cosh(2x) - \cos(2\tau))^{\gamma+2}}dx = 2^{\gamma+2} f(\gamma,\tau,2,2) \tag{4.193a}$$

$$\int_{-\infty}^{\infty} \frac{\cosh(2x)}{(\cosh(2x) - \cos(2\tau))^{\gamma+2}}dx = 2^{\gamma+1}\left(f(\gamma,\tau,1,2) + f(\gamma,\tau,3,2)\right) \tag{4.193b}$$

$$\int_{-\infty}^{\infty} \frac{\cosh(4x)}{(\cosh(2x) - \cos(2\tau))^{\gamma+2}}dx = 2^{\gamma+1}\left(f(\gamma,\tau,0,2) + f(\gamma,\tau,4,2)\right) \tag{4.193c}$$

Substituting these expressions into equation (4.192), we get the complete (though once again relatively unenlightening) expression

$$\langle J_E(\tau')J_E\rangle = 2v\gamma N_c L\left(\frac{a_c t}{2\pi\hbar}\right)^2 \frac{1}{a^2\pi^2}\left(\frac{2\pi a}{v\beta}\right)^{2\gamma}\sin(2\tau') \tag{3.23b}$$
$$\times \begin{pmatrix} -2(1+\frac{\gamma}{2})f(\gamma,\tau',2,2) \\ +\cos(2\tau')(f(\gamma,\tau',1,2) + f(\gamma,\tau',3,2)) \\ +\frac{\gamma}{2}(f(\gamma,\tau',0,2) + f(\gamma,\tau',4,2)) \end{pmatrix}$$

Summary of correlation functions

The key results for the various current-current correlators are somewhat lost above in a sea of algebra, so we present them again here for clarity. In terms of an unspecified single-chain

Green's function we have:

$$\langle J_e(\tau)J_e\rangle = -2N_cL\left(\frac{a_cqt}{2\pi\hbar}\right)^2\sum_\alpha\int G_\alpha(x,\tau)G_\alpha(-x,-\tau)dx \tag{4.153}$$

$$\langle J_E(\tau)J_E\rangle = -2N_cL\gamma^2\left(\frac{a_cvt}{2\pi\hbar}\right)^2\sum_\alpha\int dx\left[(k_F+i\alpha\partial_x)G_\alpha(x,\tau)\right]\times\left[(k_F-i\alpha\partial_x)G_\alpha(-x,-\tau)\right] \tag{2.28b}$$

$$\langle J_E(\tau)J\rangle = 2v\gamma N_cL\left(\frac{a_ct}{2\pi\hbar}\right)^2\sum_\alpha\int dx\,G_\alpha(x,\tau)(k_F-i\alpha\partial_x)G_\alpha(-x,-\tau) \tag{2.28c}$$

Once we substitute the Luttinger liquid Green's function as given in equation (2.29) and simplify, we have (in terms of the scaled imaginary time $\tau' = \tau\pi/\beta$):

$$\langle J_e(\tau')J_e\rangle = 4N_cL\left(\frac{a_cqt}{2\pi\hbar}\right)^2\frac{2^\gamma a}{(2\pi a)^2}\left(\frac{\pi a}{v\beta}\right)^{2\gamma-1}\int dx'\frac{1-\cos(2\tau')\cosh(2x')}{[\cosh(2x')-\cos(2\tau')]^{\gamma+1}} \tag{4.155}$$

$$\langle J_E(\tau')J_E\rangle = N_cL\gamma^2\left(\frac{a_cvt}{2\pi\hbar}\right)^2\frac{2^{\gamma+1}}{a^3\pi^2}\left(\frac{\pi a}{v\beta}\right)^{2\gamma+1}\times\int dx'\left(\frac{a+b\cosh(2x')+c\cosh(4x')+d\cosh(6x')}{[\cosh(2x')-\cos(2\tau')]^{\gamma+3}}\right) \tag{4.184}$$

$$\langle J_E(\tau')J\rangle = 2v\gamma N_cL\left(\frac{a_ct}{2\pi\hbar}\right)^2\frac{2^{\gamma+2}}{8a^2\pi^2}\left(\frac{\pi a}{v\beta}\right)^{2\gamma}\sin(2\tau')\times\int dx'\frac{\frac{\gamma}{2}\cosh(4x')+\cos(2\tau')\cosh(2x')-\left(1+\frac{\gamma}{2}\right)}{(\cosh(2x')-\cos(2\tau'))^{\gamma+2}} \tag{4.192}$$

where in the expression for $\langle J_E(\tau')J_E\rangle$, the quantities a, b, c, and d are unitless functions of τ' as given in equation (4.185).

If we further perform the integration over x', the results are in equations (4.162), (3.23a), and (3.23b) respectively. We have not actually reproduced the exact expressions in this summary section since the results are relatively unenlightening. It is noteworthy, however, that the expressions for $\langle J_e(\tau')J_e\rangle$ and $\langle J_E(\tau')J_E\rangle$ are even about $\tau' = \frac{\pi}{2}$, while the expression for $\langle J_E(\tau')J\rangle$ is odd. This will lead to vanishing thermopower (see section 4.3 below).

Response functions

Recall that the response functions are given in terms of the current-current correlators by equations (2.2) and (2.4), reproduced here for convenience. The transport coefficients of

interest are

$$\sigma = \frac{e^2}{T} L^{(11)} \tag{2.2a}$$

$$\kappa = \frac{1}{T^2}\left[L^{(22)} - \frac{(L^{(12)})^2}{L^{(11)}}\right] \tag{2.2b}$$

$$S = -\frac{1}{eT}\frac{L^{(12)}}{L^{(11)}} \tag{2.2c}$$

where

$$L^{(il)} = \lim_{\omega\to 0}\lim_{\delta\to 0}\frac{1}{\omega}\left[\frac{-iT}{\Omega}\int_0^\beta d\tau e^{i\omega\tau}\langle T_\tau j_l(\tau) j_i(0)\rangle\right]_{i\omega\to\omega+i\delta} \tag{2.4}$$

We first use these expressions to derive power law temperature dependence for the two conductivities and to show that thermopower is 0, and then we calculate the Lorenz number numerically to find its dependence on interaction strength γ and the deviation from the Wiedemann-Franz law.

Electrical conductivity

Our first step is to convert the integral over τ to an integral over $\tau' = \tau\frac{\pi}{\beta}$, since we have written our results for the correlation functions in terms of that scaled time variable. Then equation (2.4) becomes

$$L^{(il)} = \lim_{\omega\to 0}\lim_{\delta\to 0}\frac{1}{\omega}\left[\frac{-i}{\pi\Omega}\int_0^\pi d\tau' e^{i\omega\beta\tau'/\pi}\langle T_\tau j_l(\tau') j_i(0)\rangle\right]_{i\omega\to\omega+i\delta} \tag{4.195}$$

We will want to take the limit as $\omega \to 0$, but in this case we will have neither an analytic nor numerical result on which we can directly calculate that limit since the integrand still depends on β. However, if the limit is well-defined, then the limit as $\omega\beta \to 0$ will be the same as the limit as $\omega \to 0$, so we can rewrite our expression in terms of $\omega\beta$. We call this quantity $2n$ as a reminder that the integral will only be computed for Matsubara frequencies $\omega_n = 2\pi n/\beta$. The result will lead to a function that can be analytically continued in n-space, and then the limit as the unitless variable n goes to 0 can be taken along the real axis. This gives equation (4.68), or equivalently

$$L^{(il)} = \lim_{n\to 0}\lim_{\delta\to 0}\frac{\beta}{2\pi n}\left[\frac{-i}{\pi\Omega}\int_0^\pi d\tau' e^{2in\tau'}\langle T_\tau j_l(\tau') j_i(0)\rangle\right]_{in\to n+i\delta'} \tag{4.196}$$

where $\delta' = \delta\beta/2\pi$ is still a small real number. As discussed in section 4.1 above, the value of δ' will never appear in our calculations, so its being scaled by β is not a problem. Specializing to the case of the electrical conductivity, we combine equations (2.2a) and (4.196) to get

$$\sigma = \lim_{n\to 0}\lim_{\delta\to 0}\frac{e^2}{2\pi n T^2}\left[\frac{-i}{\pi\Omega}\int_0^\pi d\tau' e^{2in\tau'}\langle J(\tau') J(0)\rangle\right]_{in\to n+i\delta'} \tag{4.197}$$

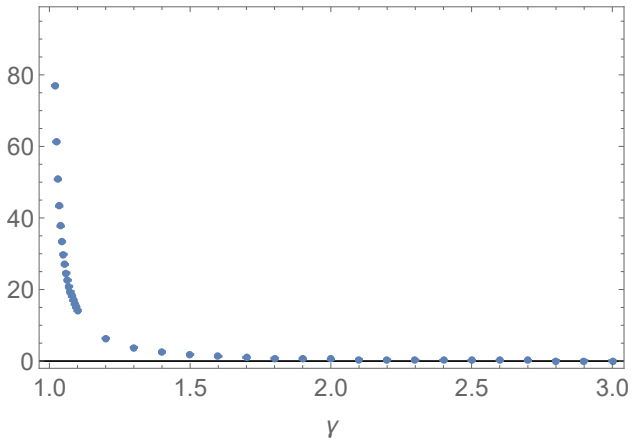

Figure 4.4: Numerical part of σ (second line of equation 4.199) for the Luttinger liquid model, evaluated with cutoff $\epsilon = 10^{-1.5}$ (see section 4.1 for a definition and explanation of the cutoff).

or in terms of the electrical current operator,

$$\sigma = \lim_{n\to 0}\lim_{\delta\to 0}\frac{1}{2\pi n T^2}\left[\frac{-i}{\pi\Omega}\int_0^\pi d\tau' e^{2in\tau'}\langle J_e(\tau')J_e(0)\rangle\right]_{in\to n+i\delta'} \tag{4.198}$$

Finally we can substitute in our expression for the current-current correlator, equation (4.162) to complete our calculation of the conductivity. The result is

$$\begin{aligned}\sigma =& \frac{4N_c L}{2\pi T^2\Omega}\left(\frac{a_c q t}{2\pi\hbar}\right)^2\frac{2a}{(2\pi a)^2}\left(\frac{2\pi a}{v\beta}\right)^{2\gamma-1} \\ &\times \lim_{n\to 0}\lim_{\delta\to 0}\left[\frac{-i}{n\pi}\int_0^\pi d\tau' e^{2in\tau'}\Big(2f(\gamma,\tau',1,1)-\cos(2\tau')\big(f(\gamma,\tau',0,1)+f(\gamma,\tau',2,1)\big)\Big)\right]_{in\to n+i\delta'}\end{aligned} \tag{4.199}$$

This leads to an overall temperature dependence of

$$\boxed{\sigma \propto T^{2\gamma-3}} \tag{4.200}$$

A plot of the numerical evaluation of the second line of equation (4.199) for various values of γ is shown in figure 4.4, with error bars calculated as described in section 4.1. (In general the errors are small enough that the error bars are barely visible.)

Thermal conductivity

The thermal conductivity is given in terms of the $L^{(ij)}$ coefficients by equation (2.2b), or

$$\kappa = \frac{1}{T^2}\left[L^{(22)} - \frac{(L^{(12)})^2}{L^{(11)}}\right] \tag{2.2b}$$

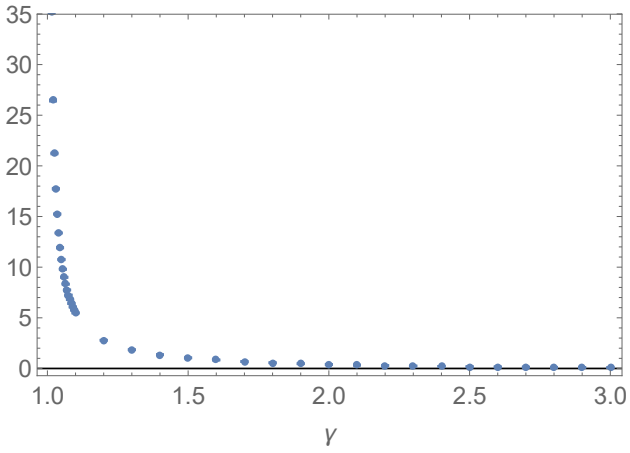

Figure 4.5: Numerical part of κ (second half of equation 4.202) for the Luttinger liquid model, evaluated with cutoff $\epsilon = 10^{-1.5}$ (see section 4.1 for a definition and explanation of the cutoff).

As we will show in the following section, 4.3, the coefficient $L^{(12)}$ vanishes in our model, so that we only need to look at the first term. In that case, we combine (2.2b) with the Kubo formula written in terms of the scaled imaginary time τ', as given in equation (4.196), which gives:

$$\kappa = \lim_{n\to 0}\lim_{\delta\to 0}\frac{1}{2\pi n T^3}\left[\frac{-i}{\pi\Omega}\int_0^\pi d\tau' e^{2in\tau'}\langle J_E(\tau')J_E(0)\rangle\right]_{in\to n+i\delta'} \tag{4.201}$$

Finally, we substitute in the expression for the current-current correlator, equation (3.23a). We then have:

$$\kappa = \frac{N_c L\gamma^2}{2\pi T^3\Omega}\left(\frac{a_c v t}{2\pi\hbar}\right)^2\frac{1}{2a^3\pi^2}\left(\frac{2\pi a}{v\beta}\right)^{2\gamma+1}\lim_{n\to 0}\lim_{\delta\to 0}\left[\frac{-i}{n\pi}\int_0^\pi d\tau' e^{2in\tau'}(\cdots)\right]_{in\to n+i\delta'} \tag{4.202}$$

where $(\cdots)$ is the expression in the large parentheses in equation (3.23a).

This leads to an overall temperature dependence of

$$\boxed{\kappa \propto T^{2\gamma-2}} \tag{4.203}$$

The numerical evaluation of the numerical part (unitless second half of equation 4.202) is shown with error bars in figure 4.5.

Thermopower

The thermopower is given in terms of the $L^{(ij)}$ coefficients by equation (2.2c), or

$$S = -\frac{1}{eT}\frac{L^{(12)}}{L^{(11)}} \tag{2.2c}$$

The numerator, $L^{(12)}$ contains a Fourier transform of the correlation function $\langle J_E(\tau)J\rangle$, and as calculated in section 4.3 above, that is given by

$$\langle J_E(\tau')J_E\rangle = 2v\gamma N_c L\left(\frac{a_c t}{2\pi\hbar}\right)^2 \frac{1}{a^2\pi^2}\left(\frac{2\pi a}{v\beta}\right)^{2\gamma}\sin(2\tau') \tag{3.23b}$$
$$\times\begin{pmatrix} -2(1+\frac{\gamma}{2})f(\gamma,\tau',2,2) \\ +\cos(2\tau')(f(\gamma,\tau',1,2)+f(\gamma,\tau',3,2)) \\ +\frac{\gamma}{2}(f(\gamma,\tau',0,2)+f(\gamma,\tau',4,2)) \end{pmatrix}$$

This correlation function is odd about $\tau' = \pi/2$, and thus as argued in section 4.1 above, we conclude that

$$L^{(12)} = 0 \tag{4.204}$$

We can then additionally conclude that the thermopower is precisely 0 in our model, which makes sense given that our Hamiltonian is particle-hole symmetric. We thus conclude that

$$\boxed{S = 0} \tag{4.205}$$

We view the equivalent of the correction to the density of states to get nonzero thermopower from section 4.2 as beyond the scope of this dissertation. For a calculation of nonzero thermopower in a model similar to ours, please see reference [98].

Lorenz number

Comparing the temperature power laws for electrical (equation 4.200) and thermal (equation 4.203) conductivities, we see that the thermal conductivity is one power higher in temperature, which means that the Lorenz number $\frac{\kappa}{\sigma T}$ will be well-defined and temperature-independent.

Furthermore, in calculating the Lorenz number we will find that all of the material-dependent quantities in the expressions for the thermal and electrical conductivities will precisely cancel and thus by evaluating the integrals over the Appell functions numerically we will be able to find precise numerical results for the Lorenz number, allowing us to explicitly find the violation of the Wiedemann-Franz law.

We will break the calculation into two parts. First we divide the unitful prefactors, and then we numerically evaluate the integrals (including performing numerical analytic continuation as described in section 4.1) to get the results shown in figures 4.4 and 4.5. The prefactor portions are:

$$\sigma_{\mathrm{p}} = \frac{4N_c L}{2\pi T^2\Omega}\left(\frac{a_c q t}{2\pi\hbar}\right)^2 \frac{2a}{(2\pi a)^2}\left(\frac{2\pi a}{v\beta}\right)^{2\gamma-1}$$
$$\kappa_{\mathrm{p}} = \frac{N_c L\gamma^2}{2\pi T^3\Omega}\left(\frac{a_c v t}{2\pi\hbar}\right)^2 \frac{1}{2a^3\pi^2}\left(\frac{2\pi a}{v\beta}\right)^{2\gamma+1}$$

Then dividing these and dividing by T we have:

$$\begin{aligned}
L_{\mathrm{p}} &= \frac{\kappa_{\mathrm{p}}}{\sigma_{\mathrm{p}} T} \\
&= \frac{\frac{N_c L \gamma^2}{2\pi T^3 \Omega} \left(\frac{a_c v t}{2\pi\hbar}\right)^2 \frac{1}{2a^3\pi^2} \left(\frac{2\pi a}{v\beta}\right)^{2\gamma+1}}{\frac{4N_c L}{2\pi T\Omega} \left(\frac{a_c q t}{2\pi\hbar}\right)^2 \frac{2a}{(2\pi a)^2} \left(\frac{2\pi a}{v\beta}\right)^{2\gamma-1}} \\
&= \frac{\frac{\gamma^2}{T^2} \left(\frac{a_c v t}{2\pi\hbar}\right)^2 \frac{2/a}{(2\pi a)^2} \left(\frac{2\pi a}{v\beta}\right)^{2}}{4 \left(\frac{a_c q t}{2\pi\hbar}\right)^2 \frac{2a}{(2\pi a)^2}} \\
&= \frac{\frac{\gamma^2}{T^2} v^2 (2/a) \left(\frac{2\pi a}{v\beta}\right)^{2}}{4q^2(2a)} \\
&= \left(\frac{k_B}{q}\right)^2 \pi^2 \gamma^2
\end{aligned}$$

Comparing with the expected value from the Wiedemann-Franz Law, which is

$$L_0 = \frac{\pi^2}{3} \left(\frac{k_B}{e}\right)^2, \tag{4.206}$$

we see that

$$L_{\mathrm{p}} = 3\, L_0 \gamma^2 \tag{4.207}$$

Thus our complete result for L can be written as

$$\begin{aligned}
L = \gamma^2 L_0 \\
\times \frac{3 \times \lim\limits_{n\to 0} \lim\limits_{\delta\to 0} \left[\frac{-i}{n\pi} \int_0^\pi d\tau' e^{2in\tau'} \big(\cdots\big)\right]_{in\to n+i\delta'}}{\lim\limits_{n\to 0} \lim\limits_{\delta\to 0} \left[\frac{-i}{n\pi} \int_0^\pi d\tau' e^{2in\tau'} \Big(2f(\gamma,\tau',1,1) - \cos(2\tau')\big(f(\gamma,\tau',0,1) + f(\gamma,\tau',2,1)\big)\Big)\right]_{in\to n+i\delta'}}
\end{aligned} \tag{4.208}$$

where

$$\big(\cdots\big) = \begin{pmatrix}
-4(2+\gamma^2-2\cos(4\tau'))f(\gamma,\tau',3,3) \\
+\cos(2\tau')(2+\gamma^2-2\cos(4\tau'))(f(\gamma,\tau',2,3)+f(\gamma,\tau',4,3)) \\
+2(1+\gamma^2-\cos(4\tau'))(f(\gamma,\tau',1,3)+f(\gamma,\tau',5,3)) \\
-\gamma^2\cos(2\tau')(f(\gamma,\tau',0,3)+f(\gamma,\tau',6,3))
\end{pmatrix} \tag{4.209}$$

The plot of L/L_0 as a function of interaction strength γ is shown in figure 4.6. To find the error bars, for each value of γ we take many samples where the numerical integrals

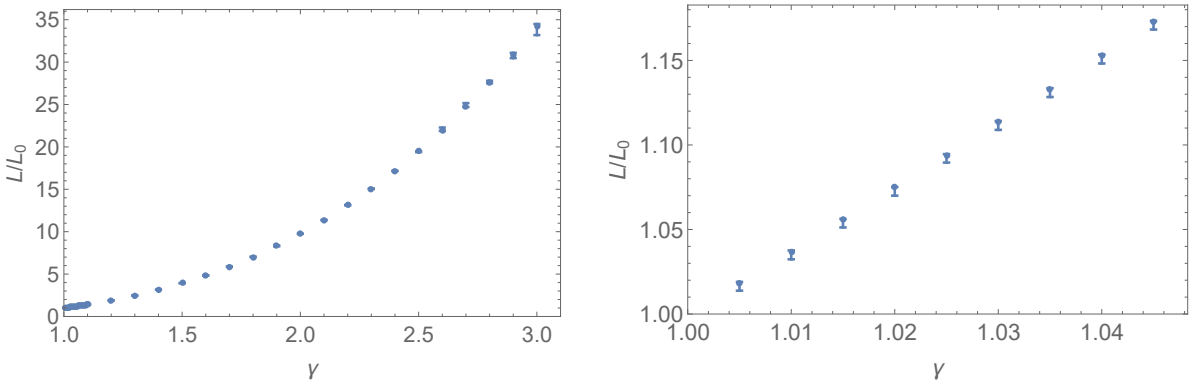

(a) (b)

Figure 4.6: (a) Numerical evaluation of the Lorenz number as a function of γ in the full Luttinger liquid model. (b) Zooming in on small interaction strengths, the Lorenz number approaches the expected value from the Wiedemann-Franz Law, L_0, in the noninteracting limit $\gamma \to 1$. Numerical integrals are evaluated with cutoff $\epsilon = 10^{-1.5}$ (see section 4.1 for a definition and explanation of the cutoff).

are allowed to vary randomly within their range of precision, and the Lorenz number is recomputed using those values; the error bar indicates the smallest interval containing 68% (one sigma) of samples in the resulting distribution of Lorenz number values. See section 4.1 for details.

We see from the graph that as expected, L/L_0 goes to 1 in the noninteracting limit $\gamma = 1$, but the Wiedemann-Franz law is violated in the presence of interactions. As in the previous model, this appears to follow a power law in γ, and we can confirm by plotting

$$a(\gamma) = \frac{\log(L/L_0)}{\log(\gamma)} \tag{4.112}$$

The result (with error bars now omitted for clarity) is shown in figure 2.3. It appears from the data that L/L_0 scales as approximately $\gamma^{3.65}$ for $\gamma \approx 1$ and $\gamma^{3.2}$ for larger γ. While there is no clear intuitive explanation for this precise exponent, there is actually a fairly simple explanation for why we should expect L/L_0 to scale as approximately γ^4 in this model and γ^2 in our earlier model.

Lorenz number scaling argument

Here we are interested only in the numerical value of L as a function of γ, so we consider

$$L \sim \frac{\kappa}{\sigma} \sim \frac{\langle J_E(\tau) J_E \rangle}{\langle J_e(\tau) J_e \rangle} \tag{4.210}$$

But if we look at our expressions for the current-current correlators,

$$\langle J_e(\tau)J_e\rangle = -2N_cL\left(\frac{a_cqt}{2\pi\hbar}\right)^2\sum_\alpha\int G_\alpha(x,\tau)G_\alpha(-x,-\tau)dx \tag{4.153}$$

and

$$\langle J_E(\tau)J_E\rangle = -2N_cL\gamma^2\left(\frac{a_cvt}{2\pi\hbar}\right)^2\sum_\alpha\int dx\ [(k_F+i\alpha\partial_x)G_\alpha(x,\tau)]\times[(k_F-i\alpha\partial_x)G_\alpha(-x,-\tau)]\,, \tag{2.28b}$$

we see two main differences:

1. $\langle J_E(\tau)J_E\rangle$ has a factor of γ^2 in front, which came from splitting the $[\nabla]$ operators into parts proportional to $\alpha\phi-\theta$ and $-\alpha\phi-\theta$ as in equation (4.168). This gave one factor of γ for each $[\nabla]$ operator, or two factors in total for the current-current correlator.

2. $\langle J_E(\tau)J_E\rangle$ has derivatives of the Green's function instead of just the function itself. But the Green's function looks roughly like

$$G(x)\sim f(x)^{-\gamma} \tag{4.211}$$

so that taking two derivatives pulls down two factors of γ.

This explains why $\langle J_E(\tau)J_E\rangle$ (and therefore κ) has roughly a factor of γ^4 that does not appear in $\langle J_e(\tau)J_e\rangle$ (and therefore σ), so that $L\sim\gamma^4$.

We also want to understand why the first model gives roughly $L\sim\gamma^2$. In that model, the distinguishing feature of $\langle J_E(\tau)J_E\rangle$ compared with $\langle J_e(\tau)J_e\rangle$ is two extra factors of energy in the integrand. To be precise, in equation (4.67), n_{il} is 2 for $\langle J_E(\tau)J_E\rangle$ and 0 for $\langle J_e(\tau)J_e\rangle$. The energy for a linearized spectrum like the one we consider is proportional to $\pm k-k_F$, and if we convert the expression to real space like in section 4.5, this precisely gives the modified derivative $k_F\pm i\partial_x$. This means that the noninteracting model still incorporates the two factors that come from derivatives of the Green's function.

What about the two factors of γ from the $[\nabla]$ operators? In the real-space version of the noninteracting calculation as presented in section 4.5, we see that the expression for the energy current operator is much simpler than in the full interacting calculation. Nothing like the $[\nabla]$ operators even appears. Thus these two factors of γ are missing.

Our conclusion based on these intuitive arguments is that in the noninteracting model we would have $L/L_0=\gamma^2$ and for the full Luttinger model we would have $L/L_0=\gamma^4$. These are indeed close to the numerically observed values, which in the large γ limit are $\gamma^{2.05}$ and $\gamma^{3.2}$ respectively. (In the latter case there is apparently a somewhat large correction due to the precise functional form of the Green's function, though the qualitative result that L is a power law in γ and with a higher power in the more complete model is consistent with the simplified γ^4 prediction.)

4.4 Luttinger Liquid Green's function derivation (and $\tilde{G}$)

In our calculations above, we have used the following expression for the Green's function of an isolated Luttinger liquid:

$$G_\alpha(x,\tau) = -\frac{e^{i\alpha k_F x}}{2\pi a}\left[\frac{-ia}{\frac{v\beta}{\pi}\sinh\left(\frac{x-iv\tau}{v\beta/\pi}\right)}\right]^{\frac{\gamma-\alpha}{2}}\left[\frac{ia}{\frac{v\beta}{\pi}\sinh\left(\frac{x+iv\tau}{v\beta/\pi}\right)}\right]^{\frac{\gamma+\alpha}{2}} \tag{2.29}$$

where γ is related to the Luttinger interaction parameter K by $\gamma = (K + K^{-1})/2$.

It is surprisingly difficult to find in the literature a precise expression for the Green's function at finite temperature that includes all prefactors in a precise way.

One particularly clean discussion of the calculation, which we found helpful and enlightening, is in reference [17]. Their equation (35), translated into the notation we use in this work, states that for $T = 0$ the Green's function is:

$$G_\alpha(x,\tau) = -\frac{e^{i\alpha k_F x}}{2\pi a}\left[\frac{-ia}{x-iv\tau}\right]^{\frac{\gamma-\alpha}{2}}\left[\frac{ia}{x+iv\tau}\right]^{\frac{\gamma+\alpha}{2}} \tag{4.212}$$

(Note that they define the Green's function as $-\langle\psi^\dagger_\alpha(x,\tau)\psi_\alpha(0,0)\rangle$, but their result is actually consistent with $-\langle\psi_\alpha(x,\tau)\psi^\dagger(0,0)\rangle$ as we have defined the Green's function here.) To go from this expression to the equivalent one at finite temperature, we can look at various papers that give the finite-T Green's function but are just missing some important prefactors like $e^{i\alpha k_F x}$. One such result is equation (30) of reference [71]. Note that if we use that result, we leave off the last factor because that arises in the semi-infinite case where the Luttinger liquid has an endpoint, which is different from infinite-length 1D chains we consider here.

From that paper, it is apparent that the correct transformation to a finite temperature result is given by

$$x \pm iv\tau \to \left(\frac{v\beta}{\pi}\right)\sinh\left(\frac{x\pm iv\tau}{v\beta/\pi}\right). \tag{4.213}$$

(Note that in the $T \to 0$ limit, the right-hand side reduces to the left-hand side as expected.) This substitution transforms the 0 temperature result (equation 4.212) into the finite temperature (equation 2.29).

We can also easily derive the correct finite-temperature result in the noninteracting case by writing ψ in terms of Fourier-space operators according to equation (3.29b) from section 4.3.

The calculation is as follows:

$$
\begin{aligned}
-G_a(x,\tau) &= \langle \psi_a(x,\tau)\psi_\alpha^\dagger(0,0)\rangle \\
&= \left\langle \left(\frac{e^{i\alpha k_F x}}{\sqrt{L}}\sum_k e^{ikx}c_{k,\alpha}(\tau)\right)\left(\frac{1}{\sqrt{L}}\sum_k c_{k,\alpha}^\dagger\right)\right\rangle \\
&= \frac{e^{i\alpha k_F x}}{L}\sum_{kk'} e^{ikx}\left\langle c_{k,\alpha}(\tau)c_{k,\alpha}^\dagger\right\rangle \\
&= \frac{e^{i\alpha k_F x}}{L}\sum_{kk'} e^{ikx}e^{-\tau E_{k\alpha}/\hbar}\left\langle c_{k,\alpha}c_{k,\alpha}^\dagger\right\rangle \\
&= \frac{e^{i\alpha k_F x}}{L}\sum_{kk'} e^{ikx}e^{-\tau E_{k\alpha}/\hbar}\left(1-n_{E_{k\alpha}}\right)\delta_{kk'} \\
&= \frac{e^{i\alpha k_F x}}{L}\sum_{k} \frac{e^{ikx}e^{-\tau E_{k\alpha}/\hbar}}{1+e^{-\beta E_{k\alpha}}}
\end{aligned}
$$

Use $E_{k\alpha} = \alpha\hbar v k$:

$$
\begin{aligned}
&= \frac{e^{i\alpha k_F x}}{L}\sum_{k} \frac{e^{ikx}e^{-\tau\alpha v k}}{1+e^{-\beta\alpha\hbar v k}} \\
&= \frac{e^{i\alpha k_F x}}{2\pi}\int \frac{e^{ikx}e^{-\tau\alpha v k}}{1+e^{-\beta\alpha\hbar v k}}\,dk
\end{aligned}
$$

Let $k' = \alpha k$:

$$
\begin{aligned}
&= \frac{e^{i\alpha k_F x}}{2\pi}\times\alpha\int_{-\alpha\times\infty}^{\alpha\times\infty} \frac{e^{i\alpha k' x}e^{-\tau v k'}}{1+e^{-\beta\hbar v k'}}\,dk \\
&= \frac{e^{i\alpha k_F x}}{2\pi}\int_{-\infty}^{\infty} \frac{e^{i\alpha k' x}e^{-\tau v k'}}{1+e^{-\beta\hbar v k'}}\,dk
\end{aligned}
$$

Since $0 < \tau < \hbar\beta$:

$$
= \frac{e^{i\alpha k_F x}}{2\pi}\left[\frac{\pi}{\beta\hbar v}\csc\left(\frac{\tau v - i\alpha x}{\beta\hbar v/\pi}\right)\right]
$$

using $\csc(a) = i\,\mathrm{csch}(ia)$:

$$
\begin{aligned}
&= \frac{e^{i\alpha k_F x}}{2\pi}\left[\frac{i\pi}{\beta\hbar v}\mathrm{csch}\left(\frac{\alpha x + i\tau v}{\beta\hbar v/\pi}\right)\right] \\
&= \frac{e^{i\alpha k_F x}}{2\pi}\left[\frac{i\alpha\pi}{\beta\hbar v}\mathrm{csch}\left(\frac{x + i\alpha\tau v}{\beta\hbar v/\pi}\right)\right]
\end{aligned}
$$

Setting $\hbar = 1$, this matches the Green's function as given in equation (2.29) in the case $\gamma = 1$.

We also want to write $\langle \psi_a^\dagger(x,\tau)\psi_\alpha(0,0)\rangle$ in terms of the Green's function. In the case that $\tau = 0$, the relationship can be derived very simply, as

$$\langle \psi_\alpha^\dagger(x)\psi_\alpha(0)\rangle = \langle \{\psi_\alpha^\dagger(x), \psi_\alpha(0)\} - \psi_\alpha(0)\psi_\alpha^\dagger(x)\rangle = \delta(x) + G_\alpha(-x,0) \tag{4.214}$$

The $\delta(x)$ part we can neglect. To see this, we will calculate $\langle \psi_a^\dagger(x,\tau)\psi_\alpha(0,0)\rangle$ in the noninteracting limit the same way we calculated $G_\alpha(x,\tau)$ above:

$$\begin{aligned}
\langle \psi_a^\dagger(x,\tau)\psi_\alpha(0,0)\rangle &= \left\langle \left(\frac{e^{-i\alpha k_F x}}{\sqrt{L}}\sum_k e^{-ikx} c_{k,\alpha}^\dagger(\tau)\right)\left(\frac{1}{\sqrt{L}}\sum_k c_{k,\alpha}\right)\right\rangle \\
&= \frac{e^{-i\alpha k_F x}}{L}\sum_{kk'} e^{-ikx}\left\langle c_{k,\alpha}^\dagger(\tau)c_{k,\alpha}\right\rangle \\
&= \frac{e^{-i\alpha k_F x}}{L}\sum_{kk'} e^{-ikx}e^{\tau E_{k\alpha}/\hbar}\left\langle c_{k,\alpha}^\dagger c_{k,\alpha}\right\rangle \\
&= \frac{e^{-i\alpha k_F x}}{L}\sum_{kk'} e^{-ikx}e^{\tau E_{k\alpha}/\hbar} n_{E_{k\alpha}}\delta_{kk'} \\
&= \frac{e^{-i\alpha k_F x}}{L}\sum_{k} \frac{e^{-ikx}e^{\tau E_{k\alpha}/\hbar}}{1+e^{\beta E_{k\alpha}}} \\
&= \frac{e^{-i\alpha k_F x}}{L}\sum_{k} \frac{e^{-ikx}e^{\tau\alpha v k}}{1+e^{\beta\alpha\hbar v k}} \\
&= \frac{e^{-i\alpha k_F x}}{2\pi}\int \frac{e^{-ikx}e^{\tau\alpha v k}}{1+e^{\beta\alpha\hbar v k}}\,dk \\
&= \frac{e^{-i\alpha k_F x}}{2\pi}\times\alpha\int_{-\alpha\times\infty}^{\alpha\times\infty} \frac{e^{-i\alpha k' x}e^{\tau v k'}}{1+e^{\beta\hbar v k'}}\,dk' \\
&= \frac{e^{-i\alpha k_F x}}{2\pi}\int_{-\infty}^{\infty} \frac{e^{-i\alpha k' x}e^{\tau v k'}}{1+e^{\beta\hbar v k'}}\,dk' \\
&= \frac{e^{-i\alpha k_F x}}{2\pi}\left[\frac{\pi}{\beta\hbar v}\csc\left(\frac{\tau v - i\alpha x}{\beta\hbar v/\pi}\right)\right] \\
&= \frac{e^{-i\alpha k_F x}}{2\pi}\left[\frac{i\pi}{\beta\hbar v}\mathrm{csch}\left(\frac{\alpha x + i\tau v}{\beta\hbar v/\pi}\right)\right] \\
&= \frac{e^{-i\alpha k_F x}}{2\pi}\left[\frac{i\alpha\pi}{\beta\hbar v}\mathrm{csch}\left(\frac{x + i\alpha\tau v}{\beta\hbar v/\pi}\right)\right]
\end{aligned}$$

From these derivations, we see that for $\tau = 0$, equation (4.214) becomes

$$\begin{aligned}\delta(x) &= \langle \psi_\alpha^\dagger(x)\psi_\alpha(0)\rangle + \langle \psi_\alpha(-x)\psi^\dagger(0)\rangle \\ &= \frac{e^{-i\alpha k_F x}}{2\pi}\int_{-\infty}^{\infty}\frac{e^{-i\alpha k' x}}{1+e^{\beta\hbar v k'}}\,dk' + \frac{e^{-i\alpha k_F x}}{2\pi}\int_{-\infty}^{\infty}\frac{e^{-i\alpha k' x}}{1+e^{-\beta\hbar v k'}}\,dk' \\ &= \frac{e^{-i\alpha k_F x}}{2\pi}\int_{-\infty}^{\infty} e^{-i\alpha k' x}\,dk' \\ &= e^{-i\alpha k_F x}\delta(x) \\ &= \delta(x)\end{aligned}$$

so that the delta function comes from integrating over the infinite set of occupied states below the Fermi level, where $(1 + e^{\beta E})$ is 1. If we do proper normal-ordering or if we recall that physically there is a finite band rather than states extending to infinitely low energy, this contribution should vanish.

We thus conclude that in the case of $\tau = 0$, we have

$$\tilde{G}_\alpha(x, 0) \equiv \langle \psi_\alpha^\dagger(x, 0)\psi_\alpha(0, 0)\rangle = -G_\alpha(-x, 0) \tag{4.215}$$

At nonzero τ, since the Green's function depends only on the combinations $x \pm iv\tau$, we should expect that $\tilde{G}$ will behave the same way, either sending $x \pm iv\tau \to x \mp iv\tau$ or keeping $x \pm iv\tau$ invariant. Then we expect that equation (4.215) can be extended to $\tau \neq 0$ either by

$$\tilde{G}_\alpha(x, \tau) = -G_\alpha(-x, \tau) \tag{4.216}$$

or by

$$\tilde{G}_\alpha(x, \tau) = -G_\alpha(-x, -\tau) \tag{4.217}$$

Our derivations for G and $\tilde{G}$ in the noninteracting limit $\gamma = 1$ are consistent with the latter possibility, so we conclude that indeed

$$\tilde{G}_\alpha(x, \tau) = -G_\alpha(-x, -\tau) \tag{4.217}$$

Of course, this result can also be derived by just following the same calculation that led to the Green's function in the first place. We will not show that calculation here.

4.5 Confirmation via special limits and noninteracting models

To help verify our results, we will (1) compare the results of our two models in the noninteracting limit, and (2) rederive the current operators for the real-space calculation directly in the noninteracting limit. In both cases we verify that our results are correct.

Comparison in the noninteracting limit

For concreteness, we will compare the two models for one particular calculation, namely of $\langle J_e J_e \rangle$. We will begin from the noninteracting model in k-space and transform to real space to show agreement with our direct Luttinger liquid calculation. Our starting point is equation (4.63), reproduced here for convenience:

$$\langle J_e(\tau)J_e(0)\rangle = 4N_c \left(\frac{a_c q}{\hbar}\right)^2 \left(\frac{L}{2\pi}\right)^2 \int_{EE'} |t(E,E')|^2 g(E)g(E') \left[\frac{e^{\tau(E-E')}}{(1+e^{\beta E})\,(1+e^{-\beta E'})}\right] dE\, dE' \tag{4.63}$$

We follow the following steps:

$$\langle J_e(\tau)J_e(0)\rangle = 4N_c \left(\frac{a_c q}{\hbar}\right)^2 \left(\frac{L}{2\pi}\right)^2 \int_{EE'} |t(E,E')|^2 g(E)g(E') \left[\frac{e^{\tau(E-E')}}{(1+e^{\beta E})\,(1+e^{-\beta E'})}\right] dE\, dE'$$

Rewrite with $\tau' = \tau\frac{\pi}{\beta}$:

$$\langle J_e(\tau')J_e(0)\rangle = 4N_c \left(\frac{a_c q}{\hbar}\right)^2 \left(\frac{L}{2\pi}\right)^2 \int_{EE'} |t(E,E')|^2 g(E)g(E') \left[\frac{e^{\tau'\beta(E-E')/\pi}}{(1+e^{\beta E})\,(1+e^{-\beta E'})}\right] dE\, dE'$$

Convert to an integrals over k and k':

$$= 4N_c \left(\frac{a_c q}{\hbar}\right)^2 \left(\frac{L}{2\pi}\right)^2 \int_{kk'} |t(k,k')|^2 \left[\frac{e^{\tau'\beta(E_k-E_{k'})/\pi}}{(1+e^{\beta E_k})\,(1+e^{-\beta E_{k'}})}\right] dk\, dk'$$

Substitute Fourier transforms for $t(k,k')$ using equation (4.232) from section 4.6:

$$= 4N_c \left(\frac{a_c q}{\hbar}\right)^2 \left(\frac{L}{2\pi}\right)^2 \int_{kk'} \left|\frac{1}{L}\int dx\, dx' \left[t_\alpha(x-x')e^{-i\alpha k_F(x-x')}\right] e^{-ikx}e^{ik'x'}\right|^2 \times \left[\frac{e^{\tau'\beta(E_k-E_{k'})/\pi}}{(1+e^{\beta E_k})\,(1+e^{-\beta E_{k'}})}\right] dk\, dk'$$

$$= \frac{4N_c}{(2\pi)^2} \left(\frac{a_c q}{\hbar}\right)^2 \int \begin{matrix} dx_1\, dx_2 \\ dx_3\, dx_4 \\ dk\, dk' \end{matrix} \left[t_\alpha(x_1-x_2)e^{-i\alpha k_F(x_1-x_2)}\right] e^{-ikx_1}e^{ik'x_2} \left[t_\alpha(x_3-x_4)^* e^{i\alpha k_F(x_3-x_4)}\right] \times e^{ikx_3}e^{-ik'x_4} \left[\frac{e^{\tau'\beta(E_k-E_{k'})/\pi}}{(1+e^{\beta E_k})\,(1+e^{-\beta E_{k'}})}\right]$$

$$= \frac{4N_c}{(2\pi)^2} \left(\frac{a_c q}{\hbar}\right)^2 \int \begin{matrix} dx_1\, dx_2 \\ dx_3\, dx_4 \end{matrix} \left[t_\alpha(x_1-x_2)e^{-i\alpha k_F(x_1-x_2)}\right] \left[t_\alpha(x_3-x_4)^* e^{i\alpha k_F(x_3-x_4)}\right] \times \left[\int dk\, \frac{e^{\tau'\beta E_k/\pi}e^{-ik(x_1-x_3)}}{1+e^{\beta E_k}}\right] \left[\int dk'\, \frac{e^{-\tau'\beta E_{k'}/\pi}e^{ik'(x_2-x_4)}}{1+e^{-\beta E_{k'}}}\right]$$

Since $\tau' \in [0, \pi]$, both integrals over k converge. We also have to be careful here because our starting point included both right- and left-moving branches of the band structure by including a factor of two, so here we must pick one by specifying E_k. For left-movers, $E_k = -\hbar v k$, while for right-movers $E_k = \hbar v k$. Here we assume right-movers. Performing the integrals, we get:

$$= \frac{4N_c}{(2\pi)^2}\left(\frac{a_c q}{\hbar}\right)^2 \int \begin{matrix} dx_1\, dx_2 \\ dx_3\, dx_4 \end{matrix} \left[t_\alpha(x_1 - x_2)e^{-i\alpha k_F(x_1-x_2)}\right]\left[t_\alpha(x_3 - x_4)^* e^{i\alpha k_F(x_3-x_4)}\right] \times \left[-\frac{i\pi}{v\beta}\mathrm{csch}\left(\frac{\pi}{v\beta}(x_3 - x_1) - i\tau'\right)\right]\left[\frac{i\pi}{v\beta}\mathrm{csch}\left(\frac{\pi}{v\beta}(x_2 - x_4) + i\tau'\right)\right]$$

As in our real-space calculation, we use $t(x, x') = \frac{t}{2\pi}\delta(x - x')$, as derived in section 4.6 below, to get:

$$= \frac{4N_c}{(2\pi)^4}\left(\frac{a_c q t}{\hbar}\right)^2 \int dx_1\, dx_3 \left[-\frac{i\pi}{v\beta}\mathrm{csch}\left(\frac{\pi}{v\beta}(x_3 - x_1) - i\tau'\right)\right]\left[\frac{i\pi}{v\beta}\mathrm{csch}\left(\frac{\pi}{v\beta}(x_1 - x_3) + i\tau'\right)\right]$$
$$= -\frac{4N_c}{(2\pi)^4}\left(\frac{a_c q t}{\hbar}\right)^2 \left(\frac{\pi}{v\beta}\right)^2 \int dx_1\, dx_3 \left[\mathrm{csch}\left(\frac{\pi}{v\beta}(x_1 - x_3) + i\tau'\right)\right]^2$$

Rewrite with center of mass and relative coordinates using equation 4.148 to get:

$$= -\frac{4N_c}{(2\pi)^4}\left(\frac{a_c q t}{\hbar}\right)^2 \left(\frac{\pi}{v\beta}\right)^2 \int dx\, (L - |x|) \left[\mathrm{csch}\left(\frac{\pi}{v\beta}x + i\tau'\right)\right]^2$$
$$\approx -\frac{4N_c L}{(2\pi)^4}\left(\frac{a_c q t}{\hbar}\right)^2 \left(\frac{\pi}{v\beta}\right)^2 \int dx \left[\mathrm{csch}\left(\frac{\pi}{v\beta}x + i\tau'\right)\right]^2$$

Finally, we rescale x to $x' = \frac{\pi}{v\beta}x$, getting:

$$\langle J_e(\tau')J_e(0)\rangle = -\frac{4N_c L}{(2\pi)^4}\left(\frac{a_c q t}{\hbar}\right)^2 \left(\frac{\pi}{v\beta}\right) \int dx' \left[\mathrm{csch}\,(x' + i\tau')\right]^2$$

Compare this with our Luttinger model result. One intermediate step in that calculation looked like,

$$\langle J_e(\tau')J_e\rangle = -2N_c L\left(\frac{a_c q t}{2\pi\hbar}\right)^2 \frac{a^{2\gamma}}{(2\pi a)^2}\left(\frac{\pi}{v\beta}\right)^{2\gamma-1} \times \sum_\alpha \int dx' \left[\sinh(x' + i\tau')\sinh(x' - i\tau')\right]^{-\gamma}\left(\frac{\sinh(x' - i\tau')}{\sinh(x' + i\tau')}\right)^\alpha \quad (4.218)$$

As we did above in choosing E_k, we will look at just the right-movers. (As shown in our earlier calculations of the current-current correlator in this model, α actually drops out, so this choice is purely about making the equivalence of the expressions manifest.) Thus we

set $\alpha = 1$. We also consider the noninteracting limit $\gamma = 1$ to show the equivalence of the models in this limit. With these substitutions we have:

$$\begin{aligned}\langle J_e(\tau')J_e\rangle &= -4N_cL\left(\frac{a_cqt}{2\pi\hbar}\right)^2\frac{a^2}{(2\pi a)^2}\left(\frac{\pi}{v\beta}\right)\\ &\qquad\times\int dx'\left[\sinh\left(x'+i\tau'\right)\sinh\left(x'-i\tau'\right)\right]^{-1}\left(\frac{\sinh\left(x'-i\tau'\right)}{\sinh\left(x'+i\tau'\right)}\right)\\ &= -\frac{4N_cL}{(2\pi)^4}\left(\frac{a_cqt}{\hbar}\right)^2\left(\frac{\pi}{v\beta}\right)\int dx'\left[\sinh\left(x'+i\tau'\right)\right]^{-2}\end{aligned}$$

which as promised is in agreement with the direct calculation from the noninteracting model.

Noninteracting real-space calculation

The purpose of this section is primarily to confirm our expressions for the thermal conductivity in the real-space Luttinger liquid model, since that derivation is rather long and hence is potentially prone to errors. We confirm the structure found above where we integrate over shifted derivatives of the Green's function of the form $(k_F + i\alpha\partial_x)G$.

Noninteracting real-space Hamiltonian

We begin by finding the Hamiltonian. We want this model to match the ones above, so we begin with the Hamiltonian from our first model,

$$H = \sum_{jk} E_k c_{jk}^\dagger c_{jk} - \sum_{jkk'} t_{kk'}\left(c_{jk}^\dagger c_{j+1,k'} + \text{h.c.}\right) \tag{2.1}$$

First, we match to the real-space Luttinger liquid model by linearizing around each Fermi point and separating the left-moving and right-moving parts of the spectrum (near $\pm k_F$ respectively). In that case, $E_k = \alpha\hbar v k$ where $\alpha = \pm 1$ for right- and left-movers respectively and v is the Fermi velocity. This gives

$$H = \sum_{jk\alpha} \alpha\hbar v k c_{jk\alpha}^\dagger c_{jk\alpha} - \sum_{jkk'}\sum_{\alpha\beta} t_{kk',\alpha\beta}\left(c_{jk\alpha}^\dagger c_{j+1,k'\beta} + \text{h.c.}\right) \tag{4.219}$$

The conversion of the hopping term to real-space should give precisely the expression h'_j from our Luttinger liquid model above (equation 4.131). To convert the on-chain part of this Hamiltonian, we substitute in our expressions for $c_{k\alpha}$ in terms of $\psi_\alpha(x)$ as given in

equation (3.29a). Then we compute (temporarily dropping the index j for convenience):

$$\begin{aligned}
H &= \sum_{k,\alpha} \alpha\hbar v k c^\dagger_{k,\alpha} c_{k,\alpha} \\
&= \sum_{k,\alpha} \alpha\hbar v k \left(\frac{1}{\sqrt{L}}\int e^{ikx} e^{i\alpha k_F x}\psi^\dagger_\alpha(x)dx\right)\left(\frac{1}{\sqrt{L}}\int e^{-ikx'} e^{-i\alpha k_F x'}\psi_\alpha(x')dx'\right) \\
&= \hbar v \sum_\alpha \alpha \int e^{i\alpha k_F(x-x')}\psi^\dagger_\alpha(x)\psi_\alpha(x')\left[\frac{1}{L}\sum_k k e^{ik(x-x')}\right]dx\,dx' \\
&= \hbar v \sum_\alpha \alpha \int e^{i\alpha k_F(x-x')}\psi^\dagger_\alpha(x)\psi_\alpha(x')\left[\frac{1}{2\pi}\int k e^{ik(x-x')}dk\right]dx\,dx' \\
&= \hbar v \sum_\alpha \alpha \int e^{i\alpha k_F(x-x')}\psi^\dagger_\alpha(x)\psi_\alpha(x')(-i\partial_x)\left[\frac{1}{2\pi}\int e^{ik(x-x')}dk\right]dx\,dx' \\
&= -i\hbar v \sum_\alpha \alpha \int e^{i\alpha k_F(x-x')}\psi^\dagger_\alpha(x)\psi_\alpha(x')(\partial_x\delta(x-x'))dx\,dx'
\end{aligned}$$

Thus the whole Hamiltonian we will use is

$$\begin{aligned}
H &= \sum_j H_j = \sum_j h_j + h'_j \\
h_j &= -i\hbar v \sum_\alpha \alpha \int e^{i\alpha k_F(x-x')}\psi^\dagger_{j,\alpha}(x)\psi_{j,\alpha}(x')(\partial_x\delta(x-x'))dx\,dx' \qquad (4.220)\\
h'_j &= -\frac{1}{2}\sum_{\alpha\beta}\int dx\,dx'\left[t_{\alpha\beta}(x-x')\psi^\dagger_{j\alpha}(x)\psi_{j+1,\beta}(x') + t_{\alpha\beta}(x-x')\psi^\dagger_{j-1,\alpha}(x)\psi_{j\beta}(x') + \text{h.c.}\right]
\end{aligned}$$

Current operators

We now want to find the current operators, both for electrical current J_e and thermal current J_E. Fortunately, the expression for the on-chain Hamiltonian never appeared in our calculation of J_e above, so our answer must be the same here as in the Luttinger liquid model (section 4.3). For J_E we do need a new calculation, though fortunately it will not be particularly difficult.

As above, we find the energy current operator using the expression

$$J_Q = \lim_{k\to 0}\frac{1}{\hbar k}\sum_j [H_j, H]e^{ika_c j} \qquad (4.48)$$

To calculate the commutator, we split up the Hamiltonian into the on-chain and hopping portions and get

$$[H_j, H] = \sum_i [H_j, H_i] = \sum_i [h_j, h_i] + [h_j, h'_i] + [h'_j, h_i] + [h'_j, h'_i] \approx \sum_i [h'_j, h_i] - [h'_i, h_j] \qquad (4.221)$$

where as above the $[h_j, h_i]$ term is 0 and the $[h'_j, h'_i]$ term is second order in the hopping and thus can be neglected. We next find $[h'_j, h_i]$:

$$[h'_j, h_i] = \frac{i\hbar v}{2}\sum_{\alpha\beta\gamma}\gamma\int dx_1\,dx_2\,dx_3\,dx_4\; t_{\alpha\beta}(x_1-x_2)e^{i\gamma k_F(x_3-x_4)}(\partial_{x_3}\delta(x_3-x_4))\big[\cdots\big]$$

$$\big[\cdots\big] = \begin{bmatrix} \psi^\dagger_{j\alpha}(x_1)\psi_{j+1,\beta}(x_2) + \psi^\dagger_{j\alpha}(x_1)\psi_{j-1,\beta}(x_2) \\ +\psi^\dagger_{j+1,\alpha}(x_1)\psi_{j\beta}(x_2) + \psi^\dagger_{j-1,\alpha}(x_1)\psi_{j\beta}(x_2) \end{bmatrix}, \psi^\dagger_{i\gamma}(x_3)\psi_{i\gamma}(x_4)\Big]$$

$$= \delta_{\beta\gamma}\delta(x_2-x_3)\begin{bmatrix} \delta_{i,j+1}\psi^\dagger_{j\alpha}(x_1)\psi_{i\gamma}(x_4) + \delta_{i,j-1}\psi^\dagger_{j\alpha}(x_1)\psi_{i\gamma}(x_4) \\ +\delta_{ij}\psi^\dagger_{j+1,\alpha}(x_1)\psi_{i\gamma}(x_4) + \delta_{ij}\psi^\dagger_{j-1,\alpha}(x_1)\psi_{i\gamma}(x_4) \end{bmatrix}$$

$$-\delta_{\alpha\gamma}\delta(x_1-x_4)\begin{bmatrix} \delta_{ij}\psi^\dagger_{i\gamma}(x_3)\psi_{j+1,\beta}(x_2) + \delta_{ij}\psi^\dagger_{i\gamma}(x_3)\psi_{j-1,\beta}(x_2) \\ +\delta_{i,j+1}\psi^\dagger_{i\gamma}(x_3)\psi_{j\beta}(x_2) + \delta_{i,j-1}\psi^\dagger_{i\gamma}(x_3)\psi_{j\beta}(x_2) \end{bmatrix}$$

We then subtract the same expression but with $i \leftrightarrow j$, and then we sum over i. The terms that have δ_{ij} will all cancel in the sum since the Kronecker delta enforces $i = j$ and thus the terms will be the same when we swap $i \leftrightarrow j$, and we thus have:

$$[h'_j, H] = \frac{i\hbar v}{2}\sum_{\alpha\beta\gamma}\gamma\int dx_1\,dx_2\,dx_3\,dx_4\; t_{\alpha\beta}(x_1-x_2)e^{i\gamma k_F(x_3-x_4)}(\partial_{x_3}\delta(x_3-x_4))\big[\cdots\big]$$

$$\big[\cdots\big] = \sum_i\Bigg[\delta_{\beta\gamma}\delta(x_2-x_3)\begin{bmatrix} \delta_{i,j+1}\psi^\dagger_{j\alpha}(x_1)\psi_{i\gamma}(x_4) + \delta_{i,j-1}\psi^\dagger_{j\alpha}(x_1)\psi_{i\gamma}(x_4) \\ -\delta_{j,i+1}\psi^\dagger_{i\alpha}(x_1)\psi_{j\gamma}(x_4) - \delta_{j,i-1}\psi^\dagger_{i\alpha}(x_1)\psi_{j\gamma}(x_4) \end{bmatrix}$$

$$-\delta_{\alpha\gamma}\delta(x_1-x_4)\begin{bmatrix} \delta_{i,j+1}\psi^\dagger_{i\gamma}(x_3)\psi_{j\beta}(x_2) + \delta_{i,j-1}\psi^\dagger_{i\gamma}(x_3)\psi_{j\beta}(x_2) \\ -\delta_{j,i+1}\psi^\dagger_{j\gamma}(x_3)\psi_{i\beta}(x_2) - \delta_{j,i-1}\psi^\dagger_{j\gamma}(x_3)\psi_{i\beta}(x_2) \end{bmatrix}\Bigg]$$

$$= \delta_{\beta\gamma}\delta(x_2-x_3)\begin{bmatrix} \psi^\dagger_{j\alpha}(x_1)\psi_{j+1,\gamma}(x_4) + \psi^\dagger_{j\alpha}(x_1)\psi_{j-1,\gamma}(x_4) \\ -\psi^\dagger_{j-1,\alpha}(x_1)\psi_{j\gamma}(x_4) - \psi^\dagger_{j+1,\alpha}(x_1)\psi_{j\gamma}(x_4) \end{bmatrix}$$

$$-\delta_{\alpha\gamma}\delta(x_1-x_4)\begin{bmatrix} \psi^\dagger_{j+1,\gamma}(x_3)\psi_{j\beta}(x_2) + \psi^\dagger_{j-1,\gamma}(x_3)\psi_{j\beta}(x_2) \\ -\psi^\dagger_{j\gamma}(x_3)\psi_{j-1,\beta}(x_2) - \psi^\dagger_{j\gamma}(x_3)\psi_{j+1,\beta}(x_2) \end{bmatrix}$$

We can next use the useful fact (equation 4.45) that for any operator depending on site j, O_j,

$$\lim_{k\to 0}\frac{1}{k}\sum_j(O_{j+1}-O_j)e^{ikaj} = -ia\sum_j O_j \tag{4.45}$$

This gives

$$J_E = -ia_c\frac{iv}{2}\sum_{j\alpha\beta\gamma}\gamma\int dx_1\,dx_2\,dx_3\,dx_4\; t_{\alpha\beta}(x_1-x_2)e^{i\gamma k_F(x_3-x_4)}(\partial_{x_3}\delta(x_3-x_4))\big[\cdots\big]$$

$$\begin{aligned}\big[\cdots\big] &= \delta_{\beta\gamma}\delta(x_2-x_3)\Big[\psi^\dagger_{j-1,\alpha}(x_1)\psi_{j\gamma}(x_4) - \psi^\dagger_{j\alpha}(x_1)\psi_{j-1,\gamma}(x_4)\Big] \\ &+ \delta_{\alpha\gamma}\delta(x_1-x_4)\Big[\psi^\dagger_{j-1,\gamma}(x_3)\psi_{j\beta}(x_2) - \psi^\dagger_{j\gamma}(x_3)\psi_{j-1,\beta}(x_2)\Big]\end{aligned} \tag{4.222}$$

Next we use the delta functions from $\big[\cdots\big]$ to eliminate one index and one position coordinate, getting

$$J_E = -ia_c\frac{iv}{2}\sum_{j\alpha\gamma}\gamma\int dx\,dx_3\,dx_4\;e^{i\gamma k_F(x_3-x_4)}(\partial_{x_3}\delta(x_3-x_4))\big[\cdots\big]$$

$$\begin{aligned}\big[\cdots\big] &= t_{\alpha\gamma}(x-x_3)\left[\psi^\dagger_{j-1,\alpha}(x)\psi_{j\gamma}(x_4)-\psi^\dagger_{j\alpha}(x)\psi_{j-1,\gamma}(x_4)\right]\\ &\quad + t_{\gamma\alpha}(x_4-x)\left[\psi^\dagger_{j-1,\gamma}(x_3)\psi_{j\alpha}(x)-\psi^\dagger_{j\gamma}(x_3)\psi_{j-1,\alpha}(x)\right]\end{aligned}$$

We can then perform integration by parts to move the derivative from the delta function:

$$\begin{aligned}J_E &= -ia_c\frac{iv}{2}\sum_{j\alpha\gamma}\gamma\int dx\,dx_3\,dx_4\;\big[\cdots\big]\\ \big[\cdots\big] &= t_{\alpha\gamma}(x-x_3)e^{i\gamma k_F(x_3-x_4)}(\partial_{x_3}\delta(x_3-x_4))\left[\psi^\dagger_{j-1,\alpha}(x)\psi_{j\gamma}(x_4)-\psi^\dagger_{j\alpha}(x)\psi_{j-1,\gamma}(x_4)\right]\\ &\quad + t_{\gamma\alpha}(x_4-x)e^{i\gamma k_F(x_3-x_4)}(\partial_{x_3}\delta(x_3-x_4))\left[\psi^\dagger_{j-1,\gamma}(x_3)\psi_{j\alpha}(x)-\psi^\dagger_{j\gamma}(x_3)\psi_{j-1,\alpha}(x)\right]\\ &= t_{\alpha\gamma}(x-x_3)e^{i\gamma k_F(x_3-x_4)}(\partial_{x_3}\delta(x_3-x_4))\left[\psi^\dagger_{j-1,\alpha}(x)\psi_{j\gamma}(x_4)-\psi^\dagger_{j\alpha}(x)\psi_{j-1,\gamma}(x_4)\right]\\ &\quad - t_{\gamma\alpha}(x_4-x)e^{i\gamma k_F(x_3-x_4)}(\partial_{x_4}\delta(x_3-x_4))\left[\psi^\dagger_{j-1,\gamma}(x_3)\psi_{j\alpha}(x)-\psi^\dagger_{j\gamma}(x_3)\psi_{j-1,\alpha}(x)\right]\\ &\to -\left[\partial_{x_3}\left(t_{\alpha\gamma}(x-x_3)e^{i\gamma k_F(x_3-x_4)}\right)\right]\delta(x_3-x_4)\left[\psi^\dagger_{j-1,\alpha}(x)\psi_{j\gamma}(x_4)-\psi^\dagger_{j\alpha}(x)\psi_{j-1,\gamma}(x_4)\right]\\ &\quad + \left[\partial_{x_4}\left(t_{\gamma\alpha}(x_4-x)e^{i\gamma k_F(x_3-x_4)}\right)\right]\delta(x_3-x_4)\left[\psi^\dagger_{j-1,\gamma}(x_3)\psi_{j\alpha}(x)-\psi^\dagger_{j\gamma}(x_3)\psi_{j-1,\alpha}(x)\right]\\ &= -e^{i\gamma k_F(x_3-x_4)}\left[(i\gamma k_F+\partial_{x_3})t_{\alpha\gamma}(x-x_3)\right]\delta(x_3-x_4)\left[\psi^\dagger_{j-1,\alpha}(x)\psi_{j\gamma}(x_4)-\psi^\dagger_{j\alpha}(x)\psi_{j-1,\gamma}(x_4)\right]\\ &\quad + e^{i\gamma k_F(x_3-x_4)}\left[(-i\gamma k_F+\partial_{x_4})t_{\gamma\alpha}(x_4-x)\right]\delta(x_3-x_4)\left[\psi^\dagger_{j-1,\gamma}(x_3)\psi_{j\alpha}(x)-\psi^\dagger_{j\gamma}(x_3)\psi_{j-1,\alpha}(x)\right]\end{aligned}$$

So now we can use the delta function of x_3 and x_4 to reduce to just two coordinates, x and x':

$$J_E = -ia_c\frac{iv}{2}\sum_{j\alpha\gamma}\gamma\int dx\,dx'\;\big[\cdots\big]$$

$$\begin{aligned}\big[\cdots\big] &= -\left[(i\gamma k_F+\partial_{x'})t_{\alpha\gamma}(x-x')\right]\left[\psi^\dagger_{j-1,\alpha}(x)\psi_{j\gamma}(x')-\psi^\dagger_{j\alpha}(x)\psi_{j-1,\gamma}(x')\right]\\ &\quad + \left[(-i\gamma k_F+\partial_{x'})t_{\gamma\alpha}(x'-x)\right]\left[\psi^\dagger_{j-1,\gamma}(x')\psi_{j\alpha}(x)-\psi^\dagger_{j\gamma}(x')\psi_{j-1,\alpha}(x)\right]\end{aligned}$$

If we relabel $x \leftrightarrow x'$ and $\alpha \leftrightarrow \gamma$ in the second term of $\left[\cdots\right]$, this becomes

$$\begin{aligned} J_E &= -ia_c \frac{iv}{2} \sum_{j\alpha\gamma} \gamma \int dx\, dx' \ \left[\cdots\right] \\ \left[\cdots\right] &= -\left[(i\gamma k_F + \partial_{x'}) t_{\alpha\gamma}(x-x')\right] \left[\psi^\dagger_{j-1,\alpha}(x)\psi_{j\gamma}(x') - \psi^\dagger_{j\alpha}(x)\psi_{j-1,\gamma}(x')\right] \\ &\quad + \left[(-i\gamma k_F + \partial_x) t_{\alpha\gamma}(x-x')\right] \left[\psi^\dagger_{j-1,\alpha}(x)\psi_{j\gamma}(x') - \psi^\dagger_{j\alpha}(x)\psi_{j-1,\gamma}(x')\right] \end{aligned}$$

and we can easily see that the two lines of $\left[\cdots\right]$ are actually the same! Thus we get:

$$J_E = -a_c v \sum_{j\alpha\gamma} \gamma \int dx\, dx' \ \left[(i\gamma k_F + \partial_{x'}) t_{\alpha\gamma}(x-x')\right] \left[\psi^\dagger_{j-1,\alpha}(x)\psi_{j\gamma}(x') - \psi^\dagger_{j\alpha}(x)\psi_{j-1,\gamma}(x')\right] \tag{4.223}$$

or rewriting to make the expression slightly nicer,

$$\boxed{J_E = -ia_c v \sum_{j\alpha\gamma} \int dx\, dx' \ \left[(k_F + i\gamma\partial_x) t_{\alpha\gamma}(x-x')\right] \left[\psi^\dagger_{j-1,\alpha}(x)\psi_{j\gamma}(x') - \psi^\dagger_{j\alpha}(x)\psi_{j-1,\gamma}(x')\right]} \tag{4.224}$$

Note that if we assume as we have done in the calculations of the current-current correlators for the Luttinger liquid model above that $t_{\alpha\beta}(x-x') = \frac{t}{2\pi}\delta_{\alpha\beta}\delta(x-x')$, this becomes

$$J_E = \frac{ia_c v t}{2\pi} \sum_{j\alpha} \int dx \ \left[\left(\hat{k}_\alpha \psi^\dagger_{j-1,\alpha}(x)\right)\psi_{j\alpha}(x) - \left(\hat{k}_\alpha \psi^\dagger_{j\alpha}(x)\right)\psi_{j-1,\alpha}(x)\right] \tag{4.225}$$

where $\hat{k}_\alpha \equiv k_F - i\alpha\partial_x$.

Current-current correlators

As noted above, J_e in this model is necessarily the same as in our Luttinger liquid model from section 4.3, and thus the correlator appearing in the calculation of electrical conductivity must also be the same.

The correlator $\langle J_E(\tau) J_E \rangle$, however, could in principle disagree so we will calculate it here and show that it agrees with the noninteracting limit of our earlier result. Since our earlier result used $t_{\alpha\beta}(x-x') = t\delta_{\alpha\beta}\delta(x-x')$, we will start with the expression for J_E that already incorporates that simplification. We thus have:

$$\begin{aligned}
\langle J_E(\tau) J_E \rangle &= \left(\frac{a_c v t}{2\pi}\right)^2 \sum_{ij\alpha\beta} \int dx\, dx' \, \langle \cdots \rangle \\
\langle \cdots \rangle &= \left\langle \left(\hat{k}_\alpha \psi^\dagger_{j-1,\alpha}(x,\tau)\right) \psi_{j\alpha}(x,\tau) \left(\hat{k}_\beta \psi^\dagger_{i\beta}(x')\right) \psi_{i-1,\beta}(x') \right. \\
&\quad \left. + \left(\hat{k}_\alpha \psi^\dagger_{j\alpha}(x,\tau)\right) \psi_{j-1,\alpha}(x,\tau) \left(\hat{k}_\beta \psi^\dagger_{i-1,\beta}(x')\right) \psi_{i\beta}(x') \right\rangle \\
&= \delta_{\alpha\beta}\delta_{ij} \left\langle \left(\hat{k}_\alpha \psi^\dagger_{j-1,\alpha}(x,\tau)\right) \psi_{j-1,\alpha}(x') \right\rangle \left\langle \psi_{j\alpha}(x,\tau) \left(\hat{k}_\alpha \psi^\dagger_{j\alpha}(x')\right) \right\rangle \\
&\quad + \delta_{\alpha\beta}\delta_{ij} \left\langle \left(\hat{k}_\alpha \psi^\dagger_{j\alpha}(x,\tau)\right) \psi_{j\alpha}(x') \right\rangle \left\langle \psi_{j-1,\alpha}(x,\tau) \left(\hat{k}_\beta \psi^\dagger_{j-1,\alpha}(x')\right) \right\rangle
\end{aligned}$$

Next note that each correlator now has only a single value of j, meaning that it is a property of a single 1D chain. Since all 1D chains are assumed to be the same, the exact value j or $j-1$ is no longer important. In that case, the correlators don't actually depend on j so that the two terms are the same and the sum on j just gives a factor of N_c, the total number of chains. Thus we'll drop the j index and perform the sum. Thus overall we get a factor of $2N_c$ to get:

$$\langle J_E(\tau) J_E \rangle = 2N_c \left(\frac{a_c v t}{2\pi}\right)^2 \sum_{\alpha} \int dx\, dx' \, \left\langle \left(\hat{k}_\alpha \psi^\dagger_{\alpha}(x,\tau)\right) \psi_{\alpha}(x') \right\rangle \left\langle \psi_{\alpha}(x,\tau) \left(\hat{k}_\alpha \psi^\dagger_{\alpha}(x')\right) \right\rangle \tag{4.226}$$

We can pull the derivatives out of the correlators to get

$$\begin{aligned}
\langle J_E(\tau) J_E \rangle &= 2N_c \left(\frac{a_c v t}{2\pi}\right)^2 \\
&\quad \times \sum_{\alpha} \int dx\, dx' \, \left[(k_F - i\alpha\partial_x) \left\langle \psi^\dagger_\alpha(x,\tau)\psi_\alpha(x')\right\rangle\right] \times \left[(k_F - i\alpha\partial_{x'}) \left\langle \psi_\alpha(x,\tau)\psi^\dagger_\alpha(x')\right\rangle\right]
\end{aligned} \tag{4.227}$$

We can then rewrite in terms of a single position coordinate to get

$$\begin{aligned}
\langle J_E(\tau) J_E \rangle &= 2N_c L \left(\frac{a_c v t}{2\pi}\right)^2 \\
&\quad \times \sum_{\alpha} \int dx \, \left[(k_F - i\alpha\partial_x) \left\langle \psi^\dagger_\alpha(x,\tau)\psi_\alpha(0)\right\rangle\right] \times \left[(k_F + i\alpha\partial_x) \left\langle \psi_\alpha(x,\tau)\psi^\dagger_\alpha(0)\right\rangle\right]
\end{aligned} \tag{4.228}$$

Writing this in terms of the Green's function we have

$$\langle J_E(\tau) J_E \rangle = 2N_c L \left(\frac{a_c v t}{2\pi}\right)^2 \sum_{\alpha} \int dx \, \left[(k_F - i\alpha\partial_x) \tilde{G}_\alpha(x,\tau)\right] \times \left[(k_F + i\alpha\partial_x) G_\alpha(x,\tau)\right] \tag{4.229}$$

If this is compared with the noninteracting limit ($\gamma = 1$) of equation (2.28b) from our Luttinger liquid model calculation, we find that they agree. This provides a useful confirmation of our lengthy and therefore error-susceptible calculation in the Luttinger liquid model.

4.6 Form of the hopping, $t_{kk'}$ and $t(x, x')$

Both of our models involve some sort of hopping strength, $t_{kk'}$ in the noninteracting model and $t(x, x')$ in the full Luttinger model. In calculating the transport coefficients, we had to make some assumptions about these transport coefficients. In particular, we used the following expressions:

$$t_{kk'} = te^{-(k-k')^2 L^2/\pi} \tag{4.230a}$$

$$t(k, k') = \frac{t}{L}\delta(k - k') \text{ with } \delta(0) = L \tag{4.230b}$$

$$t(x, x') = \frac{t}{2\pi}\delta(x - x') \tag{4.230c}$$

In this section, we will derive (1) the relation between $t_{kk'}$ and $t(x, x')$ and (2) the precise expressions given above.

To find the relation between $t_{kk'}$ and $t(x, x')$, we begin by assuming that the Hamiltonians we use for our two models describe the same physical system and thus can be directly related. For convenience, we reproduce those two expressions here:

$$H = \sum_{jk} E_k c^\dagger_{jk} c_{jk} - \sum_{jkk'} t_{kk'} \left(c^\dagger_{jk} c_{j+1,k'} + \text{h.c.} \right) \tag{2.1}$$

$$H = \sum_j H_j = \sum_j h_j + h'_j \tag{4.131}$$

$$h_j = \frac{\hbar}{2\pi} \int dx \left[\frac{vK}{\hbar^2} (\nabla\theta_j)^2 + \frac{v}{K} (\nabla\phi_j)^2 \right]$$

$$h'_j = \frac{1}{2} \sum_{\alpha\beta} \int dx\, dx' \left[t_{\alpha\beta}(x - x') \psi^\dagger_{j\alpha}(x) \psi_{j+1,\beta}(x') + t_{\alpha\beta}(x - x') \psi^\dagger_{j-1,\alpha}(x) \psi_{j\beta}(x') + \text{h.c.} \right]$$

Our first step in equating these is to rewrite the hopping term of the latter Hamiltonian (equation 4.131) with only two terms instead of four so that it more closely matches the form of the noninteracting Hamiltonian. The Luttinger hopping term then becomes

$$\sum_j \sum_{\alpha\beta} \int dx\, dx' \left[t_{\alpha\beta}(x - x') \psi^\dagger_{j\alpha}(x) \psi_{j+1,\beta}(x') + \text{h.c.} \right] \tag{4.231}$$

which is just the sum over j of the expression in equation (4.133).

We now substitute in expressions for the real-space fermion operators ψ in terms of the Fourier space operators c and compare the two hopping terms to find the relation between $t_{kk'}$ and $t(x,x')$. We begin by dropping the sum over the chain index j since that appears in both expressions. We can likewise drop the Hermitian conjugate term for our comparison, since if the first term matches, that one will as well.

Then we have:

$$\begin{aligned}\sum_{kk'} t_{kk'} c^\dagger_{jk} c_{j+1,k'} &= \sum_{\alpha\beta} \int dx\, dx' \left[t_{\alpha\beta}(x-x') \psi^\dagger_{j\alpha}(x) \psi_{j+1,\beta}(x') \right] \\ &= \sum_{\alpha\beta} \int dx\, dx' \left[t_{\alpha\beta}(x-x') \left[\frac{e^{-i\alpha k_F x}}{\sqrt{L}} \sum_k e^{-ikx} c^\dagger_{jk\alpha} \right] \left[\frac{e^{i\beta k_F x'}}{\sqrt{L}} \sum_k e^{ikx'} c_{j+1,k\beta} \right] \right]\end{aligned}$$

At this point, we must deal with an inconsistency in the way we have approached our two models. In the noninteracting model, we did not split apart the two separate bands until switching from an integral over k to an integral over E, while in the real-space Luttinger model we have already done so. This is why there is a sum over α and β on the right-hand side but not on the left-hand side. To correct for this difference in approaches, we assume as above that $t_{\alpha\beta}(x-x') = \delta_{\alpha\beta} t(x-x')$ and also add in a similar dependence on α and β on the left-hand side, $t_{kk'} \to t_{kk',\alpha\beta} = \delta_{\alpha\beta} t_{kk'}$ and sum over α and β:

$$\begin{aligned}&\sum_{kk'} \sum_\alpha t_{kk'} c^\dagger_{jk\alpha} c_{j+1,k'\alpha} \\ &\qquad = \sum_\alpha \int dx\, dx' \left[t(x-x') \left[\frac{e^{-i\alpha k_F x}}{\sqrt{L}} \sum_k e^{-ikx} c^\dagger_{jk\alpha} \right] \left[\frac{e^{i\alpha k_F x'}}{\sqrt{L}} \sum_k e^{ikx'} c_{j+1,k\alpha} \right] \right] \\ &\qquad = \frac{1}{L} \sum_{kk'} \sum_\alpha \int dx\, dx' \left[t(x-x') e^{-i\alpha k_F (x-x')} \left[e^{-ikx} e^{ik'x'} \right] c^\dagger_{jk\alpha} c_{j+1,k\alpha} \right] \\ t_{kk'} &= \frac{1}{L} \int dx\, dx' \left[t(x-x') e^{-i\alpha k_F (x-x')} \left[e^{-ikx} e^{ik'x'} \right] \right]\end{aligned}$$

It appears that either $t_{kk'}$ or $t(x,x')$ must still depend on α. We will assume for now that the dependence is in $t(x,x')$ so our final result is

$$\boxed{t_{kk'} = \frac{1}{L} \int dx\, dx' \left[t_\alpha(x-x') e^{-i\alpha k_F (x-x')} \right] e^{-ikx} e^{ik'x'}} \tag{4.232}$$

We can also invert this relation to get

$$\boxed{t_\alpha(x-x') e^{-i\alpha k_F (x-x')} = \frac{L}{(2\pi)^2} \int dk\, dk'\, t_{kk'} e^{ikx} e^{-ik'x'}} \tag{4.233}$$

Now we can finally put in some example expressions for these hopping strengths. We begin with $t_{kk'}$, which we assume to be sharply peaked around $k = k'$. To be concrete, we

start with the expression

$$t_{kk'} = te^{-(k-k')^2/k_0^2} \tag{4.234}$$

where k_0 is some large momentum. This gives

$$t_\alpha(x-x')e^{-i\alpha k_F(x-x')} = \frac{Lt}{2\pi}k_0\sqrt{\pi}e^{-(k_0x/2)^2}\delta(x-x') \tag{4.235}$$

or equivalently (because of the delta function on the right-hand side)

$$t(x-x') = \frac{Lt}{2\pi}k_0\sqrt{\pi}e^{-(k_0x/2)^2}\delta(x-x') \tag{4.236}$$

On physical grounds, the real-space hopping should not grow with L, so we want $k_0 \propto L^{-1}$. In particular, we choose $k_0 = A/L$ where A is some unitless constant of order 1. Then we have:

$$t_{kk'} = te^{-(k-k')^2/(A/L)^2} \tag{4.237}$$

$$t(x-x') = \frac{At\sqrt{\pi}}{2\pi}e^{-(Ax/2L)^2}\delta(x-x') \tag{4.238}$$

In the limit $L \to \infty$, this becomes

$$t_{kk'} = t\delta_{kk'} \tag{4.239}$$

$$t(x-x') = \frac{At\sqrt{\pi}}{2\pi}\delta(x-x') \tag{4.240}$$

We also need the continuum version in k-space. Recalling that

$$\delta(x) = \lim_{\epsilon\to 0}\frac{1}{\sqrt{2\pi\epsilon}}e^{-x^2/2\epsilon}, \tag{4.241}$$

we can write

$$t_{kk'} = te^{-(k-k')^2/(A/L)^2} = t\frac{A\sqrt{\pi}}{L} \times \frac{L}{A\sqrt{\pi}}e^{-(k-k')^2/(A/L)^2} = t\frac{A\sqrt{\pi}}{L}\delta(k-k') \tag{4.242}$$

in the limit $L \to \infty$, with $\delta(0) = \frac{L}{A\sqrt{\pi}}$. Note that if we directly Fourier transform this expression for $t(k,k')$ to get $t(x,x')$, the result is

$$t(x-x') = \frac{At\sqrt{\pi}}{2\pi}\delta(x-x'), \tag{4.243}$$

precisely the same as what we found in the $L \to \infty$ limit of the Fourier transform of $t_{kk'}$. Our choice of k_0 was somewhat arbitrary apart from its proportionality to L^{-1}, so we can

also choose the constant A to have a convenient value. We pick $A = \pi^{-1/2}$ so that we end up with the very nice expressions:

$$t_{kk'} = te^{-(k-k')^2L^2/\pi} \tag{4.244}$$

$$t(k,k') = \frac{t}{L}\delta(k-k') \text{ with } \delta(0) = L \tag{4.245}$$

$$t(x,x') = \frac{t}{2\pi}\delta(x-x') \tag{4.246}$$

We can also get $t(E,E')$ by a variable transformation on $t(k,k')$. Our linear dispersion implies that $E = \pm\hbar vk$, where for a given $t(E,E')$ function we are only on the right branch or the left so that the sign of the dispersion is the same for both. This gives

$$t(E,E') = \frac{tv}{L}\delta(E-E') \quad \text{with} \quad \delta(0) = \frac{L}{v} \tag{4.71}$$

Similarly we can also get the expression in terms of βE,

$$t(\beta E,\beta E') = \frac{tv\beta}{L}\delta(\beta E-\beta E') \quad \text{with} \quad \delta(0) = \frac{L}{v\beta} \tag{4.247}$$

4.7 Definitions and identities for the F_1 hypergeometric function

In our calculations for the full Luttinger liquid model, some exact integrals have provided results in terms of the Appell hypergeometric function, $F_1(a;b_1,b_2;c;x,y)$. This is usually defined in terms of an infinite series in the two variables x and y [82, §16.13][28, §5.7.1],

$$F_1(a;b_1,b_2;c;x,y) = \sum_{i,j}\frac{(a)_{i+j}(b_1)_i(b_2)_j}{(c)_{i+j}i!j!}x^iy^j \tag{4.248}$$

where the Pochammer symbol $(a)_n$ is defined by

$$(a)_n = \frac{\Gamma(a+n)}{\Gamma(a)} = a(a+1)\cdots(a+n-1) \tag{4.249}$$

This series representation converges for $|x|$ and $|y|$ less than 1 and diverges otherwise except in the case of very specific values of the a, b, and c parameters that cause the series to truncate. (In particular, this will happen if any one of a, b_1, and b_2 is a negative integer.)

In our case, x and y are $e^{\pm 2i\tau}$, with absolute value 1, and the parameters are such that the series in fact fails to truncate, so that the infinite sum does not converge. In this case, when we give expressions in terms of F_1, we are implicitly referencing the integral representation of the function [82, §16.15][28, §5.8.2],

$$F_1(a;b_1,b_2;c;x,y) = \frac{\Gamma(c)}{\Gamma(a)\Gamma(c-a)}\int_0^1 t^{a-1}(1-t)^{c-a-1}(1-xt)^{-b_1}(1-yt)^{-b_2}\,dt, \tag{4.250}$$

valid when $\mathrm{Re}(c) > \mathrm{Re}(a) > 0$. In the regime where both the series definition and the integral representation are valid, the two expressions agree and are thus interchangeable as definitions for the Appell function. The integral expression is valid for the parameter regimes of interest for our calculations, and in particular F_1 appears in our calculations only as

$$f(\gamma,\tau,n,m) = \frac{F_1(\gamma+n;\gamma+m,\gamma+m;\gamma+n+1;e^{2i\tau},e^{-2i\tau})}{\gamma+n}, \tag{4.158}$$

so that $a = \gamma+n$, $b_1 = b_2 = \gamma+m$, $c = a+1$, $x = e^{2i\tau}$, and $y = e^{-2i\tau}$. Making these substitutions into the integral representation for F_1, equation (4.250), we find the integral representation for the f function as cited in section 4.3, namely

$$f(\gamma,\tau,n,m) = \int_0^1 t^{\gamma+n-1}(1-2t\cos(2\tau)+t^2)^{-(\gamma+m)}\,dt \tag{4.159}$$

A useful identity and its derivation

Here we derive the useful identity

$$f(\gamma,\tau,n,m) = f(\gamma,\tau,n,m+1) - 2\cos(2\tau)f(\gamma,\tau,n+1,m+1) + f(\gamma,\tau,n+2,m+1) \tag{4.251}$$

While this identity was never explicitly mentioned in the work presented above, in practice we used it to get the result (4.157) and therefore also the expressions in equations (4.160), (4.187), and (4.193). We initially did those integrals separately using the commercial software Wolfram Mathematica, which in some cases gave the results we presented above and in others gave an answer looking more like the right-hand side of (4.251). We used the identity (4.251) to verify the consistency of the results and therefore to simplify all the results as much as possible to arrive at the result given in (4.157).

Here we will provide a brief derivation of the identity. Beginning from the left-hand side of equation (4.251), we have:

$$\begin{aligned}
f(\gamma,\tau,n,m) &= \int_0^1 t^{\gamma+n-1}(1-2t\cos(2\tau)+t^2)^{-(\gamma+m)}\,dt \\
&= \int_0^1 t^{\gamma+n-1}(1-2t\cos(2\tau)+t^2)^{-(\gamma+m)} \times \left(\frac{1-2t\cos(2\tau)+t^2}{1-2t\cos(2\tau)+t^2}\right) dt \\
&= \int_0^1 t^{\gamma+n-1}(1-2t\cos(2\tau)+t^2)^{-(\gamma+m+1)} \times (1-2t\cos(2\tau)+t^2)\,dt \\
&= \int_0^1 t^{\gamma+n-1}(1-2t\cos(2\tau)+t^2)^{-(\gamma+m+1)}\,dt \\
&\quad - 2\cos(2\tau)\int_0^1 t^{\gamma+(n+1)-1}(1-2t\cos(2\tau)+t^2)^{-(\gamma+m+1)}\,dt \\
&\quad + \int_0^1 t^{\gamma+(n+2)-1}(1-2t\cos(2\tau)+t^2)^{-(\gamma+m+1)}\,dt \\
&= f(\gamma,\tau,n,m+1) - 2\cos(2\tau)f(\gamma,\tau,n+1,m+1) + f(\gamma,\tau,n+2,m+1)
\end{aligned}$$

This is actually a special case of a more general identity for the Appell function,

$$F_1 = F_1(b_1+1, b_2+1) - (x+y)\frac{a}{c}F_1(a+1, b_1+1, b_2+1, c+1) + xy\frac{(a+1)a}{(c+1)c}F_1(a+2, b_1+1, b_2+1, c+2) \tag{4.252}$$

where any unspecified arguments of the F_1 functions are assumed to be unchanged from $F_1(a, b_1, b_2, c, x, y)$. The derivation of this more general form is quite similar, but we will show it here for completeness.

$$\begin{aligned}
F_1 =& \frac{\Gamma(c)}{\Gamma(a)\Gamma(c-a)}\int_0^1 t^{a-1}(1-t)^{c-a-1}(1-xt)^{-b_1}(1-yt)^{-b_2}\,dt \\
=& \frac{\Gamma(c)}{\Gamma(a)\Gamma(c-a)}\int_0^1 t^{a-1}(1-t)^{c-a-1}(1-xt)^{-(b_1+1)}(1-yt)^{-(b_2+1)}(1-(x+y)t+xyt^2)\,dt \\
=& \frac{\Gamma(c)}{\Gamma(a)\Gamma(c-a)}\int_0^1 t^{a-1}(1-t)^{c-a-1}(1-xt)^{-(b_1+1)}(1-yt)^{-(b_2+1)}\,dt \\
& - (x+y)\frac{\Gamma(c)}{\Gamma(a)\Gamma(c-a)}\int_0^1 t^{(a+1)-1}(1-t)^{(c+1)-(a+1)-1}(1-xt)^{-(b_1+1)}(1-yt)^{-(b_2+1)}\,dt \\
& + xy\frac{\Gamma(c)}{\Gamma(a)\Gamma(c-a)}\int_0^1 t^{(a+2)-1}(1-t)^{(c+2)-(a+2)-1}(1-xt)^{-(b_1+1)}(1-yt)^{-(b_2+1)}\,dt \\
=& F_1(b_1+1, b_2+1) - (x+y)\frac{\Gamma(c)\Gamma(a+1)}{\Gamma(c+1)\Gamma(a)}F_1(a+1, b_1+1, b_2+1, c+1) \\
& + xy\frac{\Gamma(c)\Gamma(a+2)}{\Gamma(c+2)\Gamma(a)}F_1(a+2, b_1+1, b_2+1, c+2) \\
=& F_1(b_1+1, b_2+1) - (x+y)\frac{a}{c}F_1(a+1, b_1+1, b_2+1, c+1) \\
& + xy\frac{(a+1)a}{(c+1)c}F_1(a+2, b_1+1, b_2+1, c+2)
\end{aligned}$$

The prefactors are much simpler in our special case because the fact that $c = a+1$ leads to some nice simplifications.

Part II

Study of the triangular lattice Hubbard model using the density matrix renormalization group

Chapter 5

Chiral spin liquid phase of the triangular lattice Hubbard model

In this chapter, I present my study of the triangular lattice Hubbard model using the density matrix renormalization group (DMRG) method on infinitely long cylinders with finite circumference. This work is available on arXiv[111] and was done in collaboration with Johannes Motruk, Michael Zaletel, and Joel Moore.

As with the study of coupled Luttinger liquids discussed in the preceding chapters, I again use a technique developed for the study of one-dimensional systems to investigate a two-dimensional one. In particular, DMRG is a variational method within the space of matrix product states, which are efficient representations of one-dimensional gapped ground states; limiting a two-dimensional triangular lattice to finite-circumference cylinders creates effective quasi-one-dimensional systems to which DMRG can be applied.

In this chapter I present the experimental and theoretical context for the work, and I show the results of my numerical simulations on a wide variety of cylinder geometries. In particular, I clearly demonstrate that the model has three phases as a function of electron-electron interaction strength: a metallic phase with weak interactions, a magnetically ordered phase with strong interactions, and a nonmagnetic insulating phase in between. Chiral ordering from spontaneous breaking of time-reversal symmetry, a fractionally quantized spin Hall response, and characteristic level statistics in the entanglement spectrum in the intermediate phase provide strong evidence that the intermediate phase is in fact a chiral spin liquid.

Some details of the methods used are presented in the following chapter, and further data to support the conclusions reached in this chapter can be found in chapter 7.

5.1 Introduction

Quantum spin liquids[8, 97, 145] have been the subject of considerable interest since the concept was first introduced in 1973 by Anderson, who suggested that geometrical frustration on the triangular lattice could lead to a resonating valence bond ground state of

the antiferromagnetic Heisenberg model[4]. Although it is now known that the Heisenberg model on the triangular lattice in fact exhibits a three-sublattice 120° order in the ground state[46, 129], antiferromagnetic models on the triangular lattice remain some of the most promising systems to realize a phase in which spins remain disordered even down to zero temperature. The triangular lattice has seemed particularly promising since the work of Shimizu *et al.*, who found that the organic crystal κ-(BEDT-TTF)$_2$Cu$_2$(CN)$_3$, which is well-described by independent 2D layers with nearly isotropic triangular lattice structure, shows no sign of spin-ordering even down to tens of mK, indicative of a possible spin liquid ground state[105]. Subsequent studies of this crystal have found that the heat capacity is T-linear at low temperature[135], suggesting the presence of low-lying gapless excitations, but also that the thermal conductivity has no such T-linear contribution[134], indicating to the contrary that there is a gap in the energy spectrum. The true nature of spin liquid phases in this and other triangular lattice materials such as EtMe$_3$Sb[Pd(dmit)$_2$]$_2$[50, 48, 133, 49, 81, 16, 132] remains unclear.

Substantial theoretical effort has gone into answering this question, primarily in studying the antiferromagnetic Heisenberg model with additional terms, such as second-neighbor interactions and ring exchanges, that frustrate the expected three-sublattice order[79, 102, 35, 14, 73, 57, 43, 146, 34, 93, 147, 95]. The Heisenberg model and its extensions are derived from a perturbative expansion of a model of itinerant electrons, the Hubbard model[68]; by studying the Hubbard model directly, we can capture additional effects that may be important in actual materials, at the cost of increased computational effort—compared with spin-1/2 models, the size of the local Hilbert space is doubled, so the system sizes that can be accessed by full-Hilbert-space numerical methods are only about half as large.

Although there is now a wide variety of theoretical evidence pointing to the existence of a non-magnetic insulating phase of the triangular lattice Hubbard model[76, 79, 64, 94, 113, 138, 137, 5, 114, 65, 72, 74, 106], there is still little agreement on the precise nature of the phase. Some candidates, suggested by results on both the Hubbard and extended Heisenberg models, include a $U(1)$ spin liquid with a spinon Fermi sea[79, 102, 137, 14, 57, 72], a nodal spin liquid[114, 73], a gapped chiral spin liquid[53, 10, 43, 42, 131], and a $\mathbb{Z}_2$ spin liquid[146, 43]. In this work, we confirm the existence of a nonmagnetic insulating phase of the Hubbard model on the triangular lattice at half filling, provide strong evidence that it is a gapped chiral spin liquid, and comment on possible experimental signatures.

We study the triangular lattice Hubbard model on infinite cylinders with finite circumference using the density matrix renormalization group (DMRG) technique[128, 127, 86, 99], a variational method to find the ground state of a Hamiltonian within the matrix product state (MPS) ansatz. This method has previously been applied to an extended Hubbard model on a triangular lattice two-leg ladder, providing evidence for a $U(1)$ spin liquid phase with a spinon Fermi surface[72]. For systems larger than the two-leg ladder, to our knowledge there exists only one prior paper[106] that uses DMRG to study the triangular lattice Hubbard model. The authors of that study used the finite-system DMRG to confirm the existence of a nonmagnetic insulating phase; in our infinite-system DMRG study, we study the nature of the phase by investigating the entanglement spectrum and the response to adiabatic

spin-flux insertion through the cylinder as accomplished by twisting boundary conditions. We study the model on a variety of cylinders with different circumferences and boundary conditions. With some cylinder geometries we find a chiral spin liquid phase regardless of how we twist the boundary conditions, while for the others the chiral phase exists for some twisted boundary conditions and in particular for those for which the ground state is closest to obeying the symmetries of the full two-dimensional lattice. Taken together, the results for the various cylinders point to the existence of the chiral spin liquid phase in the full two-dimensional lattice as well.

The organization of the paper is as follows: in section 5.2, we introduce the model we study and the mixed-space representation used in the simulations. In section 5.3, we demonstrate the existence of metallic, nonmagnetic insulating, and magnetically ordered phases of the model, and furthermore show that the intermediate phase breaks time reversal symmetry. We present detailed results for five different cylinder geometries. Readers wishing to see even more complete data are encouraged to also read chapter 7; those interested primarily in the identification of the chiral spin liquid phase can proceed to section 5.4, in which we show that the intermediate phase is in fact a chiral spin liquid. Finally, in section 5.5, we discuss the results, placing them in the context of recent experiments and other theoretical studies.

5.2 The model

The model we study is the standard Hubbard Hamiltonian,

$$H = -t \sum_{\langle ij \rangle \sigma} c^\dagger_{i\sigma} c_{j\sigma} + \text{H.c.} + U \sum_i n_{i\uparrow} n_{i\downarrow}, \tag{5.1}$$

where $c_{i\sigma}$ ($c^\dagger_{i\sigma}$) is the fermion annihilation (creation) operator for spin σ on site i and $n = c^\dagger c$ is the number operator; $\langle \cdot \rangle$ indicates nearest neighbor pairs on the triangular lattice (Figure 5.1). We work at half filling with net zero spin, so that $\sum_i \langle n_{i\uparrow} \rangle = \sum_i \langle n_{i\downarrow} \rangle = N/2$, where N is the total number of sites. This model has a single tunable parameter, U/t. In the limit $U = 0$, the model is exactly solvable and at half filling forms a metal with a nearly circular Fermi surface; in the limit $U \to \infty$, double occupancy is disallowed, so to lowest order in perturbation theory in t/U, the model reduces to the nearest-neighbor antiferromagnetic Heisenberg model[68], whose ground state exhibits a three-sublattice spin order[46, 129]. Between these two limits of $U = 0$ and $U \to \infty$ there must be at least one phase transition, from the metallic to the Mott-insulating phase; it is in the vicinity of this metal-insulator transition that a spin liquid phase is likely to be found.

To study this model using the DMRG method, we wrap the two-dimensional triangular lattice onto an infinitely long cylinder of finite circumference. We primarily use the so-called YC boundary conditions (see reference [136], section 6.1), for which the triangles are oriented such that one of the sides runs along the circumference of the cylinder. The YC4 lattice is shown in Figure 5.1(a) as an example, with the dashed gray lines identified together with

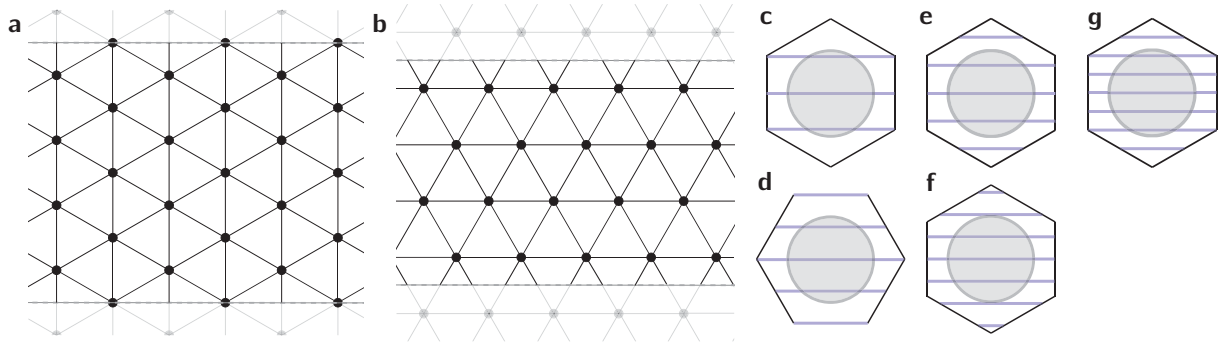

Figure 5.1: **(a)** Triangular lattice on a cylinder of circumference 4 with YC boundary conditions (YC4 cylinder); the dashed lines are identified together and run along the length of the cylinder. **(b)** XC4 cylinder. **(c)**-**(g)** Horizontal lines show allowed momenta in the Brillouin zone for the YC3, XC4, YC4, YC5, and YC6 cylinders, in order of increasing circumference. The shaded circle shows the Fermi surface for noninteracting electrons ($U = 0$).

periodic boundaries to form a cylinder. We also consider XC boundary conditions, for which one triangle side runs along the length of the cylinder. We show the XC4 lattice in Figure 5.1(b); an XCn cylinder, which exists only for even n, has a physical circumference of $n\sqrt{3}/2$ lattice constants.

Denoting translation by one lattice constant around the cylinder by T_y, the YCn cylinder has a discrete translation symmetry $T_y^n = 1$; we explicitly conserve the momentum quantum numbers associated with this symmetry by rewriting the Hamiltonian in a mixed real- and momentum-space basis with single-particle operators $c_{x,k_y,\sigma}$, which both gives substantial improvements in computational efficiency and allows us to separately find the ground state in different momentum sectors.[78, 25] Similarly, for the XCn cylinders we define the translation operator T_y^{XC} that translates between two-site unit cells around the circumference, with $\left(T_y^{XC}\right)^{n/2} = 1$; we can again exploit momentum conservation, but with only half as many quantum numbers.

In this paper, we particularly focus on the YC4 and YC6 cylinders, and we also present and discuss data for the YC3, XC4, and YC5 cylinders. For the various cylinders, the finite circumferences and periodic boundary conditions restrict the accessible momenta in the Brillouin zone as shown in Figures 5.1 (c) through (g).

5.3 Phase diagram

Our goal is to show that the Hubbard model on the full two-dimensional triangular lattice has a chiral spin liquid phase; we begin by establishing the phase diagram more generally, showing the existence of the expected metallic, nonmagnetic insulating (NMI), and magnetic phases, and we furthermore show that the NMI phase breaks time reversal symmetry.

Of course, we have access in our simulations not to the full two-dimensional model but rather to a collection of finite circumference cylinders. To overcome this impediment, we employ three methods: (1) each phase that exists in the two-dimensional model should leave characteristic signatures when restricted to a finite circumference cylinder, and we can look for these signatures; (2) for each cylinder we can twist the boundary conditions to scan the allowed momentum cuts (Figure 5.1(c)-(g)) through the full two-dimensional Brillouin zone; and (3) we can compare the results for the various cylinders and look for trends and commonalities. The third is self-explanatory; before presenting the data, we elaborate on (1) and (2).

We first discuss how the various possible phases of the two-dimensional model should manifest on the infinite cylinders we study. A metallic state will be gapless, as indicated by a nonzero value for the central charge c of the one-dimensional conformal field theory corresponding to the restriction of the two-dimensional model to the one-dimensional allowed momentum cuts; in particular, if the Fermi surface intersects N_F of the allowed momentum lines in the Brillouin zone (see Figure 5.1 (c) through (g)), the central charge will be $c = 2N_F$ (see reference [87] and section 6.3). The 120-degree magnetically ordered phase will be fully gapped ($c = 0$) and symmetric on even circumference cylinders due to the integer-spin Haldane gap[1] induced by the reduced dimension, but gapless on odd circumference cylinders; the 2D spin-order should qualitatively manifest as large peaks in the spin-structure factor at the $K^{\pm}$ points which diverge linearly with cylinder circumference. If the intermediate phase is a $U(1)$ spin liquid with a spinon Fermi surface, there will be a charge gap but no spin gap, leading to cylinder central charge $c = 2N_F - 1$ and $2k_F$-singularities in the structure factors[103, 102, 72, 30]. Finally, a gapped spin liquid will have $c = 0$ and feature several "topologically-degenerate" low-lying states whose energy splitting decreases exponentially with circumference[124], along with other topological signatures we will return to in detail. The chiral spin liquid in particular will spontaneously break time-reversal and parity symmetry, while retaining all others; time-reversal symmetry breaking is indicated by a nonzero scalar chiral order parameter $\langle \mathbf{S}_i \cdot (\mathbf{S}_j \times \mathbf{S}_k) \rangle$, where i, j, and k label the vertices of a triangle in the lattice[125]. In the simulations, all these properties must be assessed as a function of the DMRG accuracy as captured by the bond-dimension χ of the MPS ansatz.

We next discuss how, for a given cylinder geometry, twisting of boundary conditions grants access to the full two-dimensional Brillouin zone. In particular, instead of using periodic boundaries $c_{x,y=0,\sigma} = c_{x,y=L,\sigma}$, we set $c_{x,y=0,\sigma} = e^{i\theta\sigma/2} c_{x,y=L,\sigma}$, followed by the gauge transformation $c_{x,y,\sigma} \mapsto e^{i\theta\sigma y/(2L)} c_{x,y,\sigma}$. Physically, this is equivalent to inserting a flux through the cylinder of $\theta/2$ for spin up electrons and $-\theta/2$ for spin down; this corresponds to flux θ for the spin degrees of freedom. Note that because the flux insertion is opposite for spin up and spin down, this transformation does not break time reversal symmetry.

When the original Hamiltonian with periodic boundaries is written in the mixed-space picture, some coefficients will depend on the momentum k around the cylinder; the only effect of the flux insertion is to transform those coefficients, with $k = (2\pi/L)n \mapsto (2\pi/L)(n+\theta\sigma/2)$. This can be viewed as shifting the momentum cuts in the Brillouin zone, upwards for spin up and downwards for spin down, as illustrated in Figure 5.2. Thus, by scanning θ from 0

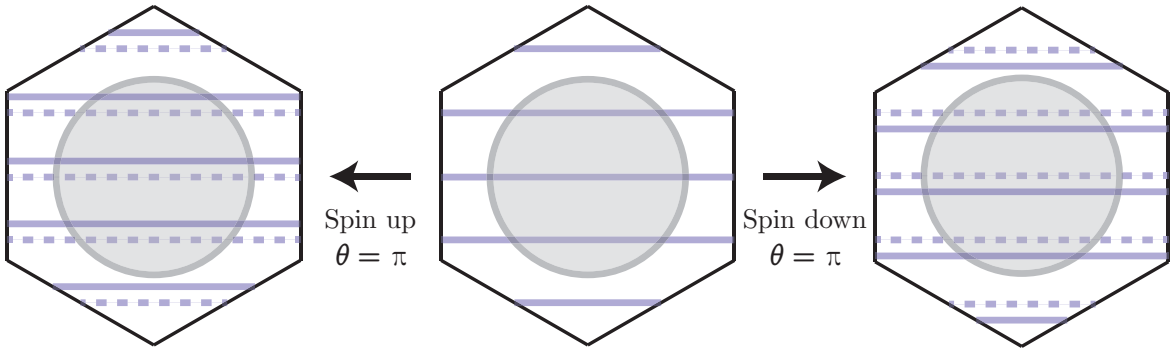

Figure 5.2: (Color online) The effect of flux insertion on the mixed-space model is to shift the allowed momentum cuts through the Brillouin zone. They shift upwards for spin up electrons and downwards for spin down electrons, thus preserving time-reversal symmetry. Note that for $\theta = 4\pi n$ for any integer n, the cuts are again in their original positions.

to 4π, we can access the full two-dimensional Brillouin zone, giving substantial additional evidence for the two-dimensional model despite using only a single cylinder geometry.

The only physical effect of this flux insertion is from the twisted boundary conditions, and in the two-dimensional limit where the cylinder circumference becomes infinitely large, the effect on local properties like order parameters and short-range correlations functions must go to zero. Thus the variation in these quantities with flux insertion serves as an indication of the degree of "two-dimensionality" of the cylinders we study and thus of the reliability of our results in predicting the behavior of the full two-dimensional model.

Note that the flux insertion can be performed adiabatically by first computing the ground state with periodic boundary conditions and then increasing θ in small increments, at each step using the converged ground state from the previous step as the initial state for the new simulation. Notably, this procedure allows for detection of spin pumping from a quantized spin Hall effect, which is a hallmark of the chiral spin liquid phase.

We now present results for the various cylinder geometries we have studied.

YC4

Out of the five different cylinders we consider, our most extensive data is for YC4, which strikes a balance between two-dimensionality (favoring larger cylinders) and ability to converge the DMRG simulations (favoring smaller ones).

On the YC4 cylinder with periodic boundaries we find three phases, corresponding to the expected metallic, nonmagnetic insulating (NMI), and spin-ordered phases of the full two-dimensional model; the phase diagram and the evidence for it are summarized in Figure 5.3.

The transition from the NMI phase to the spin-ordered phase at $U/t \approx 10.6$ is indicated

by a peak in the correlation length; the appearance of large peaks near the $K^{\pm}$ points of the Brillouin zone in the spin structure factor; and the vanishing of the chiral order parameter. The spin structure factor in particular allows us to identify the high-U side of this transition as the one-dimensional descendant of the two-dimensional magnetically ordered phase.

Because the metal is gapless, the metal to NMI transition ($U/t \approx 8$) is less obvious, but it can be observed from the destruction of the Fermi surface and from the small-k charge density structure factor (see page 186 in section 7.1), and also from the chiral order parameter; although a nonzero value of the order parameter indicates time-reversal symmetry breaking in both the metallic and NMI phases for finite bond dimension, an extrapolation in the DMRG truncation error[45] shows that the symmetry is actually unbroken in the low-U phase (see Figure 5.3(d) and page 184 in section 7.1). A further indication of the metal to NMI transition comes from finite entanglement scaling[112, 90, 88]. If we cut the infinite cylinder into two semi-infinite halves, we can calculate the entanglement entropy S between them from the eigenvalues λ_i^2 of the reduced density matrix of either side of the cut,

$$S \equiv -\sum_i \lambda_i^2 \log(\lambda_i^2). \tag{5.2}$$

In the true ground state this is an infinite sum; however, when running DMRG simulations the MPS bond dimension χ upper-bounds the number of non-zero λ_i in equation (5.2) and thereby bounds $S \leq \log(\chi)$. In a gapless state the true S is infinite, as is the correlation length ξ, but finite entanglement scaling predicts that the two quantities will scale with χ such that [19]

$$S \approx (c/6) \log(\xi), \tag{5.3}$$

which can be used to estimate the central charge c of the conformal field theory corresponding to the gapless metallic phase. We show the central charge computed using equation (5.3) in Figure 5.3(f).

In a gapped state S is finite [38, 6], so the DMRG estimate of S should converge as χ is increased; however, ξ will also converge, and the two quantities may converge at different rates so that the relative scaling between them becomes less reliable. In such a case, the central charge can be more accurately computed by direct scaling of entanglement with bond dimension,[112, 90, 88]

$$S \approx \left(1 + \sqrt{12/c}\right)^{-1} \log(\chi). \tag{5.4}$$

We show the central charge computed using equation (5.4) in Figure 5.3(g).

Until $U/t \approx 8$, the central charge is constant with respect to U/t and is near to the value $c = 6$ that we would expect for a metallic state ([87], 6.3). For $U/t \gtrsim 9$, it is clear from Figure 5.3(g) that $c = 0$, indicating that the phases are gapped. For intermediate values of $8 \lesssim U/t \lesssim 9$, the central charge is still far from converged with bond dimension, but it is plausible that it will extrapolate to zero; see page 190 in section 7.1. Note that the apparently unsystematic behavior in Figure 5.3(f) near the previously identified transition

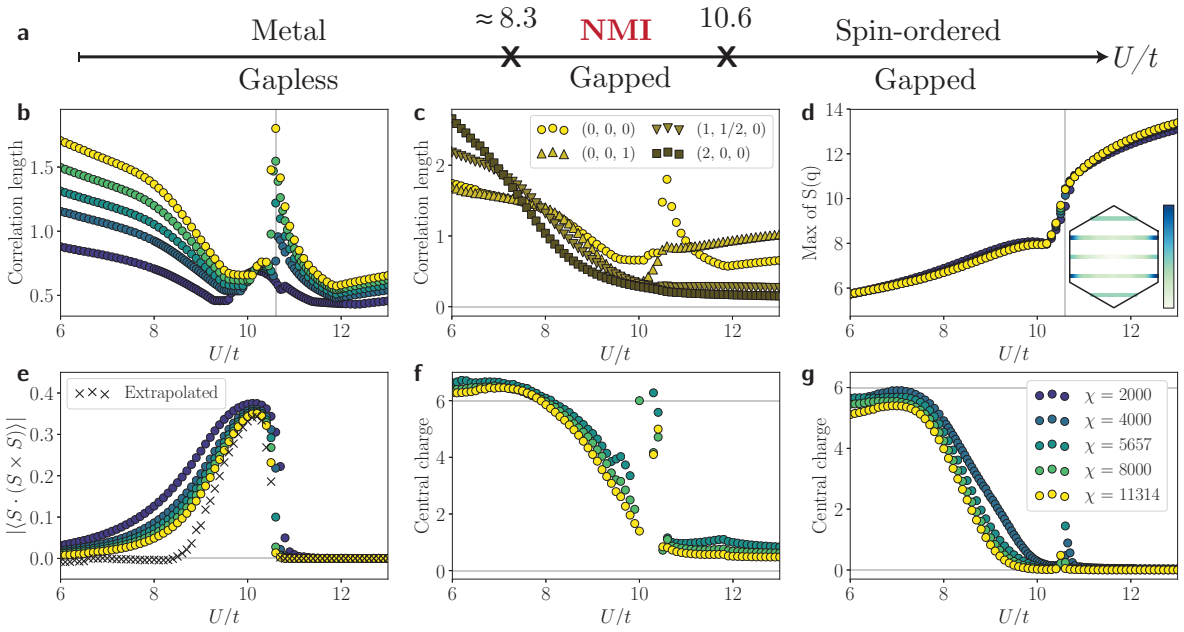

Figure 5.3: (Color online) Results for the YC4 cylinder. Results are shown for a range of MPS bond dimensions χ as indicated in the lower right legend. **(a)** A nonmagnetic insulating (NMI) phase appears between a gapless metallic phase at low U/t and a magnetic phase at high U/t. **(b)** Correlation length in the "charge neutral sector," in other words for excitations carrying no charge, spin, or momentum. The vertical line at $U/t = 10.6$ is provided as a guide to the eye. **(c)** Correlations lengths at the largest bond dimension in various charge sectors. The sector (Q, S, K) corresponds to correlations $\langle \mathcal{O}_1 \mathcal{O}_2 \rangle$ where $\mathcal{O}_1$ creates and $\mathcal{O}_2$ annihilates an excitation carrying charge Q, spin S, and momentum quantum number K. **(d)** Spin structure factor: the curve shows the maximum value of the spin structure factor in the Brillouin zone. The inset shows the spin structure factor in the high-U phase, with peaks at the closest allowed momenta to the $K^{\pm}$ points, where they would be expected for 120° magnetic ordering. Note that spin expectation values are reported here and throughout the paper with $\hbar/2 = 1$. **(d)** Chiral order parameter $\langle \mathbf{S}_i \cdot (\mathbf{S}_j \times \mathbf{S}_k) \rangle$, where i, j, and k label the three vertices of a triangle in the lattice, with an additional line showing extrapolation in the DMRG truncation error[45]; see page 184 in section 7.1 for details. **(f)** Central charge of the effective one-dimensional state as calculated by the scaling of entanglement with correlation length, equation (5.3); this is the most accurate method for gapless systems. **(g)** Central charge as calculated by the scaling of entanglement with bond dimension, equation (5.4); this is the most accurate method for gapped systems.

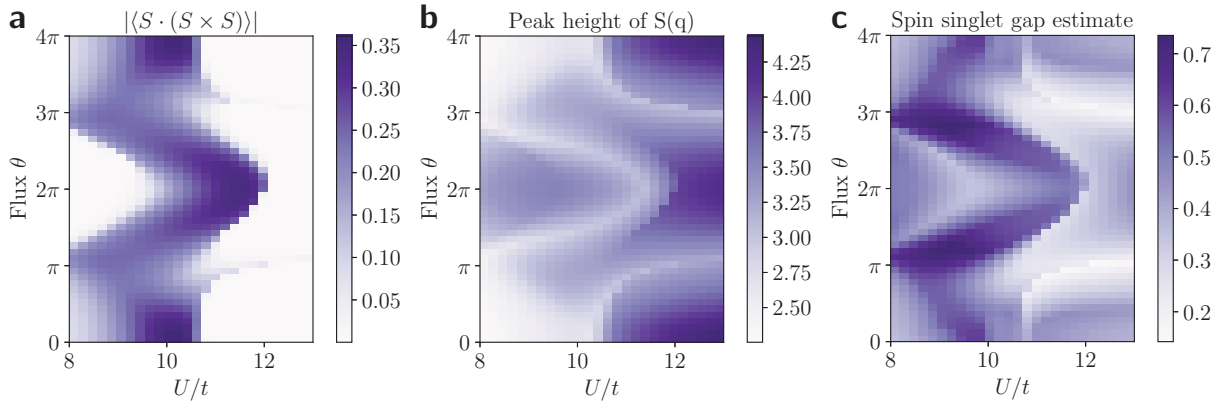

Figure 5.4: (Color online) YC4 cylinder with flux insertion θ, for $\chi = 4000$. **(a)** Absolute value of chiral order parameter. The chiral phase exists for all twisted boundary conditions, but the phase boundaries shift with θ. **(b)** Maximum of $\langle S_z S_z \rangle$ structure factor on allowed momentum cuts in the Brillouin zone. **(c)** Transfer matrix estimate of the spin singlet gap; see the text for details.

at $U/t \approx 10.6$ is due to a slight shift in the location of the peak in the correlation length with bond dimension.

We can identify the locations of both phase transitions with more precision by studying the entanglement spectrum, which is the list of values $\{-\log(\lambda_i)\}$, for the same $\{\lambda_i\}$ appearing in equation (5.2). We observe that the entire spectrum acquires an exact two-fold degeneracy for $8.3 \lesssim U/t \lesssim 10.6$ and an exact four-fold degeneracy for $10.6 \lesssim U/t$ (see page 192 in section 7.1), corresponding to the different projective representations of the symmetry group carried by the entanglement spectrum[89].

We have thus far demonstrated that the YC4 cylinder with periodic boundary conditions exhibits phases corresponding to metallic, time-reversal symmetry-breaking nonmagnetic insulating, and magnetically ordered phases in two dimensions. We now turn to the results of flux insertion.

We perform the flux insertion adiabatically, twisting the boundary conditions in intervals of $\theta = \pi/12$. Due to the much larger parameter space spanned by both U/t and θ, we restrict our computations to a single bond dimension, $\chi = 4000$. Based on the data shown in Figure 5.3, we believe this bond dimension is sufficient to capture the qualitative behavior of the system.

In Figure 5.4 we show several quantities computed as a function of both U/t and θ, namely the chiral order parameter, the maximum value of the $\langle S_z S_z \rangle$ structure factor on the allowed momentum cuts, and the inverse of the correlation length for operators carrying no spin or charge as computed from the MPS transfer matrix spectrum. In the infinite bond-dimension limit, the latter quantity would be proportional to the gap to excitations with $S_z = 0$; we present data only for a single finite bond dimensions and do not estimate

the proportionality constant as a function of U and θ, but nevertheless a comparison of this inverse correlation length across parameter space can indicate which phases are likely to have a spin-singlet gap. Throughout the rest of the paper we will refer to this quantity as the "transfer matrix estimate of the spin singlet gap." All three quantities would be independent of θ in the limit of a very wide cylinder; here we see substantial variation, but at each θ the qualitative behavior as U/t is varied remains essentially the same.

Most notably, the chiral order parameter is nonzero in a region of roughly constant width; furthermore, if for each θ we find the maximum value of the chiral order parameter versus U/t, these maxima vary with θ by only about 1/3 of the maximum at $\theta = 0$. The comparison between the three figures also reveals behavior for all θ that is in good agreement with what we found with periodic boundaries. In particular, the degree of short-range magnetic ordering rapidly increases at the right edge of the chiral phase, and furthermore the chiral phase appears to be strongly gapped, consistent with the analysis of central charge.

YC6

We next present data for the YC6 cylinder, which is the largest, and thus presumably the least impacted by finite-size effects, of those we study; this has the potential drawback that the MPS bond dimension required to achieve a given level of precision scales as roughly 4^L, so the simulations are less converged than for smaller cylinders, but we find that the qualitative behavior of the system is nevertheless clear.

The YC6 cylinder is notable not just because it is the widest of those we study but also because, as we show now, it has topologically degenerate ground states in two different momentum sectors. Because we employ a mixed real- and momentum-space basis, we can initialize the DMRG with states in different sectors of momentum around the cylinder per unit length[140], k, and thus separately find the ground state in each sector. On the YC4 cylinder, the ground state always lies in the $k = 0$ sector, but for the YC6 cylinder we observe low-lying states in two different momentum sectors, $k = 0$ and $k = \pi$. The relative energy difference between the ground states in the two sectors is shown in Figure 5.5(a). There are three apparent regimes of behavior: at low U, the $k = 0$ sector is clearly the ground state; at intermediate U, the two sectors become close in energy, and the difference is decreasing with bond dimension; at high U, the $k = \pi$ sector becomes the ground state, though again the relative difference in energy decreases with bond dimension.

The low-U phase is expected to be metallic, with central charge $c = 10$ ([87],6.3). Finite entanglement scaling indeed suggests that the phase is gapless (see page 200 in section 7.2), though an accurate measurement of the central charge would require a bond dimension currently inaccessible to us, on the order of 50,000. (Extremely high entanglement in the low-U region leads to very large DMRG truncation error, on the order of 10^{-4}, even with $\chi \sim 10,000$.) The high-U phase should be the one-dimensional descendant of the two-dimensional 120° Néel ordered phase, and indeed at approximately the same value of U/t where the $k = \pi$ sector becomes the ground state, there is a rapid increase in peak height of the spin structure factor in the $k = \pi$ sector, as shown in Figure 5.5(b). In this phase, we

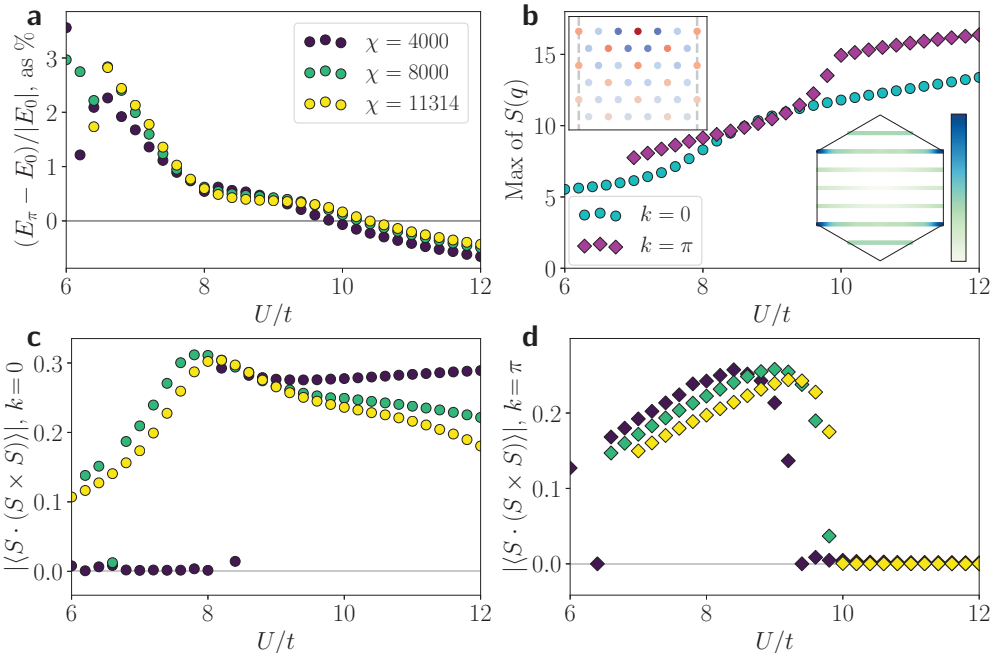

Figure 5.5: (Color online) Results for the YC6 cylinder. **(a)** Relative energy (percent difference) between ground states in the symmetry sectors with $k = \pi$ and $k = 0$ around each ring. **(b)** Maximum value of the spin structure factor for the two momentum sectors. Insets show (lower right) the high-U spin structure factor for the $k = \pi$ sector, with peaks at the $K^{\pm}$ points as expected for 120° magnetic ordering, and (upper left) the corresponding real-space $\langle \mathbf{S} \cdot \mathbf{S} \rangle$ correlations to a chosen point (center on the top). **(c)** Chiral order parameter for the $k = 0$ ground state. **(d)** Chiral order parameter for the $k = \pi$ ground state.

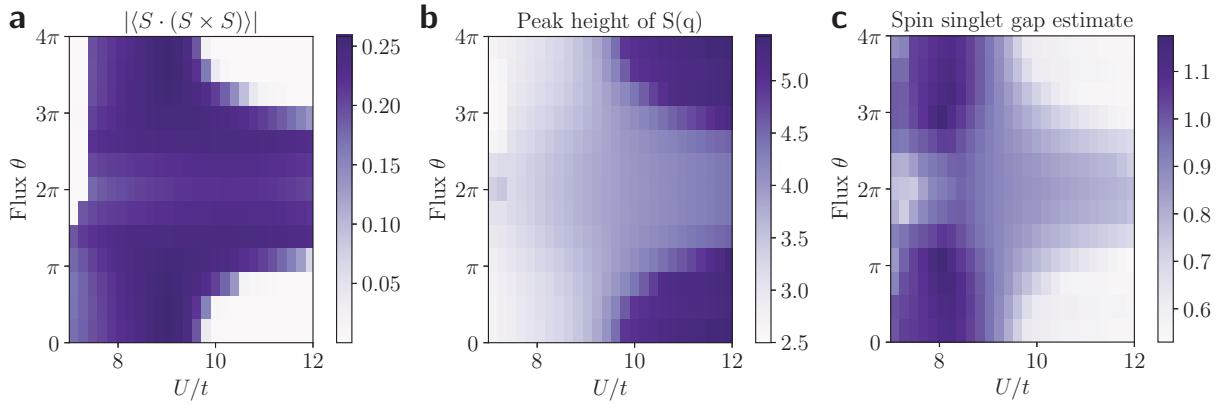

Figure 5.6: (Color online) YC6 cylinder with flux insertion θ, for $\chi = 8000$. **(a)** Absolute value of chiral order parameter. **(b)** Maximum of $\langle S_z S_z \rangle$ structure factor on allowed momentum cuts in the Brillouin zone. **(c)** Transfer matrix estimate of the spin singlet gap.

observe the expected peaks in the structure factor at the corners of the Brillouin zone (lower right inset) and short range spin-ordering in the real-space spin-spin correlations (upper left inset).

The intermediate phase, for $U/t \approx 8$ to $U/t \approx 10$, is the region where the relative energy difference between the two momentum sectors is small and approximately constant; the spin structure factors are also approximately equal. We identify the transition to the right by the onset of the afore-mentioned spin ordering. To the left, the transition can be observed by the $k = 0$ sector becoming the sole ground state and from the transition in that sector to a metallic phase; as we show in section 7.2 (page 200), the latter can be seen qualitatively from the entanglement spectrum and finite entanglement scaling—the low-U phase appears gapless while the intermediate phase is likely gapped.

As with the YC4 cylinder, spontaneous breaking of time-reversal symmetry leads to a nonzero value of the chiral order parameter in the metallic and intermediate phases, as shown for the two momentum sectors in Figure 5.5 (c) and (d), though in the metal we would expect the symmetry to be restored at larger bond dimensions. In the $k = \pi$ sector, which is the true ground state for high U, the chiral order parameter rapidly vanishes at the spin-ordering transition. In the $k = 0$ sector, the chirality does not seem to drop abruptly to zero; however, as can be seen in Figure 5.5(c), the chirality does rapidly decrease with increasing bond dimension for $U \gtrsim 10$.

We can again acquire more information about the full two dimensional model by performing adiabatic flux insertion to scan the allowed momentum cuts through the full Brillouin zone; we perform the flux insertion using the $k = \pi$ ground state as the initial state with $\theta = 0$, and we perform all computations with $\chi = 8000$. Although the bond dimension is twice that used for YC4 flux insertion, the results are much less converged. Nevertheless, some qualitative features can be captured at least qualitatively, as shown in Figure 5.6. In particular, there is a chiral phase for all θ, which has weak local magnetic order and a sizable spin singlet gap. The chiral region extending to higher U around $\theta = 2\pi$ is likely an artifact of the finite bond dimension: all local properties at 2π flux are essentially identical to those of the $k = 0$ ground state with periodic boundaries, and as noted above, the chiral order parameter is far from converged at $\chi = 8000$ above $U \gtrsim 10$.

YC5

The YC4 and YC6 phase diagrams discussed above are qualitatively similar; both show a chiral intermediate phase in the vicinity of $U/t = 10$, which is present regardless of the twisting of the boundary conditions. The same is not true for the YC5 cylinder—with periodic boundary conditions, $\theta = 0$, there is no spontaneous time-reversal symmetry breaking for any U. However, when we perform flux insertion we find that the chiral intermediate phase does still exist, for $\pi \lesssim \theta \lesssim 3\pi$ and $8 \lesssim U/t \lesssim 10$. This is shown in Figure 5.7.

To understand this data, it is important to note that, unlike for YC4 and YC6, we have used a two-ring unit cell; this allows us to initialize the DMRG simulation with a product state that is half-filled both for spin up and spin down, and additionally allows us to access

the momentum sector with momentum π around the cylinder per unit length. The two ring unit cell allows the ground state to break translation symmetry along the cylinder, which indeed occurs. Figure 5.7(a) and (b) show the chiral order parameter on the two rings of the unit cell. As shown in Figure 5.8(b), the degree of symmetry-breaking decreases as the MPS bond dimension used in running DMRG is increased, though it appears that even at infinite bond dimension the symmetry will remain broken.

The chiral phase observed for YC5 seems to be the same as that found in YC4 and YC6 even if it does not extend through all boundary condition twists θ. This is partially confirmed by considering the peak height of the $\langle S_z S_z \rangle$ structure factor and the Transfer matrix estimate of the spin singlet gap, shown in Figures 5.7(c) and (d), respectively. As with YC4 and YC6, the chiral phase has a degree of short-range spin ordering which is intermediate between that of the metal and of the high-U phase and has the largest spin singlet gap of any region of the phase diagram. We also show below, in section 5.4, that this chiral phase shows the same signatures of the topological chiral spin liquid as do the YC4 and YC6 phases.

As evidence for the existence of the chiral phase in the full two-dimensional model, the YC5 results are somewhat ambiguous. Neither $\theta = 0$, for which there is no chiral phase, nor $\theta = 2\pi$, for which the phase exists, is a priori "better" or more representative of the two-dimensional model. However, further insight can be gleaned by understanding the effect of the twisted boundaries on the spin degrees of freedom that are the relevant ones for a spin liquid phase. Indeed, we believe that the $\theta = 2\pi$ boundary conditions turn out to be the more representative ones.

In particular, we can look at the strength of $\langle S_z S_z \rangle$ correlators on bonds between adjacent sites; the results are shown for four bond dimensions up to 11314 for $U/t = 10$ in Figure 5.8(c) and (d). Evidently, for flux near $\theta = 0$, there is huge anisotropy, with spin correlations much stronger on bonds around the cylinder circumference than for diagonal ones. As flux increases from zero, the anisotropy steadily decreases and shows only a change in slope upon entering the chiral phase; the anisotropy is smallest precisely where the chiral order parameter is largest. Assuming that the true intermediate phase of the two-dimensional model does not break the model's C_3 rotation symmetry, the θ for which the YC5 cylinder exhibits a chiral phase are precisely those in which the symmetry of the spin correlations is most two-dimensional. We also test this explanation by explicitly adding anisotropy to the model to weaken the bonds around the cylinder circumference; indeed, with the hopping strength on these bonds reduced by 10%, a chiral phase appears even at zero flux (see page 208 in section 7.3).

YC3

The YC3 cylinder is the smallest, and thus presumably least representative of the two-dimensional model, of all those we have studied; we nevertheless include our data for completeness. With periodic boundaries, $\theta = 0$, we find much the same behavior as for YC4 and YC6, with an intermediate chiral phase between a metallic phase and a short-range

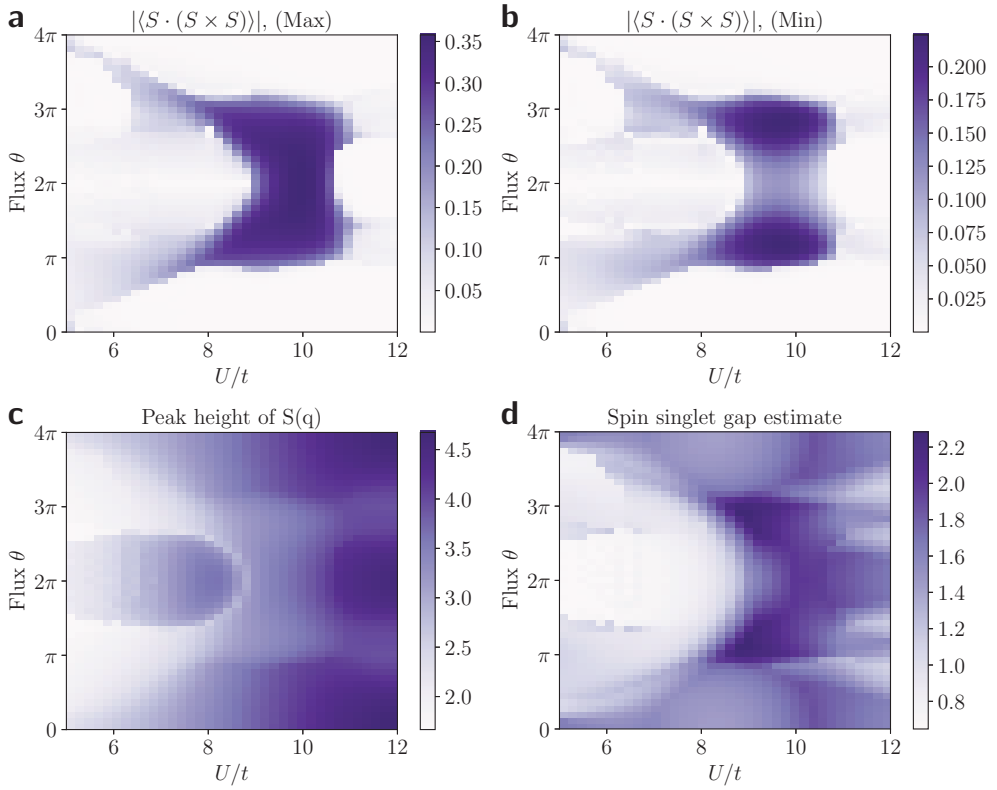

Figure 5.7: (Color online) YC5 cylinder with flux insertion θ, for $\chi = 4000$. **(a)** Absolute value of chiral order parameter; at finite bond dimension the translation symmetry is broken along the cylinder, and here we show the larger of the chiral order parameters between the two distinct rings. The chiral phase exists at intermediate U when θ is approximately in the range π to 3π. **(b)** Smaller of the two chiral order parameters. **(c)** Maximum of $\langle S_z S_z \rangle$ structure factor in the Brillouin zone. **(d)** Transfer matrix estimate of the spin singlet gap

magnetically ordered one. As partial evidence, we show the chiral order parameter versus U/t in Figure 5.9(a), with additional data available in section 7.4. Note that as with YC5, we use a larger unit cell (in this case four rings) and find that for finite bond dimension the model has a only a two-ring translation symmetry; in the figure, the two curves in for each bond dimension correspond to the chiral order parameter on the two distinct rings.

With flux insertion the behavior is quite different, and, as we show in Figure 5.9(b), the chirality vanishes for $\pi \lesssim \theta \lesssim 3\pi$, essentially the opposite of the behavior observed for YC5. In Figure 5.9(c) and (d) we also show the peak height of the spin structure factor and the transfer matrix estimate of the spin singlet gap. The relationship between these quantities and the chirality is quite different from what we observe for all three cylinder geometries discussed above, so it is not clear that the chiral phase observed here corresponds to the one found for the larger cylinders.

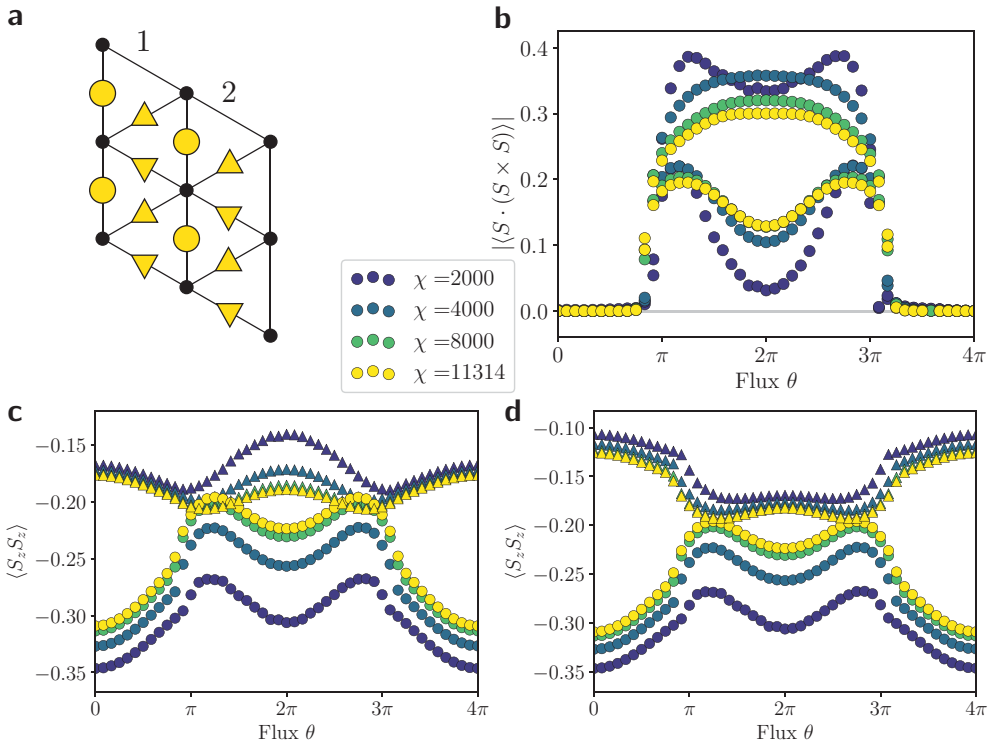

Figure 5.8: (Color online) Flux insertion for YC5 cylinder with $U/t = 10$, for a range of bond dimensions. **(a)** As noted in the text, a two-ring unit cell allows for translation symmetry-breaking. Here we label the distinct rings of the cylinder in the unit cell and the three bonds in each ring that may have different $\langle S_z S_z \rangle$ correlations. **(b)** Chiral order parameter on ring 1 (upper curves) and ring 2 (lower curves) of the unit cell. It appears that lower curve is converged for the largest χ, while the upper one is not, but it does not appear that the two will become equal even in the infinite χ limit. **(c)** $\langle S_z S_z \rangle$ for nearest neighbor bonds on ring 1 as shown in panel (a); the symbol for each data point indicates it corresponds to the bond labeled by that symbol in (a). We do not show the strength of the down-triangle bond because for each χ and θ it is equal to that of the up-triangle bond to better than one part in 10^8. In the 2D model, all three bonds are equivalent; on the YC cylinder the vertical bonds are inequivalent to the two diagonal ones. **(d)** $\langle S_z S_z \rangle$ for ring 2.

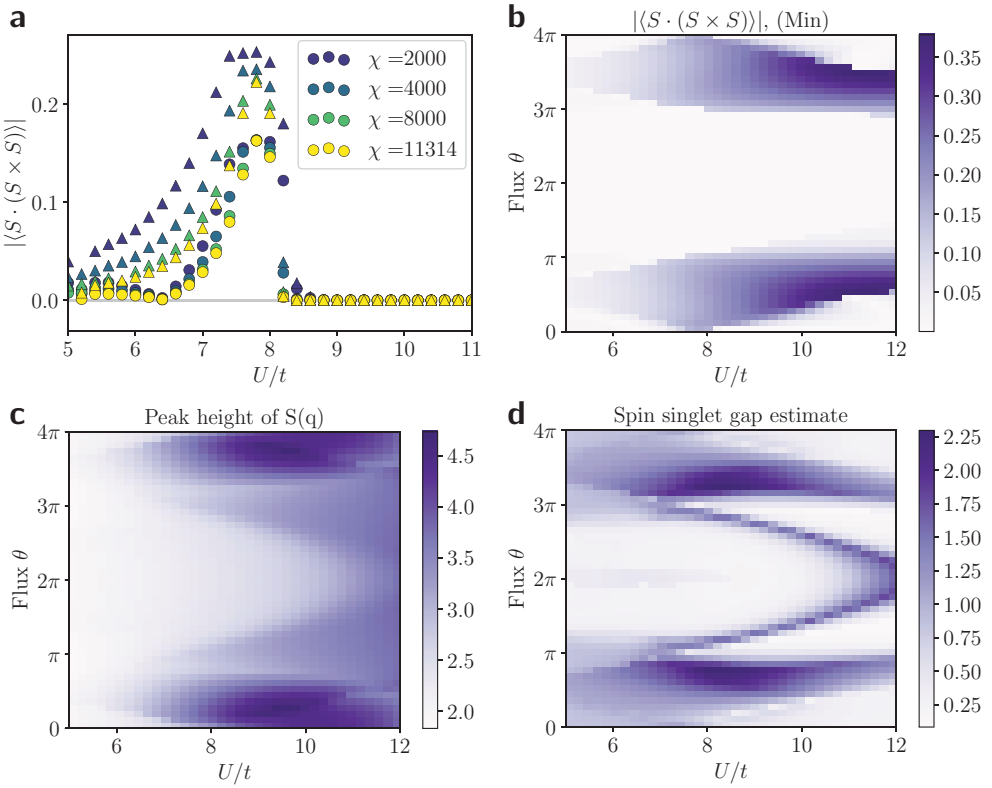

Figure 5.9: (Color online) Results for the YC3 cylinder. **(a)** Chiral order parameter on each of two ring s (circle and triangle symbols, respectively), plotted versus U/t for a range of bond dimensions. The behavior is qualitatively similar to that of YC4 and YC6. **(b)** Chiral order parameter versus U/t and flux insertion θ, for $\chi = 4000$. Here we show just the smaller of the chiral order parameters on the two rings, but the qualitative behavior is essentially identical at this bond dimension. **(c)** Peak height of the $\langle S_z S_z \rangle$ structure factor in the Brillouin zone. **(d)** Transfer matrix estimate of the spin singlet gap.

XC4

Finally, we place the model on the XC4 cylinder, which is the second smallest cylinder after YC3.[1] With periodic boundaries, we find very weak time reversal symmetry-breaking for all U/t, which decreases with bond dimension; this is shown in Figure 5.10(a). The extrapolation to infinite bond dimension is not entirely clear, but it is likely that the true ground state preserves the symmetry.

With flux insertion, we find that a chiral phase again appears, as shown in Figure 5.10(b). We also show the peak height of the $\langle S_z S_z \rangle$ structure factor and the transfer matrix estimate

[1]Ideally we would also consider the XC6 cylinder, but we are unable to reach large enough bond dimension to converge the DMRG; at our largest accessible bond dimensions, there remains a strong symmetry-breaking effect from the orientation of the DMRG snake.

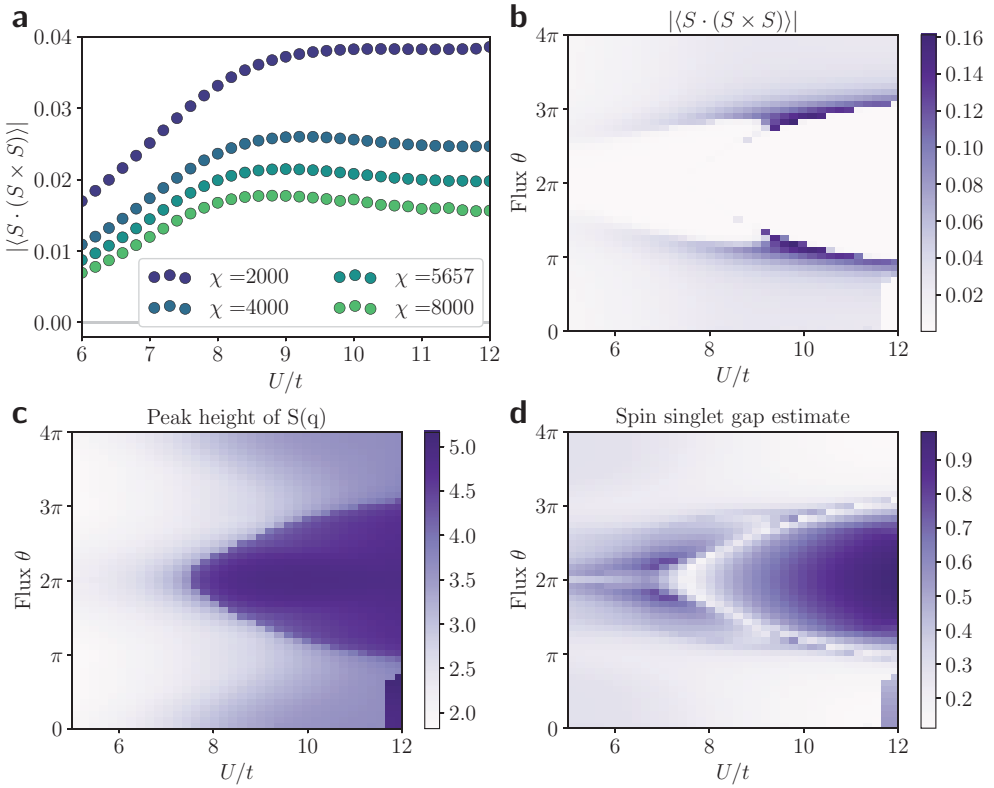

Figure 5.10: (Color online) Results for XC4 cylinder. **(a)** Chiral order parameter versus U/t for a range of bond dimensions, with periodic boundary conditions. This likely extrapolates to zero. **(b)** Chiral order parameter with flux insertion. **(c)** Maximum of $\langle S_z S_z \rangle$ structure factor on allowed momentum cuts in the Brillouin zone. **(d)** Transfer matrix estimate of the spin singlet gap.

of the spin singlet gap, in Figures 5.10(c) and (d), respectively. As with YC3, there is no clear relation between the three quantities that we found for YC4-6. However, like with YC5, the chirality appears near where the nearest neighbor spin-spin correlations are most isotropic. In the high-U, mid-flux region (with large spin singlet gap in Figure 5.10(d)), the diagonal bonds are much stronger than the horizontal ones, whereas in the rest of the phase diagram the opposite is true; the chirality is strongest precisely on the border between these two regions. Furthermore, the anisotropy is much larger in the region with exactly zero chirality than in the region where the chirality likely extrapolates to zero but is nonzero at finite bond dimension.

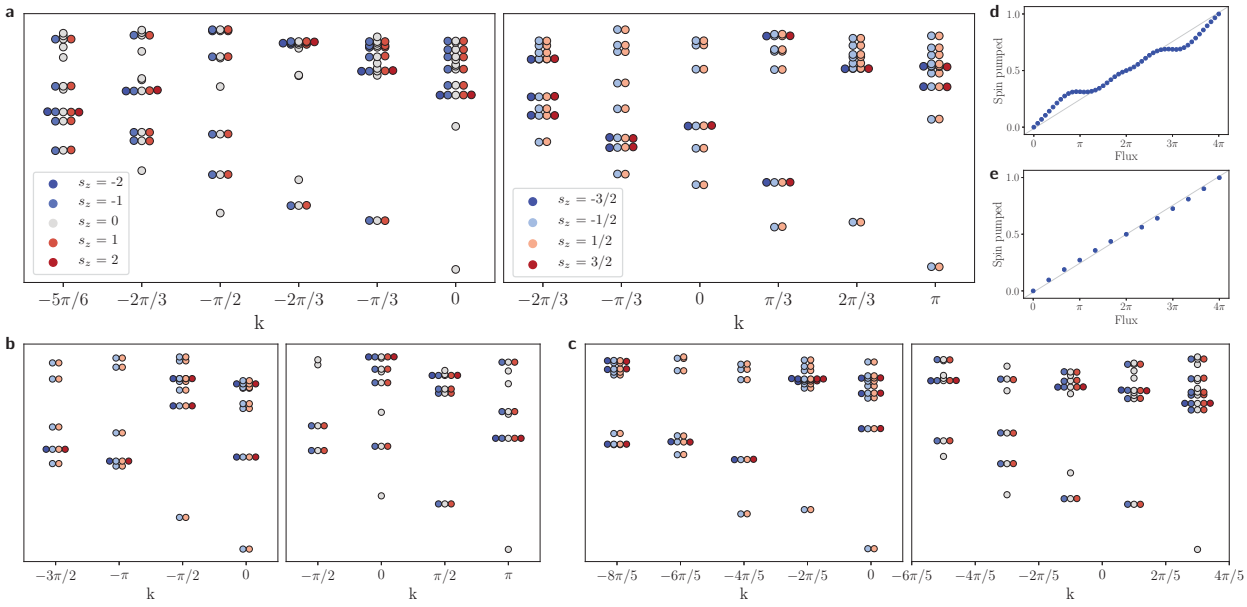

Figure 5.11: (Color online) **(a)** Momentum- and spin-resolved entanglement spectrum for the YC6 cylinder in the intermediate phase, for the ground state in the $k = 0$ (left) and $k = \pi$ (right) sectors; these correspond to the trivial and semion sectors of a chiral spin liquid (CSL) respectively. Insertion of 2π flux interchanges the two topological sectors, though as discussed in the text there is a subtlety due to working with a fermion model. **(b)** Momentum- and spin-resolved entanglement spectrum for the YC4 cylinder, with periodic boundaries at $U/t = 10.2$ (left) and with 2π flux inserted at $U/t = 11.6$ (right), corresponding to the highest chirality in each of the two topological sectors. **(c)** Entanglement spectrum for YC5 with 2π flux, $U/t = 10$, between two-ring unit cells (left) and between the rings in the unit cell (right), again corresponding to the two topological sectors. **(d)** Spin pumping as a function of flux insertion in the intermediate phase for YC4 ($U/t = 10$) and **(e)** for YC6 ($U/t = 9$).

5.4 Identification as a chiral spin liquid

We have demonstrated, for both the YC4 and YC6 cylinders, the existence of an intermediate phase which is nonmagnetic and which breaks time-reversal symmetry; we have also demonstrated that the phase is gapped for YC4 and likely gapped for YC6. We have furthermore observed this same phase for the YC5 cylinder for a range of twisted boundary conditions, and we have observed some similar behavior for the YC3 and XC4 cylinders. We now show that the chiral phase observed on the YC4-6 cylinders can in fact be identified as a chiral spin liquid (CSL)[53, 125].

A CSL is a topological phase with four degenerate ground states on the infinite cylin-

der[123]. Each minimally entangled ground state[144] spontaneously breaks time-reversal (T) and parity (P) symmetries, as indicated by a nonzero value of the chiral scalar order parameter; the two possible chiralities account for a two-fold degeneracy in the ground state manifold, which could be lifted by a P, T-breaking perturbation such as a magnetic field.

The remaining degeneracy is topological and is robust to such perturbations; the two topologically degenerate sectors, called the trivial and semion sectors, are distinguished by the respective absence or presence of a pair of semionic spinons, fractional excitations that carry spin-1/2 but no charge, separated to the ends of the cylinder at $\pm\infty$.[123, 84] In a pure spin system, insertion of 2π flux creates a pair of spinons and separates them to the ends of the cylinder, thus exchanging the two ground states and also pumping a net spin of exactly 1/2 across any cut through the cylinder; this latter property indicates that the CSL has a spin Chern number of 1/2 and a corresponding quantized spin Hall conductance[33].

In contrast, insertion of 2π spin-flux in the Hubbard model imposes antiperiodic boundary conditions on the cylinder, since $e^{2\pi i S^z} = -1$. The Hamiltonian is thus modified by 2π flux insertion, so that the question of whether the two ground state sectors are exchanged under flux insertion, as they are in a spin-model CSL, is ill-defined; instead, 2π flux insertion converts between one sector of the original Hamiltonian (with periodic boundaries) and the opposite sector of the Hamiltonian with antiperiodic boundaries, which should still lead to the same quantized spin pumping as for a spin model.

Each ground state of a CSL has a chiral edge mode with a universal low-lying spectrum; when the state is placed on an infinite cylinder, this edge spectrum appears in the entanglement spectrum for a cut between rings of the cylinder.[60, 66, 91] The edge modes are described by a chiral $SU(2)_1$ Wess-Zumino-Witten (WZW) conformal field theory[122, 20]; labeling them by spin and momentum quantum numbers (see reference [141], section 6.4), for a given spin the number of levels at successive discrete momenta around the cylinder follows the counting $(1, 1, 2, 3, 5, \cdots)$.[75] The spectrum is degenerate under $s_z \to -s_z$, where s_z is the spin quantum number of the entanglement level; the spin quantum numbers are integers in the trivial sector and half-integers in the semion sector, leading to two-fold degeneracy of the spectrum in the latter case.

We observe all of these signatures of the CSL phase. On the YC6 cylinder, we have already identified above two nearly degenerate low-lying states, in the $k = 0$ and $k = \pi$ momentum sectors; within each sector, by initializing the DMRG with different product states, we are able to converge to both chiralities (see page 201 in section 7.2), thus finding all four degenerate ground states. The chiral order parameter in each sector, indicative of time-reversal and parity symmetry-breaking, has already been shown above in Figures 5.5 (c) and (d) and Figure 5.6(a); note that these figures show the absolute value of the order parameter, which is independent of the chirality to which the DMRG spontaneously converges.

The spin- and momentum-resolved entanglement spectra for the ground states in the two sectors are shown in Figure 5.11(a), where we have excluded levels corresponding to charge fluctuations between rings of the cylinder in order to highlight the spin degrees of freedom. Both spectra show the expected WZW level counting in the low-lying states, and the spin

quantum numbers of the entanglement levels are integer for the $k = 0$ ground state and half-integer for $k = \pi$, allowing us to identify the low-lying states in the two momentum sectors with the trivial and semion topological sectors respectively.

Alternatively, 2π flux insertion should convert between the two topological sectors. We already noted in section 5.3 above that indeed the local properties like spin-spin correlations and the chiral order parameter look nearly identical between the $k = \pi$ sector with 2π flux and the $k = 0$ sector with periodic boundaries, which is consistent with this picture. (In principle these should also be equal to the local properties of the $k = \pi$ sector with periodic boundaries, but that may not be true at finite bond dimension, and may also be violated even in the true ground state due to the finite circumference of the cylinder.) In the SM, we show the equivalent of Figure 5.11(a) with the $k = 0$ entanglement spectrum replaced by the $k = \pi$ spectrum with 2π flux, and evidently it is nearly identical.

To see the equivalent of Figure 5.11(a) for the YC4 cylinder, because we find only one ground state sector, with $k = 0$, we must use the latter method. In Figure 5.11(b), we show the spin- and momentum-resolved entanglement spectrum for YC4 in the $k = 0$ sector, with periodic boundaries at $U/t = 10.2$ and with $\theta = 2\pi$ at $U/t = 11.6$; as shown in Figure 5.4(a), these values of U/t are each at the peak of the chiral order for their respective amounts of flux insertion, θ. For the YC5 cylinder, as with YC4 we find a ground state only in the $k = 0$ sector, although with two rings per unit cell, this includes both $k = 0$ and $k = \pi$ per ring. In this case, however, we cannot observe both topological sectors by looking at $\theta = 0$ and 2π since the chiral phase exists only for $\pi \lesssim \theta \lesssim 3\pi$. Instead, we make use of the fact that, for any cylinder with an odd number of spin-1/2 per ring, translation along the cylinder converts between topological sectors[142], so that we can just consider a single wavefunction and examine its entanglement spectrum both between two-ring unit cells and between the two rings in the unit cell; the result is shown in Figure 5.11(c).

With flux insertion, we also observe the quantized spin Hall effect, as shown for the YC4 and YC6 cylinders at $U/t = 9$ and 10, respectively, in Figures 5.11 (d) and (e), with a pumping of exactly spin 1/2 per 2π flux insertion. For YC6, for which the chiral order is roughly constant at $U/t = 10$, the flux insertion proceeds at a constant rate. For YC4, the shifting boundary of the chiral phase with flux insertion causes some deviation, but the qualitative behavior is the same.

5.5 Discussion

By employing the DMRG method to study the triangular lattice Hubbard model on infinite cylinders in a mixed real- and momentum-space basis, we have observed that the model exhibits three phases: a metallic phase, a nonmagnetic insulating phase, and a magnetically ordered phase. While the nature of the intermediate phase depends on the precise boundary conditions used, with flux insertion through the cylinder we find that for each cylinder geometry there is a region with spontaneous time-reversal symmetry breaking, as indicated by a nonzero chiral order parameter. In particular, this chiral intermediate phase exists for

all values of flux insertion for the YC4 and YC6 cylinders and for a large range of flux for the YC5 cylinder; the YC5 chiral intermediate phase appears precisely for those amounts of flux insertion for which spin-spin correlations are most consistent with the symmetries of the two-dimensional lattice.

Furthermore, we have shown for the YC4, YC5, and YC6 cylinders that the chiral phase shows the characteristic entanglement spectrum of a CSL with two topologically degenerate ground state sectors, and for YC4 and YC6 we have demonstrated a fractionally quantized spin Hall effect. The phase additionally appears to be gapped. Along with the nonzero chiral order parameter, this evidence strongly suggests that the nonmagnetic insulating phase is, in fact, a chiral spin liquid. This is, to our knowledge, the first clear demonstration of a chiral spin liqid in a time-reversal symmetric model of itinerant fermions.

The apparent gapped nature of the spin liquid in our simulations is consistent with the thermal conductivity measurements on κ-(BEDT-TTF)$_2$Cu$_2$(CN)$_3$ reported in reference [134]; some recent studies[81, 16] also suggest gapped thermal conductivity in $EtMe_3Sb[Pd(dmit)_2]_2$, although this is disputed[132]. On the other hand, our conclusions do not agree with those of past studies of this model using the DMRG method: the study on the two-leg ladder found a gapless spin liquid phase[72], while the DMRG study on a finite XC6 cylinder found an intermediate phase that appeared gapped but with a rapidly decaying chiral-chiral correlation function[106]. The two-leg ladder study used a modified Hamiltonian with some longer-range interactions, so the disagreement on the nature of the spin liquid is not surprising. The discrepancy with the XC6 finite cylinder study is more difficult to explain. One possibility is that, as with the XC4 and YC5 cylinders in our study, the XC6 cylinder will exhibit a chiral phase after flux insertion; we are not able to reach high enough bond dimension to converge the XC6 cylinder, and thus are unfortunately not able to test this possibility.

It is also useful to briefly consider other candidates for the intermediate phase. In particular, it is worth investigating the possibility of the intermediate phase being a Dirac spin liquid (DSL), both because there has recently been evidence in support of a DSL in frustrated spin models[39, 41] and because the CSL can be derived by gapping out the Dirac cones in a DSL, so that one might imagine a DSL in two dimensions becoming a CSL due to finite cylinder circumference or finite bond dimension. The first scenario is difficult to rule out, given that the CSL would still be the true ground state up to some cylinder circumference which could be much larger than what is accessible, but there is also no particular evidence from our data to support this scenario. The second scenario we do rule out, by analyzing the low-lying excitation spectrum using the MPS transfer matrix spectra; this analysis is described in detail in chapter 7 using a technique described in chapter 6.

If the CSL is indeed the ground state in the full two-dimensional triangular lattice Hubbard model, in real materials well described by this model we would expect regions of both possible chiralities to coexist, with a finite temperature phase transition to long-range chiral order at a temperature of the same order of magnitude as the chiral domain wall tension, possibly reduced due to entropy from the gapless edge modes located at the domain walls. We measure this domain wall tension for the YC4 cylinder by finding an optimized compos-

ite wave function that transitions from the ground state with one chirality to the ground state with the other, and we find a domain wall tension of approximately $0.0065t$ per lattice constant; this calculation is described on page 193 in section 7.1, below. Using estimates for t for real materials[105], this is about $4K \times k_B$. The corresponding phase transition may be related to the observed feature in the heat capacity, thermal conductiviy, and magnetic relaxation rate at about $6K$ in κ-(BEDT-TTF)$_2$Cu$_2$(CN)$_3$[104, 135, 134].

At very low temperatures in a single-domain sample, we would observe a quantized thermal Hall conductance, $K_{xy} = \frac{\pi^2 {k_B}^2 T}{3h}$; note that this is twice the value of the Majorana-like plateau recently reported in α-RuCl$_3$ [58]. Above the finite temperature transition, or at lower temperatures in the presence of time-reversal symmetry-breaking disorder, there would be regions of both possible chiralities, with gapless edge modes between them; below the percolation threshold, this could lead simultaneously to the observed gapless behavior in the specific heat[122, 135] and gapped behavior seen in thermal transport measurements[134].

An applied magnetic field could in principle break the degeneracy between the two chiralities, but this effect is extremely small at experimentally accessible field strengths. If the magnetic flux through a triangle in the lattice is ϕ, perturbation theory in t/U gives a term $\left[24(t^3/U^2)\sin(\phi)\left(\mathbf{S}\cdot(\mathbf{S}\times\mathbf{S})\right)/\hbar^3\right]$ in the effective spin Hamiltonian; using our measured value for the chiral order parameter and estimated parameters for κ-(BEDT-TTF)$_2$Cu$_2$(CN)$_3$[63, 105], in a 10 T field the energy splitting between ground states for the two chiralities is about 1 μeV per lattice site, so at 1 K the favored chirality would be expected to be just 1% more prevalent. It is thus not surprising that experimental results[135] do not see a significant effect from applied magnetic fields up to 10 T.

Further theoretical work must address the question of whether the chiral phase we find on the cylinders we have studied indeed extrapolates to the full two-dimensional model. Our results strongly support this conclusion: on the YC4 and YC6 cylinders the chiral phase exists for a large range of U/t independent of the flux insertion that scans the allowed momentum cuts through the full two-dimensional Brillouin zone, and furthermore on the YC5 cylinder the same phase appears when the twisted boundary conditions lead to spin correlations that approximately obey the symmetries of the full two-dimensional lattice. In other words, the chiral spin liquid is always present in the model as a competing phase, and it seems to be favored in those situations that best represent the two-dimensional system. The existence of the chiral spin liquid in two dimensions could be further confirmed either by using larger circumferences, which would be computationally expensive, or by fully 2D methods such as projected entangled pair states (PEPS)[115, 24].

Chapter 6

Techniques for two-dimensional density matrix renormalization group computations

In this chapter, I discuss a number of useful methods that my collaborators and I used in applying DMRG to a two-dimensional model by placing it on finite cylinders. In particular, I discuss:

1. Different possible boundary conditions for placing a two-dimensional lattice on a cylinder;
2. Converting the triangular lattice Hubbard model from real-space to mixed real- and momentum-space;
3. How the central charge, a property of one-dimensional systems, should appear on the quasi-one-dimensional cylinders;
4. How charges are associated with the entanglement spectrum of the MPS for the ground state;

and

5. How the transfer matrix spectrum of the MPS can be used to study the excitation spectrum of the model.

These discussions will be useful in understanding the data described in the previous chapter, and hopefully also more generally as a partial guide to studying two-dimensional systems with DMRG.

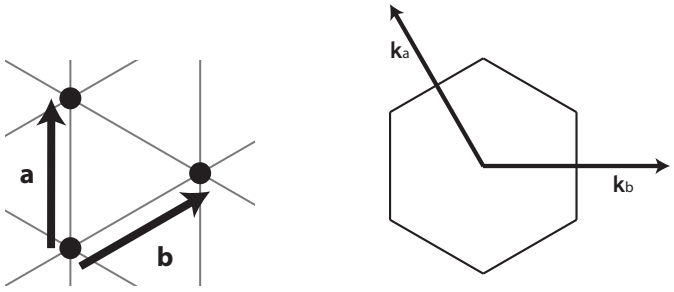

(a) (b)

Figure 6.1: (a) Lattice vectors **a** and **b** on the triangular lattice. (b) Corresponding reciprocal lattice vectors and the first Brillouin zone.

6.1 Compactification to a cylinder

The DMRG [128, 99] is a method for finding the ground state of a one-dimensional model, so it cannot be used to study a full two-dimensional system, such as the triangular lattice Hubbard model, directly. Instead, we must take 1D strips of the lattice with some finite width. In particular, we identify the two edges of the strip with each other, using periodic boundary conditions; this eliminates edge effects, giving the best approximation to the 2D model that we can achieve with a strip of finite width.

To pick the 1D strip that defines the cylinder, we follow these steps:

1. Pick two points of the lattice, and declare them to be equivalent.
2. The line between the two points is the width of the strip or equivalently the circumference of the cylinder.
3. The line passing through the identified point (ie both points, since they are the same) and perpendicular to the circumference is the glued edge of the cylinder.

It is important to note that choosing any cylinder of this type automatically guarantees periodicity of the Hamiltonian along the cylinder, so we once again have a translation-invariant system. To see this, let the lattice vectors **a** and **b** be as shown in Figure 6.1, and a the lattice spacing. Then, noting that $\mathbf{a}^2 = \mathbf{b}^2 = a^2$ and $\mathbf{a} \cdot \mathbf{b} = a^2/2$, if the edges are perpendicularly separated by $n_a\mathbf{a} + n_b\mathbf{b}$ for some integers n_a and n_b (as must be true given the above procedure), then one can check that the vector $(2n_b + n_a)\mathbf{a} - (2n_a + n_b)\mathbf{b}$ is perpendicular, and both coefficients are integers. This is a vector that points along the length of the cylinder, and it is an integer linear combination of the lattice vectors, so the Hamiltonian is invariant under this translation. (In some cases, the actual period may be smaller than this, eg if $n_b = 0$ and n_a is even.)

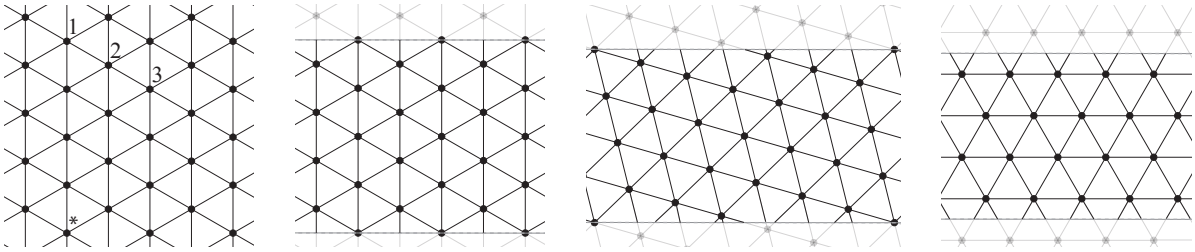

(a) (b) (c) (d)

Figure 6.2: (a) Periodic boundary conditions on the cylinder are defined by identifying the point $\star$ with the points labeled in the figure as 1, 2 and 3, which correspond to $(n_a, n_b) = (4, 0)$, $(3, 1)$, and $(2, 2)$ respectively. (b) Cylinder from identifying point $\star$ with point 1, called YC4 boundary conditions. This is the same cylinder one would get by adding sites at the hexagon centers of a zigzag nanotube. (c) Cylinder from identifying point $\star$ with point 2. Note that this case has a 26-site unit cell, making it computationally intractable. (d) Cylinder from identifying point $\star$ with point 3, called XC4 boundary conditions. This corresponds to adding sites at the hexagon centers of an armchair nanotube.

Allowed cylinders and the consequences of choosing one

We now have a general procedure for generating cylinders to which the 2D triangular lattice Hubbard Hamiltonian can be restricted in a natural way, namely by picking pairs of points on the lattice to identify with each other. If we fix the cylinder circumference (in Manhattan distance, ie the minimum number of lattice vectors to go between equivalent points; this is not the physical circumference in general) to be a particular integer, L, there are exactly $\lfloor (L+1)/2 \rfloor$ unique cylinders of this type that can be constructed, which are given by fixing one point in the 2D lattice and identifying it with with each of the $\lfloor (L+1)/2 \rfloor$ points separated by $n_a\mathbf{a} + n_b\mathbf{b}$ such that $n_a + n_b = L$ and $n_a \in \{\lfloor L/2 \rfloor, \lfloor L/2 \rfloor + 1, \cdots, L\}$. The three points for $n = 4$ are shown in Figure 6.2(a). All other lattice points that are equidistant (in Manhattan distance) from the fixed point give physically equivalent cylinders by rotating or reflecting the 2D lattice. The resulting one-dimensional strips (with a cylinder formed by identifying the edges) are shown in Figures 6.2(b), 6.2(c), and 6.2(d); the first and third cylinders are called YC4 and XC4, indicating that a lattice vector runs, respectively, along the y or the x direction[136]. In general, the YCL cylinder is one with $(n_a, n_b) = (L, 0)$ and is defined for any L, while the XCL cylinder can be constructed only when L is even and corresponds to $(n_a, n_b) = (L/2, L/2)$.

The choice of boundary conditions has important consequences, both for the physics of the model and for the computational efficiency of the DMRG. The first implication of the choice of boundary conditions is that the allowed momenta in the Brillouin zone are restricted. The allowed inequivalent momenta in the full 2D model are those in the first Brillouin zone, which is shown for this model in Figure 6.3(a). However, if we define a cylinder by identifying, with periodic boundary conditions, two points that are separated by

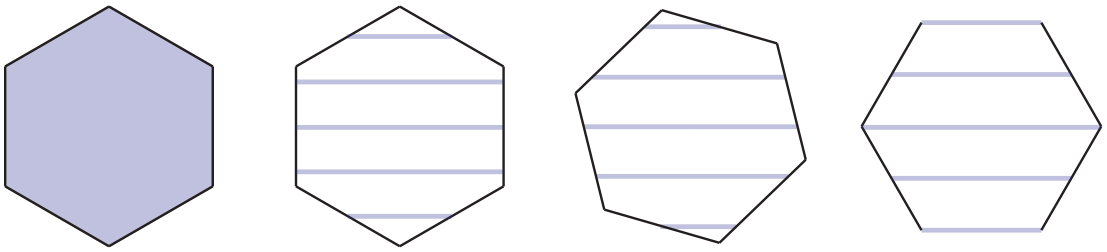

(a) (b) (c) (d)

Figure 6.3: (a) Allowed momenta in the first Brillouin zone of the full 2D triangular lattice. (b) Allowed momenta for YC4 boundary conditions. (c) Allowed momenta for the $(n_a, n_b) = (3, 1)$ boundary conditions. (d) Allowed momenta for the XC4 boundary conditions. Note that in (b)-(d), if the hexagons are tiled, then the allowed cuts form 4, 1, and 2 distinct lines respectively, corresponding to different numbers of conserved momenta in the Hamiltonian.

$n_a\mathbf{a} + n_b\mathbf{b}$, then an eigenstate at momentum $\mathbf{k} = c_a\mathbf{k}_a + c_b\mathbf{k}_b$ (c_a and c_b can be arbitrary real numbers) must satisfy $\psi_{\mathbf{k}}(\mathbf{x}) = \psi_{\mathbf{k}}(\mathbf{x} + n_a\mathbf{a} + n_b\mathbf{b})$, or equivalently (due to Bloch's theorem)

$$1 = e^{i(n_a\mathbf{a}+n_b\mathbf{b})\cdot(c_a\mathbf{k}_a+c_b\mathbf{k}_b)} = e^{2\pi i(n_a c_a+n_b c_b)} \tag{6.1}$$

which requires that $n_a c_a + n_b c_b$ be an integer. Each integer corresponds to a particular line through the Brillouin zone. For example, in the case of the YC4 cylinder, where $n_a = 4$ and $n_b = 0$, there is no restriction on c_b but c_a must be an integer multiple of $1/4$. This leads to the cuts through Brillouin zone shown in Figure 6.3(b). The corresponding cuts for the other two possible choices of boundary conditions are shown in Figures 6.3(c) and 6.3(d).

A related consequence of the choice of boundary conditions is that certain types of multi-sublattice orders may or may not be allowed. This is extremely important for the triangular lattice Hubbard model, which in the limit $U \to \infty$ reduces to the nearest neighbor Heisenberg model and thus should have a three-sublattice 120° Néel order. Notably, this order is *not allowed* on the YC4 cylinder, since the four sites around the circumference cannot be assigned to three distinct sublattices in a consistent way.

Another physical consequence of the choice of boundary condition is that the final cylinder circumference can vary in size. In the case of YC4 boundaries, the cylinder has circumference $4a$, while for XC4 boundaries it is just $2\sqrt{3}\,a$. This is also reflected in total length of the allowed cuts through the Brillouin zone; these have lengths $4\times(4\pi/a\sqrt{3})$ and $2\sqrt{3}\times(4\pi/a\sqrt{3})$ respectively. This means that with a given number of sites L in the unit cell, the YCL cylinder may be "more two-dimensional" than the corresponding XCL cylinder, though this effect is presumably less important than the question of which multi-sublattice orders are or are not allowed.

Finally, an appropriate choice of boundary conditions can dramatically speed up numerical computations by introducing additional conserved quantities. The YCL cylinders have

discrete L-fold translation symmetry around the cylinder, leading to L conserved momenta. These correspond to the cuts through the Brillouin zone. The XCL cylinders (well-defined for even L) similarly have $L/2$-fold discrete translation symmetry, giving $L/2$ conserved quantities. The distinct conserved momenta correspond to distinct allowed cuts through the Brillouin zone (figure 6.3): if the BZ is tiled, then the allowed cuts actually form 4, 1, and 2 distinct lines for the three respective boundary conditions.

As noted in section 5.2, we primarily use the YC boundary conditions. There are two main reasons: (1) by choosing different cylinder circumferences, we can try to stabilize/destabilize different phases and in particular we can frustrate the expected high-U magnetic order to make a spin liquid phase more robust and easier to observe; and (2) with YCL boundary conditions we can use a mixed real- and momentum-space basis with L conserved momenta, which both gives a dramatic improvement in computational efficiency and allows us to separately find the ground state in different momentum sectors.

6.2 Mixed-space Hamiltonian

As a reminder, the model we study is the standard Hubbard Hamiltonian,

$$H = -t \sum_{\langle ij \rangle \sigma} c^\dagger_{i\sigma} c_{j\sigma} + \text{H.c.} + U \sum_i n_{i\uparrow} n_{i\downarrow}, \tag{5.1}$$

on the triangular lattice. However, this is written in real space, whereas we actually perform the DMRG simulations reported in the previous chapter in a mixed real- and momentum-space basis, a method developed in reference [78]. Here I show precisely how that transformation works, for both cases of YC and XC boundary conditions.

YC mixed-space Hamiltonian

The first step is to convert the triangular lattice model into an effective model on the square lattice, which we do as shown in Figure 6.4(a). We then label each site by its horizontal position x and vertical position y, giving the square lattice Hamiltonian

$$H = -t \sum_{xy\sigma} \left[c^\dagger_{xy\sigma} c_{x+1,y,\sigma} + c^\dagger_{xy\sigma} c_{x,y+1,\sigma} + c^\dagger_{xy\sigma} c_{x+1,y+1,\sigma} + \text{H.c.} \right] + U \sum_{xy} n_{xy\uparrow} n_{xy\downarrow}. \tag{6.2}$$

We convert to the mixed-space basis by Fourier transforming in the y direction. For a cylinder with circumference L, this looks like

$$c_{xy\sigma} = \frac{1}{\sqrt{L}} \sum_k e^{i(2\pi/L)ky} c_{xk\sigma} \tag{6.3}$$

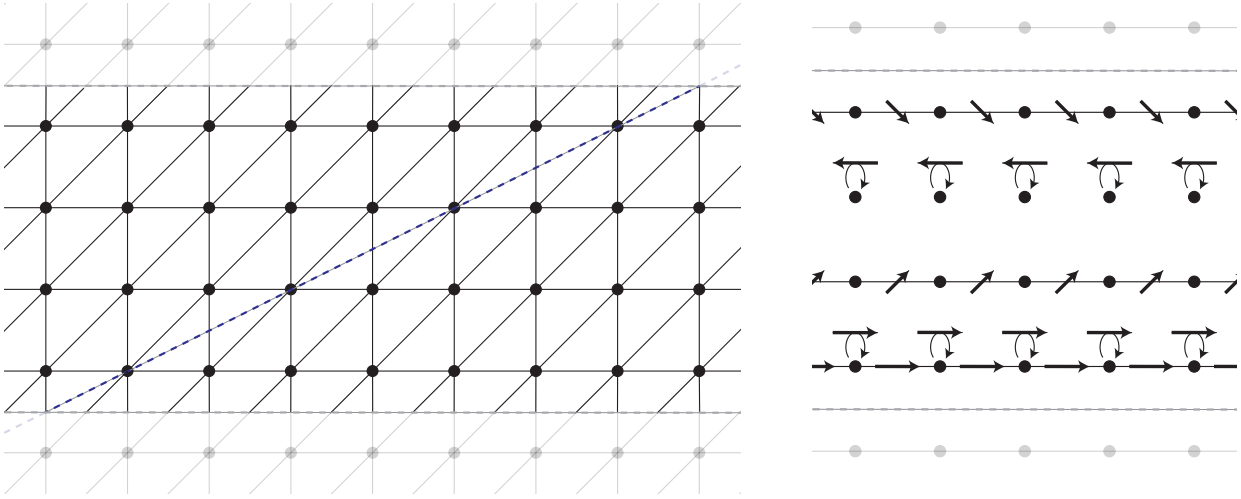

(a) (b)

Figure 6.4: The triangular lattice in Figure 6.2(b) is converted to the square lattice with diagonal couplings shown in **(a)**. As before, the dashed gray lines are identified with each other to form a cylinder. In Figure 6.2(b) that line runs straight along the physical cylinder; that same line running lengthwise for the YC4 triangular lattice now makes a helix around the square lattice cylinder, shown as a dashed blue line. In **(b)**, we show the effective lattice in the mixed real- and momentum-space, with hopping that is diagonal in the vertical coordinate, k. The arrow next to each hopping term or on-site energy indicates its strength and phase; note that the hoppings are for the $c_x^\dagger c_{x+1}$ terms and that the complex conjugate should be taken for the $cc^\dagger$ terms. Hopping terms that are exactly 0 have been omitted completely, but these are specific to the YC4 cylinder shown in the figure. In each vertical column, the different momenta are mixed by the interaction term (not shown).

where k is an integer and $(2\pi/L)k$ is the momentum when the lattice constant has been set to 1. The resulting Hamiltonian is

$$\begin{aligned} H = &- t \sum_{xk\sigma} \left[2\cos((2\pi/L)k) n_{xk\sigma} + \left(\left(1 + e^{i(2\pi/L)k}\right) c^\dagger_{xk\sigma} c_{x+1,k,\sigma} + \text{H.c.} \right) \right] \\ &+ (U/L) \sum_{xkk'q} c^\dagger_{xk\sigma} c_{x,k+q,\sigma} c^\dagger_{xk'\sigma} c_{x,k'-q,\sigma} \end{aligned} \tag{6.4}$$

with $k+q$ and $k-q$ defined mod L as usual.

To actually run the DMRG, we treat this new model as an effective square lattice on the cylinder, with on-site energies $-2t\cos\left((2\pi/L)k\right)$ and hopping only horizontally with a value also depending on k. This is shown in Figure 6.4(b).

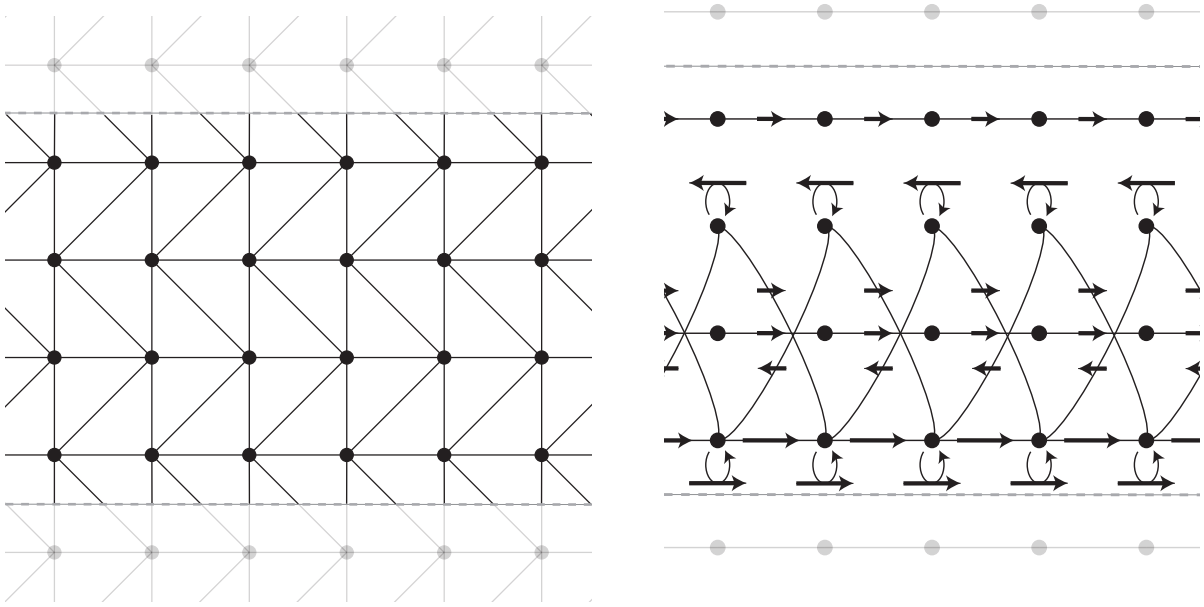

(a) (b)

Figure 6.5: The triangular lattice placed on a cylinder with XC boundary conditions as in Figure 6.2(d) is equivalent to the square lattice with alternating diagonal couplings shown in **(a)**, with the dashed lines identified with each other to form a cylinder. When the Hamiltonian is rewritten in mixed real- and momentum-space, the hopping terms (equation (6.6)) are as shown in **(b)**, where the arrow next to each hopping term or on-site energy indicates its strength and phase; terms that are exactly 0 have been omitted, but note that these are specific to the XC4 cylinder shown in the figure. In each vertical column, the different momenta are mixed by the interaction term (not shown).

XC mixed-space Hamiltonian

I now quickly repeat the same steps for a cylinder with XC boundary conditions. In this case the lattice shown in Figure 6.2(d) becomes the effective square lattice in Figure 6.5(a). Again labeling the horizontal coordinate of each point by x and the vertical coordinate by y, the real-space Hamiltonian is

$$H = -t \sum_{x\sigma} \left[\left(\sum_{y} \left(c^\dagger_{xy\sigma} c_{x,y+1,\sigma} + c^\dagger_{xy\sigma} c_{x+1,y,\sigma} \right) + \sum_{y \text{ even}} c^\dagger_{xy\sigma} c_{x+1,y+1,\sigma} + \sum_{y \text{ odd}} c^\dagger_{xy\sigma} c_{x+1,y+1,\sigma} \right) + \text{H.c.} \right] + U \sum_{xy} n_{xy\uparrow} n_{xy\downarrow}. \tag{6.5}$$

The unit cell now has two sites in the y direction, so there are only half as many distinct momenta; labeling the mixed-space unit cells by x and k_y, there will again be two sites

per unit cell. However, we do not perform the Fourier transform this way. Instead, we apply precisely the same transformation as in the YC case, equation (6.3), with the result that $k_y = (k \bmod 2) \times 4\pi/L$, compared with $k \times 2\pi/L$ for the YC cylinder. This mismatch between the operator index k and the actual momentum appears as terms in the Hamiltonian coupling k with $k \pm L/2$:

$$\begin{aligned} H = &- t \sum_{xk\sigma} \Big[2\cos((2\pi/L)k) n_{xk\sigma} + (1 + \cos((2\pi/L)k)) \left(c^\dagger_{xk\sigma} c_{x+1,k,\sigma} + \text{H.c.} \right) \\ &\qquad - \cos((2\pi/L)k) \left(c^\dagger_{xk\sigma} c_{x+1,k+L/2,\sigma} + \text{H.c.} \right) \Big] \\ &+ (U/L) \sum_{xkk'q} c^\dagger_{xk\sigma} c_{x,k+q,\sigma} c^\dagger_{xk'\sigma} c_{x,k'-q,\sigma} \end{aligned} \tag{6.6}$$

The mixed-space hopping terms for XC4 are shown in Figure 6.5(b).

6.3 Expected central charge in the metallic phase

As reported in chapter 5, we numerically observe for the YC4 cylinder a central charge $c \approx 6$. This is the expected result for the metallic phase, based on an exact tight-binding solution for the non-interacting limit of $U = 0$ on the full 2D lattice. In that limit, the Hamiltonian becomes:

$$H = -2t \sum_{kq\sigma} n_{kq\sigma} \big(\cos(2\pi k) + \cos(2\pi q) + \cos(2\pi(k-q)) \big) \tag{6.7}$$

where the momentum in the Brillouin zone is given by $\mathbf{k} = k\mathbf{k}_a + q\mathbf{k}_b$ for the reciprocal lattice vectors $\mathbf{k}_a$ and $\mathbf{k}_b$ as shown in Figure 6.1(b). In the ground state, all states with negative energy will be occupied and all with positive energy will be empty, defining a nearly circular Fermi surface with approximate radius $4\pi/(3\sqrt{3}\,a)$ [for comparison, the side length of the hexagonal Brillouin zone is $4\pi/(3a)$].

When the system is restricted to a finite cylinder, we can then count how many of the allowed momentum cuts cross the Fermi surface. This is shown visually in Figure 6.6 for the YC4 and YC6 cylinders; the number of cuts crossing the Fermi surface is 3 for YC4 and 5 for YC6.

Each distinct cut through the Fermi surface corresponds to two species of free fermion, one for spin up and one for spin down, and each free fermion contributes a central charge of 1[87]. Thus we conclude that the expected central charges at $U = 0$ and therefore throughout the metallic phase are 6 and 10 for the YC4 and YC6 cylinders, respectively.

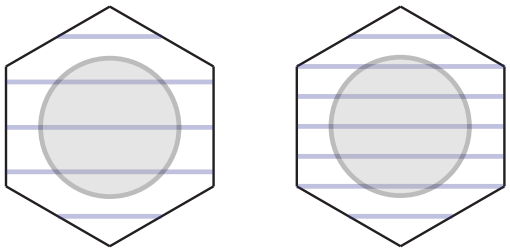

(a) (b)

Figure 6.6: **(a)** The shaded circle denotes single-particle eigenstates that are filled in the $U = 0$ limit of the model on the full two-dimensional lattice. The blue lines are the allowed momentum cuts for the YC4 cylinder; evidently, three of them cross the Fermi surface. **(b)** Same for the YC6 cylinder, with 5 lines crossing the Fermi surface.

6.4 Labeling the entanglement spectrum by quantum numbers

Recall that the entanglement spectrum is the set of values $\{\log(\lambda_i)\}$ where the $\{\lambda_i\}$ are the coefficients of the Schmidt decomposition

$$|\psi\rangle = \sum_i \lambda_i |\psi_i^L\rangle |\psi_i^R\rangle \tag{6.8}$$

for a cut between any two rings of the cylinder[66].

We use a matrix product state with all legs labeled by conserved charges, so that when we perform the Schmidt decomposition as in equation (6.8), each Schmidt state $|\psi_i^L\rangle$ is an eigenstate of three operators: total momentum around the cylinder, spin up occupation number, and spin down occupation number. We then label the λ_i by the corresponding integer eigenvalues.

However, for iDMRG the left and right Schmidt states extend to infinity, and it is not obvious how these integer charge labels correspond to "physical" values of the charge because, for example, the total spin up occupation is infinite in each of the two halves. Thus our charge labels actually give the total charge relative to some point on the cylinder (arbitrarily chosen as a result of details of the DMRG algorithm) which may be far from the cut we consider in the Schmidt decomposition.

We can fix this ambiguity by subtracting a constant offset from all charge labels so that the net charge on each of the two semi-infinite halves, defined by

$$\sum_i \lambda_i^2 Q_{\lambda_i} \tag{6.9}$$

where Q_{λ_i} is the charge label of λ_i, is 0. A more rigorous treatment of this subtraction is given in the Supplementary Material of reference [141], section II(B).

After making this correction, each Schmidt value λ_i is labeled by a set of "physical charges" including the momentum and total spin ($(n_\uparrow - n_\downarrow)/2$). The latter may be a half-integer if, as in the semion sector of a chiral spin liquid (CSL), there are fractionalized quasiparticles.

6.5 Matrix product state transfer matrix and the excitation spectrum

As noted in section 5.3, excitation gaps in the physical system can be estimated from the eigenvalues of the matrix product state (MPS) transfer matrix spectrum. Here we elaborate, showing how flux insertion can be used to partially map out the two-dimensional excitation spectrum versus k_x and k_y. This is similar to the method used in references [39, 41]. We use this technique to show that our data do not clearly indicate a susceptibility towards a Dirac spin liquid state; see sections 7.1, 7.2, and 7.3 below.

One-dimensional version

Consider a one-dimensional system, with its ground state given by an MPS. For clarity, we suppose a one-site unit cell and a right-normalized MPS with the transfer matrix as shown in Figure 6.7(a). If all legs of the MPS tensors are labeled by conserved charges, then transfer matrix eigenvalues can be labeled as well. As an example, suppose the conserved charge is S_z. Then the transfer matrix can be decomposed into independent sectors with a conserved charge on each leg, as in Figure 6.7(a). The total charge coming in from the right is $s_2 - s_4$, while the total charge going out on the left is $s_1 - s_3$. An eigenvector of this sector of the transfer matrix will have outgoing charge to the left of $s_2 - s_4$ so that the product is nonzero, and the outgoing charge of the product will be the left charge of the transfer matrix, or $s_1 - s_3$; since the product is a scalar multiple of the original vector, we can conclude that $s_1 - s_3 = s_2 - s_4$ in any sector of the diagonalized transfer matrix. (In other words, the transfer matrix being diagonalizable means that all blocks with $s_1 - s_3 \neq s_2 - s_4$ must be identically zero.) In this way, each eigenvalue of the transfer matrix can also be labeled by this conserved charge, $s_1 - s_3$.

We can then relate these conserved charges to physical excitations in the system. Assume a transfer matrix eigenvector with total outgoing conserved charge s and apply an operator S^+ inside the transfer matrix as shown in Figure 6.7(b); the outgoing conserved charge of the combined object is $s+1$, and it will transform according to the $s+1$ block of the transfer matrix. Thus if the 1 eigenvalue corresponding to the normalization of the MPS is in the $s = 0$ sector, the $s = 1$ sector of the transfer matrix will describe the physical evolution with translation in x of excitations with $S_z = 1$.

In fact, the eigenvalues of the transfer matrix spectrum give very specific information about the excitation spectrum in each charge sector. Letting the eigenvalues be denoted by $\lambda = e^{-\epsilon + i\phi}$, it is believed to be true that for each such eigenvalue there is an excitation of

(a) (b)

Figure 6.7: **(a)** The MPS transfer matrix, here shown for a right-normalized MPS with a one site unit cell, can be decomposed into blocks labeled by a conserved charge on each leg. $s_1 - s_3 = s_2 - s_4$ for every nonzero block if the transfer matrix is diagonalizable. **(b)** The charge of the transfer matrix corresponds to the physical charge of an excitation, here demonstrated via a spin-1 excitation produced by the S^+ operator.

the system with energy $E = v\epsilon$ and momentum $k_x = \phi/a$; v is a scale factor that is the same for every excitation.[143] At finite bond dimension it will be impossible to map out the full excitation spectrum since k_x is continuous, but the transfer matrix spectrum will include the minima of the excitation spectra versus k_x. Thus by looking at the low-lying eigenvalues in each charge sector, it is possible to observe the smallest excitation energies for different types of excitations and the corresponding k_x. For example, the low-lying $s = 0$ eigenvalues give the spin singlet gap; it is similarly possible to compute the triplet gap from the $s = 1$ sector.

Hubbard model and the two-dimensional excitation spectrum

Now suppose that the system is the square lattice Hubbard model (lattice constant a) on a cylinder with a circumference of L sites, in particular in mixed real- and momentum-space, with conserved quantities $(n_\uparrow, n_\downarrow, k_y)$, so that the conserved spin is $(n_\uparrow - n_\downarrow)/2$ and the conserved charge is $n_\uparrow + n_\downarrow$. Here we label the k_y eigenvalues by integers from 0 through $L - 1$ for a cylinder of circumference L, and they should be multiplied by $2\pi/a$ to get the true momentum.

Then suppose that in some charge sector, for example $k_y = 1$, $n_\uparrow = 1$, $n_\downarrow = -1$, the smallest eigenvalue is at $k_x = \pi/a$. This means that in that charge sector, the lowest energy excitation has $\Delta k_x = \pi/a$, and that it has a Δk_y corresponding to a transition between two of the allowed momentum cuts, at $k = n$ and $k = n + 1$. This would seem to indicate that $\Delta k_y = 2\pi/a$, but there is an important, and very powerful, exception.

As described in section 5.3, when we perform flux insertion that twists the boundaries oppositely for spin up and spin down electrons, we shift the momentum cuts through the Brillouin zone in opposite directions. Compared with the charge neutral sector, the excitation in sector $(1, -1, 1)$ is created by some combination of the operators $c^\dagger_{\uparrow,k+1} c_{\downarrow,k}$ and the physical shift in k_y between the annihilated electron and the created one is actually $(2\pi/a)(1+\theta/(2\pi))$.

Using this, we can, for each θ, find the Δk_x for the lowest energy excitation in each charge sector and its corresponding Δk_y, then scan θ from 0 to 4π to map out how both

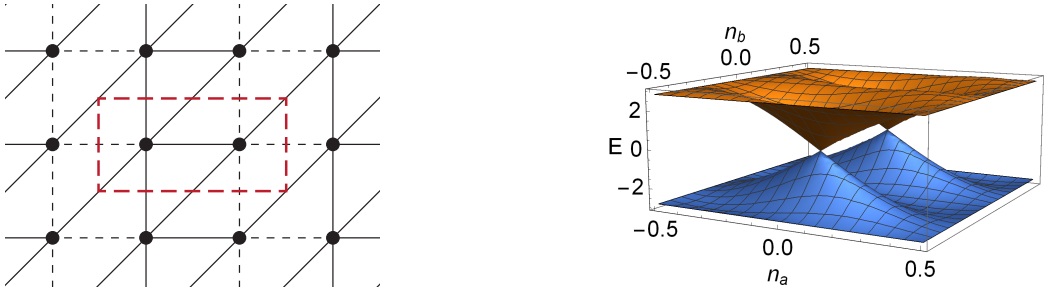

(a) (b)

Figure 6.8: **(a)** Sample tight-binding model for demonstration of excitation spectra from MPS transfer matrix spectrum. Hopping is $-t$ on solid bonds, $+t$ on dashed bonds, and interaction is zero. The red rectangle shows the unit cell. **(b)** Dispersion for this model, plotted as a function of (n_a, n_b) where $\mathbf{k} = n_a\mathbf{k}_x + n_b\mathbf{k}_y$. The reciprocal lattice vectors are $\mathbf{k}_x = (\pi/a)\hat{x}$ and $\mathbf{k}_y = (2\pi/a)\hat{y}$ where a is the lattice constant.

the minimum excitation energy and its corresponding Δk_x vary with Δk_y. (Note that the particular way that momentum cuts shift will depend on the charge sector.) This provides a one-dimensional cut through the minimum of the excitation spectrum vs k_x and k_y.[1]

To demonstrate the technique, consider the noninteracting model shown in Figure 6.8(a), with hopping $-t$ on solid bonds and $+t$ on dashed bonds; this is just the $U = 0$ Hubbard model on a distorted triangular lattice with staggered π flux. The exact solution is given by

$$E(n_a, n_b) = \pm\left(4\cos^2(2\pi n_b) + \left|e^{i2\pi n_b} + e^{-i2\pi n_a} + e^{-i2\pi(n_a+n_b)} - 1\right|^2\right) \tag{6.10}$$

$$= \pm\left(4\cos^2(2\pi n_b) + 2(2 - \cos(2\pi n_a) + \cos(2\pi n_a + 4\pi n_b))\right) \tag{6.11}$$

where n_a and n_b give the momentum as $\mathbf{k} = n_a\mathbf{k}_x + n_b\mathbf{k}_y$. This dispersion is shown in Figure 6.8(b) and evidently has Dirac cones at $(n_a, n_b) = (0, \pm 1/4)$. In Figure 6.9 we show in the left two columns the following quantities for a circumference 4 cylinder: the allowed momentum cuts through the Brillouin zone at $\theta = 0$; the allowed cuts at $\theta = 2\pi$; the low-lying transfer matrix spectrum versus θ in the spin 0 and spin 1 sectors, with eigenvalues colored by momentum quantum number; the low-lying transfer matrix spectrum for all theta versus n_a in the spin 0 and spin 1 sectors; and the low-lying spectrum for all theta versus n_b in the spin 0 and spin 1 sectors. In the right two columns we show the same for $L = 5$.

The $S_z = 0$ spectra in Figure 6.9 are discrete with respect to both momenta n_a and n_b, a fact which we briefly explain. These excitations correspond to applying either a $c^\dagger_\uparrow$ followed by $c_\uparrow$ or $c^\dagger_\downarrow$ followed by $c_\downarrow$. For n_b, at zero flux each creation and annihilation operator must lie on one of the allowed momentum cuts, and the difference in the momenta of $c^\dagger$ and

[1] One caveat to this technique: the scale factor v relating the excitation energies to the transfer matrix eigenvalues may not be constant with flux insertion. However, this does not appear to be a problem in existing results in the literature.[39, 41].

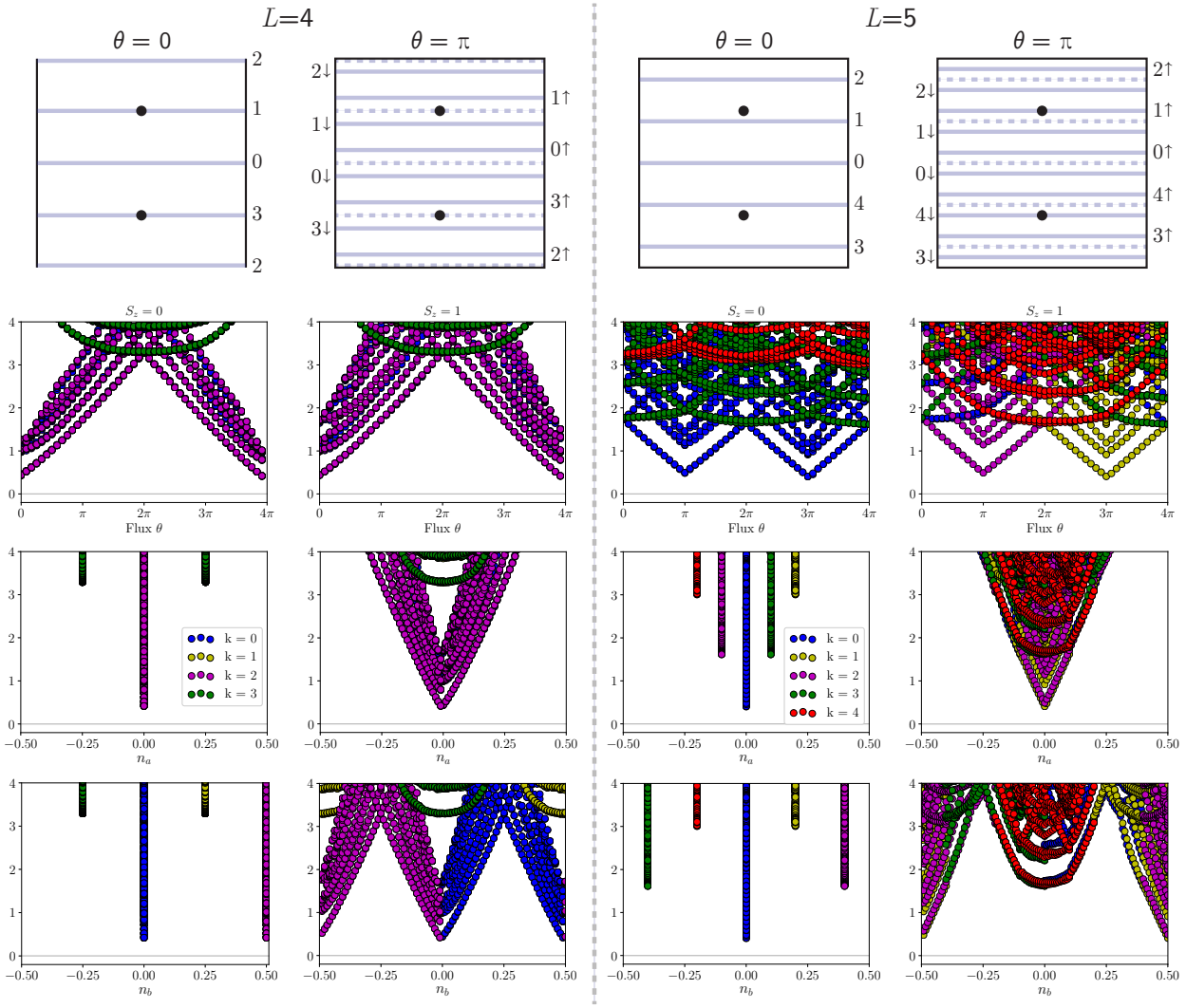

Figure 6.9: Transfer matrix spectra for the ground state of the model shown in Figure 6.8(a), computed using DMRG with a bond dimension of 4000. **Left two columns, top row:** allowed momentum cuts for a square lattice on a circumference 4 cylinder at (left) zero flux and (right) π flux. Black dots indicate the locations of the Dirac cones. **Second row:** low-lying transfer matrix spectrum versus flux θ in the $S_z = 0$ (left) and $S_z = 1$ (right) sectors. Colors indicate the momentum quantum number of each eigenvalue, as given by the legend in the third row. Notes: (1) we omit the eigenvalue of the transfer matrix that equals 1, which just gives the normalization of the state; (2) the bottoms of the Dirac cones are at nonzero energy due to finite bond dimension; and (3) some data points may be hidden, e.g. $k = 0$ behind $k = 2$. **Third row:** transfer matrix spectrum for spin 0 and spin 1 versus n_a. **Fourth row:** spectrum versus n_b. Note that part of the $S_z = 0$ spectrum is near the right edge. **Right two columns:** same data for a cylinder with circumference $L = 5$.

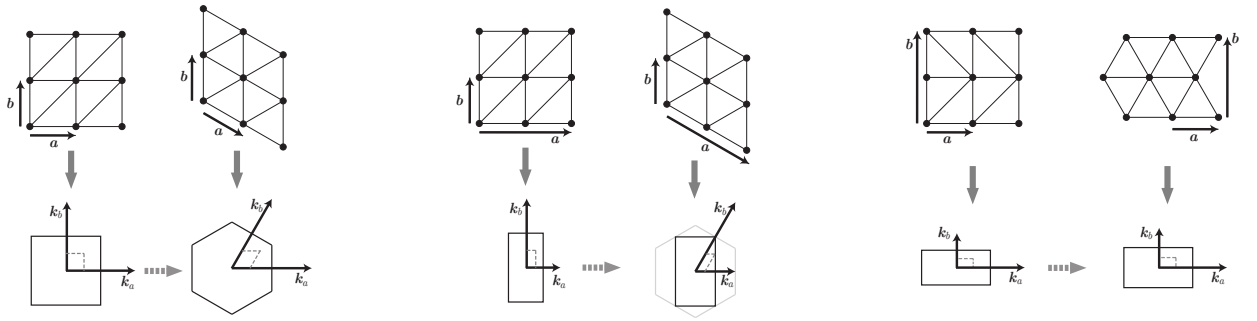

(a) (b) (c)

Figure 6.10: Conversion from momentum space on the square lattice representation of the triangular lattice back to momentum space for the original lattice. **(a)** The original triangular lattice is shown in the top right, with a one ring unit cell. For running DMRG with YC boundary conditions, we convert to the square lattice shown at top left. Using the MPS transfer matrix from the computed ground state, we find the excitation spectrum as a function of $\mathbf{k}$ in the Brillouin zone for the square lattice, bottom left; the momentum is given in terms of n_a and n_b, fractions of the reciprocal lattice vectors $\mathbf{k}_a$ and $\mathbf{k}_b$. The corresponding momenta in the Brillouin zone for the original triangular lattice, bottom right, can be computed by using the corrected $\mathbf{k}_a$ and $\mathbf{k}_b$ while keeping n_a and n_b the same; this is demonstrated by the point $n_a = n_b = 1/4$ at the intersection of the dashed gray lines. **(b)** Same but for the YC boundary conditions with a two-ring unit cell. At bottom right, we show how the reduced Brillouin zone with two rings fits into the one-ring Brillouin zone. **(c)** Same but for the XC boundary conditions.

c is discretized to one of the L allowed transitions between cuts. As flux is inserted, the momentum cuts shift, but they shift together for $c_\sigma^\dagger$ and c_σ so that the momentum transfer remains discretized. (This does not happen for $S_z = 1$ because the cuts for $c_\sigma^\dagger$ and $c_{-\sigma}$ shift oppositely.) This discretization in n_b will be present for any spinful fermion model in the $S_z = 0$ sector. The discretization in n_a, on the other hand, is specific to this model. In particular, for this model the local minima of the excitation spectrum with respect to n_a at fixed n_b remain at the same n_a when the initial and final momenta in the $\mathbf{k}_y$ direction (separated by the momentum of the excitation, n_b) are varied. Recalling from above that the transfer matrix spectrum eigenvalues generally give the local minima in the excitation spectra, this leads to discretization in n_a. In more complicated models, the $S_z = 0$ will not be exactly discretized, though it may still have a tendency to cluster around lines of discretized momentum.

To confirm that the transfer matrix really gives the two-dimensional excitation spectrum as claimed, we point out several features of the spectra. (1) For spin 0 excitations, where the momenta of $c^\dagger$ and c move together, Δk_y is quantized, and the Dirac cones appear in the $k = 0$ sector whenever an allowed momentum cut hits one. For $L = 4$, they also appear

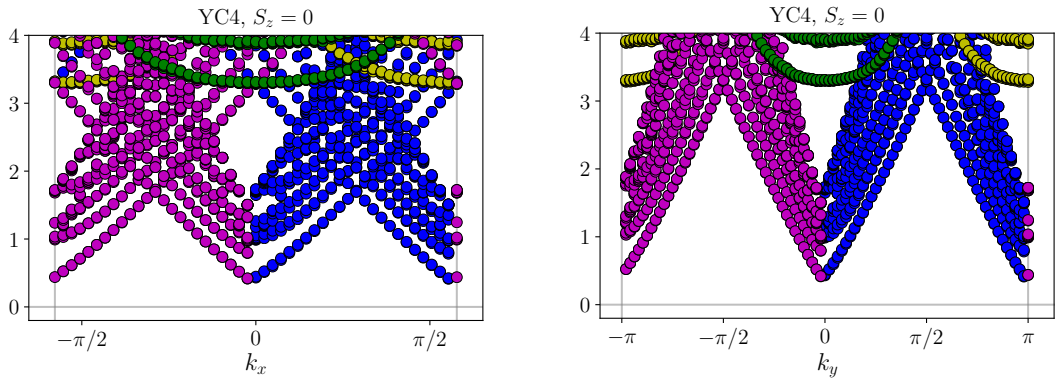

(a) (b)

Figure 6.11: **(a)** Low-lying part of the transfer matrix spectrum for the noninteracting model of Figure 6.8(a), vs k_x in the Brillouin zone of the original triangular lattice. (The lattice constant is set to 1.) Note that transitions between the Dirac cones appear at $\Delta k_x = 0$, $\pm\pi/\sqrt{3}$ as expected. **(b)** Same, versus k_y, with transitions between Dirac cones appearing as expected at $\Delta k_x = 0, \pm\pi$.

simultaneously for $k = 2$ because the separation between the cones is twice the separation between allowed cuts. (2) For spin 1 excitations, the Dirac cones appear for $L = 5$ in the $\Delta k = 2$ sector at $\theta = \pi$ corresponding to a transition from the lower cone with $k_y = 4$ for spin down to the upper one with $k_y = 1$ for spin up and at $\theta = 3\pi$ in the $\Delta k = 1$ sector corresponding to a transition from the upper cone with $k_y = 2$ for spin down to the lower one with $k_y = 3$ for spin up. (3) Dirac cones appear at $\Delta k_y = 0$ for L=5 in the spin 0 sector but not in the spin 1 sector, since cuts for spin up and spin down can never both pass through the same Dirac cone at the same time given their spacing.

On the triangular lattice

Finally, we describe how this approach can be applied to the triangular lattice. To actually perform our DMRG simulations, we convert the triangular lattice into a distorted square lattice, as shown for YC and XC boundary conditions in Figure 6.10. Following the method above will give the excitation spectrum as a function of k_x and k_y in the effective square/rectangular Brillouin zone.

We then write the overall momentum as $\mathbf{k} = n_a\mathbf{k}_x + n_b\mathbf{k}_y$ as above, and simply keep n_a and n_b constant while replacing $\mathbf{k}_x$ and $\mathbf{k}_b$ by the corresponding reciprocal lattice vectors of the triangular lattice, as shown in Figure 6.10. As an example, we can place the staggered-π flux hopping model above onto the original triangular lattice; in terms of the new k_x and k_y, the $L = 4$, spin 1 spectrum versus k_x and k_y from Figure 6.9 will be as shown in Figure 6.11.

Chapter 7

Chiral spin liquid phase of the triangular lattice Hubbard model: additional data

In this chapter I present a large amount of additional data from my study of the triangular lattice Hubbard model whose results were presented in chapter 5 above. The data is organized here by cylinder geometry, in the order YC4, YC6, YC5, YC3, and finally XC4. Perhaps of particular interest will be the data on transfer matrix spectra for the YC4, YC6, and YC5 cylinders.

7.1 YC4 additional data and analysis

Correlation lengths in different charge sectors

As described in chapter 6, the MPS transfer matrix can be decomposed into blocks in different conserved charge sectors, and this allows the computation of a correlation length ξ in each sector. In Figure 5.3(b), we show the correlation length as a function of U/t for a range of bond dimensions in the $(Q, S_z, K) = (0, 0, 0)$ sector, in other words the correlation length for operators carrying no charge, spin, or momentum around the cylinder. In Figure 3(c), we show for the highest bond dimension the correlation length in all four charge sectors that have the largest ξ for some U/t. Here we show the comparison between correlation lengths in different sectors in slightly more detail.

In Figures 7.1 and 7.2 we show the correlation lengths for the $(Q, S_z) = (0, 0)$, $(1, 1/2)$, $(0, 1)$, $(2, 0)$, and $(2, 1)$ sectors with $K = 0$ and 1; in the first figure the correlation lengths are separated by K and in the second by (Q, S_z). There are several notable features: (1) The large peak at $U/t \approx 10.6$ appears only in the $(0, 0, 0)$ sector. (2) The longest correlation length is in the $K = 1$ sector for large U, and in the $K = 0$ sector elsewhere. (3) Below $U/t \approx 8$, the longest correlation lengths correspond to charge fluctuations. Where the

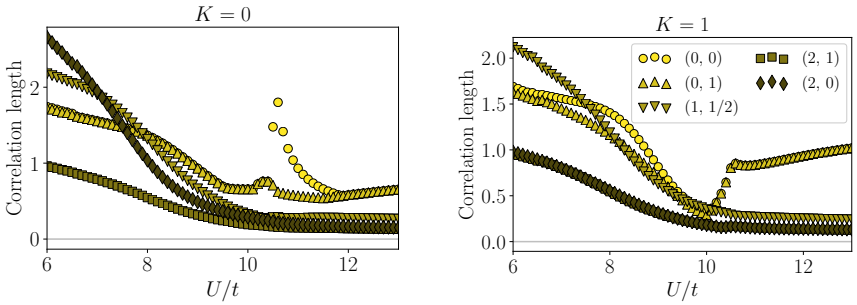

(a) (b)

Figure 7.1: Correlation lengths computed from the MPS transfer matrix ($\chi = 11314$) for operators with **(a)** $K = 0$ and **(b)** $K = 1$. Each line corresponds to a charge sector (Q, S_z), see legend in panel (b).

$(Q, S_z) = (1, 1/2)$ fluctuations have the longest correlation length, this is consistent with a metallic state. Above this, charge fluctuations are gapped and the spin correlations are the largest. (4) At lower U the $(Q, S_z) = (2, 0)$ fluctuations have the largest correlation length, potentially indicating a susceptibility to superconductivity. However, this is far from the chiral phase in which we are interested, so we have not investigated this possibility.

Chiral order parameter and extrapolation

In Figure 5.3(e), we show the chiral order parameter $\langle \mathbf{S}_i \cdot (\mathbf{S}_j \times \mathbf{S}_k) \rangle$, where i, j, and k label three lattice sites at the vertices of a triangle, as a function of U/t at different bond dimensions. We additionally show an extrapolation in the DMRG truncation error; here we explain the details of the extrapolation method.

At each value of U/t, we have values of the order parameter for five different bond dimensions, namely 2000, 4000, 5657 $\approx 4000\sqrt{2}$, 8000, and 11314 $\approx 8000\sqrt{2}$, and corresponding DMRG truncation errors, p. The error in the energy of a state should scale linearly with the truncation error, $E = E_{\text{lim}} + A \times p$,[45] but the error in other observables may scale in a more complicated manner. For the chiral order parameter, we assume a scaling of the form

$$\langle \mathbf{S}_i \cdot (\mathbf{S}_j \times \mathbf{S}_k) \rangle = \langle \mathbf{S}_i \cdot (\mathbf{S}_j \times \mathbf{S}_k) \rangle_{\text{lim}} + A \times p^B \tag{7.1}$$

used in reference [45], Figure 8. The data and best fit curves for several specific values of U/t are shown in Figure 7.3; in particular, we show $U/t = 8$ at the upper end of the metallic phase, $U/t = 10$ where the chiral order parameter is near its peak, and $U/t = 11$ in the high-U phase. (The `optimize.curve_fit` function from Python's `scipy` library fails to find the best fit of this form for $U/t \gtrsim 11.5$, beyond which we use instead a linear extrapolation from the few highest bond dimensions.)

We also show in Figure 7.4 the best fit results if we do a simple linear extrapolation from the three highest bond dimensions; we show the best fit line with the data for $U/t = 8$ and

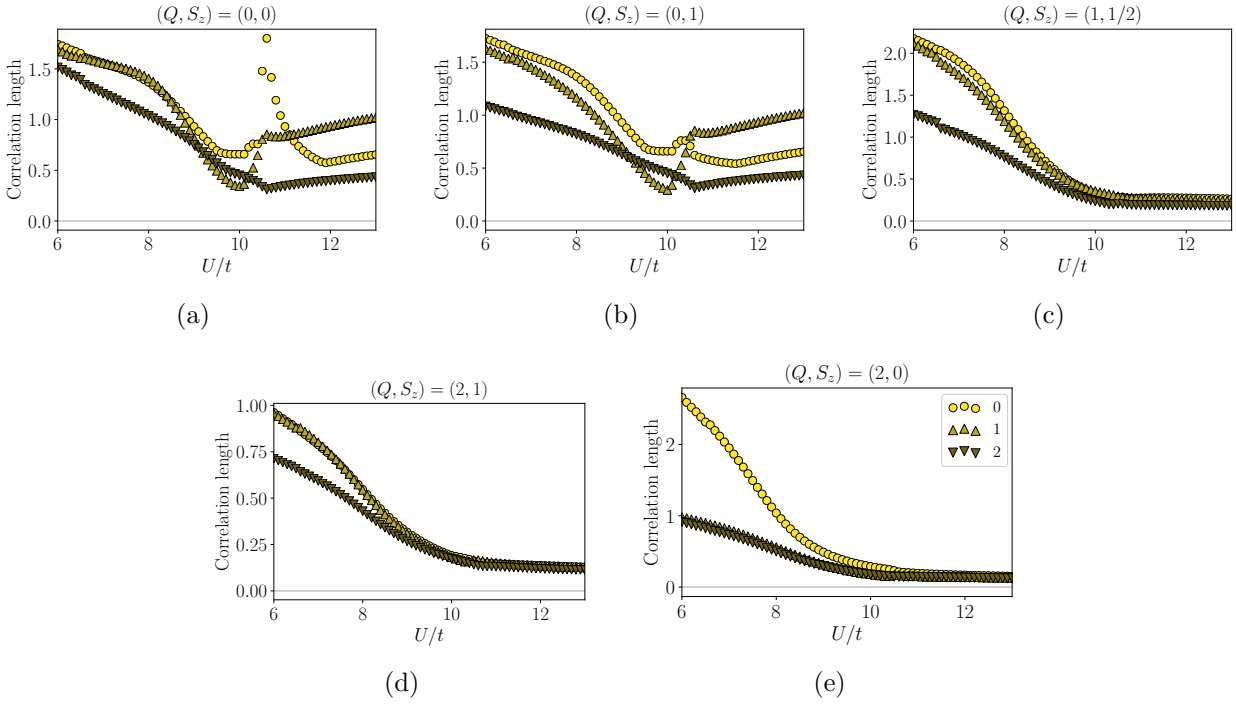

Figure 7.2: Correlation lengths for operators with $(Q, S_z) =$ **(a)** (0,0), **(b)** $(0, 1)$, **(c)** $(1, 1/2)$, **(d)** $(2, 0)$, and **(e)** $(2, 1)$. Each line corresponds to a charge sector K, see legend in panel (e).

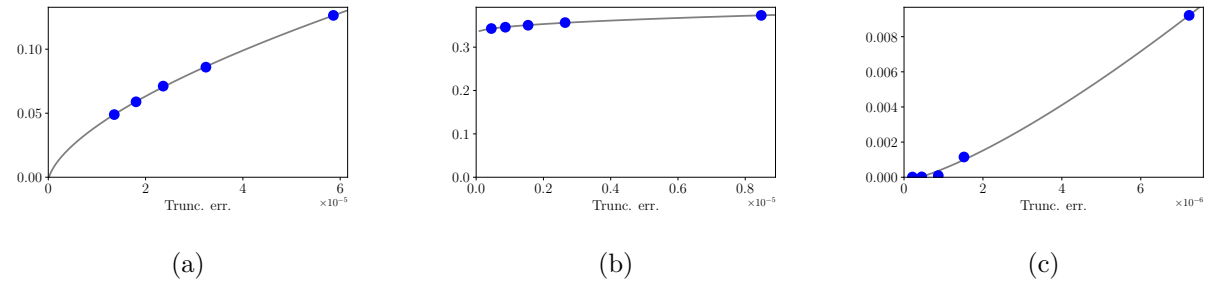

Figure 7.3: Chiral order parameter versus DMRG truncation error, for **(a)** $U/t = 8$ in the low-U phase, **(b)** $U/t = 10$ in the intermediate phase, and **(c)** $U/t = 11$ in the high-U phase. Gray lines show best fit curves of the form $C + A \times p^B$, allowing for extrapolation to the limit of no truncation error/infinite bond dimension.

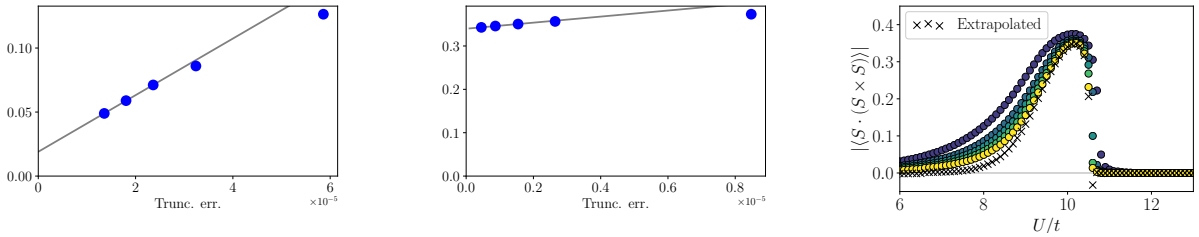

(a) (b) (c)

Figure 7.4: In **(a)** and **(b)**, we show the same data as in Figures 7.3(a) and 7.3(b) respectively, but with linear best fit lines computed using the points with the three lowest truncation errors in each case. The result is essentially unchanged in the intermediate phase. In **(c)**, we show the extrapolation as a function of U/t using this linear fit method. The actual data is the same as in Figure 5.3(e).

$U/t = 10$, as well as the equivalent of Figure 5.3(e) with the extrapolation line determined using this linear fit. (The best linear fit at $U/t = 11$ is simply a flat line at 0.) This method makes it seem that some time-reversal symmetry breaking may survive in the low-U phase, but comparing the fitted curves for $U/t = 8$ using the two methods, it appears that the nonlinear fit is significantly better, and that one predicts the expected vanishing of the chiral order parameter in the low-U phase.

Despite the disagreement at low U, in intermediate phase the two extrapolation methods give essentially similar results, as seen in Figures 7.3(b) and 7.4(b); the chiral order clearly remains nonzero in the limit of infinite bond dimension/zero truncation error.

Metal-insulator transition

Singularity at the Fermi surface

One sign of a metallic, or Fermi liquid, state is the presence of a singularity at the Fermi surface in the occupation $\langle n_k \rangle$. We do not observe a singularity at any finite MPS bond dimension, but by measuring $\langle n_k \rangle$ as a function of U/t and bond dimension we can observe the approximate location where the singularity would appear. We perform this computation for the YC4 cylinder.

We compute the correlators $\langle c^\dagger_{0,k_y,\uparrow} c_{x,k_y,\uparrow} \rangle$ for x in the range -50 to 50, then compute the occupation for spin up by

$$\langle n_{k_x,k_y,\uparrow} \rangle = \sum_{x=-50}^{50} e^{ik_x x} \langle c^\dagger_{0,k_y,\uparrow} c_{x,k_y,\uparrow} \rangle. \tag{7.2}$$

The range of 50 is about an order of magnitude larger than the correlation length, and the

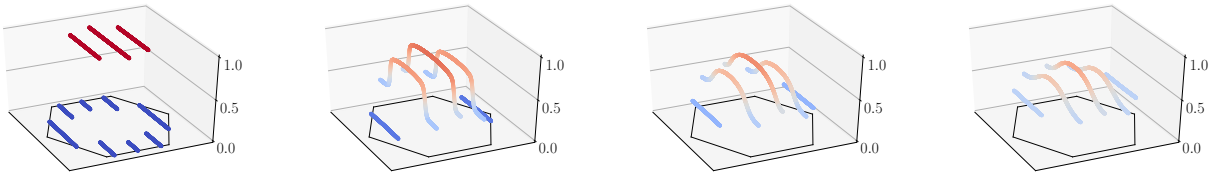

(a) (b) (c) (d)

Figure 7.5: Spin up occupation in the Brillouin zone, $\langle n_{k\uparrow} \rangle$, for **(a)** $U/t = 0$ (exact result), **(b)** $U/t = 6$ in the metallic phase, **(c)** $U/t = 9$ in the spin liquid phase, and **(d)** $U/t = 12$ in the high-U phase.

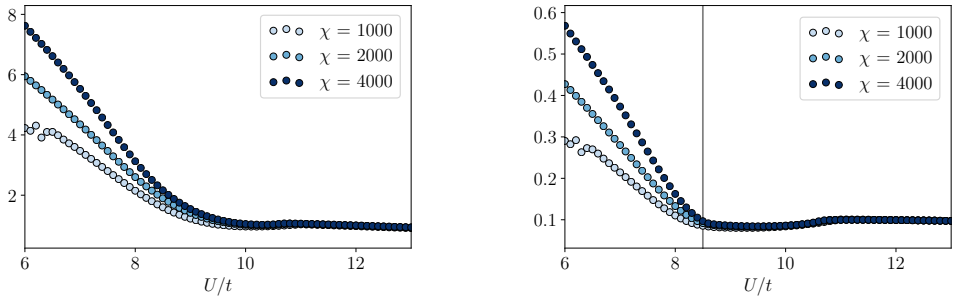

(a) (b)

Figure 7.6: **(a)** Maximum gradient of the occupation, as a function of U/t and bond dimension, showing a transition between $U/t \approx 8$ and $U/t = 10$. **(b)** Height of the peak at the Fermi surface found by including a factor of $|x|$ in the Fourier transform in equation 7.2. The vertical line at $U/t = 8.5$ appears to be the approximate location of the transition.

results are converged in the sense that when $\langle n_{k\uparrow} \rangle$ is plotted, the curves from using 40 vs 50 points are essentially indistinguishable.

In Figure 7.5 we show the spin up occupation in the Brillouin zone (computed with bond dimension $\chi = 4000$) for $U/t = 6$ in the metallic phase, $U/t = 9$ in the spin liquid phase, and $U/t = 12$ in the high-U phase, as well as the exact tight-binding result for $U = 0$ as a comparison. The behavior is clearly qualitatively different at high U compared with low U.

To make the transition more evident, we also show the maximum gradient of the occupation vs U/t for several bond dimensions in Figure 7.6(a). If there is indeed a singularity in the limit of infinite bond dimension, the maximum gradient should extrapolate to infinity, which appears to be the case at $U/t = 6$. If, on the other hand, there is no singularity, then the gradient should converge as the bond dimension increases, which is clearly the case for $U/t \gtrsim 10$. The exact location of the transition remains unclear, however, since for $8 \lesssim U/t \lesssim 10$, it is not clear whether the gradient will diverge or not.

Another possibility for observing the transition is to add a factor of $|x|$ in the Fourier transform in equation (7.2), which converts the singularity at the Fermi surface into a peak. We can then plot the peak height, which is shown in Figure 7.6(b). This allows for a somewhat more precise determination of the transition location, at $U/t \approx 8.5$.

Density structure factor

The metal-insulator transition can also be observed in the density structure factor,

$$S(\mathbf{q}) = \langle \delta n(\mathbf{q}) \delta n(-\mathbf{q}) \rangle = \frac{1}{L^2} \sum_{\mathbf{x},\mathbf{y}} e^{-i\mathbf{q}\cdot(\mathbf{x}-\mathbf{y})} \langle \delta n(\mathbf{x}) \delta n(\mathbf{y}) \rangle \tag{7.3}$$

where $\delta n(\mathbf{x}) = n(\mathbf{x}) - \langle n(\mathbf{x}) \rangle = n(\mathbf{x}) - 1$. Near $\mathbf{q} = 0$, the structure factor should satisfy $S(\mathbf{q}) \propto q^2$ if the state has a charge gap and $S(\mathbf{q}) \propto q$ if it does not. Both behaviors can be captured by the functional form

$$S(\mathbf{q}) \propto \sqrt{q^2 + m^2} - m, \tag{7.4}$$

for an "effective mass" m that goes to 0 when the state is gapless.

To distinguish between the gapped and gapless behavior, it is sufficient to consider a one-dimensional cut through $S(\mathbf{q})$, namely $S(q_x, q_y = 0)$, and this has the benefit of being quite efficient to compute in our mixed-space MPS. Our local sites are labeled by (x, k_y), and in terms of the operators $\hat{n}_{x,k_y} = c^\dagger_{x,k_y} c_{x,k_y}$ the $q_y = 0$ structure factor is

$$S(q_x) \propto \sum_{xkk'} e^{iq_x x} \big(\langle \hat{n}_{0k} \hat{n}_{xk'} \rangle - \langle \hat{n}_{0k} \rangle \langle \hat{n}_{xk'} \rangle \big). \tag{7.5}$$

We compute the $\langle \hat{n}\hat{n} \rangle$ correlations out to a distance of 200 rings of the cylinder; even at the largest bond dimension (11314) and the smallest U (with the slowest decay of the correlations), we find that numerical error is larger than the actual correlations beyond 125 rings, so this range is more than enough for accurate results.

In Figure 7.7 we show $S(q_x, q_y = 0)$ for a range of bond dimensions, with the structure factor for $U/t = 7$, 10, and 12, in the metallic, intermediate, and ordered phases, respectively; for each U, $S(q_x)$ is normalized so that the maximum is 1 for the highest bond dimension. Qualitatively, it is clear that the dispersion at $U/t = 7$ looks linear whereas at the two higher values of U it appears quadratic, which confirms that the metal-insulator transition is between 7 and 10. To get a clearer picture of the transition, we fit the part of the structure factor with $|q_x| \leq \pi/12$ to a curve of the form (7.4) and extrapolate the mass m as a power law in the DMRG truncation error. In Figure 7.8, we show the mass computed for each U and χ, as well as two different extrapolations to infinite bond dimension. The metal-insulator transition appears to occur at $U/t \approx 8$, roughly consistent with the rest of our analysis.

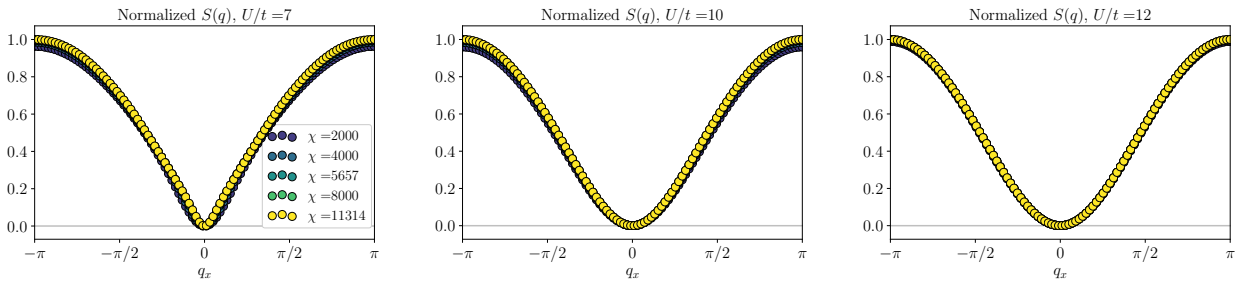

(a) (b) (c)

Figure 7.7: **(a)** $S(q_x)$ at $U/t = 7$, normalized so the maximum value for the highest bond dimension is 1. The dependence on q_x is approximately linear near the origin. **(b)** $U/t = 10$. The dependence on q_x is quadratic. **(c)** $U/t = 10$. The dependence on q_x is again quadratic.

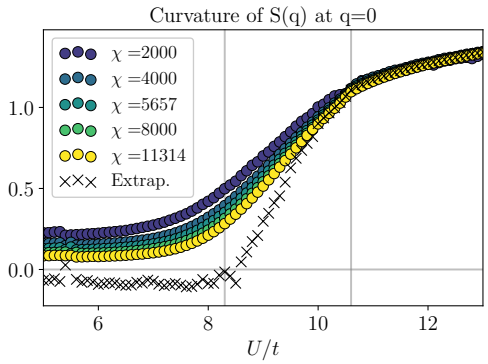

Figure 7.8: Best fit curvature, measured by the mass m of equation (7.4), near $q_x = 0$, for a range of bond dimension and extrapolated as a power law in the DMRG truncation error. Vertical lines indicate the phase transitions as argued for in chapter 5 and in section 7.1 below. Evidently this measure of the metal-insulator transition lines up well with the onset of the chiral phase. Note that at low U the extrapolation is much farther from the data than at high U, so the apparently slightly negative mass is likely still a finite bond dimension effect; if the highest bond dimension is not used, the extrapolation appears even more negative, supporting this view.

Finite entanglement scaling

In chapter 5, we show in Figure 5.3(f) and (g) the central charge, a characteristic property of the conformal field theory describing a gapless one dimensional system, computed as a function of U/t using the scaling relations[19]

$$S \approx (c/6)\log(\xi). \tag{7.6}$$

and [112, 90, 88]

$$S \approx \left(1+\sqrt{12/c}\right)^{-1} \log(\chi), \tag{7.7}$$

respectively.

Both approaches clearly show a finite central charge at low U, with a value of approximately $c = 6$, which is exactly what we expect for a metallic state on this cylinder as discussed in section 6.3 above. At high U the latter approach clearly shows $c = 0$ while the former requires some extrapolation of the finite bond dimension results. In the intermediate phase the second approach gives $c = 0$ at least for $U/t \gtrsim 9$, but the behavior between about $U/t = 8$ and 9 is unclear. To provide some further clarification, we discuss here the precise way that we compute the central charge and discuss the extrapolation to the true, infinite bond dimension ground state.

We first explain further how we calculate the central charge. At each U/t and each bond dimension, we can calculate the total entanglement entropy S for a cut between two rings of the cylinder, and also the correlation length (Figure 5.3(b)). As both become large, they should scale according to equation (7.6), but the relation will be inaccurate when both quantities are small because non-universal offsets will be comparatively large. The coefficient is thus best approximated by the derivative, $c/6 \approx d\log(\xi)/dS$, and we calculate discrete approximations to this derivative from the values of S and ξ at successive bond dimensions; the lines in Figure 5.3(f) and (g) are labeled by the larger of the two bond dimensions used in calculating the discretized derivative. So for example the yellow (most accurate) line in the figure is computed using the ground state wave functions for bond dimensions 8000 and 11314.

In Figure 7.9, we show the central charge estimates using equation (7.6) at $U/t = 9$ and at $U/t = 13$ versus $1/\chi$, where the χ used is the geometric mean of the two bond dimensions used to calculate the derivative. In the high-U phase we show a linear extrapolation to infinite bond dimension; although it appears to show a small but nonzero central charge, that is not really a reliable result. For example, the use of the geometric mean of the two bond dimensions used in computing the derivative is an arbitrary choice, particularly because the error may be determined mostly by the smaller bond dimension, and using that bond dimension for the horizontal axis would shift the graph to the right. At $U/t = 9$, it is essentially impossible to extrapolate the central charge at all as the shape of the curve is completely unclear.

In fact, in both phases, and particularly in the high-U phase, the entanglement appears to be converging with increasing bond dimension, as shown in Figure 7.10, which is indicative

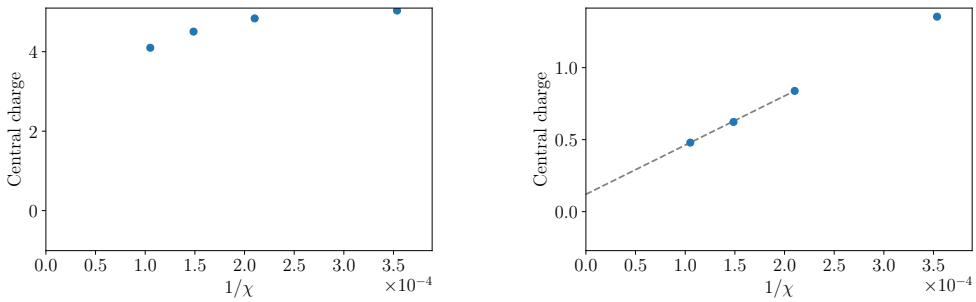

(a) (b)

Figure 7.9: Central charge vs $1/\chi$ for **(a)** $U/t = 9$ and **(b)** $U/t = 13$. Both seem to extrapolate to finite values, but this is misleading, as discussed in the text.

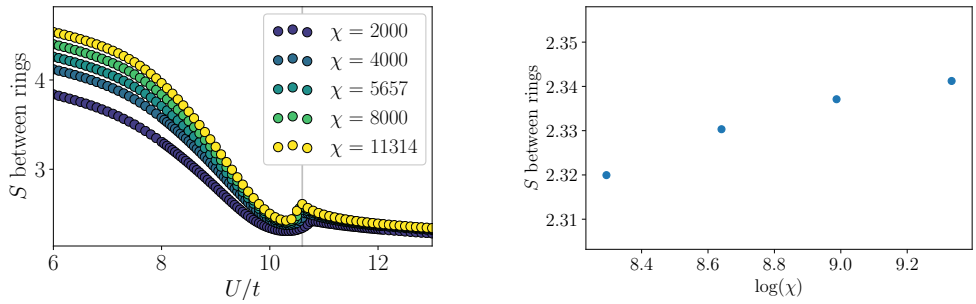

(a) (b)

Figure 7.10: **(a)** Entanglement between rings of the cylinder as a function of U/t for different bond dimensions. It is nearly converged in the intermediate and high-U phases, indicating that they are gapped. **(b)** A close-up slice at $U/t = 13$. Note that the vertical scale is only about 2% of the value of S.

of a gapped phase that should have $c = 0$. The apparent nonzero central charge comes from the fact that both the entanglement and the correlation length are still growing very slightly at the accessible bond dimensions.

Another option, then, is to compute the central charge directly from the scaling of entanglement with bond dimension, using equation (7.7). In the gapless low-U phase, this is less accurate than the computation of c from scaling with ξ, but at higher U it is indeed more converged. Slices at $U/t = 9$ and 10 in the intermediate phase and $U/t = 13$ in the high-U phase are shown in Figure 7.11. It is still not completely clear that system is gapped at $U/t = 9$, but that is likely a finite bond dimension effect, as the later point in the same phase, at $U/t = 10$, clearly shows $c = 0$.

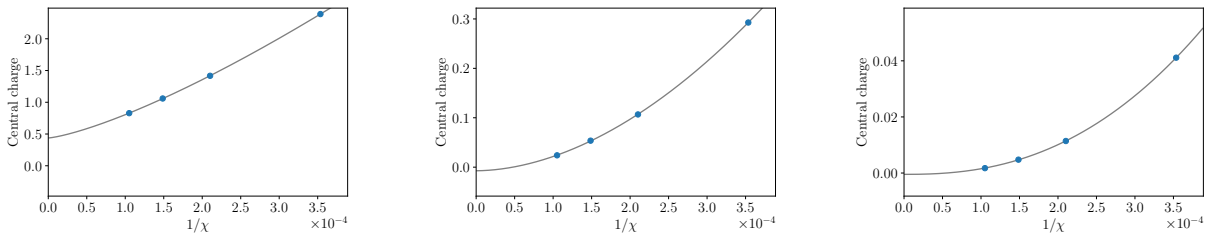

(a) (b) (c)

Figure 7.11: Central charge vs $1/\chi$, calculated by scaling with bond dimension, for **(a)** $U/t = 9$, **(b)** $U/t = 10$, and **(c)** $U/t = 13$. The latter two clearly extrapolate to 0, suggesting that both the intermediate and high-U phases are gapped. The extrapolation at $U/t = 9$ still appears to go to a nonzero value (approximately 1/2), but this is likely still a finite bond dimension effect.

Entanglement spectrum degeneracy

As reported in chapter 5, the entanglement spectrum of the ground state on the YC4 cylinder acquires an exact two-fold degeneracy when entering the intermediate phase, at $U/t \approx 8.3$, a fact that we demonstrate here. Figure 7.12 shows the low-lying levels in the entanglement spectrum in the ground state as a function of U/t.

The two lowest-lying levels appear to come together somewhere in the vicinity of $U/t = 8$, and then pairs of levels come together at $U/t = 10.6$. This onset of four-fold degeneracy from two-fold degeneracy at $U/t = 10.6$ is visually obvious in the figure: each pair of lines that come together at that point do so at a sharp angle, so that the slope of the entanglement spectrum lines appears discontinuous at that point. The precise location of the first transition, from a nondegenerate entanglement spectrum to two-fold degeneracy, is not clearly visible in the same way.

To more precisely find where the two-fold degeneracy onsets, we take all of the entanglement levels for a given value of U/t and a given bond dimension, and group them into adjacent pairs, with the lowest two levels together, the third and fourth together, and so forth. We then find the separation within each pair, and average the separation over the lowest N pairs, for some large N. (We do not average over all pairs because the highest ones will be inaccurate for any finite bond dimension.) The logarithm of this average can be plotted vs U/t for each bond dimension, which is shown for $N = 1000$ in Figure 7.13(a)(a). The curves for different bond dimensions all sit roughly on top of one another until around $U/t = 8$, where they start to deviate. For each bond dimension the separation drops towards 0 before flattening off at some finite average separation; as bond dimension increases, this flattening out happens at successively smaller separations. It is still difficult to identify the exact onset of degeneracy in the infinite bond dimension limit, but it appears to be somewhere within the region highlighted by the vertical gray bar, from $U/t = 8.1$ to 8.6. The

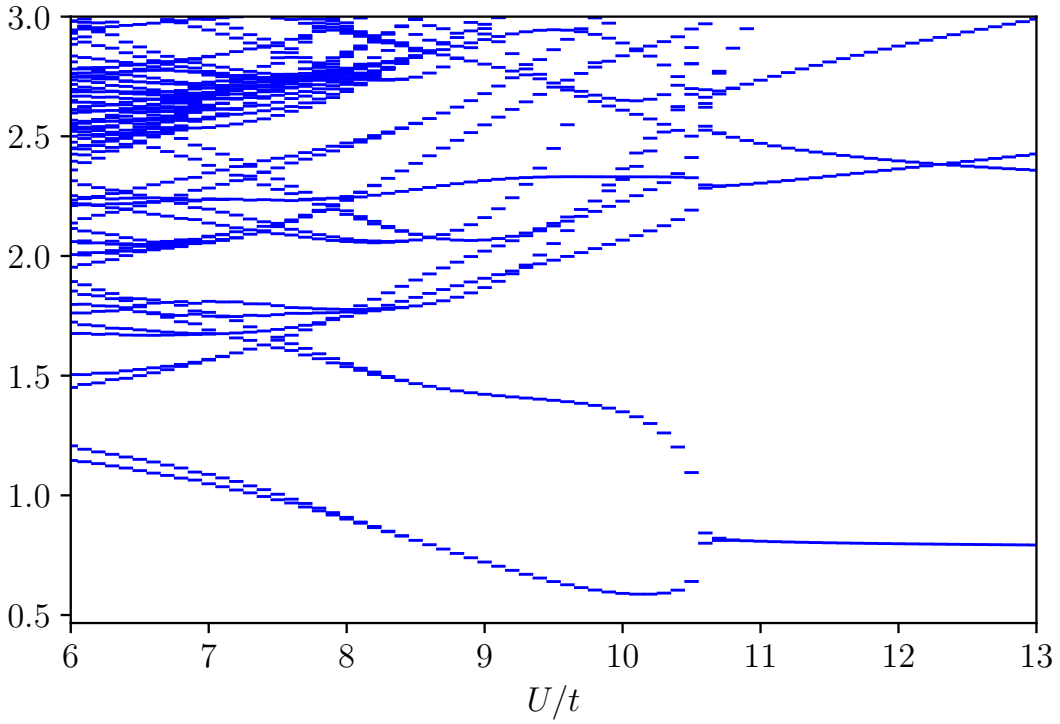

Figure 7.12: Entanglement spectrum in the ground state of the YC4 cylinder, as calculated for bond dimension $\chi = 8000$.

value of $U/t \approx 8.3$ used in Figure 5.3 is approximately the center of this region.

For confirmation that this is indeed what a finite bond dimension approximation to an exact degeneracy should look like, we have also followed the same procedure with entanglement levels divided into groups of four, plotting the average separation between the highest and lowest levels in each group, which should go to 0 at the onset of four-fold degeneracy. This is shown in Figure 7.13(b). This indeed shows essentially the same behavior at $U/t = 10.6$ as does the average pair splitting at $U/t \approx 8.3$, so we believe this is a valid and relatively rigorous way to locate the onset of degeneracy.

Chiral Domain Wall

As there is a two-fold degeneracy arising from the two possible chiralities, at nonzero temperature there will be regions of each chirality with domain walls between them. We characterize these domain walls by considering a finite cylinder segment, assuming an infinitely repeating MPS on each end; these half-infinite MPSs are taken from the ground states previously

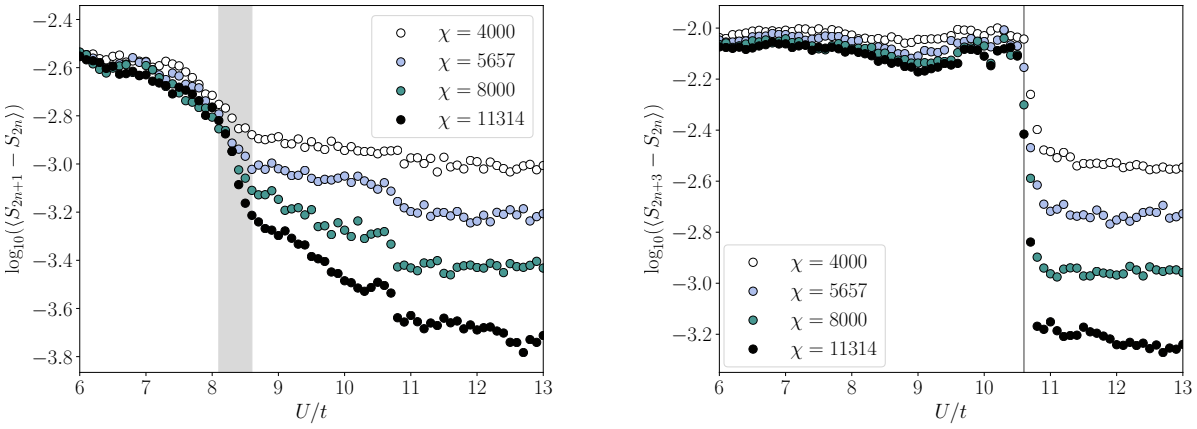

(a) (b)

Figure 7.13: **(a)** Log of the average separation within pairs of entanglement levels, with 1000 pairs included in the average. The gray bar shows the regions $U/t \in [8.1, 8.6]$; onset of 2-fold degeneracy is somewhere in this region, though the precise location is still difficult to determine. **(b)** Log of the average separation between the top and bottom entanglement levels when grouped into fours, with the lowest 500 groups included (the same total number of entanglement levels). The vertical line at $U/t = 10.6$ is the onset of 4-fold degeneracy.

found for each of the two chiralities, with opposite chiralities at the two ends. Within the finite cylinder, we optimize the MPS tensors to minimize the energy as usual, resulting in the minimal energy configuration that interpolates between the two chiralities. This is the same method used in reference [141].

Here we show results for the YC4 cylinder at $U/t = 10$, deep in the chiral phase. The shape of the domain wall can be observed by calculating the chiral order parameter $\langle \mathbf{S}\cdot(\mathbf{S}\times\mathbf{S})\rangle$ on successive triangles proceeding along the finite segment. On each ring of the cylinder, there are two inequivalent triangles, one which points left, and one which points right (see Figure 5.1), and we calculate the order parameter on both. Note that all triangles in a particular ring with a given orientation are necessarily equivalent in our mixed real- and momentum-space basis. Figure 7.14(a) shows the evolution of the chiral order parameter across a finite segment of length 24 rings, with both triangle orientations; note that at each end the chiral order parameters for the two triangle orientations converge to a single constant value, the same one shown in Figure 5.3(e). Figure 7.14(b) shows the dependence of the domain wall shape on the MPS bond dimension; although the behavior is quite different comparing the low bond dimension of 2000 with the higher ones, it appears to be essentially converged by $\chi = 4000$.

We can additionally calculate the energy cost of creating the domain wall by comparing, for each bond dimension, the minimized energy with the domain wall present with the

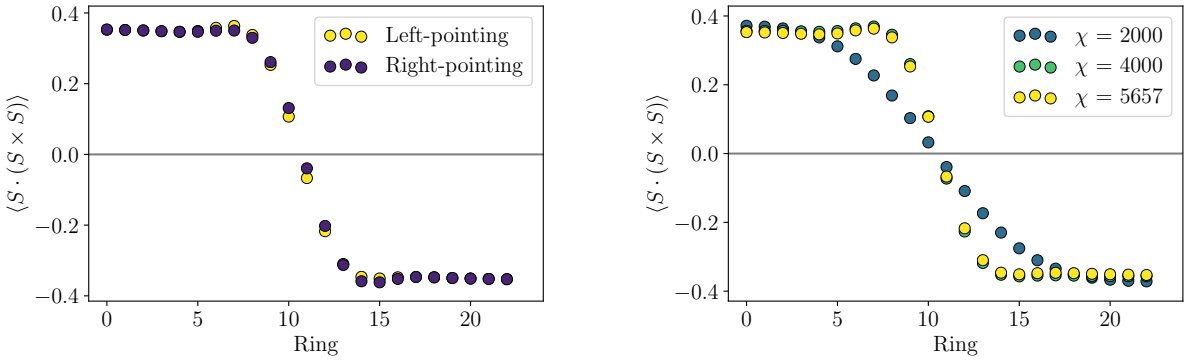

Figure 7.14: Shape of the domain wall between regions of the two different chiralities, as measured by the chiral order parameter for local triangles on each ring of a finite cylinder segment: **(a)** computed for $\chi = 5657$ for both triangle orientations, and **(b)** for the left-pointing triangles at three different bond dimensions, showing convergence by $\chi \approx 4000$.

minimized energy at the same bond dimension with just a single domain. The total energy cost of the domain wall on the YC4 cylinder, which is nearly converged for $\chi \gtrsim 4000$, is approximately $0.026t$, giving a domain wall tension of $0.0065t/a$. Using estimated values from the literature[63, 105], this gives for the organic crystal κ-(BEDT-TTF)$_2$Cu$_2$(CN)$_3$ a tension of about $(4K) \times k_B$.

Flux insertion data

In chapter 5, we show in Figure 5.4 the evolution of several quantities with flux insertion, including the chiral order parameter, the peak height of the spin structure factor, and a qualitative estimate of the spin singlet gap from the MPS transfer matrix spectrum. We also show the spin Hall effect in the chiral spin liquid (CSL) phase via spin pumping with flux insertion in Figure 11(d) and the spin- and momentum-resolved entanglement spectrum in the two topological sectors of the CSL in Figure 11(b). Here we provide some additional data on the evolution of the system with flux insertion, including fidelity, transfer matrix spectrum estimates of gaps to other types of excitations, and the evolution of the entanglement spectrum with flux insertion.

In Figure 7.15 we show a variety of quantities versus U/t and flux insertion θ. In particular, we show (a) the transfer matrix estimate of the spin triplet gap, showing the distinction between the two high-U phases; (b) the transfer matrix estimate of the charge gap, showing the metal-insulator transition; (c) the fidelity with flux insertion, showing some phase transitions clearly; (d) the entanglement between rings; and (e) the truncation error in the last sweep of the DMRG simulation, showing that the accuracy of the simulation is essentially

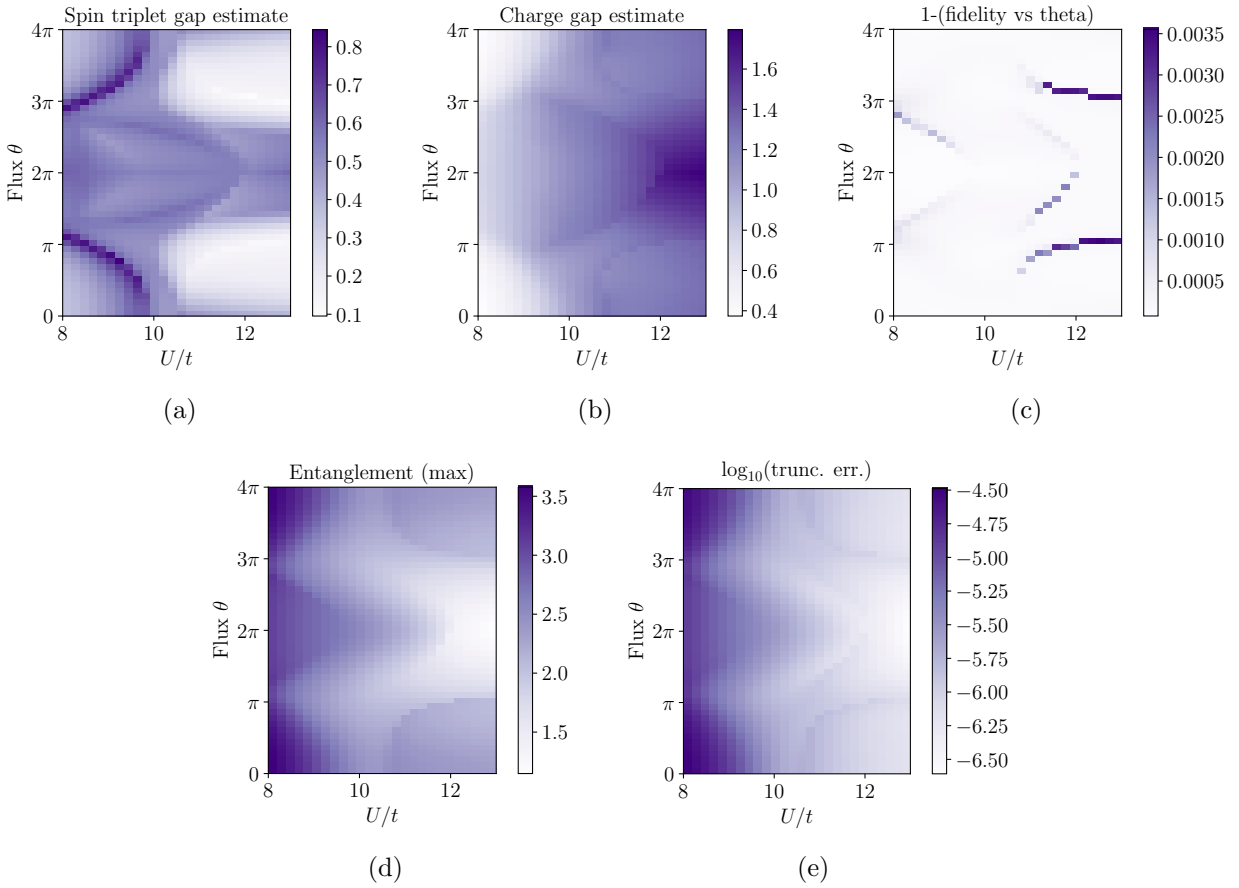

Figure 7.15: Various quantities for the YC4 cylinder vs U/t and flux insertion θ, with $\chi = 4000$. **(a)** Transfer matrix estimate of the spin triplet gap. **(b)** Transfer matrix estimate of the charge gap. **(d)** Fidelity of the flux insertion—in particular, we show $1-|\langle\psi(\theta)|\psi(\theta+\pi/12)\rangle|^2$, so that a very large value would indicate a loss of adiabaticity. We see phase boundaries but no such non-adiabatic evolution. **(d)** Entanglement between two rings of the cylinder. **(e)** Log base 10 of the truncation error at the last step of the DMRG simulation.

constant with flux insertion within each phase. All quantities clearly delineate the chiral phase.

We can also further examine the spin pumping from flux insertion at $U/t = 10$ shown in Figure 5.11(d). Compared with the spin pumping for YC6 (Figure 4(b)), there is substantially more deviation from a straight line, which arises because of the large shifts in the phase boundaries with flux insertion. In particular, the spin is pumped more quickly when the chiral order parameter is larger, and less quickly when it is smaller. This phenomenology can be seen clearly by looking at spin pumping at smaller and larger values of U which clearly cross phase boundaries; in Figure 7.16 we show the spin pumping for $U/t = 9.2$ and

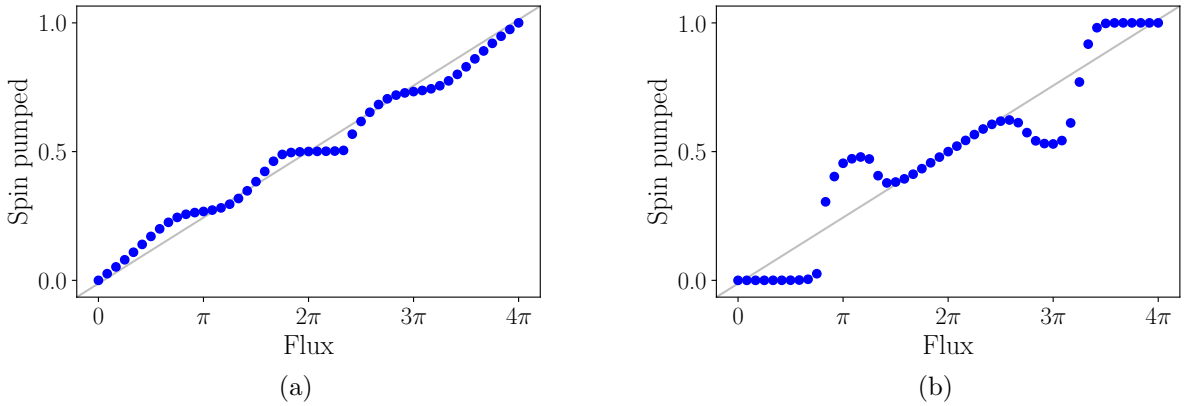

Figure 7.16: YC4 spin pumping: **(a)** $U/t = 9.2$ and **(b)** $U/t = 11.0$.

$U/t = 11$. At $U/t = 9.2$, the system is in the chiral phase until shortly before 2π flux, where it enters the left-most nonchiral region seen in Figure 5.4(a), at which point the pumped spin plateaus at exactly 1/2. The spin pumping continues upon reentering the chiral phase. (Note that for smaller U, since the sign of the chirality is randomly opposite upon reentering that phase, the spin pumps back down to 0 at 4π flux instead of up to 1.) At $U/t = 11$, there is initially no spin pumping, but it begins after entering the chiral phase; the pumping stops again once the system once more enters the nonchiral phase after 3π flux.

Transfer matrix and the two-dimensional excitation spectrum

In section 6.5 above, we discuss how the MPS transfer matrix spectrum gives the excitation spectrum of the system. In particular, for a given U, flux insertion allows us to trace out a cut through the minimum of the excitation spectrum as a function of k_x and k_y. In Figure 7.17 we show the transfer matrix spectrum for spin 1 excitations at $U/t = 10$ versus flux insertion, k_x, and k_y, at bond dimensions 2000, 4000, and 8000. Note that for this data, flux insertion was not performed adiabatically, but rather the DMRG was performed independently for each θ; however, adiabatic flux insertion at $\chi = 4000$ gives a nearly identical result.

This data is somewhat difficult to interpret due to the shifting of phase boundaries with flux insertion. Another possibility is to, for each flux θ, take the transfer matrix spectrum corresponding to the U/t with the greatest chirality in order to find the transfer matrix within a single phase. This is shown (for $\chi = 4000$) in Figure 7.18.

Comparison with Dirac spin liquid

One purpose of this analysis is to check whether the Dirac spin liquid (DSL) is another candidate state for the two-dimensional model, which seems plausible given that the DSL can become a chiral spin liquid when the Dirac cones are gapped out. A DSL on the triangular

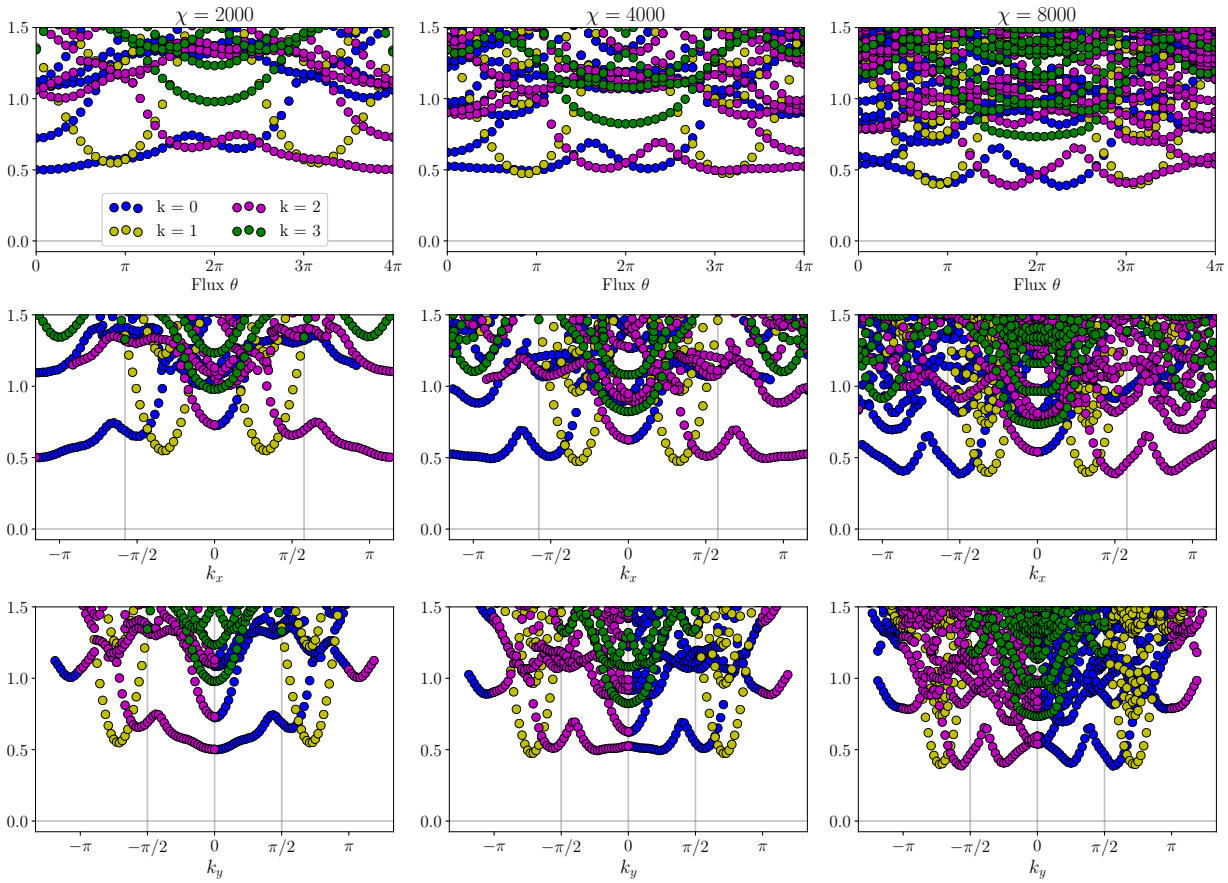

Figure 7.17: Low-lying part of the $S_z = 1$ part of the transfer matrix spectrum for $U/t = 10$ on the YC4 cylinder at $\chi = 2000$ (left column), 4000 (middle column), and 8000 (right column), plotted versus flux inserted (top row), k_x (middle row), and k_y (bottom row). (The lattice constant is set to 1.) Color corresponds to the momentum quantum number of the excitation as given in the panel in the upper left. Vertical lines correspond to momentum transfers between possible Dirac cone locations in the Dirac spin liquid; they do not clearly correspond to features observed in our data.

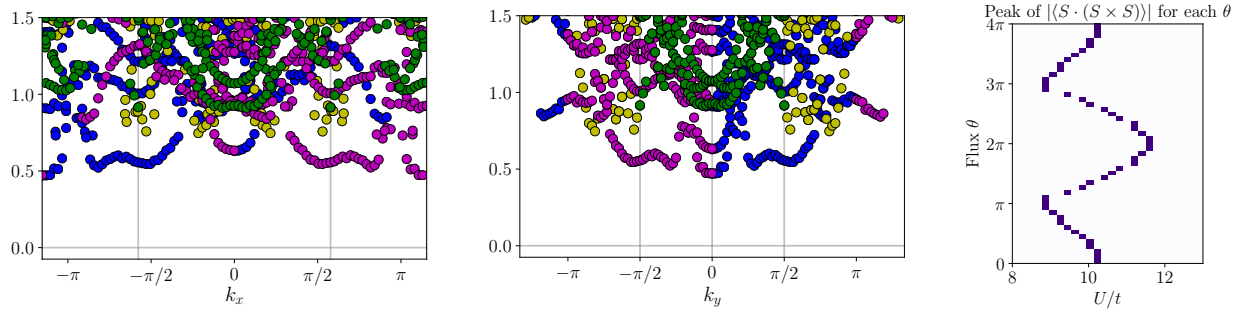

(a) (b) (c)

Figure 7.18: Low-lying transfer matrix spectrum where, for each amount of flux inserted, θ, we use the U/t with the largest chiral order parameter to "track" the chiral phase. **(a)** Spectrum plotted versus k_x. **(b)** Spectrum plotted versus k_y. **(c)** Location of the maximum U/t used for each θ.

lattice can be constructed with fermionic partons with staggered π flux. There are several valid gauge choices, one of which is the model shown in Figure 6.8(a) above; the three inequivalent gauge choices give Dirac cone pairs at $(k_x, k_y) = \pm(\pi/\sqrt{3}, 0)$, $\pm(\pi/2\sqrt(3), \pi/4)$, and $\pm(\pi/2\sqrt(3), -\pi/4)$. The momenta of the corresponding transitions are indicated by vertical lines in Figures 7.17 and 7.18.

When plotted at constant $U/t = 10$, the minima in the spectrum do not appear to line up with the transitions between expected locations of the Dirac cones. When plotted instead at the approximate center of the chiral phase, the minima are in fact at $(\Delta k_x, \Delta k_y) = \pm(2\pi/\sqrt{3}, 0)$, which corresponds to one of the Dirac cone pairs. However, this result is at a single bond dimension, and these minima do not extend far below the rest of the spectrum, so it is difficult to reach a clear conclusion.

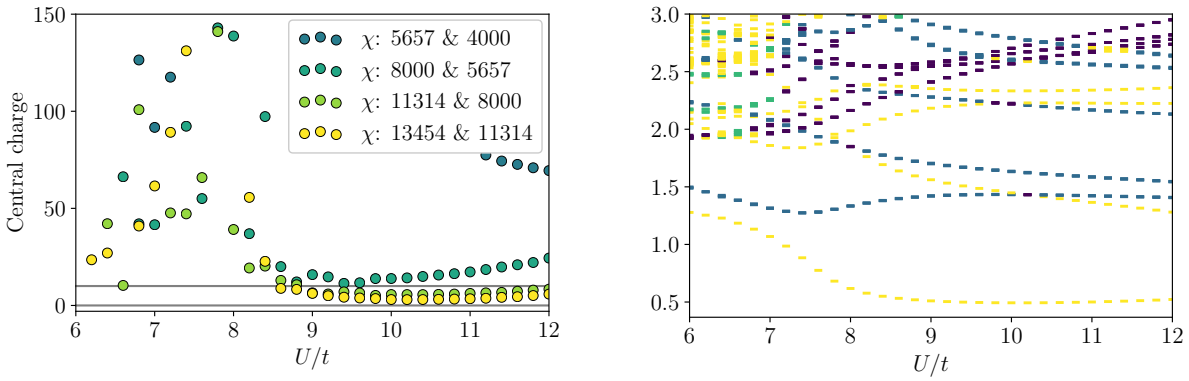

(a) (b)

Figure 7.19: Evidence for metal to spin liquid transition in the $k = 0$ sector for the YC6 cylinder: **(a)** At $U/t \approx 8.5$, there is a qualitative change in the behavior of the finite entanglement scaling. To the left the scaling of entanglement with bond dimension appears chaotic, which is not surprising for a gapless system when the bond dimension is very small compared with the size of the Hilbert space; to the right the behavior becomes systematic, because the DMRG converges much more accurately even at low bond dimensions when the system is gapped. **(b)** The same transition is also visible in the entanglement spectrum, plotted here for $\chi = 8000$. The dense levels in the upper left are characteristic of a metallic state. At $U/t \approx 7.5$ there is a large increase in the separation between the lowest levels, and the low-lying levels become much more sparse in general, showing a transition into a non-metallic state. (Note that the coloring indicates degeneracy of the levels: yellow is non-degenerate and blue is 3x degenerate).

7.2 YC6 additional data and analysis

Metal to CSL transition in $k = 0$ sector of YC6 cylinder

For the YC4 cylinder, we used finite entanglement scaling to show that the metallic phase is gapless with $c = 6$ and that the intermediate and high-U phases on that cylinder are gapped. For the YC6 cylinder, much larger bond dimensions (about 16× larger) are needed to achieve the same accuracy, so we cannot estimate the central charge accurately. However, if we plot the central charge as estimated using equation (7.7) for pairs of bond dimensions (as described in section 7.1) as a function of U/t, we can still observe a qualitative change in the behavior of the system at one particular point, as shown in Figure 7.19(a). This behavior is consistent with a gapless metallic phase at low U and a gapped phase at intermediate U.

The transition can also be observed in the entanglement spectrum. Metallic phases charactistically have very densely spaced levels, which as shown in Figure 7.19(b) is true for the YC6 cylinder when $U/t \lesssim 8$ but is no longer true beyond that point. Just to the left

of that same point, there is a corresponding rapid increase in the separation of the lowest levels; on its own, that feature would not be sharp enough to identify a transition, but in combination with everything else, it provides some additional evidence for the location of the transition.

The two indicators of a transition are slightly displaced from each other, but both are in the vicinity of $U/t \approx 8$, so we identify that region as the approximate location of the transition.

Four-fold ground state degeneracy

As shown in Figure 5.5(a), for the YC6 cylinder we find low-lying states in two different sectors of momentum around the cylinder per ring. In addition to this near-degeneracy, which as explained in chapter 5 is between the trivial and semion topological sectors, we also observe an additional two-fold degeneracy between the two different possible chiralities.

When finding the ground state using the DMRG method, one begins with some initial matrix product state; if the ground state is not degenerate and the algorithm does not get stuck in a metastable state, the final wave function should be approximately independent of the initial state. If, on the other hand, there are multiple degenerate ground states, the algorithm will converge to one or another of them depending on the initial state used. (It will also tend to converge to minimally entangled states within the ground state manifold and not superpositions of them.[141])

In our case, over a wide range of U/t for a bond dimension $\chi = 8000$, we initialized the DMRG with ten different random product states. In the center of the CSL phase, the energies of the final states within each momentum sector varied by up to about 0.01%, meaning that none of the final states were metastable. Although none of the states were numerically identical, they can be separated into two groups within which they are essentially the same, with an overlap per ring of about 0.99998; the overlap between states in opposite groups is about 0.22 per ring. That these two groups correspond to the two possible chiralities of the time-reversal symmetry-breaking phase can be seen from the momentum-resolved entanglement spectra, shown in Figure 7.20 for representative final states in each of the two groups for each topological sector for $U/t = 9$: the spectra are almost precisely related by $k \to -k$. (Note that parts (a) and (c) are essentially the same as the left and right respectively of Figure 5.11(a).)

Flux insertion data

In Figure 5.6, we show the chiral order parameter, peak height of the spin structure factor, and transfer matrix estimate of the spin singlet gap. As for the YC4 cylinder in section 7.1 above, we show here in Figure 7.21 a number of additional quantities versus U/t and inserted flux, θ, with bond dimension $\chi = 8000$. The relative behavior of the various quantities is consistent with what we found for YC4.

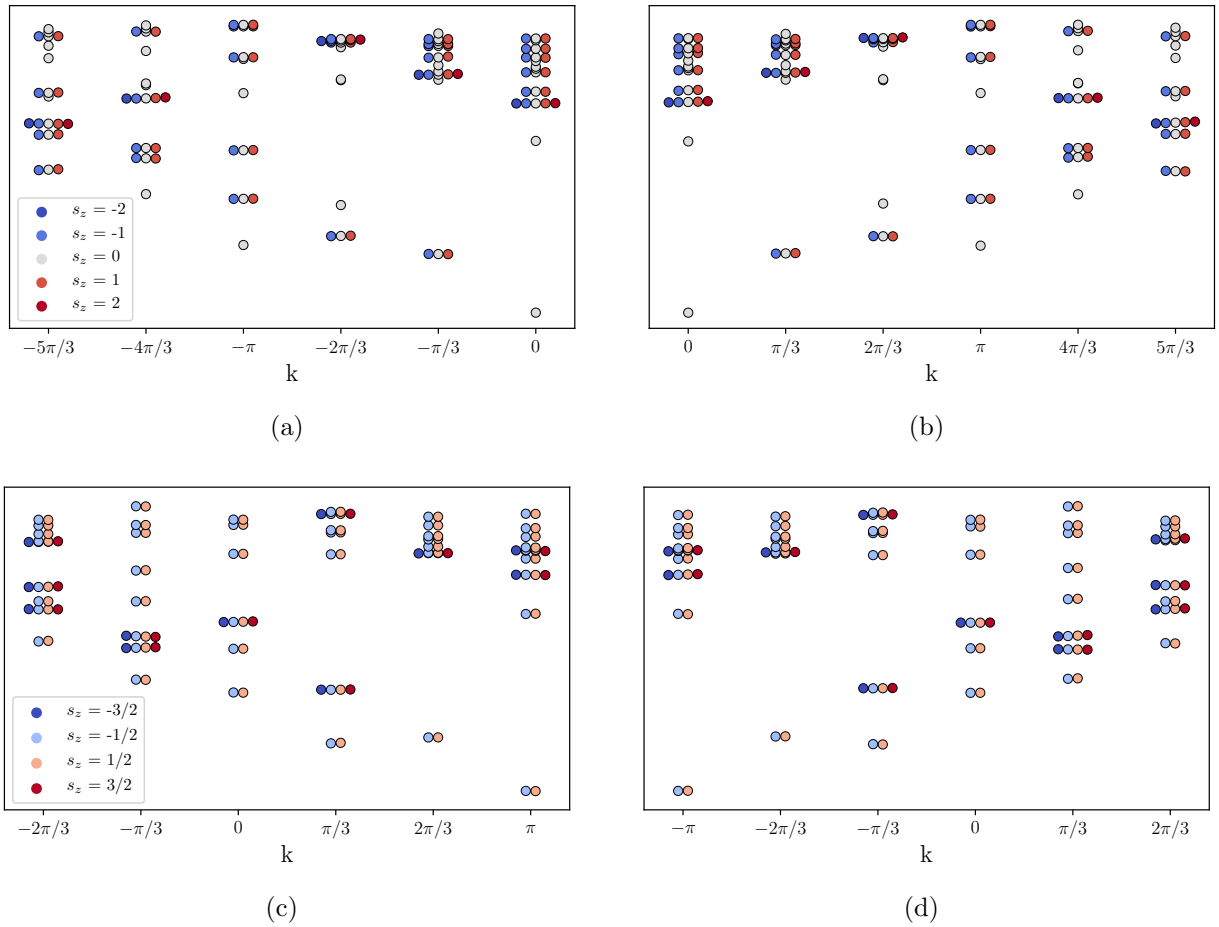

Figure 7.20: Spin- and momentum-resolved entanglement spectra for the four degenerate ground states of the YC6 cylinder with $U/t = 9$. **(a)** and **(b)** show the two chiralities for the $k = 0$ (trivial) sector, and **(c)** and **(d)** show the $k = \pi$ (semion) sector.

Unlike for YC4, here we actually observe a failure of the adiabatic flux insertion, for $U/t = 7$ and 7.2; this is visible in all quantities and is especially clear from the measurement of the overlap between the ground states with successive values of θ, Figure 7.21(c). The overlaps in this case are much smaller than those corresponding to phase boundaries, as seen at higher U; this is quite useful because it confirms that those phase boundaries do *not* indicate a loss of adiabaticity. The fact that the chiral phase gives way to a (lower energy) non-chiral phase near 2π flux might be concerning, but in fact the drop in energy is already much smaller for $U/t = 7.2$ than for $U/t = 7$, and it is likely that this is just the right-most edge of the metallic phase. So this could correspond to the nonchiral region extending to about $U/t = 10$ for YC4, and it is simply easier to maintain adiabaticity with flux insertion for YC6 at $\chi = 8000$ than YC4 with $\chi = 4000$ even with the much larger θ step, so that

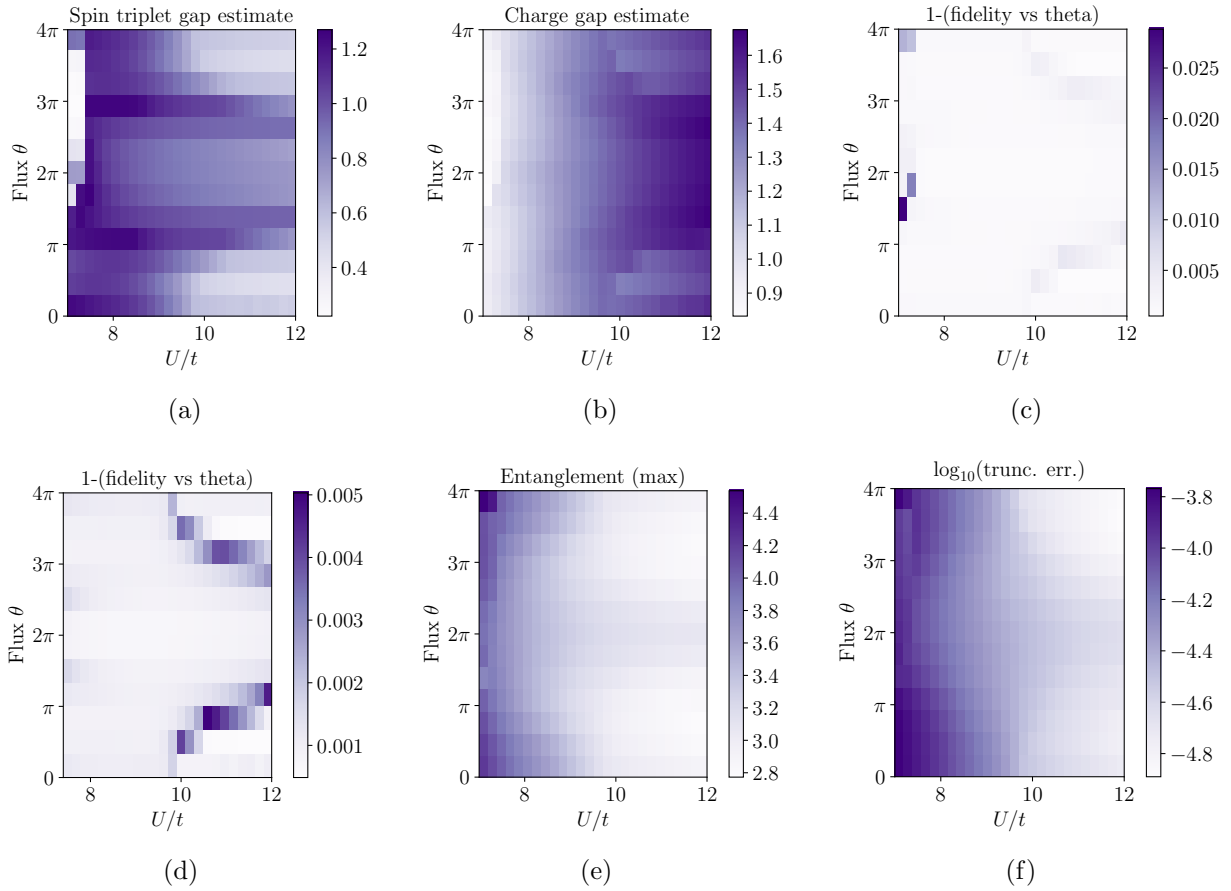

Figure 7.21: Various quantities for the YC6 cylinder vs U/t and flux insertion θ. **(a)** Transfer matrix estimate of the spin triplet gap. **(b)** Transfer matrix estimate of the charge gap. **(c)** Fidelity of the flux insertion, measued by $1 - |\langle\psi(\theta)|\psi(\theta + \pi/3)\rangle|^2$. For the two smallest values of U there is a loss of adiabaticity. **(d)** Fidelity with the left two columns removed to more clearly show the results in the rest of the phase diagram. **(e)** Entanglement between two rings of the cylinder. **(f)** Log base 10 of the truncation error at the last step of the DMRG simulation. The error is quite large even at high U, indicating that these are the least converged of our results; this is why the chiral phase appears to extend to high U near 2π flux.

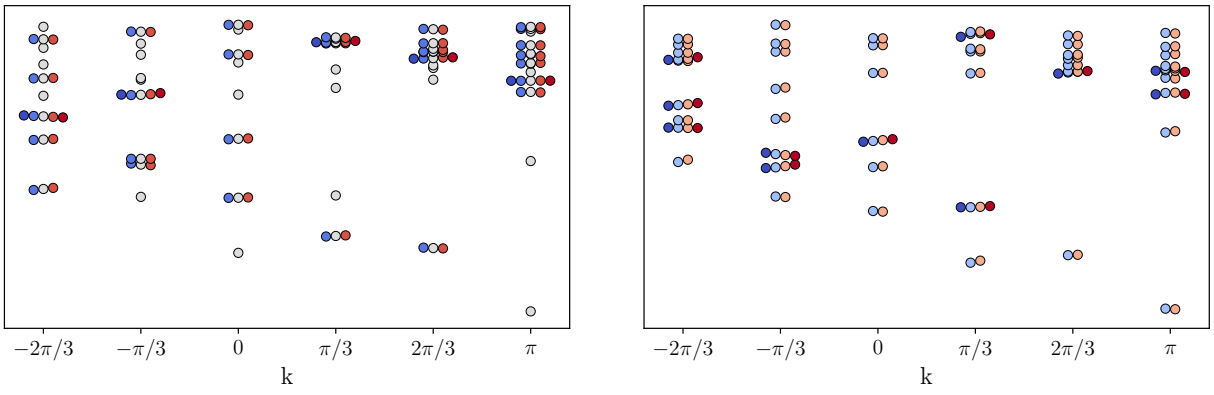

Figure 7.22: The transformation of the YC6 spin- and momentum-resolved entanglement spectrum with flux insertion for $U/t = 9$, beginning in the semion sector (as shown in Figure 7.20(c)): **(a)** 2π flux converts the system to the trivial sector (compare with Figure 7.20(a)) and **(b)** an additional 2π flux, or 4π total, returns to the initial state.

the transition into this phase happens later than it ought to. (Additionally, at 4π flux the nonchiral phase is much higher in energy than the chiral one, again supporting the fact that adiabatic evolution is easier to achieve here.)

We also briefly discuss the evolution of the entanglement spectrum. In Figure 5.11(a), we show the spin- and momentum-resolved entanglement spectrum in the trivial and semion sectors; these two sectors are the respective ground states at $U/t = 9$ in the $k = 0$ and $k = \pi$ momentum sectors. Alternatively, we can observe both sectors using flux insertion, as we did for the YC4 cylinder (Figure 5.11(b)). Beginning with the ground state with periodic boundaries in the $k = \pi$ sector, with entanglement spectrum given in Figure 7.20(c), and adiabatically inserting 2π flux indeed produces an entanglement spectrum consistent with the trivial sector of the CSL, as shown in Figure 7.22(a). An additional 2π flux converts back to the semion sector, as shown in Figure 7.22(b). The spin multiplets in the spectrum are slightly less well converged after the flux insertion, but the qualitative behavior is exactly the same as at 0 flux.

Transfer matrix and the two-dimensional excitation spectrum

As with YC4, we compute the transfer matrix spectrum for spin 1 excitations versus flux θ, k_x, and k_y. In particular, we show in Figure 7.23 the spectrum for $U/t = 9$, deep in the chiral phase, at bond dimension 8000. The relatively low bond dimension given the circumference makes it difficult to reach any meaningful conclusions as to whether the observed state is consistent with a chiral spin liquid formed by gapping out a Dirac spin liquid. Note however that the observed minima at this bond dimension are not consistent

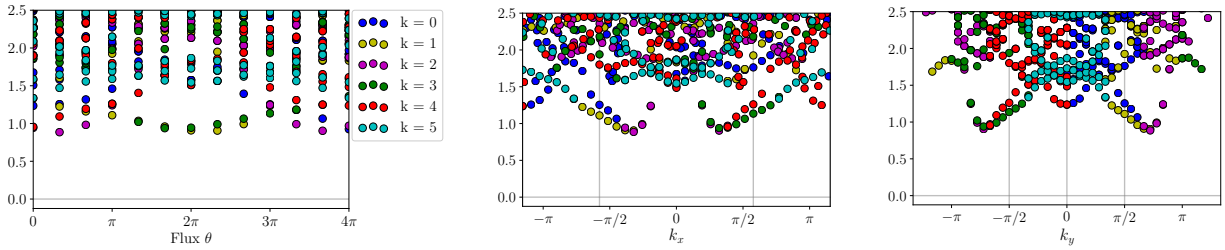

(a) (b) (c)

Figure 7.23: $S_z = 1$ part of the transfer matrix spectrum for the YC6 cylinder with $U/t = 9$, with $\chi = 8000$. Color indicates the momentum quantum number of each transfer matrix eigenvalue. Vertical lines correspond to possible locations of Dirac cones for a Dirac spin liquid. **(a)** Plotted versus flux inserted, θ. **(b)** Plotted versus k_x. **(c)** Plotted versus k_y.

with the expected momenta of transitions between Dirac cones, though there are local minima at $(k_x, k_y) = \pm(2\pi/\sqrt{3}, 0)$.

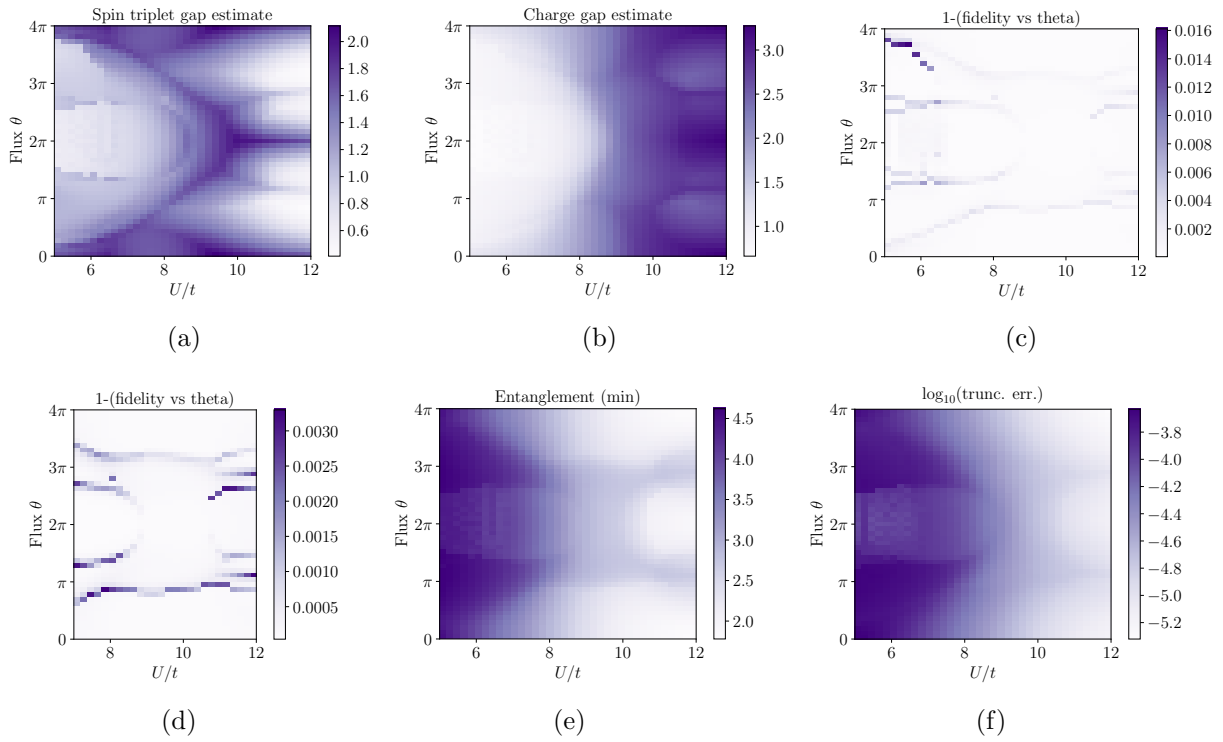

Figure 7.24: Various quantities for the YC5 cylinder vs U/t and flux insertion θ. **(a)** Transfer matrix estimate of the spin triplet gap. **(b)** Transfer matrix estimate of the charge gap. **(c)** Fidelity of the flux insertion, measued by $1 - |\langle\psi(\theta)|\psi(\theta + \pi/12)\rangle|^2$. At small U there is a loss of adiabaticity between 3π and 4π flux. **(d)** Fidelity with the leftmost columns removed to more clearly show the results in the rest of the phase diagram. **(e)** Entanglement between two rings of the cylinder. There is symmetry-breaking between the two rings of the unit cell; here we show the smaller of the two entanglements—between the two rings in the unit cell and between unit cells. **(f)** Log base 10 of the truncation error at the last step of the DMRG simulation.

7.3 YC5 additional data and analysis

Flux insertion data

In Figure 5.7, we show the chiral order parameter, peak height of the spin structure factor, and transfer matrix estimate of the spin singlet gap. Here we show in Figure 7.24 a number of additional quantities versus U/t and inserted flux, θ, with bond dimension $\chi = 8000$. In the chiral phase, the relative behavior of the various quantities is consistent with what we found for YC4 and YC6.

As with YC6, adiabatic flux insertion leads to metastable states at low U, as seen by the assymetry around 2π flux at low U; there is a sudden jump back to the ground state

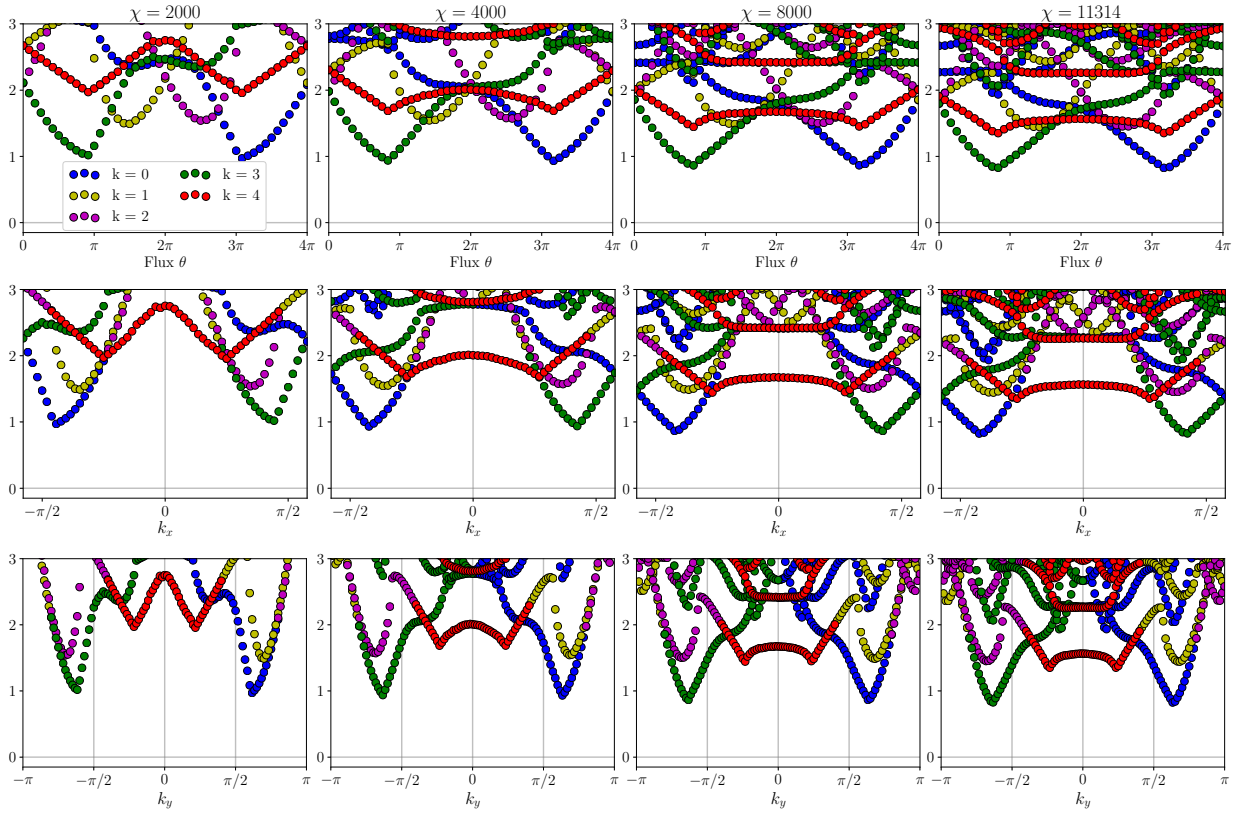

Figure 7.25: Low-lying part of the $S_z = 1$ part of the transfer matrix spectrum for $U/t = 10$ on the YC5 cylinder at $\chi = 2000$ (left column), 4000 (second column), 8000 (third column), and 11314 (right column), plotted versus flux inserted (top row), k_x (middle row), and k_y (bottom row). (The lattice constant is set to 1.) Color corresponds to the momentum quantum number of the excitation as given in the panel in the upper left. Vertical lines correspond to possible Dirac cone locations in the Dirac spin liquid; they do not clearly correspond to features observed in our data.

between 3π and 4π flux as seen by the line of low fidelity in Figure 7.24(c).

Transfer matrix and the two-dimensional excitation spectrum

We again compute the transfer matrix spectrum for spin 1 excitations versus flux θ, k_x, and k_y. In particular, we show in Figure 7.25 the spectrum for $U/t = 10$ at bond dimensions 2000, 4000, 8000, and 11314.

As with YC4 and YC6, above, we investigate how the transfer matrix spectrum does or does not correspond to a possible Dirac spin liquid (DSL). In this case, our particular goal is to check the possibility that the non-chiral state found near 0 flux could be a DSL, which becomes gapped out near 2π flux, thus becoming a chiral spin liquid instead. We see no

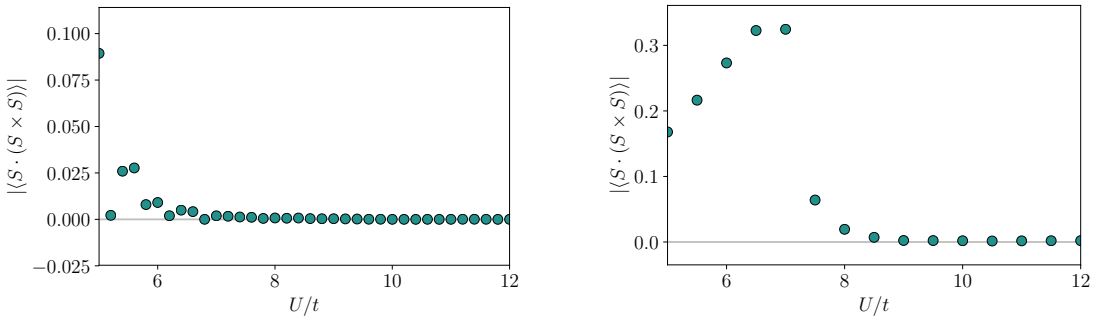

(a) (b)

Figure 7.26: Chiral order parameter versus U/t at zero flux for $\chi = 4000$. **(a)** With isotropic hopping in the Hubbard model, there scalar chiral order parameter is zero. It appears nonzero at low U, but this is not systematic and is likely a finite bond dimension effect. **(b)** When hopping on bonds around the cylinder is weakened by 10%, the chirality becomes large, of the same order as that observed for YC4.

evidence for this conclusion.

There are minima in the excitation spectrum at the values of θ where the transition between chiral and non-chiral states occurs, and these points will plausibly become gapless in the infinite bond dimension limit; however, the momenta corresponding to these gapless points are completely different from the transitions between expected locations of Dirac cones for the DSL, indicated by the vertical lines in Figure 7.25 (also at the edges of the plotted region in k_x).

Instead of a transition between DSL and CSL, the most plausible explanation is that there is simply a gap closing at a second-order transition between the chiral spin liquid and a bond-ordered state (see chapter 5).

Appearance of chirality with hopping anisotropy

In chapter 5 we argue that the nonchiral state at intermediate U near zero flux may be prevented from becoming the chiral spin liquid due to a large degree of anisotropy in the spin interactions. To test this, we explicitly introduce a hopping anisotropy in the model, weakening the bonds around the cylinder by 10%, thus producing more isotropic spin interactions that are therefore more consistent with the symmetries of the two-dimensional model. This indeed gives rise to nonzero scalar chirality at zero flux, as shown in Figure 7.26.

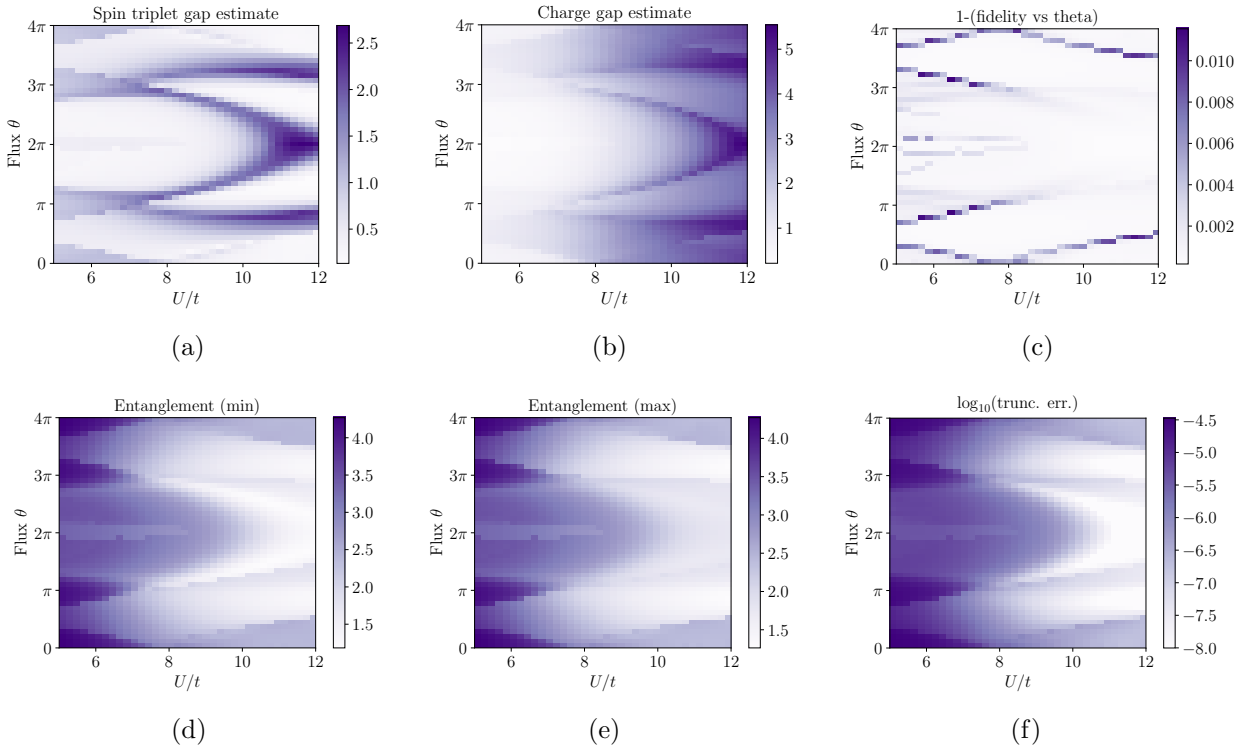

Figure 7.27: Various quantities for the YC3 cylinder vs U/t and flux insertion θ. **(a)** Transfer matrix estimate of the spin triplet gap. **(b)** Transfer matrix estimate of the charge gap. **(c)** Fidelity of the flux insertion, measued by $1 - |\langle\psi(\theta)|\psi(\theta + \pi/12)\rangle|^2$. **(d)** Entanglement between two rings of the cylinder. The unit cell is four rings, and here we show the smallest entanglement across any of the four distinct cuts. **(e)** Here we show just the largest of the four entanglements; it is nearly identical to the smallest. **(f)** Log base 10 of the truncation error at the last step of the DMRG simulation.

7.4 YC3 additional data and analysis

Flux insertion data

In Figure 5.9, we show the chiral order parameter, peak height of the spin structure factor, and transfer matrix estimate of the spin singlet gap. Here we show in Figure 7.27 a number of additional quantities versus U/t and inserted flux, θ, with bond dimension $\chi = 4000$. The relative behaviors of the various quantities do not match what we observed for the larger cylinders, so it is unclear whether the region with nonzero chirality corresponds to a chiral spin liquid.

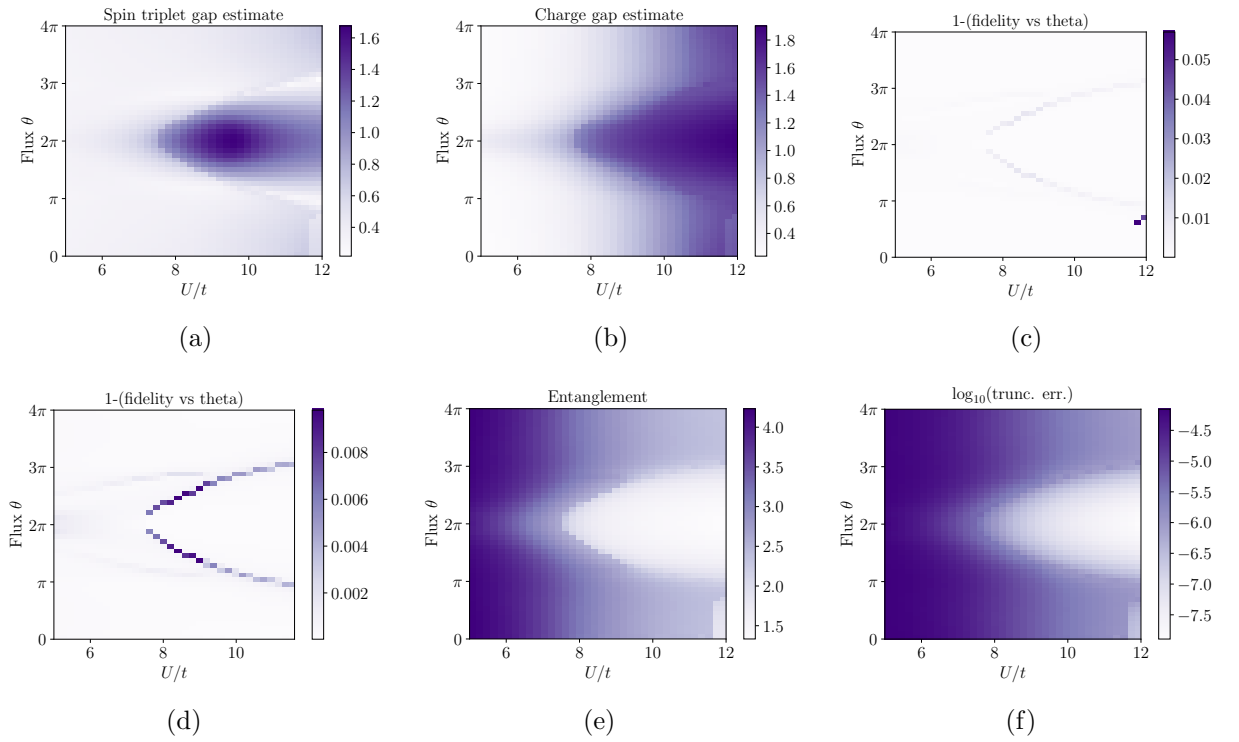

Figure 7.28: Various quantities for the XC4 cylinder vs U/t and flux insertion θ. **(a)** Transfer matrix estimate of the spin triplet gap. **(b)** Transfer matrix estimate of the charge gap. **(c)** Fidelity of the flux insertion, measued by $1 - |\langle\psi(\theta)|\psi(\theta + \pi/12)\rangle|^2$. **(d)** Fidelity with the rightmost columns removed to more clearly show the results in the rest of the phase diagram. **(e)** Entanglement between two rings of the cylinder. **(f)** Log base 10 of the truncation error at the last step of the DMRG simulation.

7.5 XC4 additional data and analysis

Flux insertion data

In Figure 5.10, we show the chiral order parameter, peak height of the spin structure factor, and transfer matrix estimate of the spin singlet gap. Here we show in Figure 7.27 a number of additional quantities versus U/t and inserted flux, θ, with bond dimension $\chi = 4000$. Again the relative behaviors of the various quantities do not match what we observed for the larger cylinders, and also the chirality at zero flux likely goes to zero with increasing bond dimension (as shown in Figure 5.10(a)), so it is unclear whether the region with nonzero chirality corresponds to a chiral spin liquid.

Note that as with YC6 and YC5, there is some nonadiabaticity in the flux insertion, in this case at $U/t = 11.8$ and 12. The state at near zero flux is metastable, about 1% higher in energy than the state near 4π flux.

Bibliography

[1] I Affleck. "Quantum spin chains and the Haldane gap". In: *Journal of Physics: Condensed Matter* 1.19 (1989), p. 3047. URL: http://stacks.iop.org/0953-8984/1/i=19/a=001.

[2] Ian Affleck. "Luttinger liquid parameter for the spin-1 Heisenberg chain in a magnetic field". In: *Phys. Rev. B* 72 (13 2005), p. 132414. DOI: 10.1103/PhysRevB.72.132414.

[3] Alexander Altland and Ben Simons. *Condensed Matter Field Theory – 2nd ed.* Cambridge: Cambridge University Press, 2010.

[4] P.W. Anderson. "Resonating valence bonds: A new kind of insulator?" In: *Materials Research Bulletin* 8.2 (1973), pp. 153 –160. ISSN: 0025-5408. DOI: https://doi.org/10.1016/0025-5408(73)90167-0.

[5] A. E. Antipov et al. "Electron energy spectrum of the spin-liquid state in a frustrated Hubbard model". In: *Phys. Rev. B* 83 (11 2011), p. 115126. DOI: 10.1103/PhysRevB.83.115126.

[6] I. Arad et al. "An area law and sub-exponential algorithm for 1D systems". In: *ArXiv e-prints* (Jan. 2013). arXiv: 1301.1162 [quant-ph].

[7] Neil W. Ashcroft and N. David Mermin. *Solid State Physics*. Harcourt, 1976.

[8] Leon Balents. "Spin liquids in frustrated magnets". In: *Nature* 464 (2010), p. 199. DOI: 10.1038/nature08917.

[9] A. F. Bangura et al. "The Wiedemann-Franz law in the putative one-dimensional metallic phase of PrBa2Cu4O8". In: *Scientific Reports* 3 (2013), p. 3261. DOI: 10.1038/srep03261.

[10] G. Baskaran. "Novel local symmetries and chiral-symmetry-broken phases in S=(1/2 triangular-lattice Heisenberg model". In: *Phys. Rev. Lett.* 63 (22 1989), pp. 2524–2527. DOI: 10.1103/PhysRevLett.63.2524.

[11] Gerardo Beni. "Thermoelectric power of the narrow-band Hubbard chain at arbitrary electron density: Atomic limit". In: *Phys. Rev. B* 10 (6 1974), pp. 2186–2189. DOI: 10.1103/PhysRevB.10.2186.

[12] S. Biermann et al. "Quasi One-Dimensional Organic Conductors: Dimensional Crossover and Some Puzzles". In: *Strongly Correlated Fermions and Bosons in Low-Dimensional Disordered Systems*. Ed. by I. V. Lerner et al. Dordrecht: Springer Netherlands, 2002, pp. 81–102. ISBN: 978-94-010-0530-2. DOI: 10.1007/978-94-010-0530-2_5.

[13] Iaroslav V. Blagouchine. "A theorem for the closed-form evaluation of the first generalized Stieltjes constant at rational arguments and some related summations". In: *Journal of Number Theory* 148 (2015), pp. 537–592. DOI: 10.1016/j.jnt.2014.08.009.

[14] Matthew S. Block et al. "Spin Bose-Metal and Valence Bond Solid Phases in a Spin-1/2 Model with Ring Exchanges on a Four-Leg Triangular Ladder". In: *Phys. Rev. Lett.* 106 (15 2011), p. 157202. DOI: 10.1103/PhysRevLett.106.157202.

[15] C. Blumenstein et al. "Atomically controlled quantum chains hosting a Tomonaga-Luttinger liquid". In: *Nat Phys* 7 (10 2011), pp. 776–780. DOI: 10.1038/nphys2051.

[16] P. Bourgeois-Hope et al. "Thermal conductivity of the quantum spin liquid candidate EtMe3Sb[Pd(dmit)2]2: No evidence of mobile gapless excitations". In: *arXiv e-prints* (2019). arXiv: 1904.10402 [cond-mat.str-el].

[17] Bernd Braunecker, Cristina Bena, and Pascal Simon. "Spectral properties of Luttinger liquids: A comparative analysis of regular, helical, and spiral Luttinger liquids". In: *Phys. Rev. B* 85 (3 2012), p. 035136. DOI: 10.1103/PhysRevB.85.035136.

[18] Olga Bubnova et al. "Semi-metallic polymers". In: *Nat Mater* 13 (2 2014), pp. 190–194. DOI: 10.1038/nmat3824.

[19] Pasquale Calabrese and John Cardy. "Entanglement entropy and quantum field theory". In: *Journal of Statistical Mechanics: Theory and Experiment* 2004.06 (2004), P06002. DOI: 10.1088/1742-5468/2004/06/p06002.

[20] L. Cincio and G. Vidal. "Characterizing Topological Order by Studying the Ground States on an Infinite Cylinder". In: *Phys. Rev. Lett.* 110 (6 2013), p. 067208. DOI: 10.1103/PhysRevLett.110.067208.

[21] David G. Clarke and S. P. Strong. "Single particle hopping between luttinger liquids: A spectral function approach". In: *Ferroelectrics* 177.1 (1996), pp. 1–15. DOI: 10.1080/00150199608216948.

[22] David G. Clarke, S. P. Strong, and P. W. Anderson. "Conductivity between Luttinger Liquids in the Confinement Regime and c-Axis Conductivity in the Cuprate Superconductors". In: *Phys. Rev. Lett.* 74 (22 1995), pp. 4499–4502. DOI: 10.1103/PhysRevLett.74.4499.

[23] David G. Clarke, S. P. Strong, and P. W. Anderson. "Incoherence of single particle hopping between Luttinger liquids". In: *Phys. Rev. Lett.* 72 (20 1994), pp. 3218–3221. DOI: 10.1103/PhysRevLett.72.3218.

[24] Philippe Corboz et al. "Simulation of strongly correlated fermions in two spatial dimensions with fermionic projected entangled-pair states". In: *Phys. Rev. B* 81 (16 2010), p. 165104. DOI: 10.1103/PhysRevB.81.165104.

[25] G. Ehlers, S. R. White, and R. M. Noack. "Hybrid-space density matrix renormalization group study of the doped two-dimensional Hubbard model". In: *Phys. Rev. B* 95 (12 2017), p. 125125. DOI: 10.1103/PhysRevB.95.125125.

[26] S. Ejima, F. Gebhard, and S. Nishimoto. "Tomonaga-Luttinger parameters for doped Mott insulators". In: *EPL (Europhysics Letters)* 70.4 (2005), p. 492. DOI: 10.1209/epl/i2005-10020-8.

[27] Satoshi Ejima, Florian Gebhard, and Satoshi Nishimoto. "Tomonaga-Luttinger parameters and spin excitations in the dimerized extended Hubbard model". In: *Phys. Rev. B* 74 (24 2006), p. 245110. DOI: 10.1103/PhysRevB.74.245110.

[28] Arthur Erdélyi et al. *Higher Transcendental Functions. Vol. I.* Reprinted by Robert E. Krieger Publishing Co. Inc., 1981. Table errata: Math. Comp. v. 65 (1996), no. 215, p. 1385, v. 41 (1983), no. 164, p. 778, v. 30 (1976), no. 135, p. 675, v. 25 (1971), no. 115, p. 635, v. 25 (1971), no. 113, p. 199, v. 24 (1970), no. 112, p. 999, v. 24 (1970), no. 110, p. 504, v. 17 (1963), no. 84, p. 485. New York-Toronto-London: McGraw-Hill Book Company, Inc., 1953, pp. xxvi+302.

[29] Antoine Georges, Thierry Giamarchi, and Nancy Sandler. "Interchain conductivity of coupled Luttinger liquids and organic conductors". In: *Phys. Rev. B* 61 (24 2000), pp. 16393–16396. DOI: 10.1103/PhysRevB.61.16393. eprint: cond-mat/0001063v1.

[30] Scott D. Geraedts et al. "The half-filled Landau level: The case for Dirac composite fermions". In: *Science* 352.6282 (2016), pp. 197–201. ISSN: 0036-8075. DOI: 10.1126/science.aad4302.

[31] Thierry Giamarchi. *Quantum Physics in One Dimension*. Oxford: Clarendon Press, 2003.

[32] Anne M. Glaudell et al. "Impact of the Doping Method on Conductivity and Thermopower in Semiconducting Polythiophenes". In: *Advanced Energy Materials* 5.4 (2015). 1401072, 1401072–n/a. ISSN: 1614-6840. DOI: 10.1002/aenm.201401072.

[33] Shou-Shu Gong, Wei Zhu, and D. N. Sheng. "Emergent Chiral Spin Liquid: Fractional Quantum Hall Effect in a Kagome Heisenberg Model". In: *Scientific Reports* 4 (2014), p. 6317. DOI: 10.1038/srep06317.

[34] Shou-Shu Gong et al. "Global phase diagram and quantum spin liquids in a spin-$\frac{1}{2}$ triangular antiferromagnet". In: *Phys. Rev. B* 96 (7 2017), p. 075116. DOI: 10.1103/PhysRevB.96.075116.

[35] Tarun Grover et al. "Weak Mott insulators on the triangular lattice: Possibility of a gapless nematic quantum spin liquid". In: *Phys. Rev. B* 81 (24 2010), p. 245121. DOI: 10.1103/PhysRevB.81.245121.

[36] O. Gunnarsson, M. W. Haverkort, and G. Sangiovanni. "Analytical continuation of imaginary axis data using maximum entropy". In: *Phys. Rev. B* 81 (15 2010), p. 155107. DOI: 10.1103/PhysRevB.81.155107.

[37] F D M Haldane. "'Luttinger liquid theory' of one-dimensional quantum fluids. I. Properties of the Luttinger model and their extension to the general 1D interacting spinless Fermi gas". In: *Journal of Physics C: Solid State Physics* 14.19 (1981), p. 2585. DOI: 10.1088/0022-3719/14/19/010.

[38] M B Hastings. "An area law for one-dimensional quantum systems". In: *Journal of Statistical Mechanics: Theory and Experiment* 2007.08 (2007), P08024. DOI: 10.1088/1742-5468/2007/08/p08024.

[39] Yin-Chen He et al. "Signatures of Dirac Cones in a DMRG Study of the Kagome Heisenberg Model". In: *Phys. Rev. X* 7 (3 2017), p. 031020. DOI: 10.1103/PhysRevX.7.031020.

[40] A. J. Heeger et al. "Solitons in conducting polymers". In: *Rev. Mod. Phys.* 60 (3 1988), pp. 781–850. DOI: 10.1103/RevModPhys.60.781.

[41] Shijie Hu et al. "Dirac Spin Liquid on the Spin-1/2 Triangular Heisenberg Antiferromagnet". In: *arXiv e-prints*, arXiv:1905.09837 (2019), arXiv:1905.09837. arXiv: 1905.09837 [cond-mat.str-el].

[42] Wen-Jun Hu, Shou-Shu Gong, and D. N. Sheng. "Variational Monte Carlo study of chiral spin liquid in quantum antiferromagnet on the triangular lattice". In: *Phys. Rev. B* 94 (7 2016), p. 075131. DOI: 10.1103/PhysRevB.94.075131.

[43] Wen-Jun Hu et al. "Competing spin-liquid states in the spin-$\frac{1}{2}$ Heisenberg model on the triangular lattice". In: *Phys. Rev. B* 92 (14 2015), p. 140403. DOI: 10.1103/PhysRevB.92.140403.

[44] Yichen Huang, C. Karrasch, and J. E. Moore. "Scaling of electrical and thermal conductivities in an almost integrable chain". In: *Phys. Rev. B* 88 (11 2013), p. 115126. DOI: 10.1103/PhysRevB.88.115126.

[45] C. Hubig, J. Haegeman, and U. Schollwöck. "Error estimates for extrapolations with matrix-product states". In: *Phys. Rev. B* 97 (4 2018), p. 045125. DOI: 10.1103/PhysRevB.97.045125.

[46] David A. Huse and Veit Elser. "Simple Variational Wave Functions for Two-Dimensional Heisenberg Spin-1/2 Antiferromagnets". In: *Phys. Rev. Lett.* 60 (24 1988), pp. 2531–2534. DOI: 10.1103/PhysRevLett.60.2531.

[47] M. B. Isichenko. "Percolation, statistical topography, and transport in random media". In: *Rev. Mod. Phys.* 64 (4 1992), pp. 961–1043. DOI: 10.1103/RevModPhys.64.961.

[48] T Itou et al. "13 C NMR study of the spin-liquid state in the triangular quantum antiferromagnet EtMe 3 Sb[Pd(dmit) 2] 2". In: *Journal of Physics: Conference Series* 145.1 (2009), p. 012039. DOI: 10.1088/1742-6596/145/1/012039.

[49] T. Itou et al. "Instability of a quantum spin liquid in an organic triangular-lattice antiferromagnet". In: *Nature Physics* 6 (2010), p. 673. DOI: 10.1038/nphys1715.

[50] T. Itou et al. "Quantum spin liquid in the spin-1/2 triangular antiferromagnet $EtMe_3Sb[Pd(dmit)_2]_2$". In: *Phys. Rev. B* 77 (10 2008), p. 104413. DOI: 10.1103/PhysRevB.77.104413.

[51] Andrew J. A. James and Robert M. Konik. "Understanding the entanglement entropy and spectra of 2D quantum systems through arrays of coupled 1D chains". In: *Phys. Rev. B* 87 (24 2013), p. 241103. DOI: 10.1103/PhysRevB.87.241103.

[52] Mark Jarrell and J.E. Gubernatis. "Bayesian inference and the analytic continuation of imaginary-time quantum Monte Carlo data". In: *Physics Reports* 269.3 (1996), pp. 133 –195. ISSN: 0370-1573. DOI: http://dx.doi.org/10.1016/0370-1573(95)00074-7.

[53] V. Kalmeyer and R. B. Laughlin. "Equivalence of the resonating-valence-bond and fractional quantum Hall states". In: *Phys. Rev. Lett.* 59 (18 1987), pp. 2095–2098. DOI: 10.1103/PhysRevLett.59.2095.

[54] C. L. Kane and Matthew P. A. Fisher. "Thermal Transport in a Luttinger Liquid". In: *Phys. Rev. Lett.* 76 (17 1996), pp. 3192–3195. DOI: 10.1103/PhysRevLett.76.3192.

[55] C. L. Kane and Matthew P. A. Fisher. "Transmission through barriers and resonant tunneling in an interacting one-dimensional electron gas". In: *Phys. Rev. B* 46 (23 1992), pp. 15233–15262. DOI: 10.1103/PhysRevB.46.15233.

[56] C. L. Kane and Matthew P. A. Fisher. "Transport in a one-channel Luttinger liquid". In: *Phys. Rev. Lett.* 68 (8 1992), pp. 1220–1223. DOI: 10.1103/PhysRevLett.68.1220.

[57] Ryui Kaneko, Satoshi Morita, and Masatoshi Imada. "Gapless Spin-Liquid Phase in an Extended Spin 1/2 Triangular Heisenberg Model". In: *Journal of the Physical Society of Japan* 83.9 (2014), p. 093707. DOI: 10.7566/JPSJ.83.093707.

[58] Y. Kasahara et al. "Majorana quantization and half-integer thermal quantum Hall effect in a Kitaev spin liquid". In: *Nature* 559 (2018), p. 227. DOI: 10.1038/s41586-018-0274-0.

[59] G-H. Kim et al. "Engineered doping of organic semiconductors for enhanced thermoelectric efficiency". In: *Nat Mater* 12 (8 2013), pp. 719–723. DOI: 10.1038/nmat3635.

[60] Alexei Kitaev and John Preskill. "Topological Entanglement Entropy". In: *Phys. Rev. Lett.* 96 (11 2006), p. 110404. DOI: 10.1103/PhysRevLett.96.110404.

[61] Jonas A. Kjäll et al. "Phase diagram of the anisotropic spin-2 XXZ model: Infinite-system density matrix renormalization group study". In: *Phys. Rev. B* 87 (23 2013), p. 235106. DOI: 10.1103/PhysRevB.87.235106.

[62] J. Knolle and R. Moessner. "A Field Guide to Spin Liquids". In: *Annual Review of Condensed Matter Physics* 10.1 (2019), pp. 451–472. DOI: 10.1146/annurev-conmatphys-031218-013401.

[63] Tokutaro Komatsu et al. "Realization of Superconductivity at Ambient Pressure by Band-Filling Control in κ- (BEDT-TTF)2Cu2(CN)3". In: *Journal of the Physical Society of Japan* 65.5 (1996), pp. 1340–1354. DOI: 10.1143/JPSJ.65.1340.

[64] B. Kyung and A.-M. S. Tremblay. "Mott Transition, Antiferromagnetism, and d-Wave Superconductivity in Two-Dimensional Organic Conductors". In: *Phys. Rev. Lett.* 97 (4 2006), p. 046402. DOI: 10.1103/PhysRevLett.97.046402.

[65] Manuel Laubach et al. "Phase diagram of the Hubbard model on the anisotropic triangular lattice". In: *Phys. Rev. B* 91 (24 2015), p. 245125. DOI: 10.1103/PhysRevB.91.245125.

[66] Hui Li and F. D. M. Haldane. "Entanglement Spectrum as a Generalization of Entanglement Entropy: Identification of Topological Order in Non-Abelian Fractional Quantum Hall Effect States". In: *Phys. Rev. Lett.* 101 (1 2008), p. 010504. DOI: 10.1103/PhysRevLett.101.010504.

[67] M.-R. Li and E. Orignac. "Heat conduction and Wiedemann-Franz law in disordered Luttinger liquids". In: *EPL (Europhysics Letters)* 60.3 (2002), p. 432. DOI: 10.1209/epl/i2002-00282-0.

[68] A. H. MacDonald, S. M. Girvin, and D. Yoshioka. "$\frac{t}{U}$ expansion for the Hubbard model". In: *Phys. Rev. B* 37 (16 1988), pp. 9753–9756. DOI: 10.1103/PhysRevB.37.9753.

[69] Gerald D. Mahan. *Many-Particle Physics – 2nd ed.* New York: Plenum Press, 1990.

[70] Gerald D. Mahan. *Many-Particle Physics – 3rd ed.* New York: Springer Science + Business Media, 2000.

[71] Ann E. Mattsson, Sebastian Eggert, and Henrik Johannesson. "Properties of a Luttinger liquid with boundaries at finite temperature and size". In: *Phys. Rev. B* 56 (24 1997), pp. 15615–15628. DOI: 10.1103/PhysRevB.56.15615.

[72] Ryan V. Mishmash et al. "Continuous Mott transition between a metal and a quantum spin liquid". In: *Phys. Rev. B* 91 (23 2015), p. 235140. DOI: 10.1103/PhysRevB.91.235140.

[73] Ryan V. Mishmash et al. "Theory of a Competitive Spin Liquid State for Weak Mott Insulators on the Triangular Lattice". In: *Phys. Rev. Lett.* 111 (15 2013), p. 157203. DOI: 10.1103/PhysRevLett.111.157203.

[74] Kazuma Misumi, Tatsuya Kaneko, and Yukinori Ohta. "Mott transition and magnetism of the triangular-lattice Hubbard model with next-nearest-neighbor hopping". In: *Phys. Rev. B* 95 (7 2017), p. 075124. DOI: 10.1103/PhysRevB.95.075124.

[75] J. E. Moore and F. D. M. Haldane. "Edge excitations of the $\nu=$ spin-singlet quantum Hall state". In: *Phys. Rev. B* 55 (12 1997), pp. 7818–7823. DOI: 10.1103/PhysRevB.55.7818.

[76] Hidekazu Morita, Shinji Watanabe, and Masatoshi Imada. "Nonmagnetic Insulating States near the Mott Transitions on Lattices with Geometrical Frustration and Implications for κ-(ET)2Cu2(CN)3". In: *Journal of the Physical Society of Japan* 71.9 (2002), pp. 2109–2112. DOI: 10.1143/JPSJ.71.2109.

[77] Moser, J. et al. "Transverse transport in (TM)2X organic conductors: possible evidence for a Luttinger liquid". In: *Eur. Phys. J. B* 1.1 (1998), pp. 39–46. DOI: 10.1007/s100510050150.

[78] Johannes Motruk et al. "Density matrix renormalization group on a cylinder in mixed real and momentum space". In: *Phys. Rev. B* 93 (15 2016), p. 155139. DOI: 10.1103/PhysRevB.93.155139.

[79] Olexei I. Motrunich. "Variational study of triangular lattice spin-1/2 model with ring exchanges and spin liquid state in $\kappa-(\mathrm{ET})_2\mathrm{Cu}_2(\mathrm{CN})_3$". In: *Phys. Rev. B* 72 (4 2005), p. 045105. DOI: 10.1103/PhysRevB.72.045105.

[80] Subroto Mukerjee. "Thermopower of the Hubbard model: Effects of multiple orbitals and magnetic fields in the atomic limit". In: *Phys. Rev. B* 72 (19 2005), p. 195109. DOI: 10.1103/PhysRevB.72.195109.

[81] J. M. Ni et al. "Absence of magnetic thermal conductivity in the quantum spin liquid candidate EtMe3Sb[Pd(dmit)2]2 – revisited". In: *arXiv e-prints* (2019). arXiv: 1904.10395 [cond-mat.str-el].

[82] *NIST Digital Library of Mathematical Functions*. http://dlmf.nist.gov/, Release 1.0.13 of 2016-09-16. F. W. J. Olver, A. B. Olde Daalhuis, D. W. Lozier, B. I. Schneider, R. F. Boisvert, C. W. Clark, B. R. Miller and B. V. Saunders, eds.

[83] Rodrigo Noriega et al. "A general relationship between disorder, aggregation and charge transport in conjugated polymers". In: *Nat Mater* 12 (11 2013), pp. 1038–1044. DOI: 10.1038/nmat3722.

[84] Masaki Oshikawa and T. Senthil. "Fractionalization, Topological Order, and Quasiparticle Statistics". In: *Phys. Rev. Lett.* 96 (6 2006), p. 060601. DOI: 10.1103/PhysRevLett.96.060601.

[85] Žiga Osolin and Rok Žitko. "Padé approximant approach for obtaining finite-temperature spectral functions of quantum impurity models using the numerical renormalization group technique". In: *Phys. Rev. B* 87 (24 2013), p. 245135. DOI: 10.1103/PhysRevB.87.245135.

[86] Stellan Östlund and Stefan Rommer. "Thermodynamic Limit of Density Matrix Renormalization". In: *Phys. Rev. Lett.* 75 (19 1995), pp. 3537–3540. DOI: 10.1103/PhysRevLett.75.3537.

[87] Philippe Francesco, Pierre Mathieu, and David Sénéchal. *Conformal Field Theory*. Springer-Verlag New York, 1997.

[88] B. Pirvu et al. "Matrix product states for critical spin chains: Finite-size versus finite-entanglement scaling". In: *Phys. Rev. B* 86 (7 2012), p. 075117. DOI: 10.1103/PhysRevB.86.075117.

[89] Frank Pollmann et al. "Entanglement spectrum of a topological phase in one dimension". In: *Phys. Rev. B* 81 (6 2010), p. 064439. DOI: 10.1103/PhysRevB.81.064439.

[90] Frank Pollmann et al. "Theory of Finite-Entanglement Scaling at One-Dimensional Quantum Critical Points". In: *Phys. Rev. Lett.* 102 (25 2009), p. 255701. DOI: 10.1103/PhysRevLett.102.255701.

[91] Xiao-Liang Qi, Hosho Katsura, and Andreas W. W. Ludwig. "General Relationship between the Entanglement Spectrum and the Edge State Spectrum of Topological Quantum States". In: *Phys. Rev. Lett.* 108 (19 2012), p. 196402. DOI: 10.1103/PhysRevLett.108.196402.

[92] Onofre Rojas, S. M. de Souza, and N. S. Ananikian. "Geometrical frustration of an extended Hubbard diamond chain in the quasiatomic limit". In: *Phys. Rev. E* 85 (6 2012), p. 061123. DOI: 10.1103/PhysRevE.85.061123.

[93] S. N. Saadatmand and I. P. McCulloch. "Detection and characterization of symmetry-broken long-range orders in the spin-$\frac{1}{2}$ triangular Heisenberg model". In: *Phys. Rev. B* 96 (7 2017), p. 075117. DOI: 10.1103/PhysRevB.96.075117.

[94] Peyman Sahebsara and David Sénéchal. "Hubbard Model on the Triangular Lattice: Spiral Order and Spin Liquid". In: *Phys. Rev. Lett.* 100 (13 2008), p. 136402. DOI: 10.1103/PhysRevLett.100.136402.

[95] J. Sahoo et al. "Classical phase diagram of the stuffed honeycomb lattice". In: *ArXiv e-prints* (May 2018). arXiv: 1805.09831 [cond-mat.str-el].

[96] N. Sai et al. "Electronic excitations and metal-insulator transition in poly(3-hexylthiophene) organic field-effect transistors". In: *Phys. Rev. B* 75 (4 2007), p. 045307. DOI: 10.1103/PhysRevB.75.045307.

[97] Lucile Savary and Leon Balents. "Quantum spin liquids: a review". In: *Reports on Progress in Physics* 80.1 (2017), p. 016502. DOI: 10.1088/0034-4885/80/1/016502.

[98] Yoni Schattner, Vadim Oganesyan, and Dror Orgad. "Transverse thermoelectric response as a probe for existence of quasiparticles". In: *Phys. Rev. B* 94 (23 2016), p. 235130. DOI: 10.1103/PhysRevB.94.235130.

[99] Ulrich Schollwöck. "The density-matrix renormalization group in the age of matrix product states". In: *Annals of Physics* 326.1 (2011). January 2011 Special Issue, pp. 96 –192. ISSN: 0003-4916. DOI: https://doi.org/10.1016/j.aop.2010.09.012.

[100] H. J. Schulz. "Correlation exponents and the metal-insulator transition in the one-dimensional Hubbard model". In: *Phys. Rev. Lett.* 64 (23 1990), pp. 2831–2834. DOI: 10.1103/PhysRevLett.64.2831.

[101] P. Segovia et al. "Observation of spin and charge collective modes in one-dimensional metallic chains". In: *Nature* 402 (6761 1999), pp. 504–507. DOI: 10.1038/990052.

[102] D. N. Sheng, Olexei I. Motrunich, and Matthew P. A. Fisher. "Spin Bose-metal phase in a spin-$\frac{1}{2}$ model with ring exchange on a two-leg triangular strip". In: *Phys. Rev. B* 79 (20 2009), p. 205112. DOI: 10.1103/PhysRevB.79.205112.

[103] D. N. Sheng et al. "Strong-coupling phases of frustrated bosons on a two-leg ladder with ring exchange". In: *Phys. Rev. B* 78 (5 2008), p. 054520. DOI: 10.1103/PhysRevB.78.054520.

[104] Y. Shimizu et al. "Emergence of inhomogeneous moments from spin liquid in the triangular-lattice Mott insulator $\kappa-(\mathrm{ET})_2\mathrm{Cu}_2(\mathrm{CN})_3$". In: *Phys. Rev. B* 73 (14 2006), p. 140407. DOI: 10.1103/PhysRevB.73.140407.

[105] Y. Shimizu et al. "Spin Liquid State in an Organic Mott Insulator with a Triangular Lattice". In: *Phys. Rev. Lett.* 91 (10 2003), p. 107001. DOI: 10.1103/PhysRevLett.91.107001.

[106] Tomonori Shirakawa et al. "Ground-state phase diagram of the triangular lattice Hubbard model by the density-matrix renormalization group method". In: *Phys. Rev. B* 96 (20 2017), p. 205130. DOI: 10.1103/PhysRevB.96.205130.

[107] F Siringo and D E Logan. "Local moment formation in disordered systems: a low-filling quasi-atomic limit". In: *Journal of Physics: Condensed Matter* 3.25 (1991), p. 4747. DOI: 10.1088/0953-8984/3/25/020.

[108] J. Sirker. "The Luttinger Liquid And Integrable Models". In: *International Journal of Modern Physics B* 26.22 (2012), p. 1244009. DOI: 10.1142/S0217979212440092.

[109] Robert Steyrleuthner et al. "The Role of Regioregularity, Crystallinity, and Chain Orientation on Electron Transport in a High-Mobility n-Type Copolymer". In: *Journal of the American Chemical Society* 136.11 (2014). PMID: 24524296, pp. 4245–4256. DOI: 10.1021/ja4118736.

[110] Aaron Szasz, Roni Ilan, and Joel E. Moore. "Electrical and thermal transport in the quasiatomic limit of coupled Luttinger liquids". In: *Phys. Rev. B* 95 (8 2017), p. 085122. DOI: 10.1103/PhysRevB.95.085122.

[111] Aaron Szasz et al. "Observation of a chiral spin liquid phase of the Hubbard model on the triangular lattice: a density matrix renormalization group study". In: *arXiv e-prints* (2018). arXiv: 1808.00463 [cond-mat.str-el].

[112] L. Tagliacozzo et al. "Scaling of entanglement support for matrix product states". In: *Phys. Rev. B* 78 (2 2008), p. 024410. DOI: 10.1103/PhysRevB.78.024410.

[113] Luca F. Tocchio et al. "Spin-liquid and magnetic phases in the anisotropic triangular lattice: The case of $\kappa-(ET)_2X$". In: *Phys. Rev. B* 80 (6 2009), p. 064419. DOI: 10.1103/PhysRevB.80.064419.

[114] Luca F. Tocchio et al. "Spin-liquid versus spiral-order phases in the anisotropic triangular lattice". In: *Phys. Rev. B* 87 (3 2013), p. 035143. DOI: 10.1103/PhysRevB.87.035143.

[115] F. Verstraete and J. I. Cirac. "Renormalization algorithms for Quantum-Many Body Systems in two and higher dimensions". In: *arXiv e-prints* (July 2004). arXiv: 0407066 [cond-mat.str-el].

[116] V. Vescoli et al. "Dimensionality-Driven Insulator-to-Metal Transition in the Bechgaard Salts". In: *Science* 281.5380 (1998), pp. 1181–1184. ISSN: 0036-8075. DOI: 10.1126/science.281.5380.1181.

[117] Guifré Vidal. "Efficient Classical Simulation of Slightly Entangled Quantum Computations". In: *Phys. Rev. Lett.* 91 (14 2003), p. 147902. DOI: 10.1103/PhysRevLett.91.147902.

[118] H. J. Vidberg and J. W. Serene. "Solving the Eliashberg equations by means of N-point Padé approximants". In: *Journal of Low Temperature Physics* 29.3 (1977), pp. 179–192. ISSN: 1573-7357. DOI: 10.1007/BF00655090.

[119] Nicholas Wakeham et al. "Gross violation of the Wiedemann-Franz law in a quasi-one-dimensional conductor". In: *Nature Communications* 2 (2011), p. 396. DOI: 10.1038/ncomms1406.

[120] Eric W. Weisstein. *Appell Hypergeometric Function*. From *MathWorld*–A Wolfram Web Resource. http://mathworld.wolfram.com/AppellHypergeometricFunction.html.

[121] Eric W. Weisstein. *Stieltjes Constants*. From *MathWorld*–A Wolfram Web Resource. http://mathworld.wolfram.com/StieltjesConstants.html.

[122] X. G. Wen. "Gapless boundary excitations in the quantum Hall states and in the chiral spin states". In: *Phys. Rev. B* 43 (13 1991), pp. 11025–11036. DOI: 10.1103/PhysRevB.43.11025.

[123] X. G. Wen. "Vacuum degeneracy of chiral spin states in compactified space". In: *Phys. Rev. B* 40 (10 1989), pp. 7387–7390. DOI: 10.1103/PhysRevB.40.7387.

[124] X. G. Wen and Q. Niu. "Ground-state degeneracy of the fractional quantum Hall states in the presence of a random potential and on high-genus Riemann surfaces". In: *Phys. Rev. B* 41 (13 1990), pp. 9377–9396. DOI: 10.1103/PhysRevB.41.9377.

[125] X. G. Wen, Frank Wilczek, and A. Zee. "Chiral spin states and superconductivity". In: *Phys. Rev. B* 39 (16 1989), pp. 11413–11423. DOI: 10.1103/PhysRevB.39.11413.

[126] Xiao-Gong Wen. *Quantum Field Theory of Many-Body Systems*. New York: Oxford University Press, 2004.

[127] Steven R. White. "Density-matrix algorithms for quantum renormalization groups". In: *Phys. Rev. B* 48 (14 1993), pp. 10345–10356. DOI: 10.1103/PhysRevB.48.10345.

[128] Steven R. White. "Density matrix formulation for quantum renormalization groups". In: *Phys. Rev. Lett.* 69 (19 1992), pp. 2863–2866. DOI: 10.1103/PhysRevLett.69.2863.

[129] Steven R. White and A. L. Chernyshev. "Neél Order in Square and Triangular Lattice Heisenberg Models". In: *Phys. Rev. Lett.* 99 (12 2007), p. 127004. DOI: 10.1103/PhysRevLett.99.127004.

[130] Steven R. White and Adrian E. Feiguin. "Real-Time Evolution Using the Density Matrix Renormalization Group". In: *Phys. Rev. Lett.* 93 (7 2004), p. 076401. DOI: 10.1103/PhysRevLett.93.076401.

[131] Alexander Wietek and Andreas M. Läuchli. "Chiral spin liquid and quantum criticality in extended $S = \frac{1}{2}$ Heisenberg models on the triangular lattice". In: *Phys. Rev. B* 95 (3 2017), p. 035141. DOI: 10.1103/PhysRevB.95.035141.

[132] Minoru Yamashita. "Boundary-limited and glassy-like phonon thermal conduction in $EtMe_3Sb[Pd(dmit)_2]_2$". In: *arXiv e-prints* (2019). arXiv: 1905.08420 [cond-mat.str-el].

[133] Minoru Yamashita et al. "Highly Mobile Gapless Excitations in a Two-Dimensional Candidate Quantum Spin Liquid". In: *Science* 328.5983 (2010), pp. 1246–1248. ISSN: 0036-8075. DOI: 10.1126/science.1188200.

[134] Minoru Yamashita et al. "Thermal-transport measurements in a quantum spin-liquid state of the frustrated triangular magnet -(BEDT-TTF)2Cu2(CN)3". In: *Nature Physics* 5 (2008), p. 44. DOI: 10.1038/nphys1134.

[135] Satoshi Yamashita et al. "Thermodynamic properties of a spin-1/2 spin-liquid state in a κ-type organic salt". In: *Nature Physics* 4 (2008), p. 459. DOI: 10.1038/nphys942.

[136] Simeng Yan, David A. Huse, and Steven R. White. "Spin-Liquid Ground State of the S = 1/2 Kagome Heisenberg Antiferromagnet". In: *Science* 332.6034 (2011), pp. 1173–1176. ISSN: 0036-8075. DOI: 10.1126/science.1201080.

[137] Hong-Yu Yang et al. "Effective Spin Model for the Spin-Liquid Phase of the Hubbard Model on the Triangular Lattice". In: *Phys. Rev. Lett.* 105 (26 2010), p. 267204. DOI: 10.1103/PhysRevLett.105.267204.

[138] Takuya Yoshioka, Akihisa Koga, and Norio Kawakami. "Quantum Phase Transitions in the Hubbard Model on a Triangular Lattice". In: *Phys. Rev. Lett.* 103 (3 2009), p. 036401. DOI: 10.1103/PhysRevLett.103.036401.

[139] Jonathan D. Yuen et al. "Nonlinear transport in semiconducting polymers at high carrier densities". In: *Nat Mater* 8 (7 2009), pp. 572–575. DOI: 10.1038/nmat2470.

[140] Michael P. Zaletel, Yuan-Ming Lu, and Ashvin Vishwanath. "Measuring space-group symmetry fractionalization in $\mathbb{Z}_2$ spin liquids". In: *Phys. Rev. B* 96 (19 2017), p. 195164. DOI: 10.1103/PhysRevB.96.195164.

[141] Michael P. Zaletel, Roger S. K. Mong, and Frank Pollmann. "Topological Characterization of Fractional Quantum Hall Ground States from Microscopic Hamiltonians". In: *Phys. Rev. Lett.* 110 (23 2013), p. 236801. DOI: 10.1103/PhysRevLett.110.236801.

[142] Michael P. Zaletel and Ashvin Vishwanath. "Constraints on Topological Order in Mott Insulators". In: *Phys. Rev. Lett.* 114 (7 2015), p. 077201. DOI: 10.1103/PhysRevLett.114.077201.

[143] V Zauner et al. "Transfer matrices and excitations with matrix product states". In: *New Journal of Physics* 17.5 (2015), p. 053002. DOI: 10.1088/1367-2630/17/5/053002.

[144] Yi Zhang et al. "Quasiparticle statistics and braiding from ground-state entanglement". In: *Phys. Rev. B* 85 (23 2012), p. 235151. DOI: 10.1103/PhysRevB.85.235151.

[145] Yi Zhou, Kazushi Kanoda, and Tai-Kai Ng. "Quantum spin liquid states". In: *Rev. Mod. Phys.* 89 (2 2017), p. 025003. DOI: 10.1103/RevModPhys.89.025003.

[146] Zhenyue Zhu and Steven R. White. "Spin liquid phase of the $S = \frac{1}{2}$ $J_1 - J_2$ Heisenberg model on the triangular lattice". In: *Phys. Rev. B* 92 (4 2015), p. 041105. DOI: 10.1103/PhysRevB.92.041105.

[147] Zhenyue Zhu et al. "Topography of Spin Liquids on a Triangular Lattice". In: *Phys. Rev. Lett.* 120 (20 2018), p. 207203. DOI: 10.1103/PhysRevLett.120.207203.